Heavy Neutrino-Antineutrino Oscillations in Quantum Field Theory

and Their Lepton Number Violating Signatures at Colliders

Inauguraldissertation

zur
Erlangung der Würde eines Doktors der Philosophie
vorgelegt der
Philosophisch-Naturwissenschaftlichen Fakultät
der Universität Basel

von

Johannes Rosskopp

2023

Genehmigt von der Philosophisch-Naturwissenschaftlichen Fakultät
auf Antrag von

Erstbetreuer: Prof. Stefan Antusch
Zweitbetreuer: Prof. Christoph Bruder
Externer Experte: Prof. Joachim Kopp

Basel, den 28.03.2023

<div style="text-align:right">Prof. Dr. Marcel Mayor, Dekan</div>

Acknowledgements

Publications

The thesis is cumulative and contains the publications [1–4] to which the author of this thesis has contributed during his PhD studies between March 2019 and March 2023 under the supervision of Prof. Dr. Stefan Antusch.

- S. Antusch and J. Rosskopp, "Heavy Neutrino-Antineutrino Oscillations in Quantum Field Theory,"
  JHEP **03** (2021), 170 doi:10.1007/JHEP03(2021)170 [arXiv:2012.05763 [hep-ph]]

- S. Antusch, J. Hajer and J. Rosskopp, "Simulating lepton number violation induced by heavy neutrino-antineutrino oscillations at colliders,"
  JHEP **03** (2023), 110 doi:10.1007/JHEP03(2023)110 [arXiv:2210.10738 [hep-ph]].

- S. Antusch, J. Hajer and J. Rosskopp, "Beyond lepton number violation at the HL-LHC: Resolving heavy neutrino-antineutrino oscillations," [arXiv:2212.00562 [hep-ph]].

- S. Antusch, J. Hajer and J. Rosskopp, "Decoherence effects on lepton number violation from heavy neutrino-antineutrino oscillations," [arXiv:2307.06208 [hep-ph]].

Hereby, I (Johannes Rosskop, the author of this thesis) declare that all the fundamental work which led to the results presented in this thesis has been done by myself.
In particular:
The formal derivations in [1] and [4]
The algorithm to compute decoherence effects, used in [4]
The implementations of the phenomenological symmetry protected seesaw scenario (pSPSS) in FEYNRULES used in [2]
The patch of MADGRAPH, used in [3]
The C++ implementation of the cut based analysis, used in [3]
The generation of signal, and background events in, used in [3]
The derivation and application of the statistical methods, used in [3]

Contents

Chapter 1

Introduction

While the Standard Model (SM) of particle physics describes many phenomena with great precision, it is clear that it cannot be the final theory. A possible path towards a complete description of nature would be to understand the shortcomings of the SM and find solutions. One shortcoming presents itself in the neutrino sector. While the charged leptons obtain masses, the SM neutrinos remain massless. This prediction is in contrast to observations, in particular, flavour oscillations in solar neutrinos. Therefore an extension to the SM is needed that addresses this point.

The reason that SM neutrinos are massless can be understood by studying the electroweak (EW) theory. While the gauge group of the SM reads $SU(3)_c \times SU(2)_L \times U(1)_Y$, the EW theory does not describe quantum chromodynamics (QCD), which symmetry group is $SU(3)_c$. The gauge group of a theory is also called the symmetry group since its generators yield transformations that can be applied to the quantum fields of the corresponding theory without changing the equations of motion. The EW gauge group is $SU(2)_L \times U(1)_Y$. The part of the Lagrangian governing the fermionic terms reads

$$\mathcal{L}_{\mathrm{EW},f} = i\overline{L}_\alpha D_\mu \gamma^\mu l_\alpha + \overline{L}_\alpha Y^{\alpha\beta} l_\beta H + \mathrm{H.c.} \; .$$

L_α and H are the charged lepton and Higgs $SU(2)$ doublets, respectively, where the flavour index runs over the three families $\alpha = e, \mu, \tau$. The lepton doublet contains the left chiral charged leptons e_α and the SM neutrinos ν_α, while the right-handed charged lepton fields are denoted by l_α. $Y^{\alpha\beta}$ contains all Yukawa couplings, and the covariant derivative is defined by

$$D_\mu L_\alpha = \left(\partial_\mu - iqT_a A_\mu^a\right)L_\alpha \,,$$

where the implicit sum over T_a and A^a contains all gauge fields and respective generators the spinor L_α transforms under.

A major part of the EW theory, and of the SM, is the spontaneous symmetry breaking, in this case, called electroweak symmetry breaking (EWSB), implemented via the Higgs mechanism. The potential of the Higgs is such that its neutral component acquires a vacuum expectation value (VEV). This way, the SM gauge group is broken down

$$SU(3)_c \times SU(2)_L \times U(1)_Y \to SU(3)_c \times U(1)_{EM} \,,$$

where $U(1)_{EM}$ describes the electromagnetic interaction. It is worth noting that the SM contains an accidental symmetry that preserves the lepton number.

As a result of the symmetry breaking, Dirac mass terms for the charged leptons are generated

$$\overline{L}_\alpha Y^{\alpha\beta} l_\beta H \rightarrow (m_D)^\alpha \, \overline{e}_\alpha l_\alpha \,,$$

where it is assumed that a bi-unitary transformation was performed, such that the charged lepton mass matrix is diagonal. The Dirac mass term consists of a left chiral and a right chiral field and is proportional to the Higgs VEV. For this reason, it is not possible to write down a Dirac mass term for them. A second possibility to obtain a massive particle is writing down a Majorana mass term. For this, the respective field describing the particle has to be neutral under all symmetries. While neutrinos are electrically neutral and also do not interact via the strong interaction, they are part of the SM lepton doublet L_α and therefore charged under the $SU(2)_L$ and the $U(1)_Y$. For those reasons, a Majorana mass term for the SM neutrinos is not allowed; hence they remain massless.

As mentioned in the beginning, the absence of neutrino masses poses a problem. To see the reason for this, observations of neutrinos produced in the sun, so-called solar neutrinos, can be considered. The solar neutrino problem was discovered in the late 1960s, where the obtained upper bound on electron neutrinos was significantly smaller than expected [5]. Neutrino flavour oscillations were suggested as a possible solution for the seemingly vanishing neutrinos by Pontecorvo and Gribov in 1969 [6]. Understanding the proposed solution requires understanding the distinction between mass eigenstates and interaction eigenstates. While mass eigenstates diagonalise the kinetic part of the Lagrangian, neutrino interaction eigenstates diagonalise the interaction Lagrangian. Therefore, neutrinos are produced as interaction eigenstates but propagate as mass eigenstates. If, e.g., a solar neutrino is produced as an electron flavour eigenstate, it is expressed as a complex linear combination of mass eigenstates for propagation. This linear combination is also called a superposition. When those mass eigenstates travel from the sun to the earth, their complex phases vary differently if their masses are different. Consequently, once they arrive at a detector stationed on earth, the complex superposition has changed. The solar neutrino might no longer be in a well-defined flavour state but, instead, in a superposition of different flavour states. This superposition can be projected onto the electron flavour eigenstate to obtain the probability of the neutrino interacting as an electron neutrino. Varying masses of the light neutrinos result in a varying probability of the solar neutrino still being in its original flavour eigenstate. This constitutes a solution to the solar neutrino problem. While the electron neutrinos have not vanished, they have oscillated into a different flavour during propagation from the sun to the earth. Since the proposal of neutrino flavour oscillations as a solution to the solar neutrino problem, precise measurements resulted in experimental values for the two mass squared differences of the light neutrinos as well as additional neutrino parameters, such as the three mixing angles of the (PMNS) lepton mixing matrix. However, requiring the neutrinos to be massive, such that they can produce two mass differences, requires an extension of the SM.

Besides adding higher dimensional terms to the SM Lagrangian, the only possibility to obtain massive neutrinos is to extend the particle content of the SM. Note that ultimately higher dimensional terms also have to be explained by adding additional particles at a higher energy scale. At its coarsest, there are only two approaches to extend the SM with additional particles. In a top-down approach, a model is developed at a high energy scale that exhibits theoretically interesting features. A prominent example of such is a grand unified theory (GUT) [7–14]. A GUT aims to unify the electroweak and strong interactions under a gauge group of at least the same rank as the SM. The particle content then has to be arranged in representations of this gauge group, which, e.g., in the case of SU(5) or SO(10), adds new particles compared to the SM. The gauge group of the GUT has to be broken down to the gauge group of the SM at

low energies, which can be realised using spontaneous symmetry breaking. The problematic part is then to arrange the parameters of the GUT in such a way that the experimentally validated predictions of the SM are reproduced at low energies. A somewhat contrary option that circumvents these difficulties is to use a bottom-up approach. This strategy uses the SM as a framework and adds new particles to it. Making these additional particles either very heavy, compared to testable energy scales, or their coupling to the SM very small, the predictions of the SM are typically preserved. For this reason, the bottom-up approach is considered in this thesis. The minimal extension needed to explain the two measured mass differences of the light neutrinos is adding two sterile neutrinos. The term sterile is used to emphasise that they are singlets under the SM gauge group. Sometimes, the term right-handed neutrino is used, which is treated as a synonym in this work.

Even though the mass-squared differences of the light neutrinos are experimentally accessible, the absolute mass scale is harder to probe. There are some general cosmological arguments that set upper bounds [15–17]. From this, and from the fact that massless SM neutrinos explain most experiments so well, the mass scale of the light neutrinos has to be orders of magnitude smaller compared to the other massive SM particles.

The perhaps simplest possibility to obtain mass terms for the light neutrinos consists in adding Dirac mass terms. In the same fashion as for the charged leptons, a Yukawa term is formed by a SM lepton doublet, a Higgs doublet and a right-handed neutrino which yields

$$\overline{L}_\alpha Y^{\alpha a} N_a \tilde{H} + \text{H.c.} \,, \tag{1.0.1}$$

where $\tilde{H}$ is defined such that EWSB filters out the neutrino from the lepton doublet and N_a denote the right-handed neutrinos added to the SM. After EWSB, this Yukawa term produces a Dirac mass term for the light neutrinos. Similar to the charged leptons, this mass term is proportional to the Higgs VEV. To obtain neutrino masses at the order $m_\nu \lesssim 0.1\,\text{eV}$, the Yukawa couplings of the additional terms have to be tiny $y \lesssim \mathcal{O}(10^{-12})$. While this is a valid possibility, it opens up the question of why the neutrino Yukawa couplings are so small. Additionally, at least from the point of view of a bottom-up approach, it seems ad-hoc to have no Majorana mass term for the added right-handed neutrinos, even though they are singlets under the SM gauge group.

A possible solution that addresses both points is provided by the Type-I seesaw mechanism [18–24], in which a Majorana mass matrix for the sterile neutrinos is added, see [25]. Rotating into a basis in which the Majorana mass matrix is diagonal with eigenvalues at the scale m_M and the Dirac masses at the scale m_D, the light neutrino masses are naively expected to be at the scale m_D^2/m_M. Compared to the pure Dirac case, it is now possible to have bigger Dirac masses - and therefore bigger Yukawa couplings - if the Majorana mass scale is sufficiently large.

When introducing Majorana mass terms for the sterile neutrinos, the lepton number may no longer be conserved. This enables processes that violate the lepton number symmetry of the SM and introduce lepton number violation (LNV). Such processes are a key indicator for physics beyond the SM and are, therefore, a main target of experimental searches. The, until now, missing evidence of LNV puts constraints on the parameters of the seesaw machanism [26–29].

A major aspect of this thesis is to explore sterile neutrinos within reach of current collider experiments. In a simplistic view, a particle collider is a machine that accelerates beams of particles, collides them and measures the outcoming particles with sophisticated detectors. If two colliding beam particles interact with each other, they produce an event. The possible interactions and their kinematics are described by the underlying theory, e.g. the SM. Measurements that

are under tension with the predictions from the SM may therefore be a hint towards new physics. Following this simplistic view, we can summarise a particle collider by two numbers. Its integrated luminosity L and centre of mass energy E_{CM}. The E_{CM} is a measure of the energy available in collisions the collider produces. If, for example, a new particle is proposed at a mass $m \gg E_{CM}$, the collider is not able to produce events that contain this particle[1]. Even if the energy is large enough to produce the desired event containing the proposed particle, a discovery would not be guaranteed. This is because the chances that the desired event takes place are given by its cross-section.

A number of expected events can be obtained by considering how many events the collider is able to produce in a given time. This is the purpose of the integrated luminosity L. The number of expected events at a collider is then given by the integrated luminosity times the cross-section of the event

$$n = \sigma * L.$$

Therefore, a small cross-section requires a large integrated luminosity for the collider to produce a certain amount of events. The high luminosity phase of the LHC (HL-LHC) has a center of mass energy of $7\,\mathrm{TeV}$ and a integrated luminosity of $3\,ab^{-1}$, assuming a run time of about 12 years [30].

To be within reach of the HL-LHC, the sterile neutrinos are required to have masses below a few TeV while, at the same time, moderately sized Yukawa couplings to produce at least one event with a given integrated luminosity of around $3\,ab^{-1}$ are needed. Especially interesting observations might be possible for sterile neutrinos, lighter than the W boson. For those, the decay of a heavy neutrino into a W boson is energetically inaccessible, which increases the neutrinos' lifetime such that they become long-lived. As a consequence, after production, the heavy neutrinos may travel a measurable distance before they decay, forming a displaced vertex.

If the heavy neutrinos are within reach of the HL-LHC, a mechanism is needed to protect the smallness of the light neutrinos in order to satisfy experimental constraints. Such a mechanism is provided by the symmetry protected seesaw scenario (SPSS) [31, 32]. Here, a lepton-number-like symmetry is defined, which extends the lepton-number symmetry of the SM by assigning charges to the sterile neutrinos. As long as the *lepton number-like* symmetry (LNLS) is intact, the light neutrinos are massless and LNV processes are forbidden. In the case of two sterile neutrinos, the LNLS ensures that the two Majorana degrees of freedom (DOFs) can be rearranged to form a Dirac particle. The solution is to break the LNLS by a small parameter. This introduces both a small amount of LNV and a small mass splitting between the heavy neutrinos. Subsequently, they can no longer be arranged into a Dirac particle. In this case, the heavy neutrino pair is called pseudo-Dirac.

Considering the phenomenology of such a SPSS, new strategies are needed to observe beyond standard model physics since the naive LNV observables are suppressed due to the protective lepton-number-like symmetry. An interesting feature that proves useful in that regard is particle oscillations. Whenever there is a process in which the intermediate particles have different masses, oscillations should be considered. However, since the time scale of such oscillations is proportional to the inverse of the mass splitting of the intermediate particles, oscillations are typically so fast that they average out at experimentally accessible scales. In the case of the SPSS, the mass splitting of the heavy neutrinos is proportional to the small symmetry-breaking parameter. Therefore, particle oscillations due to propagating heavy neutrinos can be relevant in this case.

---

[1] Here, the word *contain* is defined as to only apply to on-shell particles that participate in the interactions.

In [1], it is shown that if only the heavy neutrinos are considered as propagating particles, flavour oscillations are subdominant compared to so-called heavy neutrino-antineutrino oscillations (HNANOs). In this type of oscillation, the interaction eigenstates are a neutrino produced together with a charged antilepton and an antineutrino produced together with a charged lepton. During the propagation of heavy neutrino mass eigenstates, the superposition oscillates between neutrinos and antineutrinos. Since the mass difference between light and heavy neutrino mass eigenstates is assumed to be much larger than the mass splitting among the light and heavy neutrinos, the light neutrinos do not have to be taken into account as propagating DOFs. Therefore, the resulting phenomenon is called heavy neutrino-antineutrino oscillation.

Due to the approximate LNLS, a neutrino projected onto the heavy mass eigenstates predominantly decays into a charged lepton, while a antineutrino projected onto the heavy mass eigenstates decays predominately into charged antileptons. The projected neutrino is called heavy neutrino, while the projected antineutrino is called heavy antineutrino. If an (anti)neutrino is produced and decays again as an (anti)neutrino, the resulting event is lepton number conserving (LNC). However, if the produced heavy neutrino oscillates and decays as an antineutrino, or similarly for an antineutrino decaying as a neutrino, the resulting event is LNV. Therefore, neutrino-antineutrino oscillations manifest themselves as an oscillating pattern between LNC and LNV events. A measurement of this oscillation pattern would allow for the reconstruction of the heavy neutrino mass differences and thus reveal some hints about the underlying mechanism of neutrino mass generation.

Typically particle oscillations, such as light neutrino flavour oscillations, are discussed in a quantum mechanical (QM) framework in which all particles are treated as plane waves. This, however, does not discuss the so-called observability conditions, which allow computing under which circumstances oscillations are suppressed. The derivation of HNANOs is put on a more solid base by using the quantum field theoretical (QFT) framework of external wave packets. While the derivation of oscillation formulae is technically more involved compared to the plane wave QM treatment, the final oscillation probability takes a simple form. Apart from the standard oscillation phase, the effects of the wave packets are gathered in a damping term λ. This damping is not only relevant to the feasibility of measuring and reconstructing the oscillation pattern but also has a major impact on the total ratio between LNV and LNC events in some parts of the parameter space.

In summary, sterile neutrinos are a minimal extension to the SM, able to explain the light neutrino masses under the right circumstances. When taking experimental bounds on the resulting heavy neutrino couplings and masses into account, the only possibility to have them in the reach of current collider experiments is a SPSS. The main work of this thesis focuses on describing LNV observables for such a SPSS. While most studies in this field have been done under the assumptions that the heavy neutrinos, which are also called heavy neutral leptons (HNLs) in this context, exhibit either the phenomenology of Dirac particles or of Majorana particles, the SPSS suggest the notion of a pseudo-Dirac particle. This exhibits new phenomenology, such as HNANOs, and requires a different treatment in the interpretation of existing searches for HNLs, which is explored in this work.

The papers in this thesis are organised as follows. In [1], the QFT wave packet formalism is introduced. The details of the computation are presented, and general formulae for the probability of HNANOs are obtained. These results are applied to the minimal low-scale linear seesaw model. The resulting simple oscillation formulae are presented and discussed at leading order (LO) and next-to leading order (NLO).

[2] contains a general discussion about collider-detectable heavy neutrinos that allow generating masses for the SM neutrinos via a SPSS. Subsequently, the phenomenological symmetry protected seesaw scenario (pSPSS) is introduced, which contains the minimal set of parameters to describe the phenomenology of a seesaw model with a slightly broken LNLS, including HNANOs. An implementation of the pSPSS in FeynRules is presented, as well as a patch of MadGraph that allows to simulate HNANOs. The implementations are then used to simulate the oscillation pattern in the proper time frame of heavy neutrinos and in the lab frame. Further, a discussion about the LNV over LNC event ratio R_{ll} is presented, in which the introduced implementations yield insights into the dependence of R_{ll} on various cuts.

In [3] the implementation of the pSPSS and the patched version of MadGraph followed by Pythia and Delphes are used to simulate HNANOs for three example parameter points at a CMS-like detector. Possible background processes for the considered signal process are discussed and partially simulated. A cut-based analysis, implemented in C++, is used to isolate the signal process from the simulated background. A statistical analysis based on log-likelihood ratios is presented in detail and subsequently applied to find the significance with which HNANOs can be discovered at the HL-LHC.

In [4] the details of the suppression of oscillations due to decoherence of the mass eigenstate superposition are discussed in detail. A distance-averaged oscillation formula is derived and presented for short and medium lifetimes of heavy neutrinos. For the SPSS and a given signal process, a simple suppression factor as a function of the heavy neutrinos' mean mass and mass splitting is obtained numerically. Finally, the effects of suppressed oscillations on the LNV over LNC event ratio R_{ll} are demonstrated.

Chapter 2

Heavy neutrino-antineutrino oscillations in quantum field theory

Abstract:

It has been proposed that the coherent propagation of long-lived heavy neutrino mass eigenstates can lead to an oscillating rate of lepton number conserving (LNC) and violating (LNV) events, as a function of the distance between the production and displaced decay vertices. We discuss this phenomenon, which we refer to as heavy neutrino-antineutrino oscillations, in the framework of quantum field theory (QFT), using the formalism of external wave packets. General formulae for the oscillation probabilities and the number of expected events are derived and the coherence and localisation conditions that have to be satisfied in order for neutrino-antineutrino oscillations to be observable are discussed. The formulae are then applied to a low scale seesaw scenario, which features two nearly mass degenerate heavy neutrinos that can be sufficiently long lived to produce a displaced vertex when their masses are below the W boson mass. The leading and next-to-leading order oscillation formulae for this scenario are derived. For an example parameter point used in previous studies, the kinematics of the considered LNC/LNV processes are simulated, to check that the coherence and localisation conditions are satisfied. Our results show that the phenomenon of heavy neutrino-antineutrino oscillations can indeed occur in low scale seesaw scenarios and that the previously used leading order formulae, derived with a plane wave approach, provide a good approximation for the considered example parameter point.

2.1 Introduction

After neutrino oscillations have been proposed by Pontecorvo in the late 50's [33], they have led to great insight into the (light) neutrino parameters. First introduced as neutrino-antineutrino oscillations, Maki, Nakagawa and Sakata considered oscillations into different flavours in 1962 [34]. Pontecorvo proposed in 1967 the possibility of solar neutrino oscillation, after which the solar neutrino problem was discovered [5]. In 1969, Pontecorvo and Gribov proposed neutrino flavour oscillations as a possible solution to this problem [6]. Since then, precise measurements of the light neutrino oscillations resulted in experimental values for the two mass squared differences of the light neutrinos as well as of the three mixing angles of the (PMNS) lepton mixing matrix and have provided a first indication of the range of the Dirac CP phase.

Despite this great success regarding the light neutrino parameters, the origin of the light neutrino masses, which requires an extension of the present Standard Model (SM) of elementary particles, is still unknown. One way to generate them consists in introducing right-chiral neutrinos as SM singlets. They can have Majorana mass terms as well as Yukawa couplings to the left-chiral SM neutrinos and the Higgs doublet. After electroweak symmetry breaking, the particle spectrum contains the three light neutrinos plus additional heavy neutrino mass eigenstates. If such heavy neutrinos are within reach of collider experiments, and if they are sufficiently long-lived, oscillations among the heavy neutrino and antineutrino interaction eigenstates could lead to great insight into the heavy neutrino parameters and thus into the neutrino mass generation mechanism.[1]

In parallel to the applications of neutrino oscillations also the framework in which they are described has evolved. The first approach to neutrino oscillations has been a quantum mechanical description in which the neutrinos are treated as plane waves. For neutral K meson oscillations, a quantum field model including wave packets was proposed in 1963 in Ref. [35]. In 1981, the authors of [36] pointed out conceptual problems of the plane wave approach for light neutrino oscillations and suggested a wave packet treatment as solution. To resolve the remaining difficulties, [37] introduced a quantum field theoretical model similar to [36], in which the propagating particle (assumed stable) is treated as an internal line in a Feynman diagram and the external particles are described by wave packets. A review of the existing quantum field theoretical approaches is given in [38], where also a framework employing external wave packets is discussed that can be used to describe the oscillations of unstable particles.

To describe heavy neutrino-antineutrino oscillations, a density matrix formalism (based on [39]) has been used in [40] for heavy neutrinos produced from meson decays. Using this formalism, formulae for the oscillation of the LNC and LNV decay rates have been calculated. The authors of [41] used a formalism for meson oscillations and plane wave arguments to derive formulae for heavy neutrino-antineutrino oscillations. These formulae are then applied to heavy neutrinos produced from W_R decays in a left-right symmetric extension of the SM, for heavy neutrino parameters testable at the LHC. There it was shown that without resolving the heavy neutrino-antineutrino oscillations, the integrated effect can induce a non-trivial ratio between LNV and LNC processes at colliders (for other early papers calculating non-trivial LNV/LNC ratios, without specifying oscillation formulae, see e.g. [42, 43]). The parameter region in which such non-trivial ratios are expected have been discussed e.g. in [44, 45]. In [44] it has been shown,

---

[1] We define a neutrino (antineutrino) as the neutral lepton that is produced together with a charged antilepton (lepton) and a W boson. The heavy neutrino (antineutrino) interaction eigenstates are defined as the projection of the neutrino (antineutrino) state onto the subspace of heavy mass eigenstates.

using the oscillation formulae from plane wave arguments (cf. [41]), that the signature of heavy neutrino-antineutrino oscillations can be resolved at collider experiments, considering minimal low scale type I seesaw extensions of the SM.

It has been shown in [44] that in the case of the low scale minimal linear seesaw model and inverse light neutrino mass hierarchy, the light neutrino mass splittings predict the heavy neutrino mass splitting, resulting in an oscillation length of order $\mathcal{O}(10\,\mathrm{cm})$ that could be resolved e.g. at the (high-luminosity phase of) LHCb. Furthermore, it has been pointed out that in a realistic experimental setting, where the momenta of the heavy neutrinos are given by a distribution, reconstructing these momenta and considering the oscillations as a function of the heavy (anti)neutrino proper time is required to resolve the oscillation patterns. The method has been demonstrated for an example parameter point, consistent with the present searches and non-collider constraints [44].

Currently there is an increasing interest in exploring heavy neutrino-antineutrino oscillations. For example, oscillations for rare W boson decays at LHC are further studied in [46, 47], and from tau decays in [48, 49] (using the formulae of [40]). The authors of [50] use plane wave arguments (together with a discussion of coherence conditions) to discuss the oscillations for a rather general right-handed neutrino mass matrix in a left-right symmetric extension of the SM. Discussions of how the insight into the low scale seesaw parameters from heavy neutrino-antineutrino oscillations can help to test whether the baryon asymmetry of the universe can be produced by the leptogenesis mechanism, are given e.g. in [51, 52]. So far, no QFT treatment using external wave packets has been performed for heavy neutrino-antineutrino oscillations yet.

The goal of this paper is to put the discussion of heavy neutrino-antineutrino oscillations on a more solid theoretical ground by treating them in the framework of QFT. We use the formalism of external wave packets (cf. [38]) to obtain a more fundamental derivation of the formulae for heavy neutrino-antineutrino oscillations, as well as a more fundamental discussion of the coherence and localisation conditions that have to be satisfied such that oscillations are observable. In addition, we apply our formulae to a specific realisation of the symmetry protected seesaw scenario (SPSS) [31, 32] and expand them in small lepton number violating parameters. The paper is organised as follows: In section 2 the formalism of heavy neutrino-antineutrino oscillations is described, the oscillation formulae as well as formulae for the expected number of events are derived and the coherence and localisation conditions are discussed. Section 3 contains the applications to the specific SPSS model and section 4 the approximations of the oscillation formulae and the discussion of the LO and NLO effects. In section 5 we conclude.

2.2 QFT Formalism for Heavy Neutrino-Antineutrino Oscillations

As mentioned above, we define neutrinos (antineutrinos) as those particles produced from the decay of a W boson, together with a charged antilepton (lepton), respectively. As a specific example we consider in the following the dilepton-dijet signature at pp colliders, which can be LNC as well as LNV. The relevant Feynman diagrams, in which the W boson is produced from pp collisions, are shown in figures 2.1a and 2.1b. With a W boson decaying into an antilepton, the produced neutrino state is a superposition of neutrino mass eigenstates, where we only consider the heavy mass eigenstates. We define this projection of the (anti)neutrino interaction eigenstate onto the heavy neutrino mass eigenstates as "heavy neutrino interaction eigenstate".

The neutrinos then propagate over a macroscopic distance after which they decay into either a lepton or an antilepton and an off-shell W boson, which in turn decays into two jets. If the neutrino superposition decays into a lepton and an off-shell W boson, the process is lepton number conserving (LNC) and if it decays into an antilepton it is lepton number violating (LNV). Although we focus on this example process, our results can be readily adapted to other processes as well.[2]
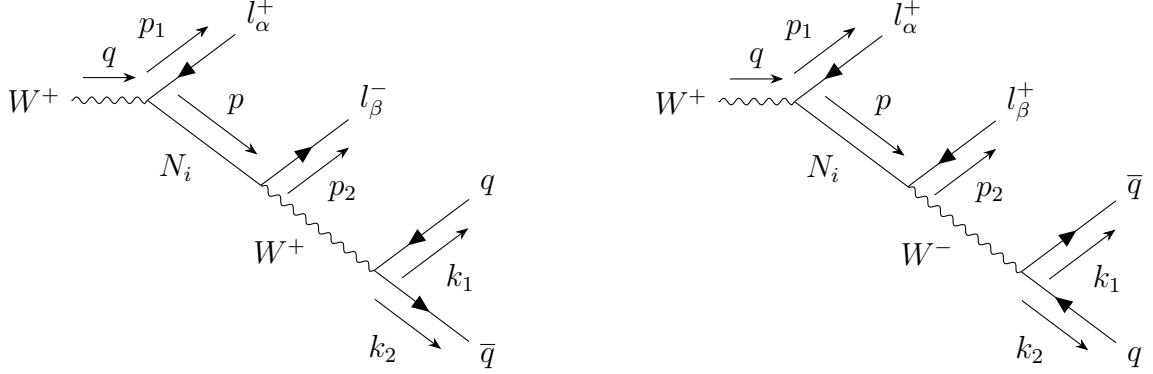
(a) Feynman diagram for the LNC process   (b) Feynman diagram for the LNV process

Figure 2.1: Feynman diagrams describing the LNC and LNV processes.

Starting with the general formula for the connected amplitude

$$\mathcal{A} = \langle f | \hat{T}\left(\exp\left(-i \int \mathrm{d}^4 x \, \mathcal{H}_I \right)\right) - \mathbf{1} | i \rangle \,, \tag{2.2.1}$$

where $\mathcal{H}_I$ is the interaction Hamiltonian and $\hat{T}$ the time ordering operator, we follow the procedure described in [38] for the LNC and LNV processes separately.

Using standard QFT methods in the canonical quantisation formalism, the process described by the Feynman diagrams figures 2.1a and 2.1b is obtained by expanding the exponential up to second order in the electroweak coupling constant. The external states are considered to be wave packets that are centred at the space-time points of production or detection as in [38]. This introduces integrals over the momenta of the external particles together with functions describing the shape of the wave packets, which we denote as Ψ, as well as space-time translation operators in the form of exponentials accompanying each wave packet. The propagator of the intermediate particle is obtained by contraction of the relevant fields in configuration space. Using the Fourier transformation it is written down in momentum space, introducing the integral over the neutrino momentum p. The relevant Feynman rules, which are applicable also to the LNV process, can be found in [53]. The amplitudes for the processes described by the Feynman diagrams figures 2.1a and 2.1b can be written as

$$\mathcal{A}_{\alpha\beta}^{LNC} := \sum_j V_{j\beta} \mathcal{A}_j^{LNC} V_{j\alpha}^* \,, \tag{2.2.2}$$

$$\mathcal{A}_{\alpha\beta}^{LNV} := \sum_j V_{j\beta}^* \mathcal{A}_j^{LNV} V_{j\alpha}^* \,, \tag{2.2.3}$$

<hr>

[2] The process in which the initial W^+ is replaced by a W^- differs only in the leptonic mixing factors (later denoted by V), which are complex conjugate to the ones appearing in the process with an initial W^+.

where α and β denote the flavour indices of the charged leptons at production and detection and LNC and LNV refers to the lepton number violating or lepton number conserving process, respectively. The sum runs over the propagating mass eigenstates, which are denoted by the indices i and j in this paper. The relevant part of the lepton mixing matrix, rotating the heavy neutrino mass eigenstates into the active neutrino interaction eigenstates is denoted by V and the so-called partial amplitude $\mathcal{A}_j^{LNX}$ is defined as

$$
\mathcal{A}_j^{LNX} := \int \mathrm{d}^4\mathrm{x} \int \mathrm{d}^4\mathrm{x}' \int [\mathrm{dq}] \Psi(\boldsymbol{q}, \boldsymbol{Q}) e^{-iqx} \int [\mathrm{dp_1}] \Psi^*(\boldsymbol{p_1}, \boldsymbol{P_1}) e^{ip_1 x}
$$
$$
\int [\mathrm{dp_2}] \Psi^*(\boldsymbol{p_2}, \boldsymbol{P_2}) e^{ip_2 x'} \int [\mathrm{dk_1}] \Psi^*(\boldsymbol{k_1}, \boldsymbol{K_1}) e^{ik_1 x'} \int [\mathrm{dk_2}] \Psi^*(\boldsymbol{k_2}, \boldsymbol{K_2}) e^{ik_2 x'} \qquad (2.2.4)
$$
$$
\int \frac{\mathrm{d}^4\mathrm{p}}{(2\pi)^4} e^{ipx} e^{-ipx'} \ e^{-ip(x_1-x_0)} M_j^{LNX}(p, Q, P_1, P_2, K_1, K_2) \frac{1}{p^2 - m_{\nu_j}^2} \ ,
$$

where $\Psi(\boldsymbol{k}, \boldsymbol{K})$ describes a wave packet centred at three momentum $\boldsymbol{K}$. The integration measure for the three momenta is written in a short hand notation where

$$
[d\boldsymbol{k}] = \frac{d^3\boldsymbol{k}}{(2\pi)^3 \sqrt{2E_k}} \ ,
$$

with E_k being the energy of the respective particle. The interaction amplitude M_j^{LNX} is defined as the matrix element of the LNX process without the lepton mixing matrix elements and without the denominator of the propagator, where LNX can refer either to LNC or LNV. Note that we have suppressed the spin and polarisation labels of the external particles to simplify notation. The production (x_0) and detection (x_1) points in spacetime are defined with respect to the laboratory frame. Therefore the propagation distance, which is defined as $\boldsymbol{L} := \boldsymbol{x_1} - \boldsymbol{x_0}$, is also to be understood in the laboratory frame. The propagation time is given by $T := x_1^0 - x_0^0$.

The authors of [38] proceed with the partial amplitude by evaluating the integrals over the three momenta of the external particles, which can be done analytically if the wave packets are assumed to have a Gaussian shape and if the interaction amplitude is approximated at the mean momenta of the external particles. The approximated interaction amplitude is written as $M_j^{LNX}(p, Q, P_1, X^N) := M_j^{LNX}(p, Q, P_1, P_2, K_1, K_2)$, where X^N denotes the mean momenta of the decay products of the heavy neutrinos. This is followed by the integration over x and x' corresponding to the production and detection vertices.

The last step in the computation of the partial amplitude consists in the integration over the four momentum of the intermediate particle, which shows up in the propagator. The energy integral is done by the use of the Jacob-Sachs theorem [54], which basically puts the intermediate particle on-shell. The integration over the three momentum is done in three regimes separately depending on the propagation distance of the intermediate particle. The following steps are valid in the longitudinal dispersion regime, which is applicable when the propagation distance is larger than the dispersion length (cf. [38]). In section 2.2.1 it is argued that this regime is indeed the relevant one when we estimate the widths of the wave packets from measurement uncertainties. In this regime the three-momentum of the j-th neutrino mass eigenstate is approximated around the point of stationary phase $\boldsymbol{p}_{cl,j}$, which is the "classical" momentum given by

$$
\boldsymbol{p}_{cl,j} = m_j \gamma_{cl} \boldsymbol{v}_{cl} \ , \qquad (2.2.5)
$$

where the classical velocity is defined as $\boldsymbol{v}_{cl} = \boldsymbol{L}/T$ with the corresponding gamma factor $\gamma_{cl} = (1 - |\boldsymbol{v}_{cl}|^2)^{-1/2}$. The classical energy is defined accordingly as

$$
E_{cl,j} = \sqrt{m_j^2 + |\boldsymbol{p}_{cl,j}|^2} \ . \qquad (2.2.6)
$$

In the LNC case, the interaction amplitude M_j^{LNX} is dependent on $\boldsymbol{p}$, which we approximate at the point $\boldsymbol{p}_{cl,j}$ as well.

The "oscillation probability densities" are proportional to the absolute value squared of the respective amplitudes, averaged over the macroscopic propagation time

$$P_{\alpha\beta}^{LNX}(\boldsymbol{L}, Q, P_1, X^N) \propto \int dT \mathcal{A}_{\alpha\beta}^{LNX} (\mathcal{A}_{\alpha\beta}^{LNX})^* . \tag{2.2.7}$$

To proceed with this integration Laplace's method is used in which the macroscopic propagation time is expanded around $\tilde{T}_0$ (cf. [38])

$$T \approx \tilde{T}_0 = \frac{\tilde{E}_0 |\boldsymbol{L}|}{|p_0|} , \tag{2.2.8}$$

where $p_0 := \boldsymbol{p}_0 \cdot \boldsymbol{L}/|\boldsymbol{L}|$. The mean energy is defined as $\tilde{E}_0 := \sqrt{\tilde{m}_0^2 + |\boldsymbol{p}_0|^2}$, with the arithmetic mean of the heavy neutrino masses $\tilde{m}_0$. The four momentum p_0 is defined via the mean momenta of the external particles using energy-momentum conservation at the production and/or detection vertex, which yields

$$p_0 := Q - P_1 = P_2 + K_1 + K_2 . \tag{2.2.9}$$

A related mass can be defined as

$$m_0^2 := E_0^2 - \boldsymbol{p}_0^2 . \tag{2.2.10}$$

Note that these so called "reconstructed" quantities, which are labelled with a subscript $(\ )_0$, represent experimentally accessible quantities. As described below (see section 2.2.1), the reconstructed mass m_0 is related to the physical masses of the heavy neutrinos. In particular we note that if the heavy neutrinos are almost mass degenerate such that $m_i \approx \tilde{m}_0$, equation (2.2.50) can be used to argue that $\tilde{m}_0 \approx m_0$ within the momentum uncertainty given by the wave packets widths. Using equation (2.2.8) yields

$$\boldsymbol{p}_{cl,j} = m_j \frac{1}{\sqrt{1 - \frac{|\boldsymbol{p}_0|^2}{\tilde{E}_0^2}}} \frac{|p_0|}{\tilde{E}_0} \frac{\boldsymbol{L}}{|\boldsymbol{L}|} . \tag{2.2.11}$$

Due to the wave packet nature of the intermediate particle there is a non-zero probability to measure the decay vertex in a direction $\boldsymbol{L}$ from the production vertex not parallel to $\boldsymbol{p}_0$. However, those orthogonal directions are exponentially suppressed and negligible if the momentum uncertainties are small, i.e. if σ_p (see section 2.A) is smaller than the orthogonal momentum $\boldsymbol{p}_0 \times \boldsymbol{L}/|\boldsymbol{L}|$. We therefore introduce an integration over the direction of $\boldsymbol{L}$, which is evaluated by approximating $\boldsymbol{L}/|\boldsymbol{L}| \approx \boldsymbol{p}_0/|\boldsymbol{p}_0|$. This approximation allows to identify $p_0 = |\boldsymbol{p}_0|$. Also, with $m_j \approx m_0$, which holds for nearly mass degenerate heavy neutrinos as mentioned above, the four momenta $p_{cl,i}$ and p_0 are approximately equal.

The time integration together with the integration over the direction of $\boldsymbol{L}$ leads to

$$\begin{aligned} P_{\alpha\beta}^{LNX}(L, Q, P_1, X^N) &:= \int_{4\pi} L^2 d\Omega_{\boldsymbol{L}} P_{\alpha\beta}^{LNX}(\boldsymbol{L}, Q, P_1, X^N) \\ &= \sum_{i,j} N_g^2 M_i^{LNX}(p_{cl,i}, Q, P_1, X^N)(M_j^{LNX}(p_{cl,j}, Q, P_1, X^N))^* \\ &\quad \times \mathcal{V}_{\alpha\beta\ ij}^{LNX} \exp\left(-2\pi i \frac{L}{L_{ij}^{osc}}\right) , \end{aligned} \tag{2.2.12}$$

where $L := |\boldsymbol{L}|$ has been defined. We note that in the case of the no-dispersion regime, following the steps in [38], one obtains the same equation equation (2.2.12) and therefore the next considerations (until section 2.2.1) hold for both regimes. The proportionality constant N_g^2 can be obtained by the following normalisation condition, which has to be computed $\forall\{L, \alpha\}$

$$\sum_{\text{spins}} \int_{\text{PS}^N} dX^N \sum_\beta \left(\left[P_{\alpha\beta}^{LNC} + P_{\alpha\beta}^{LNV} \right](L, Q, P_1, X^N) \right) = 1 \ , \tag{2.2.13}$$

where $\int dX^N$ denotes an integral over the whole phase space of the decay products of the heavy neutrino PS^N and $\sum_{\text{spins}}$ represents the sum over all outgoing spins/polarisations and the average over all incoming spins/polarisations. Lepton mixing matrix factors are contained in $\mathcal{V}_{\alpha\beta\ ij}^{LNX}$, which is defined as

$$\begin{aligned} \mathcal{V}_{\alpha\beta\ ij}^{LNC} &:= V_{\beta i} V_{\alpha i}^* V_{\beta j}^* V_{\alpha j} \ , \\ \mathcal{V}_{\alpha\beta\ ij}^{LNV} &:= V_{\beta i}^* V_{\alpha i}^* V_{\beta j} V_{\alpha j} \ . \end{aligned} \tag{2.2.14}$$

The oscillation length is given by

$$L_{ij}^{osc} = \frac{4\pi |\boldsymbol{p}_0|}{m_i^2 - m_j^2} \ , \tag{2.2.15}$$

where $\boldsymbol{p}_0$ is defined in equation (2.2.9). Additional terms which can be neglected, given the adequate kinematic and experimental conditions, are discussed in section 2.2.1.

Together with the normalisation condition, the oscillation probability densities $P_{\alpha\beta}^{LNX}(L, Q, P_1, X^N)$ are defined as densities with respect to the mean momenta of the decay products of the heavy neutrino. If this density is integrated over the considered phase space of the heavy neutrino decay products $PS_p^N \subset PS^N$ an oscillation probability is obtained as

$$P_{\alpha\beta}^{LNX}(L, Q, P_1) = \int_{\text{PS}_p^N} dX^N P_{\alpha\beta}^{LNX}(L, Q, P_1, X^N) \ . \tag{2.2.16}$$

The results describe the probabilities that the superposition of heavy neutrino mass eigenstates, produced by the decay of a W boson together with an antilepton of flavour α, produces an (anti)lepton of flavour β if it decays after a distance L in the direction of $\boldsymbol{p}_0$ via an LNC (LNV) process.[3] When summing these probabilities over the flavour of the final (anti)lepton, the resulting quantity $\sum_\beta P_{\alpha\beta}^{LNV}(L, Q, P_1)$ can be interpreted as the probability that the produced heavy neutrino interaction eigenstate has oscillated into a heavy antineutrino interaction eigenstate. The quantity $\sum_\beta P_{\alpha\beta}^{LNC}(L, Q, P_1)$ can be interpreted as the probability that the heavy neutrino interaction eigenstate has "survived", i.e. has not oscillated into a heavy antineutrino interaction eigenstate.

At this point equation (2.2.16) together with the additional terms, to be discussed in section 2.2.1, can be regarded as the most general result. We now proceed simplifying it, in order to gain further insight. To this end, we first show under which conditions the interaction amplitudes can be factored out of the sum over mass eigenstates, and subsequently be absorbed into the normalisation constant.[4] After that we commit to a specific model within the SPSS,

---

[3] The normalisation condition is such that decays into other final states than the ones given in figures 2.1a and 2.1b are not considered.

[4] We note that in the case of light neutrino flavour oscillations, when the possibility of oscillating into light antineutrinos is neglected, this is always possible. On the contrary, in the here considered case of heavy neutrino-antineutrino oscillations it is an approximation.

which features two almost degenerate heavy neutrinos.

The interaction amplitude is dependent on the masses of the propagating neutrinos through the numerator of the propagator, which reads $(\not{p}_{cl,j} + m_j)$. The neutrino masses are expressed as a deviation from the mean neutrino mass $\tilde{m}_0$.[5] In the case of just two heavy neutrinos, with masses m_4 and m_5, where w.l.o.g. $m_4 < m_5$ can be assumed, one finds that

$$
\begin{aligned}
m_4 &= (1 - \lambda_m)\tilde{m}_0 \\
m_5 &= (1 + \lambda_m)\tilde{m}_0 \;,
\end{aligned}
\tag{2.2.17}
$$

where the dimensionless mass splitting parameter λ_m is defined as

$$
\lambda_m = \frac{m_5 - m_4}{m_5 + m_4} \;,
\tag{2.2.18}
$$

and the mean mass is just given by

$$
\tilde{m}_0 = (m_4 + m_5)/2 \;.
\tag{2.2.19}
$$

Using the definition equation (2.2.5), the classical momentum can also be expressed using the mass splitting parameter, which yields

$$
\begin{aligned}
\boldsymbol{p}_{cl,4} &= (1 - \lambda_m)\tilde{\boldsymbol{p}}_{cl,0} \\
\boldsymbol{p}_{cl,5} &= (1 + \lambda_m)\tilde{\boldsymbol{p}}_{cl,0} \;,
\end{aligned}
\tag{2.2.20}
$$

where the mean momentum is defined as $\tilde{\boldsymbol{p}}_{cl,0} = \tilde{m}_0 \gamma_{cl} \boldsymbol{v}_{cl}$. Note that using equations (2.2.17) and (2.2.20) it is easy to reparameterize the four momentum of an on-shell particle. This makes it possible to factor out the mass dependence from the interaction amplitudes, yielding

$$
M_i^{LNX}(p_{cl,i}, Q, P_1, X^N)(M_j^{LNX}(p_{cl,j}, Q, P_1, X^N))^* = \Lambda_{ij}|M^{LNX}(\tilde{p}_{cl,0}, Q, P_1, X^N)|^2 \;,
\tag{2.2.21}
$$

where Λ_{ij} contains the factors describing the mass and momentum splitting and is given by

$$
\Lambda_{ij} = \begin{cases}
(1 - \lambda_m)^2 & \text{if } i = j = 4 \\
(1 + \lambda_m)^2 & \text{if } i = j = 5 \\
(1 - \lambda_m^2) & \text{if } i \neq j \;.
\end{cases}
\tag{2.2.22}
$$

The interaction amplitudes of the processes figures 2.1a and 2.1b can be written down by using the Feynman rule conventions described in [53], which are applicable also to the lepton number violating diagram. This yields

$$
\begin{aligned}
iM_j^{LNC}(p_{cl,j}, Q, P_1, X^N) = i\frac{4G_F}{\sqrt{2}} &\left(\overline{u}(K_1)\; \Gamma^\nu\; v(K_2) \right) \\
&\left(\overline{u}(P_2)\; \Gamma_\nu\; i(\not{p}_{cl,j} + m_j)\; \frac{ig_2}{\sqrt{2}}\; \Gamma_\mu\; v(P_1) \right)\epsilon_\mu^*(Q) \;,
\end{aligned}
\tag{2.2.23}
$$

and

$$
\begin{aligned}
iM_j^{LNV}(p_{cl,j}, Q, P_1, X^N) = i\frac{4G_F}{\sqrt{2}} &\left(\overline{u}(K_2)\; \Gamma^\nu\; v(K_1) \right) \\
&\left(\overline{u}(P_2)\; \Gamma_\nu'\; i(\not{p}_{cl,j} + m_j)\; \frac{ig_2}{\sqrt{2}}\; \Gamma_\mu\; v(P_1) \right)\epsilon_\mu^*(Q) \;,
\end{aligned}
\tag{2.2.24}
$$

---

[5] The following reparameterization can easily be extended to more than two mass eigenstates.

where g_2 is the coupling of the $SU(2)$ gauge bosons and G_F is the Fermi constant. The vertices Γ^μ and Γ'^μ are given by $\gamma^\mu P_L$ and $-\gamma^\mu P_R$ respectively, with the left and right chirality projection operators defined as

$$P_{L/R} := \frac{1}{2}(1 \mp \gamma^5) \ . \tag{2.2.25}$$

Note that, as above we have suppressed spinor and color indices as well as indices denoting the spin and polarisation of the external particles. For the neutrino we chose the fermion flow from left to right in figures 2.1a and 2.1b.

Further simplifications are possible if the spin correlation between the production and detection vertex are neglected, i.e. if the numerator of the propagator can be written as

$$(\slashed{\tilde{p}}_{cl,0} + \tilde{m}_0) = \sum_s \overline{u}_s(\tilde{p}_{cl,0})u_s(\tilde{p}_{cl,0}) \approx \sum_{s,s'} \overline{u}_s(\tilde{p}_{cl,0})u_{s'}(\tilde{p}_{cl,0}) \ . \tag{2.2.26}$$

This approximation is also done in the narrow width approximation and makes it possible to factorize the interaction amplitude into a production interaction amplitude and a detection interaction amplitude. Using this approximation, the interaction amplitudes for the LNC and LNV process are identical.

If the spin correlation is not neglected, the interaction amplitudes of the LNC and LNV process differ due to the chirality structure. For a given process it could be possible that the interaction amplitudes depend on the orientation of the momenta of the external particles in such a way that a probabilistic classification into LNC or LNV becomes possible, which could be interesting, e.g. for the SHiP experiment [55].

In order to simplify the expression equation (2.2.12), following the above discussion, the spin correlation between the production and detection vertices are neglected. This allows to absorb the mass splitting independent parts of the interaction amplitudes in equation (2.2.12) into the normalisation constant.

This leads to the following oscillation probability, which is independent of the mean momenta of the decay products of the heavy neutrino, spins and polarisations of the external particles

$$P_{\alpha\beta}^{LNX}(L,Q,P_1) := \sum_{\text{spins}} \int_{\text{PS}^N} dX^N \ P_{\alpha\beta}^{LNX}(L,Q,P_1,X^N) \ . \tag{2.2.27}$$

Due to these simplifications the oscillation probability only depends on Q and P_1 in the combination $|\boldsymbol{p}_0| = |\boldsymbol{Q} - \boldsymbol{P}_1|$, which yields

$$P_{\alpha\beta}^{LNX}(L,|\boldsymbol{p}_0|) = \sum_{i,j} N^2 \Lambda_{ij} \ \mathcal{V}_{\alpha\beta \ ij}^{LNX} \exp\left(-2\pi i \frac{L}{L_{ij}^{osc}}\right) \ . \tag{2.2.28}$$

The normalisation condition for the simplified oscillation probability is given by

$$\sum_\beta \left(\left[P_{\alpha\beta}^{LNC} + P_{\alpha\beta}^{LNV}\right](L,|\boldsymbol{p}_0|) \right) = 1 \qquad \forall\{L,|\boldsymbol{p}_0|\} \ . \tag{2.2.29}$$

In section 2.4 the normalisation constant is evaluated explicitly for a specific example model of interest.

To proceed further we assume the experimental conditions and model parameters to be such that the heavy neutrinos travel a macroscopic distance before they decay, forming a displaced vertex. The number of expected events that feature such a displaced vertex can be expressed as a formula similar to the one described in [56]. This formula has to be modified in order to cover the circumstances of this paper. In particular an expression for the probability that the heavy neutrino decays in an LNC (LNV) manner involving a specific lepton flavour between a minimum and maximum distance is needed. Following the discussion in [38] regarding unstable oscillating particles, it is shown that the only relevant modification to the oscillation formula is given by the exponential discussed in section 2.2.1. If the masses and decay widths of the heavy neutrinos are nearly identical, it is possible to define a common decay length as

$$\tilde{L}_0^{decay} := \frac{p_0}{\tilde{m}_0 \tilde{\Gamma}_0} \ , \qquad (2.2.30)$$

where the common decay width is defined as

$$\tilde{\Gamma}_0 := \frac{\Gamma_4 + \Gamma_5}{2} \ . \qquad (2.2.31)$$

The exponential

$$\exp\left(-\frac{L}{\tilde{L}_0^{decay}}\right) \qquad (2.2.32)$$

describes the probability that a particle is still present at distance L. Therefore the probability density that the particle decays at distance L is given by the derivative

$$-\frac{d}{dL} \exp\left(-\frac{L}{\tilde{L}_0^{decay}}\right) \ . \qquad (2.2.33)$$

With this the probability that a particle decays in an LNX process into flavour β between $x_{min}(\vartheta)$ and $x_{max}(\vartheta)$ is given by

$$P_{dv\ \alpha\beta}^{LNX}(x_{min}(\vartheta), x_{max}(\vartheta), |\boldsymbol{p}_0|) = \int_{x_{min}(\vartheta)}^{x_{max}(\vartheta)} P_{\alpha\beta}^{LNX}(L, |\boldsymbol{p}_0|) \left(-\frac{d}{dL} \exp\left(-\frac{L}{\tilde{L}_0^{decay}}\right)\right) dL \ , \quad (2.2.34)$$

where the subscript dv stands for displaced vertex and ϑ denotes the angle of the heavy neutrino with respect to the beam axis. Usually the interval $[x_{min}(\vartheta), x_{max}(\vartheta)]$ will be chosen to lie inside the detector, such that the decay products can be measured. The detector geometry can be taken into account by the dependence on ϑ. The number of expected LNX events in which an antilepton of flavour α is measured at the production vertex and a lepton (LNC) or antilepton (LNV) of flavour β is measured at the detection vertex is given by

$$N_{\alpha\beta}^{LNX} = \tilde{\sigma}_{N,0} \ \tilde{Br}_{ljj,0} \ \mathcal{L} \ \int D_N(\vartheta, |\boldsymbol{p}_0|) \ P_{dv\ \alpha\beta}^{LNX}(x_{min}(\vartheta), x_{max}(\vartheta), |\boldsymbol{p}_0|) \ d\vartheta d|\boldsymbol{p}_0| \ , \qquad (2.2.35)$$

where $\tilde{\sigma}_{N,0}$ is the mean production cross section of the heavy neutrinos, which depends on model parameters such as the masses of the heavy neutrinos and the details of the lepton mixing matrix. $\tilde{Br}_{ljj,0}$ is the mean branching ratio for the decay of a heavy neutrino into a lepton and two jets and $\mathcal{L}$ is the time integrated luminosity. Therefore, the factor $\tilde{\sigma}_{N,0} \ \tilde{Br}_{ljj,0} \ \mathcal{L}$ describes the total number of events in which a heavy neutrino is produced and decays into a lepton and two jets. It is assumed that the branching ratios as well as the production cross sections for different mass eigenstates are nearly identical in order for such an approximation to be appropriate. The remaining factor $D_N(\vartheta, |\boldsymbol{p}_0|)$ accounts for the probability density that the reconstructed heavy

neutrino has momentum of modulus $|\boldsymbol{p}_0|$ and is produced with an angle ϑ with respect to the beam axis. As discussed above, $P_{dv\ \alpha\beta}^{LNX}(x_{min}(\vartheta), x_{max}(\vartheta), |\boldsymbol{p}_0|)$ gives the probability that the heavy neutrino decays in an LNX manner into flavour β inside the interval $[x_{min}(\vartheta), x_{max}(\vartheta)]$. Note that if one wanted to consider the spin correlation, one has to use equation (2.2.16) in the definition of equation (2.2.34).

2.2.1 Observability Conditions and Dispersion Length

In order for the oscillations to be observable there are several conditions which have to be satisfied. This subsection describes those conditions and estimates their viability for typical parameters of long-lived heavy neutrinos detectable at, e.g. HL-LHCb. We consider as an explicit example a parameter point for the minimal low scale linear seesaw model that has also been used in Ref. [44].

To compute all relevant parameters it is necessary to know the kinematics of the process and the widths of the external wave packets. One approach to estimate these widths is based on the following considerations: Since the final particles at production and detection are reconstructed by measurements at a detector, the uncertainty of the measurement should be reflected by the widths of the respective wave packets. For charged leptons a relative momentum uncertainty in the range $(\Delta p/p)_{lepton} = [0.5\%, 1\%]$ holds for particles with a long enough track, cf. [57], which we therefore use for the widths of the charged lepton wave packets. The momentum resolution for the quarks, which are reconstructed from displaced jets, is much harder to determine. For a conservative estimate we therefore use a large range for their relative momentum uncertainty $(\Delta p/p)_{quark} = [5\%, 30\%]$ (and thus for the possible widths of the quark wave packets). Finally, the width of the wave packet of the initial W boson is taken to be its decay width ($\Gamma_W \approx 2\,\mathrm{GeV}$).

Alternatively, one can also try to estimate the widths of the wave packets in position space based on the consideration that the uncertainty is determined by interactions with detector/beam particles and their respective widths. For the W boson one could use the proton-proton distance in the proton bunches, which at the LHC is about 5×10^{-6} cm, whereas for the leptons and quarks one might take a wave packet width of the order of an atom radius, i.e. about 10^{-8} cm. This would lead to significantly smaller widths in momentum space compared to the estimate using the measurement uncertainty, such that the appropriate regime is the no-dispersion regime (cf. [38]). We have checked that the relevant observability conditions in this case are all satisfied for our example parameter point, and our results from equations (2.2.16), (2.2.35), (2.4.2), and (2.4.3) can also be used for these estimates of the wave packet widths. From now on we will focus on the estimates for the wave packet widths from the momentum space considerations.

The kinematics of the processes described by figures 2.1a and 2.1b have been simulated, assuming two nearly degenerate heavy neutrinos. Since the purpose of the simulation is to compute the parameters necessary to check the observability conditions and not to simulate the oscillation process itself, all particles can be treated as plane waves, where their momentum represents the momentum of the peak of the wave packet. Simulating enough events, where the momentum of the W boson is taken in the range 340 GeV to 2 TeV. It is then possible to check if the observability conditions are fulfilled. For the simulation the parameter values in table 2.1 have been used. It has also been assumed for simplicity that there are two heavy neutrino mass eigenstates with masses m_4 and m_5.

parameter	value
γ	≈ 50
$\tilde{m}_0$ [GeV]	7
δm_{45}^2 [GeV^2]	-1.04×10^{-11}
$(\Delta p/p)_{lepton}$	$0.5\% - 1\%$
$(\Delta p/p)_{quark}$	$5\% - 30\%$

Table 2.1: Parameters used for simulating the kinematics of the processes in figures 2.1a and 2.1b, in order to evaluate the observability conditions for the example minimal low scale seesaw parameter point used in [44]. γ denotes the gamma factor of the heavy neutrinos, $\tilde{m}_0$ their mean mass (which in the simulation coincides with m_0), and the squared mass splitting $\delta m_{45}^2 = m_4^2 - m_5^2$ in the scenario of [44] is predicted by the measured values of the light neutrino mass splittings. The used range for the uncertainties in the measurement of the momenta of the external charged leptons and jets are denoted as $(\Delta p/p)_{lepton}$ and $(\Delta p/p)_{quark}$.

The observability conditions are given as exponential suppression factors. If it is not clear that they are satisfied those exponential factors have to be included into the probability equation (2.2.12) or equation (2.2.28), respectively. It is worth mentioning that including exponential terms into the probability changes the normalisation constant, which can be computed using equation (2.2.13) or equation (2.2.29). The quantities used in the computation of the observability conditions are defined in section 2.A.

The *oscillation length* sets the scale of the experiment, since it is the length at which the measurements should be taken in order to observe oscillations. As stated above it is given by

$$L_{ij}^{osc} = \frac{4\pi|\boldsymbol{p}_0|}{m_i^2 - m_j^2} \ .$$

With the parameters in table 2.1 (with $\gamma = 50$) it can be computed to be

$$L_{45}^{osc} \approx 8.34 \text{ cm} \ , \tag{2.2.36}$$

where the two heavy neutrino mass eigenstates are labelled with subscript numbers 4 and 5.

The *effective width* σ_{peff} (see [38]) can be interpreted as the width of the wave packets of the heavy neutrinos. A rough estimate of the effective width can be obtained by neglecting the detection process and by approximating the lepton in the production process as a plane wave. Due to energy-momentum conservation, the shape of the effective wave packets of the heavy neutrinos is then given by the one of the initial W boson, which width is approximated by its decay width. However, simulating the kinematics of the process and computing the width numerically shows that it is in the range

$$\sigma_{peff}^{sim} \in [4.5 \times 10^{-3}, \ 32] \text{ GeV} \ , \tag{2.2.37}$$

showing that the estimate $\sigma_{peff} \approx 2$ GeV is indeed very rough.

The *dispersion length* is the threshold at which the spread of the wave packets of the heavy neutrinos becomes significant in all directions. At distances larger than the dispersion length the methods of the longitudinal dispersion regime have to be used. The dispersion length is given by [38]

$$L_j^{disp} = v_0 \frac{E_0^2}{2m_j^2 \sigma_{peff}^2} \ , \tag{2.2.38}$$

18

where $v_0 = |\boldsymbol{p}_0|/E_0$ with $\boldsymbol{p}_0$ and E_0 being the momentum and the energy given by the mean momenta of the external particles and energy-momentum conservation at either vertex as defined above. The simulation using the parameter values from table 2.1 shows that $L_{osc} > 1000\,L_{disp}$. The assumption that the longitudinal dispersion regime is the relevant one, in the case in which the wave packet widths are estimated from measurement uncertainties, is therefore well justified.

The observability conditions can be divided into two groups. The so-called coherent effects, which are taken into account at the level of the wave function and the so-called incoherent effects, which are included at the level of the probability.

Coherent Effects

The so-called *coherence length* describes the decoherence of the wave packets, which can have two origins. The oscillations either vanish if the wave packets become separated due to different group velocities, or if the wave packets spread beyond the oscillation length, in which case the oscillations are averaged to zero. In momentum space both of these effects are taken into account by the exponential

$$\exp\left(-\frac{L}{L_{ij}^{coh}}\right), \tag{2.2.39}$$

where (see [38])

$$L_{ij}^{coh} = \frac{1}{\sqrt{2\pi}}\frac{|\boldsymbol{p}_0|}{\sigma_{peff}}L_{ij}^{osc}. \tag{2.2.40}$$

These terms can be neglected if the momentum of the intermediate particle is much larger than the width of its effective wave packet. Using the parameters in table 2.1, all simulated events satisfy at least

$$L_{45}^{coh} > 10\,L_{45}^{osc}. \tag{2.2.41}$$

It is therefore justified to neglect the effects of decoherence in the first oscillation cycles for the parameter values in table 2.1.

We remark that the oscillation length and therefore the coherence length for oscillations including both the light and heavy neutrino mass eigenstates is smaller than 10^{-12} m. Therefore it is appropriate to neglect the light neutrino mass eigenstates in the oscillations.

Localisation conditions determine whether there is decoherence from the start. The relevant exponential suppressing the oscillations reads (see [38])

$$\exp\left(-\frac{(\delta m_{ij}^2)^2}{32|\boldsymbol{p}_0|^2}\left(\frac{v_0^2}{\sigma_m^2} + \frac{\rho^2}{\sigma_{peff}^2}\right)\right), \tag{2.2.42}$$

where $\delta m_{ij}^2 := m_i^2 - m_j^2$. The effective width of the propagating neutrino is given in momentum space by σ_{peff}. The parameters σ_m and ρ are determined by the widths of the external particles and their velocities (see [38]). Using the parameters from table 2.1 it follows that

$$\frac{(\delta m_{ij}^2)^2}{32|\boldsymbol{p}_0|^2}\left(\frac{v_0^2}{\sigma_m^2} + \frac{\rho^2}{\sigma_{peff}^2}\right) < 10^{-10} \tag{2.2.43}$$

is satisfied in all events. This allows to neglect the effects from localisation in the oscillation formula for parameter values as in table 2.1.

In the process considered in this paper the heavy neutrinos are *unstable intermediate particles*. Therefore the full propagator should be used in equation (2.2.4). As discussed in [38] this leads to the exponential decrease factor

$$\exp\left(-\frac{L}{L_{ij}^{decay}}\right) , \qquad (2.2.44)$$

where the decay length is given by

$$L_{ij}^{decay} = \frac{2|\boldsymbol{p}_0|}{m_i \Gamma_i + m_j \Gamma_j} , \qquad (2.2.45)$$

that has to be included in the sum over the mass eigenstates in equation (2.2.28). With the definitions

$$\tilde{m}_0 = \frac{m_5 + m_4}{2} \qquad \tilde{\Gamma}_0 = \frac{\Gamma_5 + \Gamma_4}{2} , \qquad (2.2.46)$$

and

$$\delta m = m_5 - m_4 \qquad \delta \Gamma = \Gamma_5 - \Gamma_4 , \qquad (2.2.47)$$

the decay exponential can be written as

$$\exp\left(-\frac{L}{L_{ij}^{decay}}\right) = \exp\left(-\frac{L(\tilde{m}_0 \tilde{\Gamma}_0 + \frac{1}{4}\delta m \delta \Gamma)}{|\boldsymbol{p}_0|}\right) \exp\left(\pm\frac{\delta_{ij}}{2}\frac{L(\delta m \tilde{\Gamma}_0 + \delta \Gamma \tilde{m}_0)}{|\boldsymbol{p}_0|}\right) , \qquad (2.2.48)$$

where for $i = j = 4$ the plus sign and for $i = j = 5$ the minus sign is used. The first exponential can be absorbed into the normalisation constant using the condition equation (2.2.29), since it does not depend on the mass indices i and j. If e.g. the decay widths of the mass eigenstates are too different, the second exponential can lead to a suppression of the oscillation pattern. On the other hand, the exponential is negligible if the mass eigenstates are nearly degenerate and if the decay widths are nearly equal. For the example point considered in this paper one can verify that $L(\delta m \tilde{\Gamma}_0 + \delta \Gamma \tilde{m}_0) \ll p_0$ such that this conditions is satisfied.

Since the detection of the decay products allows to reconstruct the invariant mass of the propagating particle, a *condition that relates the mass of the propagating particle with the detection uncertainty* is expected. This condition stems from the exponential

$$\exp\left(-\frac{(\delta m_i^2 + \delta m_j^2)^2}{32\sigma_m^2 E_0^2}\right) , \qquad (2.2.49)$$

that appears in the derivation of the amplitude (see [38]). Here $\delta m_i^2 = m_i^2 - m_0^2$. It requires that

$$\frac{|m_i^2 + m_j^2 - 2m_0^2|}{E_0} < \sigma_m , \qquad (2.2.50)$$

where m_i and m_j are the masses of the heavy neutrinos and m_0 is as given above[6]

$$m_0^2 := E_0^2 - |\boldsymbol{p}_0|^2 . \qquad (2.2.51)$$

The parameter σ_m (see [38]) is related to the widths and velocities of the external particles. Since the detection process is described by the interaction with those external particles, their

---

[6] We remark that m_0 should not be confused with $\tilde{m}_0$, which is the geometric mean of the heavy neutrino masses.

widths are in turn related to the precision of the momentum measurement. In conclusion this condition enforces the neutrinos to be either nearly degenerate in mass or highly relativistic, such that the propagating mass eigenstates are within the uncertainty of the momentum measurement. The simulation shows that $\sigma_m \in [0.0035 \text{ GeV}, 32 \text{ GeV}]$, such that the above condition is satisfied for the parameters in table 2.1.

In the processes considered in this paper (figures 2.1a and 2.1b) a W boson is decaying in flight and is therefore an *unstable source*. In principle one would have to treat the W boson as a propagator connecting the diagrams figures 2.1a and 2.1b and the particles producing the W boson. This extra propagator would however result in technical difficulties. The authors of [58–60] have used perturbation theory in a quantum mechanical model to describe neutrino oscillations and found an additional localisation condition, which suppresses oscillations if the unstable source moves a distance greater than the oscillation length during its lifetime. The unstable source has been assumed to have a mean momentum at rest in those derivations. A QFT approach to light neutrino oscillations has been used in [61], where a similar localisation condition to the one above has been derived. The authors of [62] considered a moving unstable source, i.e. a pion decaying in flight, in a QFT treatment. They obtained the constraint

$$\left(2\pi \frac{\boldsymbol{v}_\pi \cdot \boldsymbol{v}_0}{\boldsymbol{v}_0^2 - \boldsymbol{v}_\pi \cdot \boldsymbol{v}_0}\right) \frac{|\boldsymbol{p}_\pi|}{m_\pi \Gamma_\pi} \ll L_{ij}^{osc} , \tag{2.2.52}$$

where $\boldsymbol{v}_\pi, |\boldsymbol{p}_\pi|, m_\pi, \Gamma_\pi$ are the velocity, momentum, mass and decay width of the decaying pion. In our case the initial W boson takes the place of the pion as the unstable source. The heavy neutrino is highly boosted such that the velocities $\boldsymbol{v}_W$ and $\boldsymbol{v}_0$ are almost parallel. Furthermore it holds that $\boldsymbol{v}_W \ll \boldsymbol{v}_0$ for the parameter space considered in this paper, which implies that

$$\left(2\pi \frac{\boldsymbol{v}_\pi \cdot \boldsymbol{v}_0}{\boldsymbol{v}_0^2 - \boldsymbol{v}_\pi \cdot \boldsymbol{v}_0}\right) < 2\pi . \tag{2.2.53}$$

Even putting the momentum of the W boson as 2 TeV, which is the maximum of the range considered in this paper, we find that

$$\frac{|\boldsymbol{p}_W|}{m_W \Gamma_W} < 2.5 \times 10^{-15} \text{ m} . \tag{2.2.54}$$

This constraint is therefore negligible for the process and parameter space considered. As an additional remark, note that the above mentioned localisation conditions describe the suppression stemming from the fact that the production vertex is not known due to the finite lifetime and movement of the unstable source. At current and considered future colliders the W boson decays promptly, due to its large decay width, which makes the possible decay region much smaller than any macroscopic oscillation length. Already this argument shows that the additional localisation condition, due to the instability of the W, should be satisfied.

As discussed in [59], the unstable source can also lead to a loss of coherence for distances larger than the coherence length

$$L_\Gamma^{coh} = -\frac{4E_0^2}{\delta m_{ij}^2 \Gamma} . \tag{2.2.55}$$

For the parameters in table 2.1, this additional coherence length can be neglected compared to the one given in equation (2.2.40).

Incoherent effects

If the *propagation distance is not precisely known*, which is the case if the production or detection points are measured with some uncertainty, neutrinos that have travelled different distances overlap and wash out the oscillation pattern. This effect can be described by the following exponential (see [38])

$$\exp\left(-2\pi^2\left(\frac{\Delta L}{L_{ij}^{osc}}\right)^2\right) , \qquad (2.2.56)$$

where we have assumed that the propagation distance of the neutrinos is given by a Gaussian with width ΔL. Oscillations vanish if $\Delta L \geq L_{ij}^{osc}$. In our case the oscillation length is around 8cm and therefore much bigger than the uncertainty in the resolution of the position of the primary and secondary vertex.

In a real experiment there is a *distribution of mean momenta of the external particles*, such that the reconstructed momentum of the intermediate particle, denoted by $\boldsymbol{p}_0$, follows a distribution as well. The effect is already included in equation (2.2.35), where the factor $D_N(\vartheta, |\boldsymbol{p}_0|)$ describes the distribution of $|\boldsymbol{p}_0|$. A distribution of $|\boldsymbol{p}_0|$ leads to a washout of the oscillation pattern, since different oscillation lengths superimpose. In order to resolve the oscillation patterns it is therefore helpful [44] to plot the oscillation probability as a function of the reconstructed proper time using the following relations

$$|\boldsymbol{p}_0| = m_0\gamma_0|\boldsymbol{v}_0| = m_0\gamma_0\frac{L}{T_0} = m_0\frac{L}{\tau_0} , \qquad (2.2.57)$$

where the reconstructed gamma factor is defined as $\gamma_0 = (\sqrt{1 - |\boldsymbol{v}_0|^2})^{-1}$, the reconstructed velocity is as before $\boldsymbol{v_0} = \boldsymbol{p}_0/E_0$, the reconstructed time is given by $T_0 = L/|\boldsymbol{v}_0|$ and the reconstructed proper time is given by $\tau_0 = T_0/\gamma_0$. This leads to the following oscillation exponential

$$\exp\left(-2\pi i\frac{L}{L_{45}^{osc}}\right) = \exp\left(-i\frac{\tilde{m}_0}{m_0}\delta m\tau_0\right) , \qquad (2.2.58)$$

where equations (2.2.19) and (2.2.47) have been used. Using an oscillation probability based on plane wave arguments, the above method has been demonstrated for an example parameter point (assuming $\tilde{m}_0 = m_0$) in [44]. Note that, as mentioned above, the quantities denoted by a subscript $(\ )_0$ are the ones which are reconstructed by experimental measurements of the external particles in the process.

2.3 Low Scale Seesaw with Symmetry Protection

To further develop and apply the above results, we consider SPSS models (cf. [31, 32]) i.e. low scale seesaw models where the smallness of the light neutrino masses is protected by a slightly broken "lepton number"-like symmetry. As a particular example we focus on the "minimal low scale linear seesaw" model with only two right-handed (sterile) neutrinos, that has also been discussed as an example in [44]. The Lagrangian of this model takes the following form

$$\mathcal{L} = \mathcal{L}_{\mathrm{SM}} - \overline{N}_R^1 \Lambda (N_R^2)^c - Y_\alpha \overline{N}_R^1 \tilde{\phi}^\dagger L^\alpha - Y'_\alpha \overline{N}_R^2 \tilde{\phi}^\dagger L^\alpha + H.c. , \qquad (2.3.1)$$

where $\mathcal{L}_{\mathrm{SM}}$ is the Standard Model (SM) Lagrangian, $\alpha = (e, \mu, \tau)$ is a family index and $\tilde{\phi} := \epsilon\phi^*$ with the Levi Civita symbol ϵ and the SM Higgs doublet ϕ. The Yukawa couplings to the sterile neutrinos are denoted by Y_α and Y'_α. In the symmetry limit of the model, the Yukawa couplings

Y'_α are zero, and the "lepton number"-like symmetry is only broken slightly by the Yukawa coupling Y'_α, for which we assume that $Y'_\alpha \ll Y_\beta$ for all entries. Possibilities to realise a low scale linear seesaw in the context of SO(10) Grand Unified Theories have been discussed e.g. in [63, 64].

After electroweak symmetry breaking the part of the Lagrangian responsible for neutrino masses and mixing can be written as

$$\mathcal{L}_{mass} = -\frac{1}{2}(\overline{n}^c)^T M_\nu n + \text{H.c.} , \qquad (2.3.2)$$

where $n = (\nu_{e_L}, \nu_{\mu_L}, \nu_{\tau_L}, (N_R^1)^c, (N_R^2)^c)^T$ and

$$M_\nu = \begin{pmatrix} 0 & \boldsymbol{m} & \boldsymbol{m'} \\ \boldsymbol{m}^T & 0 & \Lambda \\ (\boldsymbol{m'})^T & \Lambda & 0 \end{pmatrix} =: \begin{pmatrix} 0 & m \\ m^T & M_{\nu_h} \end{pmatrix} . \qquad (2.3.3)$$

The symbols $\boldsymbol{m}$ and $\boldsymbol{m'}$ denote column vectors given by $\boldsymbol{Y}v_{EW}/\sqrt{2}$ and $\boldsymbol{Y'}v_{EW}/\sqrt{2}$, respectively. $v_{EW} \approx 246$ GeV is the electroweak vacuum expectation value. The mass matrix can be diagonalised using a Takagi decomposition

$$M_\nu^D = U^T M_\nu U. \qquad (2.3.4)$$

This can be achieved following the steps in [65] where first a block diagonalisation with an exponential ansatz is performed, followed by a diagonalisation of the active neutrino 3x3 and sterile neutrino 2x2 block. Expanding the exponential to second order yields

$$U = \begin{pmatrix} 1 - \frac{1}{2}\theta\theta^\dagger & \theta \\ -\theta^\dagger & 1 - \frac{1}{2}\theta\theta^\dagger \end{pmatrix} \begin{pmatrix} U_3 & 0 \\ 0 & U_2 \end{pmatrix} , \qquad (2.3.5)$$

where $\theta = m^*(M_{\nu_h}^*)^{-1}$. It can be easily checked that the mass matrix is indeed block diagonalized to second order in θ.

Furthermore, one finds that

$$U_2 = \frac{e^{-\frac{i}{2}\arg(\boldsymbol{m'}\,\boldsymbol{m}^*)}}{\sqrt{2}} \begin{pmatrix} \frac{i\boldsymbol{m'}\,\boldsymbol{m}^*}{|\boldsymbol{m'}\,\boldsymbol{m}^*|} & \frac{\boldsymbol{m'}\,\boldsymbol{m}^*}{|\boldsymbol{m'}\,\boldsymbol{m}^*|} \\ -i & 1 \end{pmatrix} \qquad (2.3.6)$$

diagonalizes the heavy neutrino 2x2 block. Regarding the heavy neutrino-antineutrino oscillations, the interesting part of the mixing matrix is the upper right 3×2 block, which describes the mixing between the active neutrino interaction eigenstates and the heavy neutrino mass eigenstates. In the oscillation formula we called this part V. From equations (2.3.5) and (2.3.6) we find that

$$V = \frac{1}{\sqrt{2}}\left(-i(\boldsymbol{\theta})^*e^{-i\phi} + i(\boldsymbol{\theta'})^*e^{i\phi} \quad (\boldsymbol{\theta})^*e^{-i\phi} + (\boldsymbol{\theta'})^*e^{i\phi}\right) . \qquad (2.3.7)$$

where the phase is defined as $2\phi = \arg((\boldsymbol{\theta'}) \cdot (\boldsymbol{\theta})^*)$ and the expansion parameters are defined as

$$\boldsymbol{\theta} = \frac{\boldsymbol{m}}{\Lambda} = \frac{\boldsymbol{Y}\,v_{EW}}{\sqrt{2}\Lambda} \qquad (2.3.8)$$

$$\boldsymbol{\theta'} = \frac{\boldsymbol{m'}}{\Lambda} = \frac{\boldsymbol{Y'}\,v_{EW}}{\sqrt{2}\Lambda} . \qquad (2.3.9)$$

Note that θ can be seen as a function of $\boldsymbol{\theta}$ and $\boldsymbol{\theta'}$. From the hierarchy between the Yukawa couplings of the sterile neutrinos it follows that $\boldsymbol{\theta'} \ll \boldsymbol{\theta}$. We restrict ourselves to maximally first

order in the elements of $\boldsymbol{\theta}'$ in the following.

As a remark one can see that higher order terms in $\boldsymbol{\theta}$ can be absorbed in a slight rescaling of the Yukawa couplings $\boldsymbol{Y}$, since in the symmetry limit (where $\boldsymbol{\theta}' = 0$) V has the exact form

$$V_{symm} = \frac{1}{\sqrt{2 + 2|\boldsymbol{\theta}|^2}} \begin{pmatrix} -i(\boldsymbol{\theta})^* & (\boldsymbol{\theta})^* \end{pmatrix} . \tag{2.3.10}$$

Therefore those terms do not qualitatively change the oscillation formulae that are obtained in section 2.4.

Using the expansion equation (2.3.7) it is also possible to obtain expressions for the masses of the heavy neutrinos and thus also for the mass splitting parameter λ_m, introduced in equation (2.2.18), which can be expressed as

$$\lambda_m = \frac{2|\boldsymbol{m}' \cdot \boldsymbol{m}^*|}{2\Lambda^2 + |\boldsymbol{m}'|^2 + |\boldsymbol{m}|^2} \leq |\boldsymbol{\theta}' \cdot \boldsymbol{\theta}^*| \ll \mathcal{O}(\boldsymbol{\theta}') . \tag{2.3.11}$$

Another important parameter entering the oscillation formula is the quadratic mass splitting δm_{45}^2, which enters the formula for the oscillation length. It can be expressed as

$$\delta m_{45}^2 = -4\tilde{m}_0^2 \lambda_m = -2\tilde{m}_0 \delta m , \tag{2.3.12}$$

where the mean mass of the heavy neutrinos $\tilde{m}_0$ is defined in equation (2.2.19) and can be expressed as

$$\tilde{m}_0 = \frac{2\Lambda^2 + |\boldsymbol{m}|^2}{2\Lambda} + \mathcal{O}(\boldsymbol{\theta}') . \tag{2.3.13}$$

2.4 Approximations of the Oscillation Formula

Using the results from section 2.3 the oscillation probability equation (2.2.28) can be expanded in the small parameters $\boldsymbol{\theta}'$ appearing in the lepton mixing matrix and λ_m which has been introduced in equation (2.2.18) to account for the mass splitting of the heavy neutrinos. Also, as we discussed, the mass splitting parameter λ_m can be neglected at leading order as it is much smaller than $\mathcal{O}(\boldsymbol{\theta}')$, see equation (2.3.11). The following definitions are used

$$I_\beta := \mathrm{Im}(\theta_\beta^* \theta_\beta' \exp(-2i\Phi)) ,$$

$$\phi_{ij} := -\frac{2\pi}{L_{ij}^{osc}} = -\frac{m_i^2 - m_j^2}{2|\boldsymbol{p}_0|} ,$$

$$\Phi := \frac{1}{2}\mathrm{Arg}(\boldsymbol{\theta}' \cdot \boldsymbol{\theta}^*) .$$

To derive the approximate oscillation formulae, the normalisation constant is computed using the condition equation (2.2.29), yielding

$$N_g^2 = \frac{1}{\sum_\beta |\theta_\alpha|^2 |\theta_\beta|^2 + \dots} , \tag{2.4.1}$$

where the ellipses contain orders higher than $\mathcal{O}(\boldsymbol{\theta}')$. With this the probability equation (2.2.28) can be expanded in $\boldsymbol{\theta}'$. Note that we keep the exponential $\exp(i\Phi_{ij}L)$ exact. Up to first order in

$\boldsymbol{\theta}'$, the probability equation (2.2.28) in the LNC case yields

$$P_{\alpha\beta}^{LNC}(L) = \frac{1}{2\sum_\beta |\theta_\alpha|^2 |\theta_\beta|^2} \Bigg(|\theta_\alpha|^2 |\theta_\beta|^2 (1 + \cos(\phi_{45}L)) $$
$$- 2(I_\beta |\theta_\alpha|^2 - I_\alpha |\theta_\beta|^2) \sin(\phi_{45}L) \Bigg) \ . \tag{2.4.2}$$

In the LNV case the expansion of equation (2.2.28) up to first order in $\boldsymbol{\theta}'$ yields

$$P_{\alpha\beta}^{LNV}(L) = \frac{1}{2\sum_\beta |\theta_\alpha|^2 |\theta_\beta|^2} \Bigg(|\theta_\alpha|^2 |\theta_\beta|^2 (1 - \cos(\phi_{45}L)) $$
$$- 2(I_\beta |\theta_\alpha|^2 + I_\alpha |\theta_\beta|^2) \sin(\phi_{45}L) \Bigg) \ , \tag{2.4.3}$$

where in both cases the LO terms are written in the first line and the NLO terms in the second line. Note that if the initial W boson is replaced by a W^-, the leptonic mixing matrix factors are complex conjugate to the ones in the process where the initial boson is a W^+. This results in a sign change of the NLO contributions. The leading order term in those expansions describe the oscillations from neutrinos into antineutrinos, whereas the first order term describes flavour oscillations. This can be seen by adding up the LNC and LNV probabilities, which means that the sign of the outgoing lepton is ignored. This should make the oscillations of neutrinos into antineutrinos vanish, and indeed the oscillatory part of the leading order terms cancel each other. We are left with

$$P_{\alpha\beta}^{LNC}(L) + P_{\alpha\beta}^{LNV}(L) = \frac{1}{\sum_\beta |\theta_\alpha|^2 |\theta_\beta|^2} \Bigg(|\theta_\alpha|^2 |\theta_\beta|^2 - 2I_\beta |\theta_\alpha|^2 \sin(\phi_{45}L) \Bigg) \ . \tag{2.4.4}$$

Summing over the outgoing flavours makes the oscillatory part of the above equation vanish. This happens because $\sum_\beta \theta_\beta^* \theta_\beta' \exp(-2i\Phi) \in \mathbb{R}$, and therefore $\sum_\beta I_\beta = 0$.

With the "lepton number"-like symmetry being broken, one also expects lepton number violation in the limit where the distance L goes to zero. As mentioned above, the no-dispersion regime, which is the relevant one in this limit, results in the same formulae for the oscillation probabilities if the observability conditions are met. From equation (2.4.3) it can therefore be seen that there is no lepton number violation at zero distance. This leads to the conclusion that this effect has to be introduced at a higher order and is therefore much smaller than the lepton number violation due to oscillations. That this effect is indeed present at higher orders can be confirmed by numerically diagonalizing the lepton mass matrix and using equation (2.2.28) to compute the oscillation probability.

Taking only the leading order into account, the only relevant model parameters are the Yukawa couplings Y_α, or equivalently the mixing parameters θ_α, and the quadratic mass splitting δm_{45}^2 appearing in ϕ_{45}. The leading order effects can therefore be described by the symmetry limit of the SPSS [31, 32] plus the quadratic mass splitting as an additional parameter. This holds even more generally, for all realisations of the SPSS.

If the mechanism of light neutrino masses is given by the minimal linear seesaw described in equation (2.3.1), one can reparameterize the model in terms of active neutrino parameters according to [66]. Assuming an inverse ordering of the light neutrino masses m_{ν_i} yields

$$Y_\alpha = \frac{y}{\sqrt{2}} \sqrt{1+\rho} \, U_{\alpha 2}^* + \sqrt{1-\rho} \, U_{\alpha 1}^* \tag{2.4.5}$$

$$Y'_\alpha = \frac{y'}{\sqrt{2}}\sqrt{1+\rho}\, U^*_{\alpha 2} - \sqrt{1-\rho}\, U^*_{\alpha 1} \tag{2.4.6}$$

where U denotes the unitary PMNS matrix,

$$\rho = \frac{\sqrt{1+r}-1}{\sqrt{1+r}+1} \tag{2.4.7}$$

and

$$r = \frac{|m^2_{\nu_1} - m^2_{\nu_2}|}{|m^2_{\nu_1} - m^2_{\nu_3}|}\ . \tag{2.4.8}$$

Note that we have absorbed the parameter ϵ appearing in [66] into the definitions of Y' and y'. An interesting observation is that the heavy neutrino mass splitting is given by the light neutrino mass splitting [44]

$$m_5 - m_4 = m_{\nu_2} - m_{\nu_1}\ , \tag{2.4.9}$$

and therefore the squared mass splitting is given by

$$\delta m^2_{45} = -2\tilde{m}_0(m_{\nu_2} - m_{\nu_1})\ . \tag{2.4.10}$$

Taking the values of the active neutrino mixing angles and mass squared differences from [67, 68], the only undetermined parameter is the Majorana phase α. Analyzing the parameterization of the Yukawa couplings one finds that the products $Y_\alpha Y^*_\alpha$, $Y'_\alpha Y'^*_\alpha$, $Y'_\alpha Y^*_\alpha$ are only independent of the Majorana phase when summed over the flavour index. The oscillation probabilities equations (2.4.2) and (2.4.3) are visualized in figures 2.2a, 2.2b, 2.3a, and 2.3b. The values of the oscillation probabilities makes it clear that any higher order effects on the oscillation patters will be extremely challenging to observe under realistic conditions for the chosen example parameters from table 2.1.
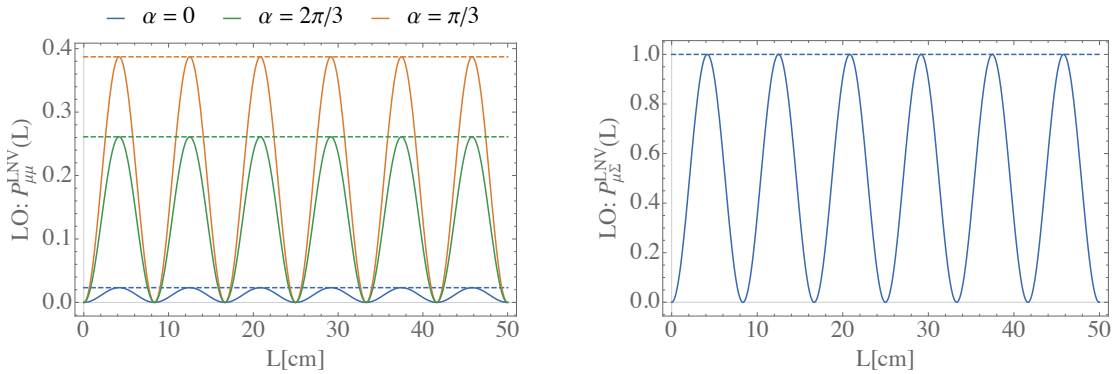
(a) Heavy neutrino-antineutrino oscillation probabilities $P^{LNV}_{\mu\mu}(L)$ at LO (cf. equation (2.4.3)), shown as solid lines for different values of the Majorana phase α. The dashed lines show the sum of the LNC and LNV probability, i.e. $P^{LNC}_{\mu\mu}(L) + P^{LNV}_{\mu\mu}(L)$. The legend labels lines of increasing amplitude from left to right.

(b) Heavy neutrino-antineutrino oscillation probabilities $P^{LNV}_{\mu\Sigma}(L) := \sum_\beta P^{LNV}_{\mu\beta}(L)$ at LO (cf. equation (2.4.3)), shown as solid lines. The dashed lines show the sum of the LNC and LNV probability, i.e. $P^{LNC}_{\mu\Sigma}(L) + P^{LNV}_{\mu\Sigma}(L)$. Both probabilities are independent of the Majorana phase α.

Figure 2.2: Heavy neutrino-antineutrino oscillation probabilities at LO.
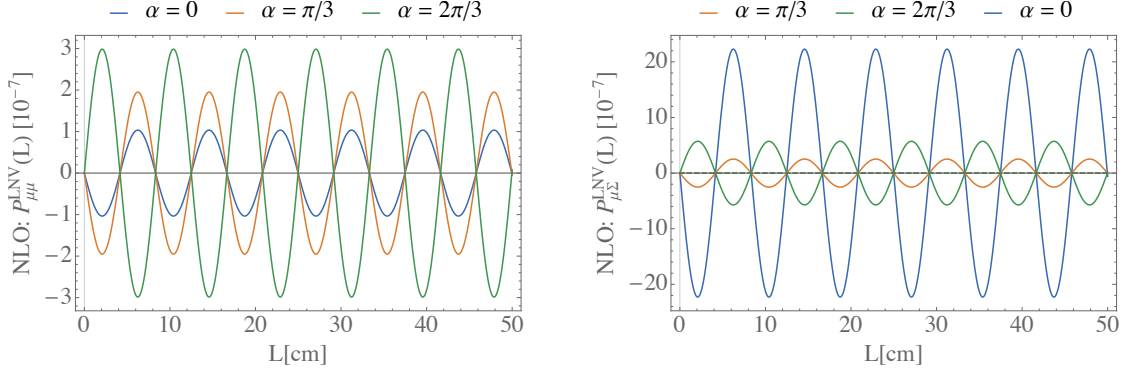
(a) NLO contributions to the heavy neutrino-antineutrino oscillation probabilities $P_{\mu\mu}^{LNV}(L)$ (cf. equation (2.4.3)), shown as solid lines for different values of the Majorana phase α. The NLO contribution to the LNC probability vanishes for equal incoming and outgoing flavours. The legend labels lines of increasing amplitude from left to right.

(b) NLO contributions to the heavy neutrino-antineutrino oscillation probabilities $P_{\mu\Sigma}^{LNV}(L) := \sum_\beta P_{\mu\beta}^{LNV}(L)$ (cf. equation (2.4.3)), shown as solid lines. The sum of the LNC and LNV probability, i.e. $P_{\mu\Sigma}^{LNC}(L) + P_{\mu\Sigma}^{LNV}(L)$ is identical zero. The legend labels lines of increasing amplitude from left to right.

Figure 2.3: NLO contributions to the heavy neutrino-antineutrino oscillation probabilities.

2.5   Summary and Conclusions

In this paper we have applied the framework of quantum field theory (QFT) with external wave packets (cf. [38]) to derive the probabilities for the oscillations between long-lived heavy neutrino and antineutrino interaction eigenstates (cf. footnote 1), where we define a neutrino (antineutrino) as the neutral lepton that is produced together with a charged antilepton (lepton) and a W boson. These heavy neutrino-antineutrino oscillations can lead to an oscillating rate of lepton number conserving (LNC) and violating (LNV) events at colliders, as a function of the distance between the (anti)neutrino production and displaced decay vertices.

Our most general formula for the oscillation probability is equation (2.2.16) together with the additional terms discussed in section 2.2.1. The latter can be neglected given the adequate kinematic and experimental conditions, and are referred to as observability conditions. The oscillation probability densities can be further simplified to equation (2.2.28) by neglecting the spin correlation between the production and detection vertex. Including the decay probabilities of the heavy neutrinos, formulae for the expected number of LNC/LNV events with a certain displacement between primary and secondary vertex have been given in equation (2.2.35).

The simplified formulae for the oscillation probabilities have been applied to low scale seesaw models where the smallness of the light neutrino masses is protected by a slightly broken "lepton number"-like symmetry, i.e. to the SPSS (cf. [31, 32]). As a particular example we have focused on the "minimal low scale linear seesaw" model with only two nearly mass-degenerate heavy neutrinos, that has also been discussed as an example in [44]. Within this class of models, an expansion of the probabilities in the small "lepton number"-like symmetry breaking parameters $\boldsymbol{\theta'}$ has been performed, yielding the LO and NLO contributions (cf. equations (2.4.2) and (2.4.3)).

For the example parameter point used in Ref. [44], we have discussed the observability conditions (cf. section 2.2.1) and found that they are all satisfied. However, if the momentum

$\boldsymbol{p}_0$ is given by a distribution, which is the case if the mean momenta of the external particles follow a distribution as discussed in section 2.2.1, the oscillation pattern can be washed out as has already been pointed out in [44]. The proposed solution to this is to reconstruct the four momentum p_0 (from the measurements) and to consider the oscillations as a function of the heavy neutrino reconstructed proper time. In [44] it has been demonstrated, using estimated uncertainties for the HL-LHCb and the above-mentioned example parameter point, that the proposed solution is indeed feasible.

Comparing our simplified LO results with the existing literature, we found that we agree with the results from [40] (when we set their parameters $\theta_{21}^{LNV} = -\pi$ and $\theta_{21}^{LNC} = 0$ to match the considered low scale seesaw scenario). Our LO formulae also agree with the ones derived using the formalism for meson oscillations and plane wave arguments and used e.g. in [41, 44]. Our results in the most general form, i.e. equation (2.2.16) together with the additional terms discussed in section 2.2.1, allow to discuss effects beyond LO and to check the observability conditions (or include them explicitly in the calculations).

Our NLO results showed that beyond the LO heavy neutrino-antineutrino oscillations, the probablities are also modulated by "flavour oscillations", as discussed in section 2.4. On the other hand, for the case of the "minimal low scale linear seesaw" model (with parameters around the considered example point), it has turned out that the NLO effects are very small, with a suppression which makes them undetectable at the currently considered future collider experiments. While this does not necessarily have to be the case for other choices of parameters, it indicates that there is a parameter region of interest for the LHC (and future colliders) where the LO formulae are sufficient. In this region the only model parameters relevant for heavy neutrino-antineutrino oscillations, in terms of the SPSS parameters, are the three flavour-dependent active-sterile mixing angles θ_α and the mass squared difference δm_{45}^2 between the two heavy neutrinos.

In summary, our results show that the phenomenon of heavy neutrino-antineutrino oscillations can indeed occur in low scale seesaw scenarios and that the previously used leading order formulae, derived with a plane wave approach, provide a good approximation for (at least) the considered example parameter point. Our results help to put existing studies based on LO formulae on a more solid theoretical ground (by providing the observability conditions which have to be checked in the QFT framework) and can be used in future studies to explore the phenomenon in other parameter regions and for different types of low scale seesaw models.

Appendix 2.A   Formulas for the Observability Conditions

In the following, the formulas to compute the observability conditions of section 2.2.1 are given. For more details we refer to [38].

The particles at production are labeled P_i and their wave packets are assumed to have a Gaussian form of width σ_{xP_i} in configuration space. The wave packet peaks, in momentum space, at momentum $\boldsymbol{P}_i$ and since they are assumed to be on-shell, their peak energy is given by $E_{P_i} = \sqrt{m_{p_i}^2 + |\boldsymbol{P}_i|^2}$. The peak velocity is then defined as $\boldsymbol{v}_{P_i} = \boldsymbol{P}_i/E_{P_i}$. For the particles at detection the letter P is simply replaced by D. The velocity $\boldsymbol{v}_0$ is defined using energy-momentum conservation at the production and/or detection vertex, which yields

$$\boldsymbol{v}_0 := \boldsymbol{p}_0/E_0 \ .$$

Labelling the incoming particles at production $P_{i,in}$ and the outgoing ones $P_{i,out}$ yields

$$E_0 := \sum_{P_{i,in}} E_{P_{i,in}} - \sum_{P_{i,out}} E_{P_{i,out}} \tag{2.A.1}$$

and

$$\boldsymbol{p}_0 := \sum_{P_{i,in}} \boldsymbol{P}_{i,in} - \sum_{P_{i,out}} \boldsymbol{P}_{i,out} \ . \tag{2.A.2}$$

The relevant parameters are defined as follows.

$$\frac{1}{\sigma_{xP}^2} = \sum_{P_i} \frac{1}{\sigma_{xP_i}^2} \qquad \frac{1}{\sigma_{xD}^2} = \sum_{D_i} \frac{1}{\sigma_{xD_i}^2} \tag{2.A.3}$$

$$\sigma_{pP} = \frac{1}{2\sigma_{xP}} \qquad \sigma_{pD} = \frac{1}{2\sigma_{xD}} \tag{2.A.4}$$

$$\boldsymbol{v}_P = \sigma_{xP}^2 \sum_{P_i} \frac{\boldsymbol{v}_{P_i}}{\sigma_{xP_i}} \qquad \boldsymbol{v}_D = \sigma_{xD}^2 \sum_{D_i} \frac{\boldsymbol{v}_{D_i}}{\sigma_{xD_i}} \tag{2.A.5}$$

$$\Sigma_P = \sigma_{xP}^2 \sum_{P_i} \frac{|\boldsymbol{v}_{P_i}|^2}{\sigma_{xP_i}} \qquad \Sigma_D = \sigma_{xD}^2 \sum_{D_i} \frac{|\boldsymbol{v}_{D_i}|^2}{\sigma_{xD_i}} \tag{2.A.6}$$

$$\sigma_{eP}^2 = \sigma_{pP}^2 \left(\Sigma_P - |\boldsymbol{v}_P|^2 \right) \qquad \sigma_{eD}^2 = \sigma_{pD}^2 \left(\Sigma_D - |\boldsymbol{v}_D|^2 \right) \tag{2.A.7}$$

$$\frac{1}{\sigma_p^2} = \frac{1}{\sigma_{pP}^2} + \frac{1}{\sigma_{pD}^2} \tag{2.A.8}$$

The following symbols are defined in the longitudinal dispersion regime, on which we focused in this paper. We denote a velocity ($\boldsymbol{v}$) projected onto the direction in which the oscillation distance is measured ($\hat{\boldsymbol{L}}$) as ν.[7]

$$\frac{1}{\sigma_{peff}^2} = \frac{1}{\sigma_{pP}^2} + \frac{1}{\sigma_{pD}^2} + \frac{(\nu_0 - \nu_P)^2}{\sigma_{eP}^2} + \frac{(\nu_0 - \nu_D)^2}{\sigma_{eD}^2} \tag{2.A.9}$$

$$\sigma_{xeff} = \frac{1}{2\sigma_{peff}} \tag{2.A.10}$$

$$\rho = \sigma_{peff}^2 \left(\frac{1}{\sigma_{pP}^2} + \frac{1}{\sigma_{pD}^2} - \frac{\nu_P(\nu_0 - \nu_P)}{\sigma_{eP}^2} - \frac{\nu_D(\nu_0 - \nu_D)}{\sigma_{eD}^2} \right) \tag{2.A.11}$$

$$\frac{1}{\sigma_m^2} = \sigma_{peff}^2 \left(\frac{1}{\sigma_p^2} \left(\frac{1}{\sigma_{eP}^2} + \frac{1}{\sigma_{eD}^2} \right) + \frac{(\nu_P - \nu_D)^2}{\sigma_{eP}^2 \sigma_{eD}^2} \right) \tag{2.A.12}$$

---

[7] If one does only measure the scalar distance of oscillation, one might replace the direction $\boldsymbol{L}/|\boldsymbol{L}|$ with the direction $\boldsymbol{p}_0/|\boldsymbol{p}_0|$, which can be interpreted as the main direction in which the heavy neutrinos travel.

Chapter 3

Simulating lepton number violation induced by heavy neutrino-antineutrino oscillations at colliders

Abstract:

We study pseudo-Dirac pairs of two almost mass-degenerate sterile Majorana neutrinos which generate light neutrino masses via a low-scale seesaw mechanism. These pseudo-Dirac heavy neutral leptons can oscillate between interaction eigenstates that couple to leptons and antileptons and thus generate oscillations between lepton number conserving and lepton number violating processes. With the pSPSS, we introduce a minimal framework capable of describing the dominant features of low-scale seesaws at colliders and present a FEYNRULES implementation usable in Monte Carlo generators. Additionally, we extend MADGRAPH to simulate heavy neutrino-antineutrino oscillations and present results from such simulations.

3.1 Introduction

The discovery of flavour oscillations between SM neutrinos [69] implies that they have nonzero masses. One possible extension of the SM able to generate neutrino masses consists of adding sterile neutrinos, that are singlets under all SM symmetries, to its particle content [18–24]. Testing whether these sterile neutrinos are indeed the *missing piece* that explains the light neutrino masses is one of the key questions towards a more complete theory of elementary particles.

With sterile neutrinos added to the SM, there are two main routes resulting in nonzero neutrino masses. In the first case, only Dirac mass terms are present. The Yukawa coupling term is formed by sterile neutrinos, the Higgs field and the lepton doublets, analogous to the mechanism generating charged fermion masses. After EWSB, this Yukawa term generates Dirac neutrino masses. However, to yield the phenomenologically required small masses for the light neutrinos, the size of the Yukawa couplings has to be tiny $\boldsymbol{y} \lesssim \mathcal{O}(10^{-12})$.

Since the sterile neutrinos are SM singlets, it is possible to add a Majorana mass term to the SM Lagrangian [25]. Therefore, realising light Dirac neutrinos requires a mechanism to eliminate this term and enforce exact LNC. As soon as some LNV is present, the light neutrinos are of Majorana-type [70]. One way to probe these considerations are searches for neutrinoless double β (0νββ) decay [71] since its observation would prove LNV. The two main routes for nonzero neutrino masses are depicted in the upper part of figure 3.1, and in this work we focus on the case that the light neutrinos have Majorana masses.

As an alternative to 0νββ decays, one can also search for LNV induced by the sterile neutrinos at colliders. While this sounds promising at first sight, one can argue on general grounds that LNV, observable at the large hadron collider (LHC), would lead to too heavy light neutrino masses, and thus it should be impossible to observe LNV [72]. An effect that has not been taken into account in such considerations are heavy neutrino-antineutrino oscillations ($N\overline{N}$Os) [1], see also [40, 41, 44]. In particular, their interplay with the potential longevity of the heavy neutrinos is the main subject of this paper. Despite the smallness of the LNV terms in the Lagrangian, $N\overline{N}$Os can introduce LNV processes at the same order as LNC processes, depending on the lifetime and oscillation period of the sterile neutrinos. Since the oscillations are an interference phenomenon, they are able to probe mass splittings of heavy neutrinos so small that they would otherwise be unobservable in collider studies. Including the $N\overline{N}$Os correctly in collider studies is thus a crucial aspect when simulating seesaw extensions of the SM to explain the light neutrino masses.

This paper is organised as follows: In section 3.2, we describe the possible domains of seesaw models and argue that collider testable seesaw models are protected by a LNLS resulting in pseudo-Dirac pairs of heavy neutrinos. Afterwards, in section 3.3, we give the relevant results for the description of $N\overline{N}$Os in the external wave packet formalism and derive the integrated effects of these oscillations. Subsequently, we introduce the SPSS [31, 32] in section 3.4, first in the symmetric limit, then extended by small symmetry violating terms, and finally as the pSPSS with the minimal set of parameters able to describe the dominant collider effects of low-scale type I seesaws. In section 3.5, we introduce the FEYNRULES model file of the pSPSS and describe the necessary steps to extend MADGRAPH to be able to simulate $N\overline{N}$Os. In section 3.6, we present selected results from a Monte Carlo (MC) study using this software implementation. Finally, we conclude in section 3.7. Additionally, we comment in section 3.A on the discussion about whether it is possible to distinguish Majorana and Dirac particles from each other using their decay width. Last but not least, the code for the MADGRAPH patch is presented in section 3.B.
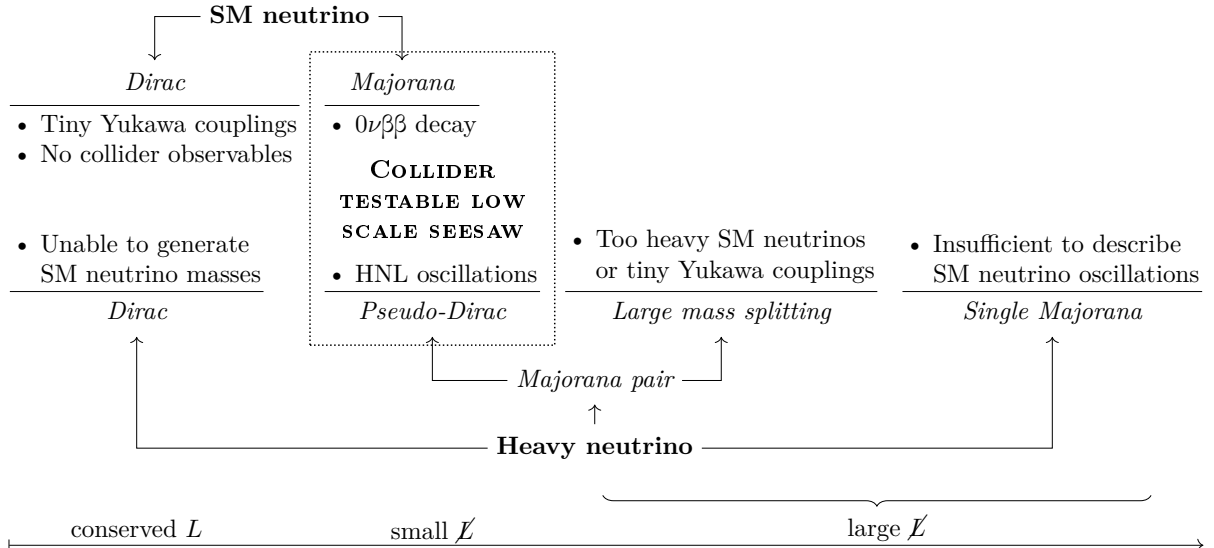
Figure 3.1: Comparison between the different possible choices for active and sterile neutrinos discussed in the text. Note that for collider-accessible heavy neutrinos that generate Majorana masses for the light neutrinos via a low-scale seesaw with couplings far above the naive seesaw line, only pseudo-Dirac pairs of two nearly mass-degenerate Majorana DOFs are a viable option.

3.2 Seesaw models

With $i = 1, \ldots, n$ sterile neutrinos N_i and both Dirac and Majorana mass terms extending the SM Lagrangian, one arrives at a general theoretical framework where the sterile neutrino Lagrangian[1]

$$\mathcal{L}_N = -\sum_i y_\alpha^{(i)} \overline{N_i^c} \widetilde{H}^\dagger \ell_\alpha - \frac{1}{2} \sum_i m_M^{(i)} \overline{N_i^c} N_i + \text{H.c.} , \qquad (3.2.1)$$

is added to the SM Lagrangian. Here H and ℓ are the SM Higgs and lepton SU(2) doublets, respectively, $\boldsymbol{y}^{(i)}$ is the neutrino Yukawa coupling vector $(y_1^{(i)}, y_2^{(i)}, y_3^{(i)})^\intercal$, and $m_M^{(i)}$ is the Majorana mass parameter.[2] To illustrate how small neutrino masses can emerge from this framework, we consider the minimal case of two sterile neutrinos $n = 2$. It is minimal since neutrino flavour oscillations require at least two of the light neutrino masses to be nonzero, which in turn requires at least two sterile neutrino DOFs. The following discussion can be generalised to larger n, which is necessary for models such as the inverse seesaw to be phenomenological viable. After EWSB, the Lagrangian can be written in the diagonal basis for the Majorana masses m_M,

$$\mathcal{L}_N = -m_{D\alpha}^{(1)} \overline{N_1^c} \nu_\alpha - m_{D\alpha}^{(2)} \overline{N_2^c} \nu_\alpha - \frac{1}{2} m_M^{(1)} \overline{N_1^c} N_1 - \frac{1}{2} m_M^{(2)} \overline{N_2^c} N_2 + \text{H.c.} , \qquad (3.2.2)$$

where $\boldsymbol{m}_D = \boldsymbol{y} v$ with the SM Higgs VEV $v \approx 174 \, \text{GeV}$ describes the Dirac mass contribution. When m_M is sufficiently larger than $\boldsymbol{m}_D$, the light neutrino mass matrix is given by the seesaw relation, which takes the form

$$M_\nu = \frac{\boldsymbol{m}_D^{(1)} \otimes \boldsymbol{m}_D^{(1)}}{m_M^{(1)}} + \frac{\boldsymbol{m}_D^{(2)} \otimes \boldsymbol{m}_D^{(2)}}{m_M^{(2)}} . \qquad (3.2.3)$$

---

[1] For ease of notation, the sterile neutrinos are introduced as left-chiral DOFs. Note that any left-chiral field can also be described by the charge conjugate of a right-chiral field and vice versa.

[2] We indicate quantities with a suppressed vectorial index by using boldface font.
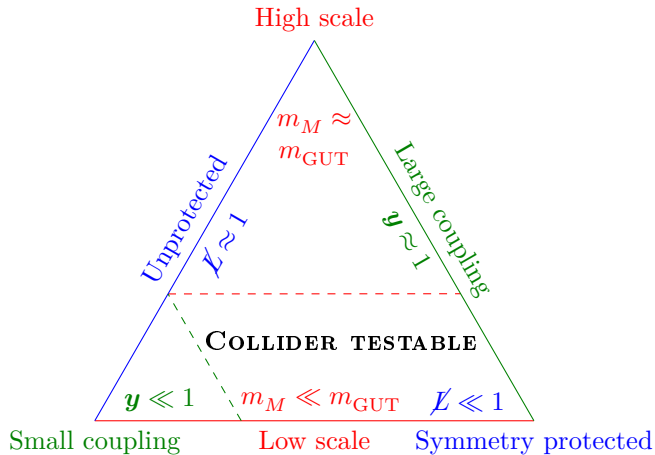
Figure 3.2: Depiction of the three limiting seesaw regimes described in the text. The phenomenologically accessible parameter space of low-scale seesaws with large enough coupling is connected to the symmetry-protected corner and indicated by dashed lines.

With these ingredients, there are three limiting cases allowing to arrive at the observed small neutrino masses:

i) **High-scale seesaw limit**   Here neutrino masses are small because the Majorana masses m_M of the sterile neutrinos are large. The neutrino Yukawa couplings y can be large in this case — up to $\mathcal{O}(1)$ for m_M close to the scale of grand unification. Due to the high mass scale involved, this limit of the seesaw mechanism cannot be probed directly at colliders.

ii) **Small coupling seesaw limit**   It is possible to simultaneously lower the sterile neutrino mass scale m_M and the size of the neutrino Yukawa couplings y without changing the generated light neutrino masses M_ν in equation (3.2.3). Envisioned future collider experiments such as the FCC-*ee* can probe this limit for some choices of parameters, but for most cases the couplings are too small for direct tests.

iii) **Symmetry-protected seesaw limit**   The third possibility emerges when the two terms in equation (3.2.3) almost cancel. Then y can be large enough, and simultaneously m_M can be small enough, such that the heavy neutrinos are within reach of collider experiments. This cancellation can be protected by a *lepton number-like* symmetry (LNLS) that generalises the lepton number L of the SM and ensures that M_ν is equal to zero in the symmetry conserving limit.[3]

The various manifestations of the *seesaw mechanism* are schematically depicted in figure 3.2. The three corners represent the three limiting cases discussed above. However, also the cases in between are viable options. For the Majorana mass scales m_M, there is a maximal value above which it is no longer possible to test this sterile neutrino directly at a given collider experiment. This means the observable seesaw models are *low-scale models* opposite to the high-scale seesaw corner. Among the low-scale seesaw models, the small coupling limit is also not testable at e.g. the LHC or even the HL-LHC. The potentially *testable* region of the (type I) seesaw mechanism is thus the area inside the dashed lines in figure 3.2; it is bound to have a certain degree of symmetry protection if one wants to avoid tuning of the parameters.

---

[3] One can achieve this cancellation also by tuning of parameters without relying on a symmetry. However, this mechanism of cancellation is unstable under radiative corrections, cf. [72]. We will not consider this possibility further here, only noting that in this case, it is expected that the LNV effects would be generically unsuppressed.

Figure 3.3: A neutrino interaction eigenstate is produced together with an antilepton. After some time, the superposition of mass eigenstates n_i has oscillated into a heavy neutrino N or antineutrino $\overline{N}$ interaction eigenstate that decays into an antilepton l^+ or lepton l^-, such that the total process is LNV or LNC.

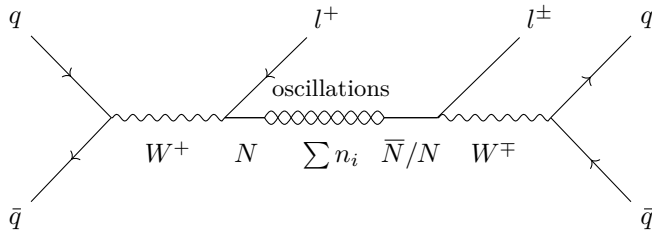Although the model of two sterile neutrinos with exact LNLS serves as a valuable starting point for the construction of viable seesaw models with small symmetry breaking, it is itself not able to generate neutrino masses due to the unbroken symmetry. With the symmetry intact, the two Majorana DOFs are mass degenerate and combine precisely to form a single Dirac particle. However, a small amount of symmetry breaking not only generates small neutrino masses but at the same time causes a small mass splitting between the two Majorana DOFs. Such pseudo-Dirac heavy neutrinos can exhibit heavy neutrino-antineutrino oscillation ($N\overline{N}$O) potentially detectable at collider experiments. For large symmetry breaking, this feature vanishes as the mass splitting becomes too big and decoherence sets in so that the two sterile neutrinos appear as two separate Majorana particles. At the same time, the generated SM neutrino masses become too large if the model has no additional mechanism to prevent this from happening. We depict these considerations in the lower part of figure 3.1.

Although realistic low-scale seesaw models predict pseudo-Dirac heavy neutrinos, the majority of searches for HNLs have been performed in either the pure Dirac or single Majorana scenario. In an effort to distinguish between these two models, it has sometimes been argued that one can discriminate Majorana from Dirac HNLs using their decay width. In section 3.A, we describe in detail why this is not the case. The main insight is that the factor of two appearing when comparing the decay widths counts the number of Majorana DOFs forming the observed HNL. However, two Majorana particles can only be described as a Dirac particle when their Yukawa couplings have a relative phase of $-i$, which cannot be determined using the decay width, cf. section 3.A.

3.3 Heavy neutrino-antineutrino oscillations

Generically, neutral particles can oscillate into their antiparticles [33, 73, 74] as known e.g. from meson oscillations [75–78]. The distinction between particle and antiparticle in the case of sterile neutrinos can be made by distinguishing a neutrino interaction eigenstate by the charge of the associated lepton it is produced with. If it is produced together with a lepton l^-, it is an antineutrino and if it is produced together with an antilepton l^+, it is a neutrino. The corresponding mass eigenstates n_i interfere when propagating, which results in an oscillation between different interaction eigenstates as a function of travelling distance. Heavy neutrinos N and antineutrinos $\overline{N}$ are defined as the projection of neutrino and antineutrino states onto the heavy mass eigenstates. This mechanism leads to heavy neutrino-antineutrino oscillations ($N\overline{N}$Os). In the collider testable region of figure 3.2, the mass splitting can be small enough for the $N\overline{N}$Os to be observable and of macroscopic length. If $N\overline{N}$Os are present, one expects processes such as the one shown in figure 3.3 to occur, leading to patterns as depicted in figure 3.4. Furthermore, in cases in which the parameters do not allow for macroscopic oscillations to be

(a) Short oscillation period.　(b) Intermediate oscillation period.　(c) Long oscillation period.
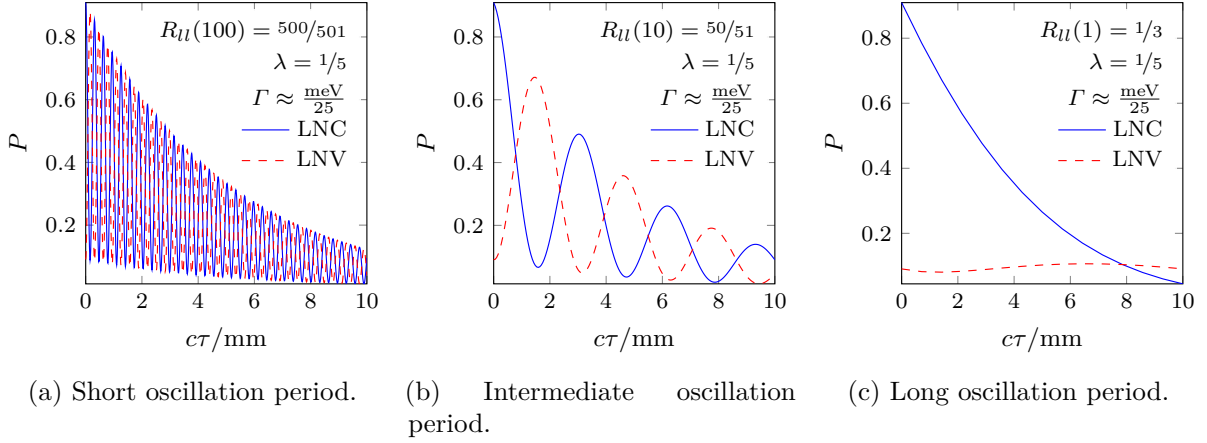
Figure 3.4: Oscillations of the probability P that the process shown in figure 3.3 is LNC or LNV as a function of the proper time τ. The oscillation period depends on the mass splitting Δm, the overall decay depends on the decay width Γ, and the decoherence depends on the damping parameter λ, all of which are defined in section 3.3.2. Panel (a) shows a short oscillation period with $\Delta m/\Gamma = 100$, panel (b) shows an intermediate oscillation period with $\Delta m/\Gamma = 10$, and panel (c) shows a long oscillation period with $\Delta m/\Gamma = 1$. All oscillations are shown for $\Gamma \approx \frac{\text{meV}}{25}$ and $\lambda = 1/5$ and R_{ll} is defined in section 3.3.3.

resolvable, an integrated effect could still be measured.

3.3.1　External wave packets

In order to predict the oscillatory behaviour of new particles, a holistic QFT framework is necessary that, in contrast to the simplified QM framework, is able to not only capture potential oscillations but can also predict the potential damping of these oscillations due to the loss of coherence of the mass eigenstate superposition. Compared to the plane wave description of particle oscillations, the QFT external wave packet approach discussed in [38] and adapted to the case of $N\overline{N}$Os in [1] allows the derivation of the phenomenon free of contradictions. This is due to the fact that the inherent uncertainty of wave packets in momentum and position space allows the simultaneous production of several on-shell mass eigenstates that can subsequently interfere to produce oscillations. Furthermore, the approximate localisation of wave packets is necessary to introduce the notion of a travelled distance and time, which is not possible using infinitely extended plane waves. Additionally, several effects potentially leading to the decoherence of the mass eigenstate superposition are included and discussed under the name of *observability conditions* [4]. *External* refers to the fact that only the external particles are explicitly assumed to be wave packets, whereas in an intermediate wave packed approach, the intermediate particles, such as in this case the heavy neutrinos, are directly described by wave packets. However, even in the external wave packet approach, it is possible to interpret the intermediate particles as wave packets where some clarifications about the causal nature of this interpretation can be found in [38, 79].

For the external wave packet models, the assumptions about the shape and the widths of the involved wave packets are a major source of uncertainty when deducing results. Also, the formalism discussed in [1, 38] was mainly developed having long-lived quasi mass-degenerate particles in mind. In particular, the theorem of Jacob-Sachs [54] is only valid above a certain time threshold, below which additional corrections have to be taken into account. In [1, 4], the regions, as well as the effects of the above-mentioned corrections, are discussed in detail, and it is shown that in phenomenological studies of nearly mass-degenerate, quasi long-lived heavy

neutrinos, the effects of the corrections can be neglected for a range of external wave packet widths spanning orders of magnitude.

3.3.2 Oscillations at leading order

In the case of slightly broken LNLS governing the physics of pseudo-Dirac heavy neutrinos, the complete LO contributions to the $N\overline{N}O$ can be described using only two parameters in addition to the seesaw model in the LNC limit [1, 4]. Hence instead of working with the whole family of realistic seesaw models and their parameters, one can instead introduce, in addition to the heavy neutrino mass m and the active-sterile mixing parameter $\boldsymbol{\theta}$ defined in equation (3.4.6), just the mass splitting of the heavy neutrinos Δm and the damping parameter λ. As an effective parameter, Δm captures the effects induced by the LNLS breaking parameters, and λ entails the decoherence effects appearing in certain parameter regions of the QFT description of neutral particle oscillations. To LO, the formulae for the oscillation probabilities as a function of the proper time τ are

$$P_{\text{osc}}^{\text{LNC/LNV}}(\tau) = \frac{1 \pm \cos(\Delta m \tau)\exp(-\lambda)}{2}\,, \tag{3.3.1}$$

hence the oscillation period is given by $\tau_{\text{osc}} = 2\pi/\Delta m$. The overall decay of the heavy neutrino is given by the usual probability density for the decay of unstable particles

$$P_{\text{decay}}(\tau) = -\frac{\mathrm{d}}{\mathrm{d}\tau}\exp(-\Gamma\tau) = \Gamma\exp(-\Gamma\tau)\,. \tag{3.3.2}$$

as function of the decay width $\Gamma = \Gamma(m,\theta)$. Therefore, the total probability for an unstable and oscillating particle to decay in a proper time window is given by

$$P_{ll}^{\text{LNC/LNV}}(\tau_{\text{min}},\tau_{\text{max}}) = \int_{\tau_{\text{min}}}^{\tau_{\text{max}}} P_{\text{osc}}^{\text{LNC/LNV}}(\tau)P_{\text{decay}}(\tau)\,\mathrm{d}\tau\,, \tag{3.3.3}$$

and the number of expected events in a collider experiment is then

$$N^{\text{LNC/LNV}} = \mathscr{L}\sigma\,\text{BR}\int D(\vartheta,\gamma)P_{ll}^{\text{LNC/LNV}}(\tau_{\text{min}}(\vartheta,\gamma),\tau_{\text{max}}(\vartheta,\gamma))\,\mathrm{d}\vartheta\,\mathrm{d}\gamma\,, \tag{3.3.4}$$

where the factor $D(\vartheta,\gamma)$ accounts for the probability density that the heavy neutrino has Lorentz factor γ and is produced with an angle ϑ with respect to the beam axis, $\mathscr{L}$ is the luminosity of the collider, and σ and BR are the sterile neutrino production cross section and branching ratio of the process under consideration. The parameters τ_{min} and τ_{max} are defined by the detector geometry when transitioning from proper time coordinates to the lab frame via $\tau(\vartheta,\gamma) = (\gamma^2-1)^{-1/2}L(\vartheta)$.

3.3.3 Integrated effect

In an experimental situation in which it is not possible to resolve the oscillation patterns, an integrated effect could still be measurable by comparing the number of events with opposite-, and same-sign leptons originating from processes such as the one presented in figure 3.3. Evaluating the integral (3.3.3) in order to obtain the probability of LNC and LNV decays between the minimal proper time τ_{min} and the maximal proper time τ_{max} results in the difference

$$P_{ll}^{\text{LNC/LNV}}(\tau_{\text{min}},\tau_{\text{max}}) = \Gamma\frac{P^{\text{LNC/LNV}}(\tau_{\text{max}}) - P^{\text{LNC/LNV}}(\tau_{\text{min}})}{2}\,, \tag{3.3.5}$$

where the indefinite integral is given by

$$P^{\text{LNC/LNV}}(\tau) = P(\tau,\Gamma,0) \pm \frac{P(\tau,\Gamma_-,\lambda) + P(\tau,\Gamma_+,\lambda)}{2}\,, \tag{3.3.6}$$

36
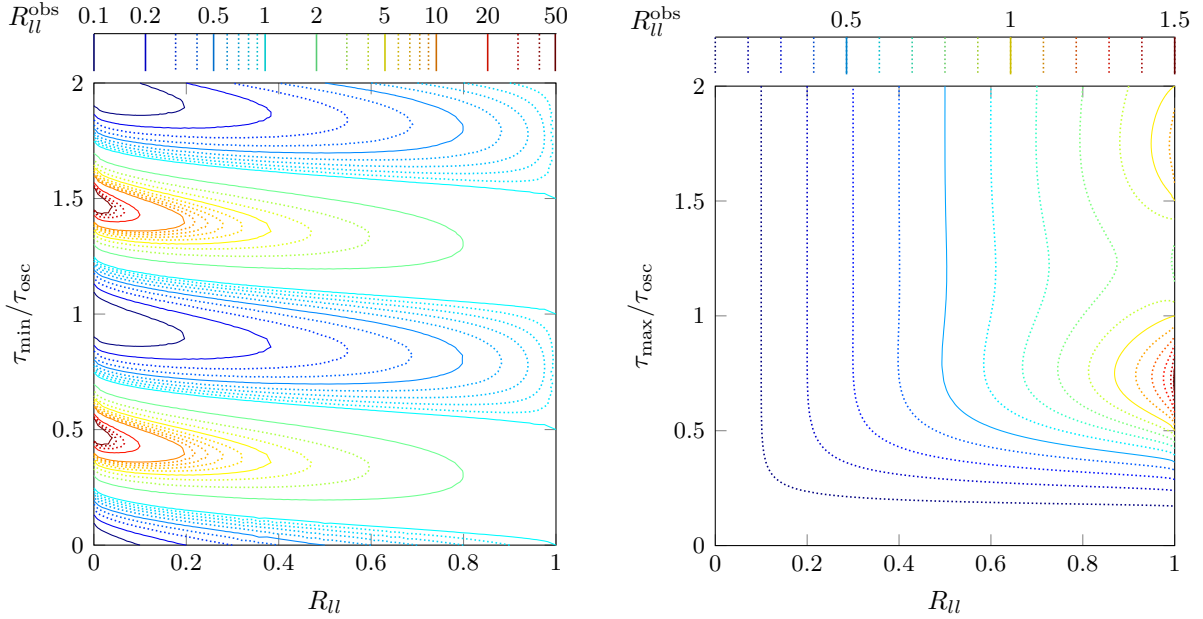
(a) $R_{ll}^{\text{obs}}(R_{ll}, \tau_{\text{min}}/\tau_{\text{osc}})$ while $\tau_{\text{max}} \to \infty$.   (b) $R_{ll}^{\text{obs}}(R_{ll}, \tau_{\text{max}}/\tau_{\text{osc}})$ while $\tau_{\text{min}} \to 0$.

Figure 3.5: Impact of the finite detector size on the measurement of R_{ll}. The plots show the observable R_{ll}^{obs} as a function of τ/τ_{osc} and the theoretical R_{ll}, calculated by taking the limits (3.3.8) simultaneously. In panel (a) τ_{min} is variable and $\tau_{\text{max}} \to \infty$ while in panel (b) τ_{max} is variable and $\tau_{\text{min}} \to 0$. Note that only in the region where the contours are vertical R_{ll} coincides with R_{ll}^{obs} and that R_{ll}^{obs} is not bound to be smaller or equal to one and even has poles in panel (a).

with

$$P(\tau, \Gamma, \lambda) = \int e^{-\lambda - \Gamma \tau} \, \mathrm{d}\tau = -\frac{e^{-\lambda - \Gamma \tau}}{\Gamma}\,, \qquad\qquad \Gamma_\pm = \Gamma \pm i\Delta m\,. \qquad (3.3.7)$$

In the limit that the experiment can observe all decays from the origin to infinity and under the assumption that the parameter point under consideration does allow to neglect decoherence effects, which is equivalent to

$$\tau_{\text{min}} \to 0\,, \qquad\qquad \tau_{\text{max}} \to \infty\,, \qquad\qquad \lambda \to 0\,, \qquad (3.3.8)$$

this expression simplifies to

$$P_{ll}^{\text{LNC/LNV}} = \frac{1}{2} \begin{cases} \frac{\Gamma^2}{\Delta m^2 + \Gamma^2} + 1 & \text{for LNC} \\ \frac{\Delta m^2}{\Delta m^2 + \Gamma^2} & \text{for LNV} \end{cases}\,. \qquad (3.3.9)$$

Therefore, the ratio between the two decay modes is, in this case, given by

$$R_{ll} = \frac{P_{ll}^{\text{LNV}}}{P_{ll}^{\text{LNC}}} = \frac{\Delta m^2}{\Delta m^2 + 2\Gamma^2}\,, \qquad (3.3.10)$$

which matches the result of references [41, 50]. While a Dirac heavy neutrino would have $R_{ll} = 0$ and a Majorana heavy neutrino would have $R_{ll} = 1$, a realistic pseudo-Dirac heavy neutrino can have any value in between. However, even in the simplified case of a single Majorana heavy neutrino, the measurement of $R_{ll} = 1$ would be challenging since asymmetries in the number of measured LNC and LNV events caused by the detector geometry in combination with the angular
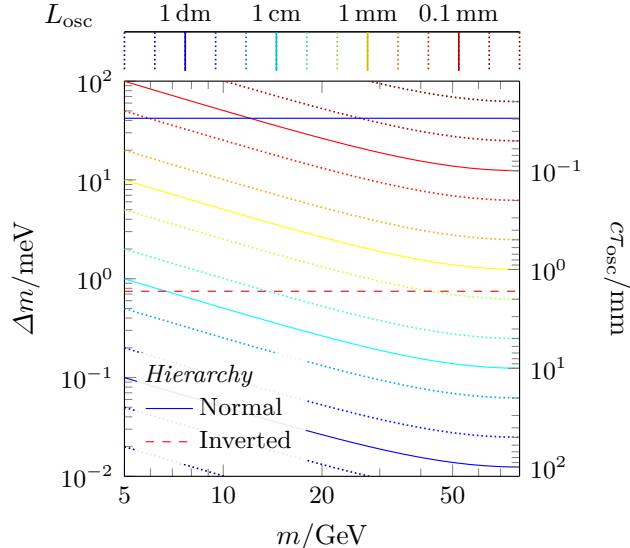
Figure 3.6: Oscillation period L_{osc} as a function of the heavy neutrino mass m and the mass splitting Δm. The Lorentz factor is estimated using W bosons at rest (3.3.14). The horizontal lines correspond to the mass splitting appearing in the two minimal linear seesaw BMs given in table 3.1.

dependence discussed in section 3.6.5 as well as the detector effects discussed in the following will have an impact on the measured R_{ll}. For pseudo-Dirac heavy neutrinos, figure 3.14 compares the dependence of R_{ll} on $\Delta m/\Gamma$ derived in (3.3.10) with a MC simulation. Additionally, the bands of $R_{ll} \in [0.1, 0.9]$ for five pseudo-Dirac benchmark models (BMs) introduced in table 3.1 are given in figure 3.18.

However, taking the finite size of the experimental setup into account by integrating only over the fiducial detector size in (3.3.5) changes the picture drastically. In this case the parameters $\tau_{\min}$ and $\tau_{\max}$ in

$$R_{ll}^{\mathrm{obs}}(\tau_{\min}, \tau_{\max}) = \frac{P_{ll}^{\mathrm{LNV}}(\tau_{\min}, \tau_{\max})}{P_{ll}^{\mathrm{LNC}}(\tau_{\min}, \tau_{\max})}\,, \tag{3.3.11}$$

cannot be taken to be zero and infinity, respectively. The consequences of this effect in the limit of vanishing damping and in terms of the proper time are presented in figure 3.5. In this representation, vertical contour lines indicate negligible deviation of R_{ll}^{obs} from R_{ll}. For a finite $\tau_{\min}$, an oscillatory pattern becomes apparent that has its minima for cuts in the vicinity of multiples of the oscillation period. The dependence on $\tau_{\max}$ is less severe and only occurs close to an R_{ll} of one. The two extreme limiting cases are

$$R_{ll}^{\mathrm{obs}} = \begin{cases} \tan^2 \dfrac{r_{\min}}{2} & \text{for } R_{ll} \to 0 \text{ and } \tau_{\max} \to \infty \\[2ex] \dfrac{r_{\max} - \sin r_{\max}}{r_{\max} + \sin r_{\max}} & \text{for } R_{ll} \to 1 \text{ and } \tau_{\min} \to 0 \end{cases}, \qquad r_m = \Delta m \tau_m\,. \tag{3.3.12}$$

While the effect for $R_{ll} \to 1$ and $\tau_{\min} \to 0$ is damped for large $\tau_{\max}$ the effect for $R_{ll} \to 0$ and $\tau_{\max} \to \infty$ remains undamped when varying $\tau_{\min}$ as long as the Lorentz factor distribution, and the decoherence can be neglected [4].

3.3.4 Oscillations in the lab frame

When boosting the oscillations described in section 3.3.2 into the lab frame, two main effects have to be considered. Firstly, the oscillation length in the lab frame, defined as

$$L_{\mathrm{osc}} = \sqrt{\gamma^2 - 1}\,\tau_{\mathrm{osc}}\,, \tag{3.3.13}$$

is, on an event-per-event basis, increased by the Lorentz factor. This well-known effect helps to compensate for the short oscillation period of some realistic BMs. For processes such as the one depicted in figure 3.3, the Lorentz factor of the heavy neutrino γ can be estimated to be

$$\gamma \approx \frac{m_W^2 + m^2}{2 m_W m}\,, \tag{3.3.14}$$

which relies on the assumption that the initial W boson decays at rest and neglects the mass of the prompt muon. The resulting resolvable oscillation length as a function of the heavy neutrino mass m and the mass splitting Δm is shown in figure 3.6.

Secondly, the oscillation pattern is washed out by the event-dependent Lorentz factor. Therefore, any study hoping to resolve $N\overline{N}$Os needs to measure enough observables to reconstruct the Lorentz factor. This makes studies relying on processes with final state neutrinos extremely challenging and is the reason why we focus on semileptonic final states as shown in figure 3.3.

3.4 Symmetry protected seesaw scenario

As detectable heavy neutrinos cannot be too heavy or too weakly coupled, they must originate from a model with an approximate LNLS and form pseudo-Dirac pairs as discussed in section 3.2. In the following, we assume that one pseudo-Dirac pair dominates the collider phenomenology. We will first introduce the type I seesaw in the limit of exact symmetry conservation in section 3.4.1. This model builds on two Majorana DOFs that form one exact Dirac particle. Subsequently, we add small symmetry-breaking terms in section 3.4.2 recovering models such as the linear and inverse seesaw. After comparing this model with the LO terms governing the $N\overline{N}$Os summarised in section 3.3.2, we introduce a phenomenological model with a minimal number of parameters that is able to describe the relevant observables in section 3.4.3.

3.4.1 Seesaw in the symmetric limit

In the symmetric limit of the symmetry protected seesaw scenario (SPSS) [31, 32], the two heavy Majorana neutrinos are protected by a LNLS. One simple choice of charges for the LNLS protecting the lepton number L is given by

$$\begin{array}{c|ccc} & \ell & N_1 & N_2 \\ \hline L & +1 & -1 & +1 \end{array}\,, \tag{3.4.1}$$

with all other fields having a charge of zero. In this case, the general Lagrangian (3.2.1) takes the form

$$\mathcal{L}_{\mathrm{SPSS}}^L = \overline{N_i^c}\, i\slashed{\partial} N_i - y_{1\alpha} \overline{N_1^c} \widetilde{H}^\dagger \ell_\alpha - \overline{N_1^c} m_M N_2 + \cdots + \mathrm{H.c.}\,, \tag{3.4.2}$$

where N_1 and N_2 are taken to be left-chiral sterile neutrinos. The ellipses capture contributions from additional sterile neutrinos, which are assumed to be heavier or much weaker coupled than the explicitly denoted pair and are expected to contribute only sub-dominantly to the collider

phenomenology of the model. After EWSB the neutrino mass Lagrangian of the interaction eigenstates $n = (\nu_e, \nu_\mu, \nu_\tau, N_1, N_2)^\mathsf{T}$ can be written as

$$\mathcal{L}_{\text{mass}} = -\frac{1}{2}\overline{n^c}M_n n + \text{H.c.}\,, \tag{3.4.3}$$

where the mass matrix is given by

$$M_n = \begin{pmatrix} 0 & M_{3\times2} \\ M_{3\times2}^\mathsf{T} & M_N \end{pmatrix} = \begin{pmatrix} 0 & \boldsymbol{m}_D & 0 \\ \boldsymbol{m}_D^\mathsf{T} & 0 & m_M \\ 0 & m_M & 0 \end{pmatrix}\,, \tag{3.4.4}$$

with $\boldsymbol{m}_D = \boldsymbol{y}_1 v$ being the Dirac mass term. The mass matrix can be approximately diagonalised using a Takagi decomposition

$$D_n = U_n^\mathsf{T} M_n U_n\,, \qquad\qquad U^\dagger U = \mathbb{1}\,, \tag{3.4.5}$$

following the steps presented in [1, 65]. Since the LNLS is conserved, the light neutrinos are massless, and the heavy neutrinos are mass degenerate [80]. Up to the second order in the active-sterile mixing parameter

$$\boldsymbol{\theta} = \frac{\boldsymbol{m}_D}{m_M}, \tag{3.4.6}$$

where $\boldsymbol{\theta} = (\theta_e, \theta_\mu, \theta_\tau)^\mathsf{T}$, their masses are

$$m_4 = m_5 = m_M\left(1 + \frac{1}{2}|\boldsymbol{\theta}|^2\right) + \mathcal{O}\big(|\boldsymbol{\theta}|^4\big)\,, \tag{3.4.7}$$

and the mixing matrix is given by

$$U_n = \begin{pmatrix} U_{\text{PMNS}} & U_{\text{CL}} \\ U_{2\times3} & U_N \end{pmatrix} = \begin{pmatrix} \mathbb{1}_{3\times3} - \frac{1}{2}\boldsymbol{\theta}^* \otimes \boldsymbol{\theta} & -\frac{i}{\sqrt{2}}\boldsymbol{\theta}^* & \frac{1}{\sqrt{2}}\boldsymbol{\theta}^* \\ 0 & \frac{i}{\sqrt{2}} & \frac{1}{\sqrt{2}} \\ -\boldsymbol{\theta}^\mathsf{T} & -\frac{i}{\sqrt{2}}(1 - \frac{1}{2}|\boldsymbol{\theta}|^2) & \frac{1}{\sqrt{2}}(1 - \frac{1}{2}|\boldsymbol{\theta}|^2) \end{pmatrix}\,, \tag{3.4.8}$$

where the upper left block is the Pontecorvo–Maki–Nakagawa–Sakata (PMNS) matrix. One can show that the upper right 3×2 charged lepton (CL) block of the mixing matrix, which relates heavy neutrinos and active SM neutrinos, has the exact form

$$U_{\text{CL}} = \frac{1}{\sqrt{1 + |\boldsymbol{\theta}|^2}}\left(-\frac{i}{\sqrt{2}}\boldsymbol{\theta}^*, \frac{1}{\sqrt{2}}\boldsymbol{\theta}^*\right)\,. \tag{3.4.9}$$

Therefore it is possible to absorb higher order corrections in $\boldsymbol{\theta}$ into a rescaling of the Yukawa coupling. In particular the exact form of U_{CL} can be recovered from the LO approximation by rescaling of the mixing parameter

$$\boldsymbol{\theta}^* \to \boldsymbol{\theta}'^* = \frac{\boldsymbol{\theta}^*}{\sqrt{1 + |\boldsymbol{\theta}|^2}}\,. \tag{3.4.10}$$

Consequently, it suffices to expand U_{CL} to LO.

Due to the mass degeneracy and phase difference of the heavy neutrinos, there are no $N\overline{N}$Os in the symmetric limit, and this theory of two Majorana particles is equivalent to a theory with a single Dirac particle. For any process with SM external particles that contains a Feynman diagram with one of the heavy neutrino mass eigenstates, also the other heavy neutrino mass eigenstate contributes. In an explicit calculation, it can be shown that the amplitudes from the different mass eigenstates cancel each other, such that LNV processes are not present, see also section 3.A. We recover the argument laid out in section 3.2 that a theory relying solely on one exact Dirac heavy neutrino is LNC and incapable of generating SM neutrino masses.

Seesaw		Hierarchy	BM
Linear	$\Delta m = \Delta m_\nu$	Normal	$\Delta m_\nu = (41.46 \pm 0.29)\,\mathrm{meV}$
		Inverted	$\Delta m_\nu = (749 \pm 21)\,\mathrm{\mu eV}$
Inverse	$\Delta m = m_\nu |\boldsymbol{\theta}|^{-2}$		$m_\nu = 0.5\,\mathrm{meV}$
			$m_\nu = 5\,\mathrm{meV}$
			$m_\nu = 50\,\mathrm{meV}$

Table 3.1: Five BMs for the linear and inverse seesaw are discussed in the text. The linear seesaw BMs represent the only two possible models in the minimal linear seesaw of a single pseudo-Dirac heavy neutrino. With more pseudo-Dirac heavy neutrinos in the spectrum, other models become feasible. Since the inverse seesaw requires at least two pairs of pseudo-Dirac neutrinos, it is not possible to uniquely connect it to the measured neutrino mass differences, and we use a wide spectrum of neutrino masses as BMs.

3.4.2 Seesaw with small symmetry breaking

In order to introduce SM neutrino masses, the symmetric limit of the SPSS can be perturbed by extending the Lagrangian (3.4.2) with additional small LNV terms

$$\mathcal{L}_{\mathrm{SPSS}}^{\not L} = -y_{2\alpha}\overline{N_2^c}\widetilde{H}^\dagger \ell_\alpha - \mu_M' \overline{N_1^c}N_1 - \mu_M \overline{N_2^c}N_2 + \cdots + \mathrm{H.c.}\,, \qquad (3.4.11)$$

where a Yukawa coupling $\boldsymbol{y}_2$ and two Majorana masses μ_M and μ_M' are introduced. The resulting mass matrix is

$$M_n = \begin{pmatrix} 0 & \boldsymbol{m}_D & \boldsymbol{\mu}_D \\ \boldsymbol{m}_D^\intercal & \mu_M' & m_M \\ \boldsymbol{\mu}_D^\intercal & m_M & \mu_M \end{pmatrix}, \qquad (3.4.12)$$

where $\boldsymbol{\mu}_D = \boldsymbol{y}_2 v$ is a Dirac mass term. These additional terms break the LNLS symmetry characterised by the charges given in equation (3.4.1). In order to ensure a small breaking of the LNLS, we require

$$\mathcal{O}\left(\frac{\boldsymbol{\mu}_D}{m_M}\right) = \mathcal{O}\left(\frac{\mu_M}{m_M}\right) = \mathcal{O}\left(\frac{\mu_M'}{m_M}\right) = \epsilon \ll 1\,, \qquad (3.4.13)$$

Since the parameters $\boldsymbol{\theta}$ can be larger than $\mathcal{O}(\epsilon)$, an expansion in small parameters might contain powers in $\boldsymbol{\theta}$ higher than in ϵ. The Takagi decomposition (3.4.5) of the mass matrix (3.4.12) results now in two distinct heavy neutrino masses of

$$m_{4/5} = m_M\left(1 + \frac{1}{2}|\boldsymbol{\theta}|^2\right) \mp \left(\cos(\phi)|\boldsymbol{\mu}_D^*\boldsymbol{\theta}| + \frac{|\mu_M^* + \mu_M'|}{2}\right) + \mathcal{O}\big(\max(\epsilon^2, \epsilon|\boldsymbol{\theta}|^2, |\boldsymbol{\theta}|^4)\big)\,. \quad (3.4.14)$$

where

$$\phi = \begin{cases} 0 & \text{for } \mu_M = \mu_M' = 0 \\ \arg(\boldsymbol{\mu}_D^*\boldsymbol{\theta}(\mu_M^* + \mu_M')) & \text{otherwise} \end{cases}. \qquad (3.4.15)$$

The upper right 2×3 part of the mixing matrix is given by

$$U_{\mathrm{CL}} = \left(\tfrac{i}{\sqrt{2}}(\boldsymbol{\theta}^* - \boldsymbol{\theta}_\epsilon^*),\ \tfrac{1}{\sqrt{2}}(\boldsymbol{\theta}^* + \boldsymbol{\theta}_\epsilon^*)\right) + \mathcal{O}\big(\max(\epsilon\boldsymbol{\theta}, |\boldsymbol{\theta}|^2\boldsymbol{\theta})\big)\,, \qquad (3.4.16)$$

where $\boldsymbol{\theta}_\epsilon = \boldsymbol{\mu}_D/m_M$ is the LNV equivalent to the active-sterile mixing parameter. In cases where higher order terms in $\boldsymbol{\theta}$ are of the same order as terms of $\mathcal{O}(\epsilon\boldsymbol{\theta})$, the rescaling (3.4.10) can be used to absorb higher order terms into a redefinition of the coupling $\boldsymbol{\theta}$. This shows that higher order terms in $\boldsymbol{\theta}$ yield no qualitative new effects, and the expansion of the mixing matrix is valid up to $\mathcal{O}(\epsilon\boldsymbol{\theta})$.
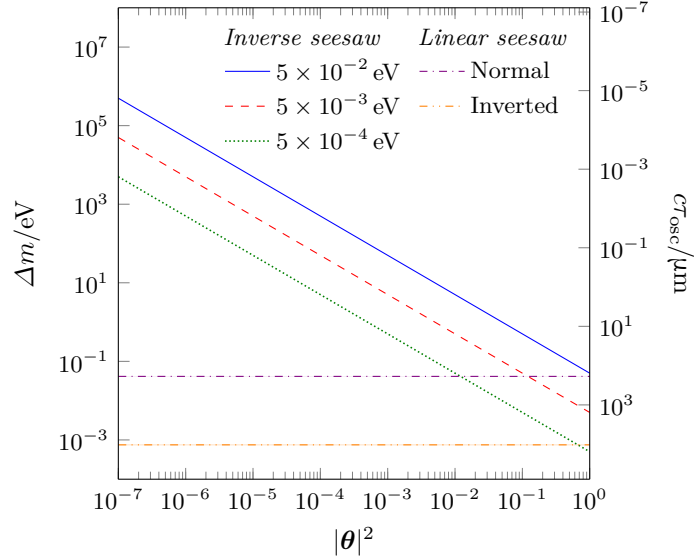
Figure 3.7: Heavy neutrino mass splitting as a function of the active-sterile mixing parameter for the five BMs of the minimal linear and inverse seesaw given in table 3.1.

The mass matrix (3.4.12) is the most generic tree-level seesaw matrix one can generate from two sterile neutrinos. It incorporates as limiting cases the linear and the inverse seesaw. In particular, the individual matrix elements have the following phenomenology:

- The Dirac contribution $\boldsymbol{\mu}_D$ yields the linear seesaw [81, 82] for which the neutrino mass matrix is given by $M_\nu = \boldsymbol{\mu}_D \otimes \boldsymbol{\theta} + \boldsymbol{\theta} \otimes \boldsymbol{\mu}_D$ and has the two nonzero eigenvalues $m_\nu = |\boldsymbol{\mu}_D||\boldsymbol{\theta}| \mp |\boldsymbol{\mu}_D^* \boldsymbol{\theta}|$. The mass splitting of the heavy neutrinos is, in this case, $\Delta m = 2|\boldsymbol{\mu}_D^* \boldsymbol{\theta}|$. When reproducing the measured light neutrino data in the minimal linear seesaw with a single pseudo-Dirac pair, the mass splitting of the heavy neutrinos is therefore equal to the mass splitting of the light neutrinos $\Delta m = \Delta m_\nu$, cf. [44].

- The Majorana contribution μ_M in the third entry on the main diagonal yields the inverse seesaw [83–85] for which the neutrino mass matrix is $M_\nu = \mu_M \boldsymbol{\theta} \otimes \boldsymbol{\theta}$. Since this expression results in a single finite eigenvalue of $m_\nu = \mu_M |\boldsymbol{\theta}|^2$ at least two pseudo-Dirac pairs are necessary to describe the observed neutrino oscillation data. The mass splitting for the pseudo-Dirac pair considered here is $\Delta m = |\mu_M|$ and can therefore be expressed in terms of the SM neutrino mass eigenvalue $\Delta m = m_\nu |\boldsymbol{\theta}|^{-2}$, cf. [44].

- The Majorana contribution μ_M' in the second entry on the main diagonal introduces a mass splitting between the heavy neutrinos of $\Delta m = |\mu_M'|$ without a LO tree-level impact on the light neutrino masses. It does, however, generate a contribution to M_ν at one loop [86, 87]. Furthermore, it can be exploited to reduce the mass splitting necessary to generate realistic neutrino masses when added to the linear or inverse seesaw.[4]

- The 3×3 block in the upper left, which contains the light neutrino masses, is zero at tree-level.

From the observed neutrino oscillation data, it is possible to extract two mass differences which can be combined in two different mass hierarchies, the normal and inverted light neutrino mass ordering. Whether the third neutrino is also massive cannot be determined with current data;

---

[4] If additionally, the linear seesaw term is present, the subdominant contribution $\Delta M_\nu = \mu_M' \boldsymbol{\theta}_\epsilon \otimes \boldsymbol{\theta}_\epsilon$ to the neutrino mass matrix is generated [88].

hence we use as minimal BMs for the linear seesaw the two possible mass differences between the two massive SM neutrinos $\Delta m_\nu^{\mathrm{normal}} = (41.46 \pm 0.29)\,\mathrm{meV}$ and $\Delta m_\nu^{\mathrm{inverted}} = (749 \pm 21)\,\mathrm{\mu eV}$ [89, 90]. At the same time, an upper bound on the sum of the neutrino masses $\sum m_\nu < 120\,\mathrm{meV}$ has been established using cosmological observations [17]. Since models relying on the inverse seesaw require at least two pseudo-Dirac pairs, the mass splitting of the heavy neutrinos is not uniquely determined by the observed light neutrino parameters. However, when defining masses for the light neutrinos as BMs, the heavy neutrino masses can be deduced. We use as corresponding BMs light neutrino masses of $m_\nu = 0.5, 5, 50\,\mathrm{meV}$. These BMs are summarised in table 3.1.

The relation between the mass splitting and the mixing parameter for the five BMs of the linear and inverse seesaw is visualised in figure 3.7. For BMs with a single LNV entry in the mass matrix (3.4.12), the minimal value for the mass splitting of $\Delta m \approx 750\,\mathrm{\mu eV}$ corresponding to a maximal oscillation period of $c\tau \approx 1\,\mathrm{cm}$ is reached in the linear seesaw with inverted ordering. In order to generate pseudo-Dirac pairs with a smaller mass splitting and, therefore, larger oscillation period, one can, on the one hand, rely on cancellations between the linear and inverse seesaw terms or cancellations involving μ_M' or, on the other hand, go beyond the minimal model consisting of a single pseudo-Dirac pair.

3.4.3 Phenomenological symmetry protected seesaw scenario

Given the small amount of symmetry breaking permissible for consistent low-scale seesaw models, most of their effects can be neglected in phenomenological studies [72]. One important exception are $N\overline{N}$Os, as they are an interference phenomenon and, as such, strongly enhanced beyond the typical expectation for an $\mathcal{O}(\epsilon)$ effect. As shown in section 3.3.2 the $N\overline{N}$Os at LO can be described with just two parameters in addition to the symmetric limit of the SPSS, which are the mass splitting of the heavy neutrinos Δm governing oscillation period in the proper time frame and the damping parameter λ governing the effects of decoherence.

Therefore, we introduce the *phenomenological symmetry protected seesaw scenario (pSPSS)* optimised for phenomenological studies. Instead of adding the symmetry-breaking terms from Lagrangian (3.4.11) to the SPSS Lagrangian (3.4.2), one can directly add the mass splitting without specifying if it originates from a linear seesaw, an inverse seesaw, or a more complicated model. The masses of the two heavy neutrinos in the pSPSS are derived from the mass in the symmetric limit and the single additional parameter Δm

$$m_{4/5} = m_M \left(1 + \frac{1}{2}|\boldsymbol{\theta}|^2 \right) \mp \frac{1}{2}\Delta m \,, \tag{3.4.17}$$

capturing the entirety of sources contributing to the mass splitting in (3.4.14). Since oscillations are an interference phenomenon, they are observable even though the mass splitting is orders of magnitude below the energies that can be hoped to be resolved in experimental setups.

Additionally, the value of the damping parameter λ has to be determined for each parameter point. As shown in [1, 4, 38], the effects of decoherence described as observability conditions, and therefore the damping parameter λ, can be neglected for the part of the parameter space where it is likely that $N\overline{N}$Os can be reconstructed. In order to allow the simulation of parameter points for which decoherence effects are important, we include the damping parameter in the pSPSS. The relevant parameters of the pSPSS are thus the three active-sterile mixing parameters $\boldsymbol{\theta}$, the heavy neutrino Majorana mass m_M, its mass splitting parameters Δm, and the damping parameter λ.

```
BLOCK PSPSS #

1  1.000000e+02   # mmaj
2  1.000000e-12   # deltam
3  0.000000e+00   # theta1
4  1.000000e-03   # theta2
5  0.000000e+00   # theta3
6  0.000000e+00   # damping
```

Table 3.2: The parameters of the pSPSS implemented in the FEYNRULES model file as they appear in the MADGRAPH `param.card`.

3.5 Software implementation

In order to simulate $N\overline{N}O$ at colliders, we have implemented the pSPSS in FEYNRULES. We provide this implementation online [91] and explain its details in section 3.5.1. Furthermore, we have patched MADGRAPH as described in section 3.5.2 in order to be able to simulate $N\overline{N}Os$.

3.5.1 FEYNRULES model file

In the following, we introduce the quantities used in the FEYNRULES [92] model file [91]. For each quantity we give, besides its mathematical symbol, also its variable name used in the model file, denoted in brackets.

According to the discussion in the previous section, the SM Lagrangian has to be extended by two sterile Majorana neutrinos denoted by N_1 (`N1L`) and N_2 (`N2L`). In the model file, an additional new physics (NP) parameter for the Higgs VEV denoted by `vevNP` has been introduced. The only difference to the usual Higgs VEV (`vev`) is the interaction order, which has been set to `{NP, -1}` instead of `{QED, -1}` in order to provide MADGRAPH with the correct power counting rules, but for all physical considerations they can be thought of as equal. Along with `vevNP`, the field `PhiNP` is introduced, which corresponds to the usual Higgs doublet `Phi` where the `vev` is replaced by `vevNP`. The masses of the heavy neutrinos are given by (3.4.17) where the Majorana mass parameter is denoted by m_M (`Mmaj`), the active-sterile mixing parameter given in (3.4.6) by $\boldsymbol{\theta}$ (`theta1`, `theta2`, `theta3`), and the mass splitting of the heavy neutrinos is implemented via the parameter Δm (`deltaM`).

The physical fields, i.e. the mass eigenstates, are extended by two self-conjugate neutrinos labelled n_4 (`n4`) and n_5 (`n5`). The mixing matrix relating the mass eigenstate neutrinos to the interaction eigenstates is denoted by U_n (`Un`) and satisfies

$$U_n^\intercal M_n U_n = \mathrm{diag}(0,0,0,m_4,m_5)\,, \tag{3.5.1}$$

up to second order in $\boldsymbol{\theta}$. The matrix U'_{CL} (`UnCL`) is the upper right 3×5 part of U_n and is necessary for the automatic index contraction in FEYNRULES. A field that contains all mass eigenstate neutrinos is introduced as n_i (`nL`). With this, the active neutrino interaction eigenstates of the SM can be rotated to the mass eigenstate neutrinos using the relation

$$n_\alpha = (U'_{\mathrm{CL}})_{\alpha i} n_i\,. \tag{3.5.2}$$

The neutrinos interact with the SM only via the lepton doublet ℓ (`LL`). The mixing is implemented using equation (3.5.2) by replacing the neutrino ν (`vl`) with the transformed neutrino (`UnCL nL`).

The kinetic terms of the sterile neutrinos
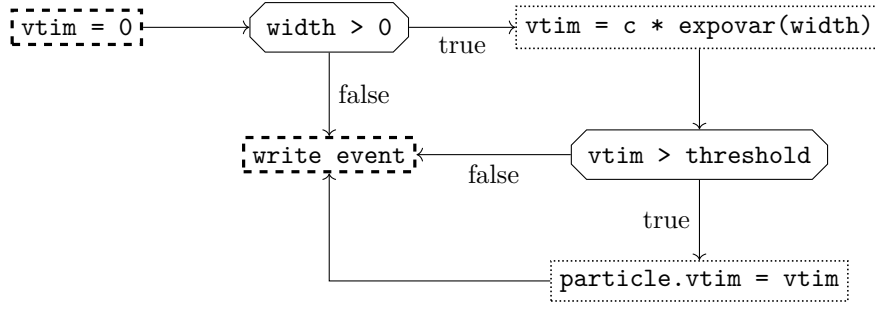
Figure 3.8: The usual routine of MadGraph assigning the proper TOF (`vtim`) to a particle (`particle`) as long as it is larger than the threshold value (`threshold`) given in the `run.card`. The process flows from the node `vtim = 0` to the node `write event`.

I (N1Lbar.Ga[mu].del[N1L, mu] + N2Lbar.Ga[mu].del[N2L, mu])

have been added to the `LFermions` Lagrangian of the SM. The mass term

- Mmaj CC[N1Lbar[sp1]].N2L[sp1]

where `sp1` is an internal spin index and the Yukawa term

yvn[ff1] (CC[N1Lbar[sp1]].LL[sp1, ii, ff1] PhiNPbar[jj] Eps[ii, jj])

where `yvn` is the Yukawa vector $y_{\alpha 1}$, `ff1` is an internal family index and `ii` and `jj` are internal SU(2) doublet indices, have been introduced in the NP Lagrangian (`LNP`). Finally, the complete Lagrangian describing SM interactions of the pSPSS is denoted by `LpSPSS`. Since the implemented mixing matrix U_n is only valid up to the second order in $\boldsymbol{\theta}$, the full Lagrangian must be expanded in $\boldsymbol{\theta}$ and terms smaller than $\mathcal{O}(|\boldsymbol{\theta}|^2)$ have to be neglected. This is achieved using the function `RemoveHigherOrder` defined in the model file that expands its arguments up to second order in $\boldsymbol{\theta}$ and is automatically applied to the relevant Lagrangian parts.

The only additional free parameters in this model collected in the `PSPSS` block are the Majorana mass m_M (`Mmaj`), the mass splitting Δm (`deltaM`), and the three active-sterile mixing parameters $\boldsymbol{\theta}$ (`theta1`, `theta2`, `theta3`). The damping parameter λ (`damping`) has also been implemented in the FeynRules model file and can be adjusted in the MadGraph `param.card`. It is set to zero by default. When it is nonzero, it has the effect of damping the oscillations as discussed in section 3.3.2. All parameters as they appear in the `param.card` are collected in table 3.2.

3.5.2 Oscillations in MadGraph

The UFO folder exported from FeynRules can be imported into MadGraph [93] using the `import model` command. In order to generate the process depicted in figure 3.3, one defines the new multi-particles

```
define mu = mu+ mu-
define ww = w+ w-
define nn = n4 n5
```

As explained below, it is necessary to force the heavy neutrino to be on-shell. This can be achieved by generating a process that contains LNC as well as LNV events via

```
generate p p > mu nn, (nn > mu j j)
```
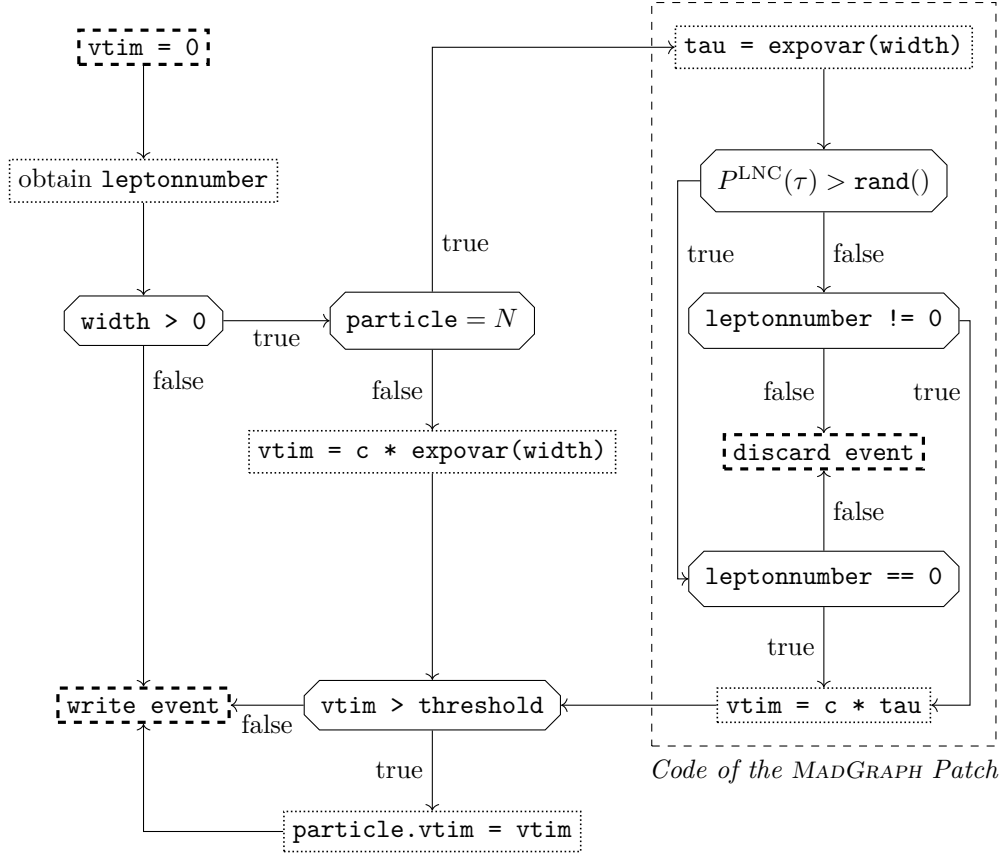
Figure 3.9: Patched MadGraph routine assigning a proper TOF (`vtim`) in the presence of oscillations to a particle (`particle`). The process flows from the node `vtim = 0` to the nodes `write event` and `discard event`.

If the heavy neutrino mass is significantly below the W mass, it is also possible to additionally ignore off-shell effects from the W boson by using

```
generate p p > ww, (ww > mu nn, (nn > mu j j))
```

A directory with the code for this process can then be obtained using the `output` command. In the following, the path of this directory is denoted by [pSPSS].

There are two reasons why it is desirable to ensure that the heavy neutrino is produced on-shell. First, the derivation of the oscillation formulae is based on the Jacob-Sachs theorem, see [38, 54], which takes the heavy neutrinos on-shell for large enough times. In practice, the constraint to be *large enough* does not give any restriction stronger than the ones already obtained in the observability conditions [4], such that in cases where there are oscillations, the heavy neutrino can be taken to be on-shell. For this paper, it has been assumed that decoherence can be neglected, and therefore effects from times smaller than the threshold are also neglected. The second reason to force the heavy neutrino to be on-shell is due to the implementation details of the MadGraph patch given here. Since parameter points that feature oscillations are close to the symmetry limit, one expects almost no LNV events for a prompt decay. Since MadGraph simulates the process as if it were prompt and adds displacement afterwards, one would not get LNV events if interference between different mass eigenstates is taken into account; see also the diagrammatic explanation in section 3.A. Taking the heavy neutrinos on-shell destroys the interference between different mass eigenstates such that LNC and LNV events are

created with equal probability. The correct interference patterns, featuring oscillations and the correct ratio of LNC and LNV events, are then added with the implementation of the patch given here.

The patch has been developed and tested with MadGraph5_aMC@NLO 2.9.10 (LTS) and is given in section 3.B. The idea behind it necessitates changing the behaviour of the function `do_add_Time_of_flight` located in the file [pSPSS]/bin/internal/madevent_interface.py,[5] which derives the decay vertex of a long-lived particle. The main routine that is executed for each particle in each event and which assigns the time of flight (TOF) to the particles is depicted in figure 3.8. This routine is changed as described in figure 3.9. The main idea is to compare the oscillation probability at a given proper time τ, to a pseudo-random variable in the range $[0, 1)$. Based on this, it is decided if the heavy neutrino should decay in a LNC or LNV process. Comparing this with the actual lepton number of the process (`leptonnumber`), which is zero in the LNC case and different from zero in the LNV case, it is then decided if the event should be kept or discarded. This algorithm ensures that any spin correlations that are present in the generated events are kept, but the drawback is that half of all events containing heavy neutrinos are discarded.[6]

In order to activate the computation of TOF, one also has to set the parameter `time_of_flight` in the `run.card` to an appropriate threshold value (`threshold`) value, e.g. to zero. Events can then be generated in the usual way using MadEvent. As described in sections 3.B and 3.6 we have carefully checked that the generated data faithfully represents the physical processes.

3.6 Example results

We have calculated various observables within the pSPSS using the model file and code modification described in section 3.5. For all of the results gathered here, we have set $\theta_e = \theta_\tau = 0$ and assumed that the effects of decoherence on the $N\overline{N}$Os can be neglected, i.e. $\lambda = 0$. In order to demonstrate that we reproduce prior results, we show as an example the heavy neutrino decay width and the expected number of events in a CMS-like detector as a function of the heavy neutrino mass and its coupling strength in section 3.6.1. Furthermore, we derive the most likely Lorentz factors as well as the fraction of events with a larger Lorentz factor in section 3.6.2. The main goal of this work is presented in section 3.6.3 where we show an example of $N\overline{N}$Os. Afterwards, the integrated effect is discussed in section 3.6.4. In section 3.6.5, the dependence of the transverse impact parameter on the angular-dependent spin correlation is presented. We conclude the results in section 3.6.6 by commenting on how displaced and prompt HNLs searches can be interpreted as bounds on the pseudo-Dirac heavy neutrino of low-scale seesaw models.

3.6.1 Observable events at an LHC experiment

We present a scan over the parameter space resulting in the decay width and the number of expected events for a given experimental setup and luminosity. For each parameter point, the decay width Γ and the cross section σ are computed, and the event obtained from MadGraph is used for a toy analysis. We present the decay width as a function of the heavy neutrino mass m and the active-sterile mixing parameter $|\boldsymbol{\theta}|^2$ in figure 3.10a. In order to derive the expected

---

[5] If one wants to patch MadGraph globally, instead of just patching the individual process, one can apply the patch to the file located in [MadGraph]/madgraph/interface/madevent_interface.py instead.

[6] A possible alternative solution that does not keep the spin correlation but does keep all events could be to change the charge of the second lepton depending on whether the event should be LNC or LNV.

(a) Decay width in eV.

(b) Number of expected events N.
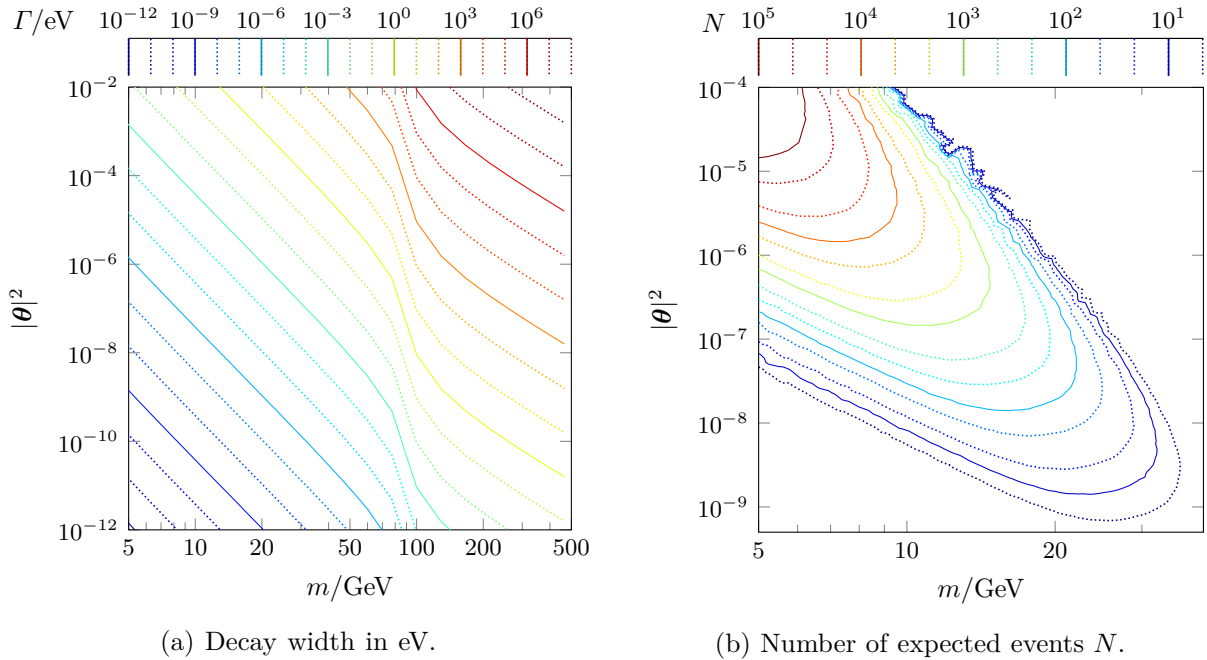
Figure 3.10: Panel (a): Scan over the decay width of the heavy neutrino as a function of its mass and the active-sterile mixing parameter $|\boldsymbol{\theta}|^2$. Panel (b): Scan over the number of expected displaced vertex events in the CMS detector for the HL-LHC with $\mathscr{L} = 3\,\mathrm{ab}^{-1}$ and cuts as defined in section 3.6.1.

number of events, we employ the most important cuts used for displaced vertex analyses at the LHC. For this example, we use cuts inspired by the CMS Phase II detector:

- Minimal transverse momentum $p_T^{\min}(\mu_{\mathrm{prompt}}) = 20\,\mathrm{GeV}$ of the prompt muon

- Minimal transverse momentum $p_T^{\min}(f_{\mathrm{disp}}) = 1\,\mathrm{GeV}$ of the displaced muon and quarks

- Maximal pseudorapidity $\eta^{\max} = 4$ for leptons and quarks

- Minimal impact parameter $d_0^{\min}(\mu_{\mathrm{disp}}) = 2\,\mathrm{mm}$ of the displaced muon

- Maximal distance of half the tracker size for displaced muon and quarks

Where the $p_T^{\min}(\mu_{\mathrm{prompt}})$ cut is used to ensure that the event is triggered, the $p_T^{\min}(f_{\mathrm{disp}})$ and $\eta^{\max}$ cuts ensure that the particles are captured by the detector, and the $d_0^{\min}(\mu_{\mathrm{disp}})$ ensures that the secondary muon is indeed reconstructed as a displaced muon. Finally, the cut on the maximal displaced distance is used to ensure that the tracks of the displaced muons and of the daughters of the quarks can be measured such that the displaced vertex can be reconstructed. With the simulated events and the above-mentioned cuts, an efficiency factor and the number of expected events are computed via

$$N_{\mathrm{exp}} = \sigma \mathscr{L} f_{\mathrm{eff}}\,, \qquad\qquad f_{\mathrm{eff}} = \frac{N_{\mathrm{after\ cuts}}}{N_{\mathrm{all\ events}}}\,, \qquad\qquad (3.6.1)$$

The resulting expected number of events as a function of the heavy neutrino mass and active-sterile mixing parameter are shown in figure 3.10b.

3.6.2 Maximal Lorentz factors

Based on the simulated events, the estimation of the Lorentz factor of the heavy neutrino in equation (3.3.14) can be tested. Since this relies on the probability distributions for the Lorentz
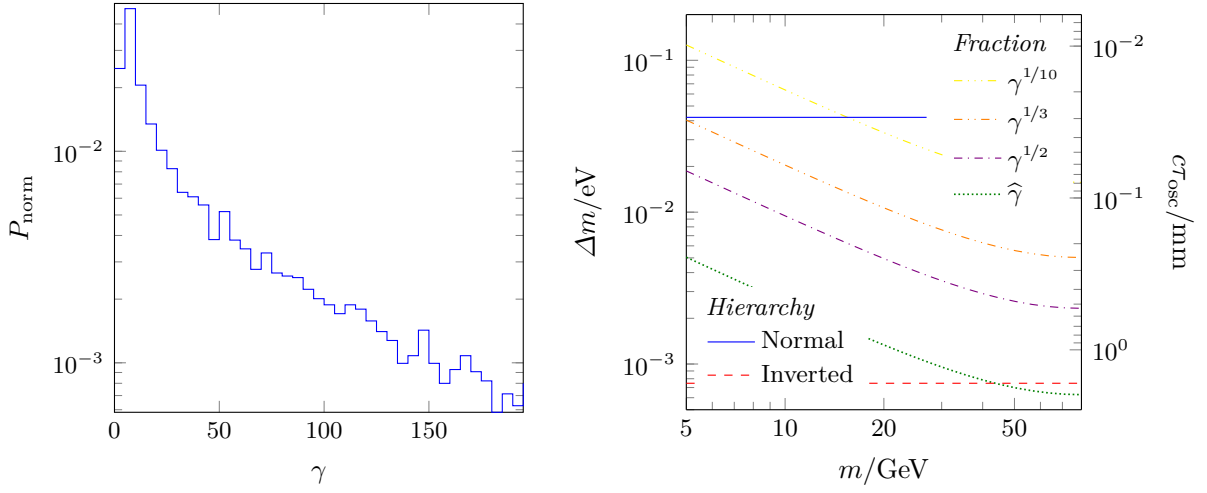
(a) Example distribution of Lorentz factors.

(b) Resolvable mass splittings for $L_{\text{osc}} = 2\,\text{mm}$.

Figure 3.11: Panel (a): Histogram of the simulated Lorentz factor probability density function (PDF) for heavy neutrinos with a mass of $7\,\text{GeV}$. Panel (b): Resolvable mass splittings for a fixed oscillation length of $L_{\text{osc}} = 2\,\text{mm}$ for event samples with different Lorentz factor thresholds γ^f. The horizontal lines correspond to the mass splitting appearing in the two minimal linear seesaw BMs given in table 3.1.

f	γ_W	α
1	1	0
1/2	3.66	3.839×10^{-7}
1/3	7.92	1.545×10^{-5}
1/10	17.36	6.525×10^{-1}
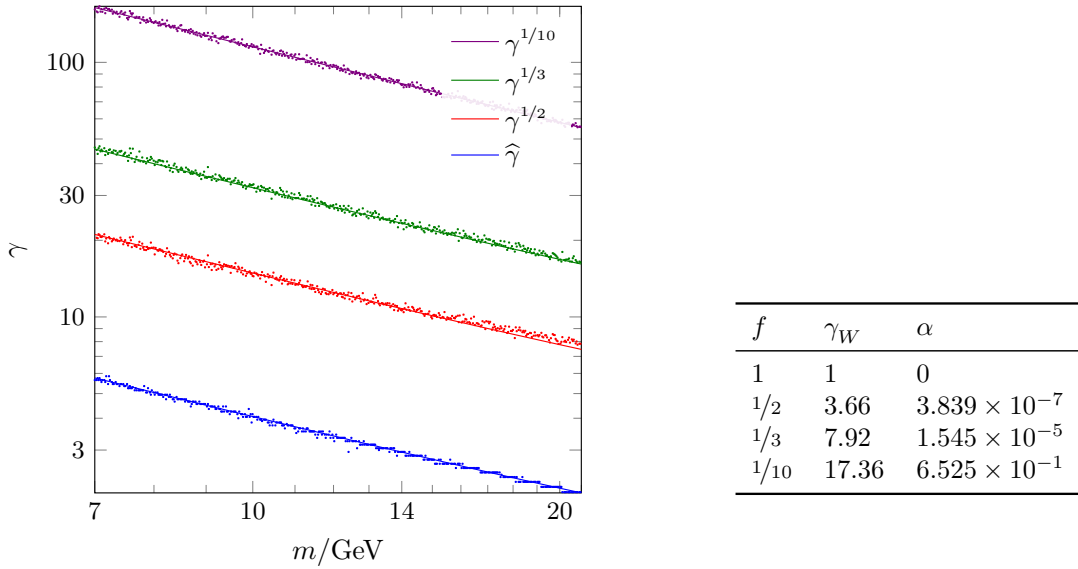
(a) Most likely Lorentz factors as function of m.

(b) Fit values

Figure 3.12: Panel (a): Most likely Lorentz factors $\widehat{\gamma}$ of heavy neutrinos as a function of their masses. The points correspond to MC data and the lines to a fit. Panel (b): fit parameter of the function (3.6.2) for the most likely Lorentz factors $\widehat{\gamma}$ after applying a threshold f.

factor of the heavy neutrinos, one example of such a Lorentz factor distribution is shown in figure 3.11a. In the following, we define the most likely Lorentz factor $\widehat{\gamma}$ as the one where the distribution has its maximum.

It is also possible to consider only a fraction of events with the largest boost in order to probe the smaller mass splittings that become accessible since the most likely Lorentz factor will be increased in such a data sample. We define the Lorentz factor threshold γ^f such that only the fraction f of events with the highest Lorentz factors is kept. The mass splittings, still resolvable for different thresholds and a fixed oscillation length of $L_{\mathrm{osc}} = 2\,\mathrm{mm}$, are depicted in figure 3.11b.

In addition to the information in equation (3.3.14), the boost of the initial W boson can also be taken into account. To that end, the momentum of the heavy neutrino in the rest frame of the W boson is multiplied by a fitting parameter $\alpha \in [0, 1]$ estimating the component parallel to the W boson momentum. Finally, the energy and parallel momentum are boosted with $-\beta_W$ from the W rest frame to the lab frame, yielding

$$\gamma \approx \gamma_W \left(\frac{m_W^2 + m^2}{2m_W m} + \alpha \frac{m_W^2 - m^2}{2m_W m} \sqrt{1 - \frac{1}{\gamma_W^2}} \right). \tag{3.6.2}$$

The parameters α and γ_W are obtained by fitting this equation to simulated data; the results are presented in figure 3.12. Comparing this most likely Lorentz factor to the estimate of the Lorentz factor equation (3.6.2) shows that $\gamma_W \approx 1$ as used in equation (3.3.14) is a good approximation when considering the full event sample as can be seen in figure 3.12a. The values for the constrained event samples have been used in the derivation of figure 3.11b.

3.6.3 Oscillations

The main purpose of this work is to provide the necessary tool to study $N\overline{N}$Os at colliders. We use the FeynRules model file of the pSPSS together with the MadGraph patch presented here to explore if such oscillations are potentially detectable at a CMS-like detector. In figure 3.13 the oscillation pattern as simulated by MadGraph is depicted in the lab frame as well as in the proper time frame. As discussed in section 3.3.4 the oscillation pattern in the lab frame is washed out since heavy neutrinos with different Lorentz factors overlap. However, the oscillations in the proper time frame of the heavy neutrino are not affected by the washout caused by the Lorentz factor, and the oscillation pattern is visible. The detectability of $N\overline{N}$Os at the CMS detector during the HL-LHC is studied in detail in [3].

3.6.4 Integrated effect

In the cases where oscillations cannot be directly resolved, there might still be non-trivial relations between LNC and LNV events. The integrated effect presented in section 3.3.3 depends on the interplay between the decay width and the oscillation period as shown in equation (3.3.10). Counting the number of the opposite- and same-sign events while scanning the parameter space over different values for the Majorana mass m_M and the mass splitting Δm reproduces the analytic dependence of (3.3.10) as shown in figure 3.14 [41, 45, 94].

Furthermore, the MC simulation reproduces the analytic calculation leading to figure 3.5 when taking the finite detector size into account as shown in figure 3.15. The MC simulation agrees with the analytic calculation for $\tau_{\min} \to 0$. However, for $\tau_{\max} \to 0$, the upper left part of the plot is inaccessible since no events are generated for these parameter points. In particular, this effect regularises the divergent parts in the corresponding analytic calculation. Although the cut in τ corresponds to the cleanest theoretical description of R_{ll} with finite detector effects, it

(a) Lab frame.
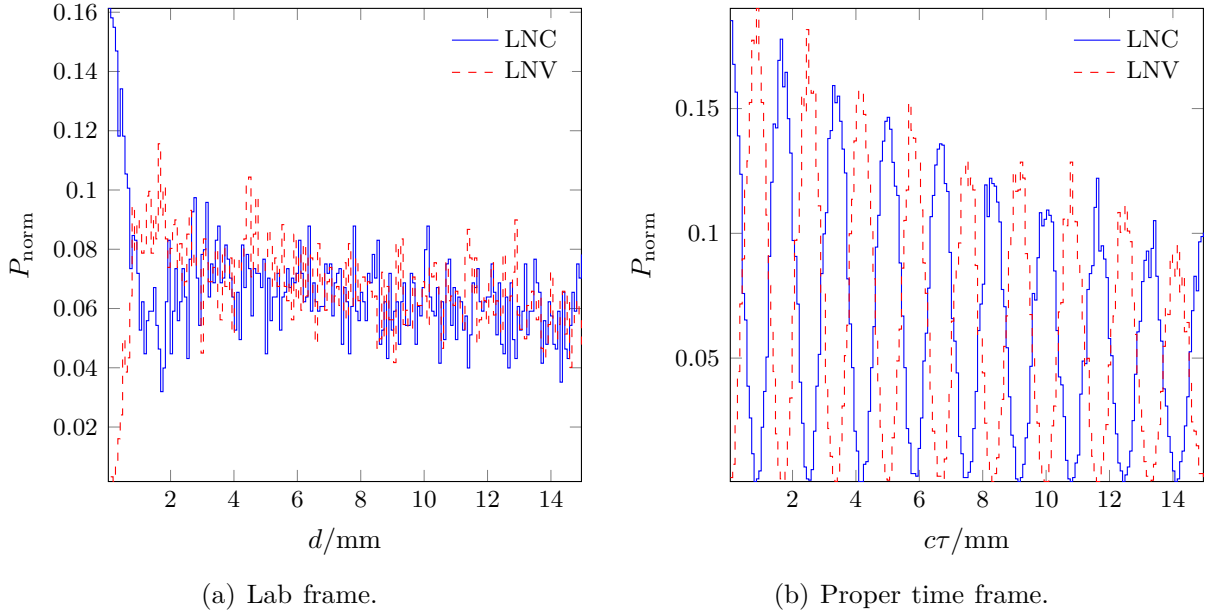
(b) Proper time frame.

Figure 3.13: PDFs of the $N\overline{N}$Os in the lab frame are shown in panel (a), and the ones in the proper time frame are shown in panel (b). The parameter point used for these plots features heavy neutrinos with a Majorana mass of $m_M = 20\,\text{GeV}$, an active-sterile mixing of $|\boldsymbol{\theta}|^2 = 10^{-8}$, and a mass splitting of $\Delta m = 748\,\text{μeV}$. The latter corresponds to the linear seesaw BM point with inverted hierarchy. The oscillations are simulated by MADGRAPH using the model file [91] presented in section 3.5.1 after applying the patch explained in section 3.5.2 and explicitly given in section 3.B. While the oscillations in the lab frame are washed out, they are clearly visible in the proper time frame.
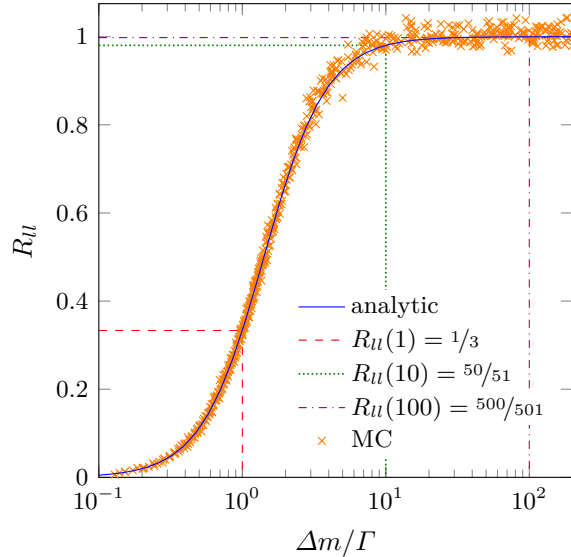
Figure 3.14: Comparison between the analytic calculation (3.3.10) and simulated events for the LNV over LNC ratio R_{ll} as a function of the ratio $\Delta m/\Gamma$. The three indicated special cases for $R_{ll}(\Delta m/\Gamma)$ correspond to the oscillations shown in figure 3.4.

(a) $R_{ll}^{\mathrm{obs}}(R_{ll}, \tau_{\min}/\tau_{\mathrm{osc}})$ while $\tau_{\max} \to \infty$.

(b) $R_{ll}^{\mathrm{obs}}(R_{ll}, \tau_{\max}/\tau_{\mathrm{osc}})$ while $\tau_{\min} \to 0$.
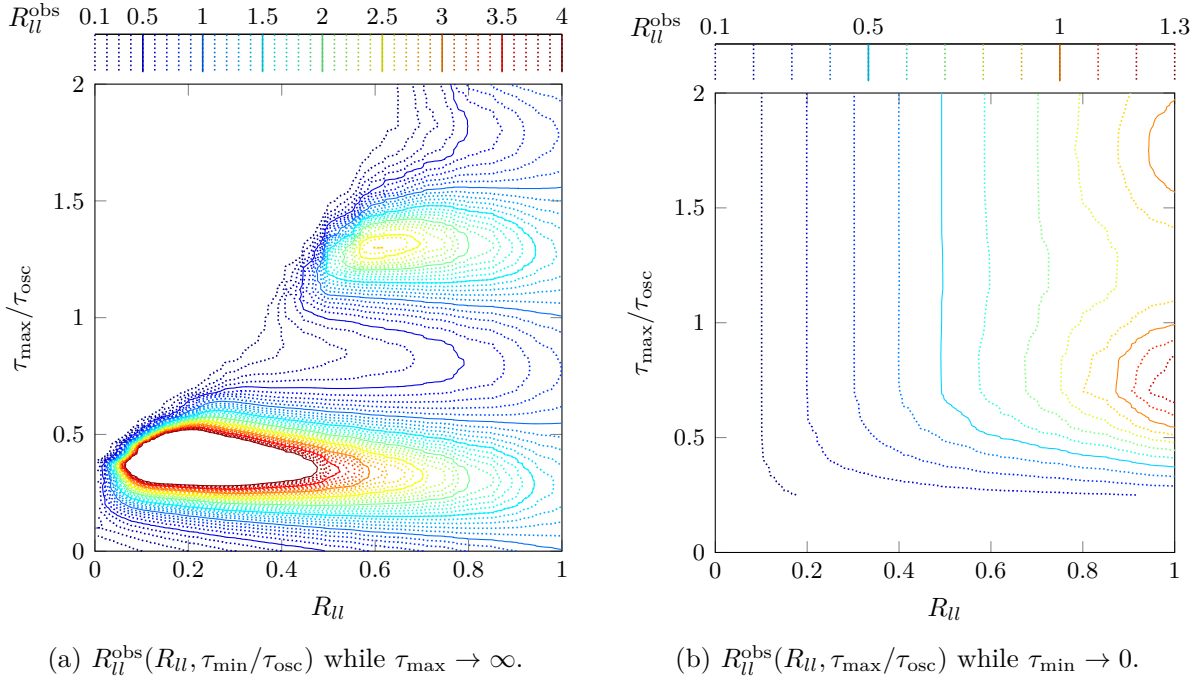
Figure 3.15: MC simulation of the reliability of the observation of R_{ll} when considering finite detectors. The variables are the same as in figure 3.5. The plot in panel (a) agrees only in the lower right half with the theoretical results figure 3.5a, since for large cut values and small R_{ll} no events are generated. The plot in panel (b) reproduces the analytic behaviour from figure 3.5b.

does not correspond to realistic physical cuts. Therefore, we present additional results using a d_0 cut, a minimal distance lab frame cut $d_{\min}$, and a maximal distance lab frame cut $d_{\max}$ in figure 3.16. Since the boost to the lab frame introduces a dependence on the Lorentz factor, we report the results for the three mass points $m = 10, 100, 1000\,\mathrm{GeV}$.

For the masses above the W threshold, the d_0 cut reproduces approximately the first maximum of the analytic calculation. Furthermore, the area in which no events are generated becomes larger, and for smaller masses, the first maximum is pushed to larger values of the oscillation period. When applying a minimal distance cut in the lab frame $d_{\min}$, parts of the behaviour described for a $\tau_{\min}$ and d_0 cut are washed out, and the vertical lines that indicate a trivial relation between R_{ll} and R_{ll}^{obs} are recovered. However, they are shifted and compressed towards lower values of R_{ll}. Nonetheless, the maximum remains, although it is shifted to larger values of the oscillation period. A maximal distance cut in the lab frame $d_{\max}$ does not show the oscillatory pattern and leads only to small distortions for cuts larger than the oscillation period. However, for cuts below one to two oscillation periods, large deviations can be observed.

We conclude that although the Lorentz factor distribution smears the finite detector effect observed in section 3.3.3, it remains important and cannot be neglected, especially when applying a d_0 cut of the order of the oscillation period.

3.6.5 Transverse impact parameter and spin correlation

The transverse impact parameter d_0 of particles emerging in a secondary vertex is defined as

$$d_0 = \frac{\boldsymbol{d}_T' \wedge \boldsymbol{p}_T'}{p_T'} = \frac{\epsilon_{ij} x_i' p_j'}{p_T'} = \frac{x' p_y' - y' p_x'}{p_T'}, \tag{3.6.3}$$

52
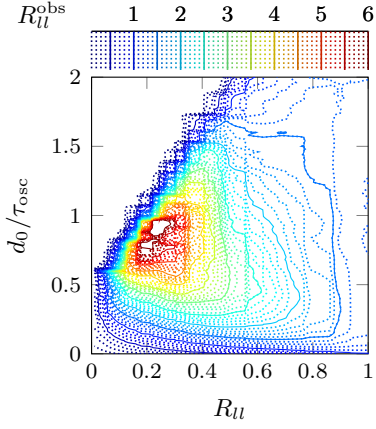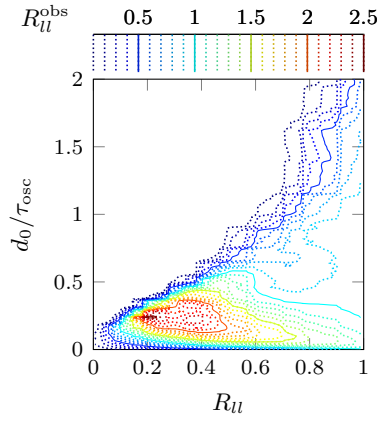
(a) d_0 cut with $m = 10\,\mathrm{GeV}$.　　(b) d_0 cut with $m = 100\,\mathrm{GeV}$.　　(c) d_0 cut with $m = 1\,\mathrm{TeV}$.
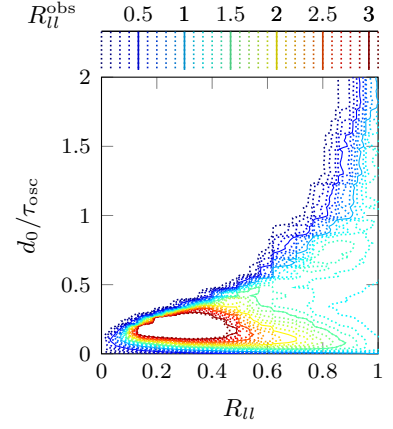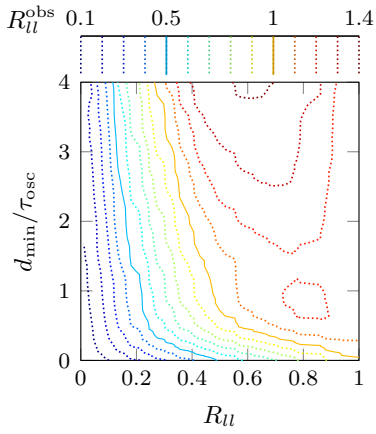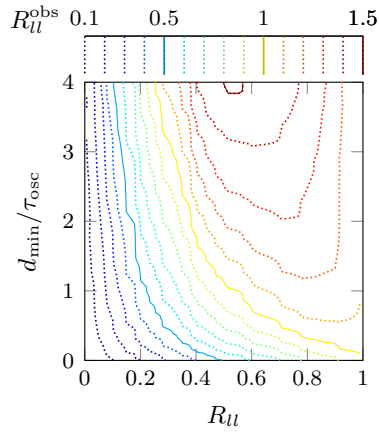
(d) d_{min} cut with $m = 10\,\mathrm{GeV}$.　　(e) d_{min} cut with $m = 100\,\mathrm{GeV}$.　　(f) d_{min} cut with $m = 1\,\mathrm{TeV}$.
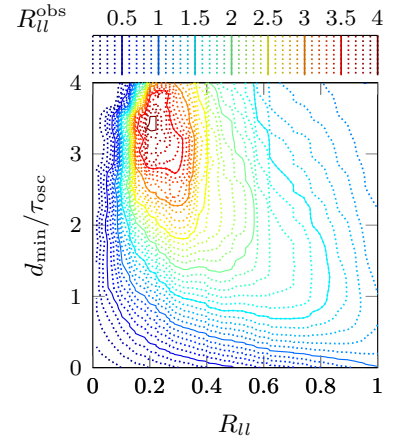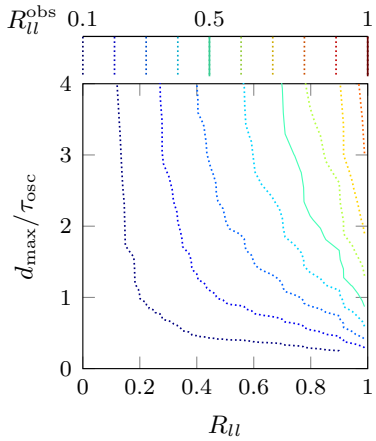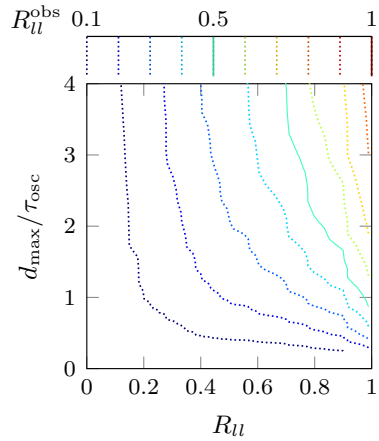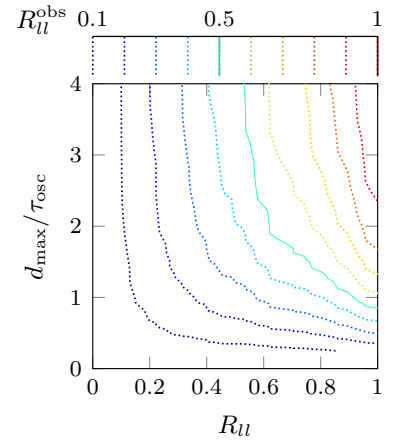
(g) d_{max} cut with $m = 10\,\mathrm{GeV}$.　　(h) d_{max} cut with $m = 100\,\mathrm{GeV}$.　　(i) d_{max} cut with $m = 1\,\mathrm{TeV}$.

Figure 3.16: Simulation of R_{ll} under consideration of a finite d_0 in (a), (b), and (c), of a finite d_{min} in (d), (e), and (f) as well as of a finite d^{min} in (g), (h), and (i). Each cut is shown for three different masses $m = 10, 100, 1000\,\mathrm{GeV}$.
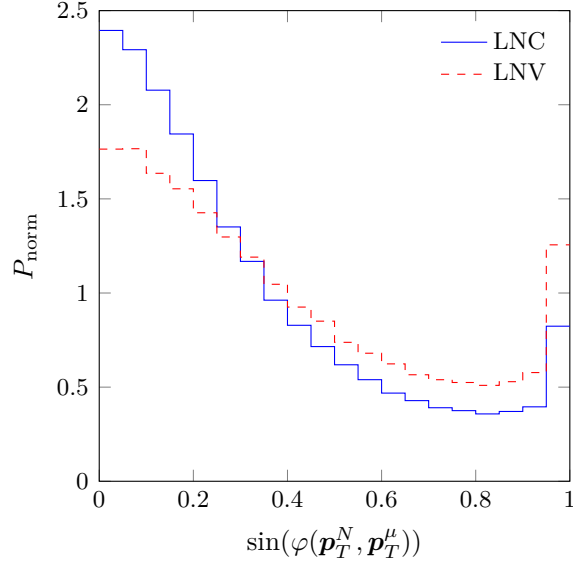
Figure 3.17: Comparison between the angular dependence of the LNC process compared to the LNV process in the observable (3.6.5) using a MC simulation.

where $\boldsymbol{d}'_T = (x', y')$ is the position of the point with the smallest distance to the z-axis and $\boldsymbol{p}'_T = (p'_x, p'_y)$ is the transverse momentum at this point.[7] In cases where the transverse momentum of the particle is large or the magnetic field is small, such that the radius of the trajectory of the particle is much larger than the relevant length scales of the detector, the trajectory is well approximated by a straight line. In this case, the value of d_0 is constant for every point on the trajectory. Therefore, it is possible to replace $\boldsymbol{d}'_T$ with the coordinates of the production vertex $\boldsymbol{d}_T = (x, y)$, which coincides with the transverse distance of the production vertex. In the case of the displaced muon, whose production vertex is the decay vertex of the heavy neutrino, one can furthermore use the relation

$$\boldsymbol{d}'_T \rightarrow \boldsymbol{d}_T = d_T \frac{\boldsymbol{p}^N_T}{p^N_T} \, , \tag{3.6.4}$$

where $\boldsymbol{p}^N_T$ is the transverse momentum of the heavy neutrino. This yields a simplified definition of the impact parameter for displaced muons, under the assumption that their trajectories can be approximated as straight lines

$$d_0 \simeq d_T \frac{\boldsymbol{p}^N_T \wedge \boldsymbol{p}^\mu_T}{p^N_T p^\mu_T} = d_T \sin(\varphi(\boldsymbol{p}^N_T, \boldsymbol{p}^\mu_T)) \, , \qquad \sin(\varphi(\boldsymbol{p}^N_T, \boldsymbol{p}^\mu_T)) = \frac{\boldsymbol{p}^N_T \wedge \boldsymbol{p}^\mu_T}{p^N_T p^\mu_T} \, . \tag{3.6.5}$$

Therefore, the impact parameter consists, besides the transverse decay length of the invisible particle, of an angular-dependent part. The angular-dependent part encodes a spin dependence which can be exploited to distinguish the LNC and LNV processes as shown in figure 3.17. One can see that just by measuring this or a related quantity such as the angle between the two charged leptons in figure 3.3, it is possible to compute probabilities for the event being LNC or LNV [55]. On the other hand, imposing a minimal d_0 cut is the standard strategy to reduce the background of displaced HNL searches as seen in section 3.6.1. The angular dependence of d_0 leads after cuts to a residual oscillation in the observable $N_{\text{LNC}} + N_{\text{LNV}}$ that naively would be expected to be free of oscillations.

---

[7] The two-dimensional wedge product results in a scalar quantity.

54
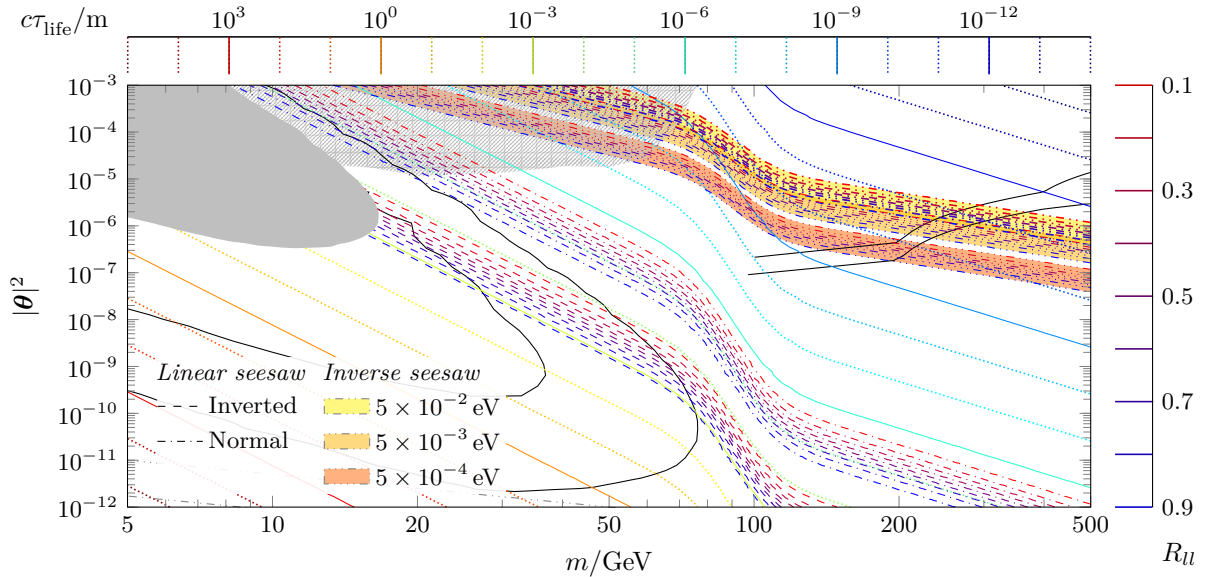
Figure 3.18: Contour lines for the heavy neutrino mean lifetime $c\tau_{\text{life}}$ in m overlayed by contour bands of $R_{ll} \in [0.1, 0.9]$ for the BMs summarised in table 3.1. While the two bands generated by the linear seesaw are well separated and reach far below the W mass threshold, the bands generated by the inverse seesaw are very close to each other and only reach below the W threshold for comparably small values of the active-sterile mixing parameter. For comparison, the regions excluded by the ATLAS and CMS experiments via displaced searches are shown as grey areas [28, 29]. The areas shaded in grey at the centre top are excluded by prompt searches [26, 27], as long as the prompt same-sign dilepton signature is valid. This is the case only for seesaw models in which R_{ll} is close to one in this region, hence to the bottom left of the R_{ll} bands of the BM under consideration. The reach of the HL-LHC [95], FCC-ee [96, 97], large hadron electron collider (LHeC) and FCC-eh [98] are shown as black lines. When producing the figure, we have neglected potential effects from a nonzero damping factor λ as well as from times shorter than the Jacob-Sachs threshold; for details, see sections 3.3.1 and 3.5.2.

3.6.6 Experimental bounds on low-scale seesaw models

Although neither pure Dirac nor single Majorana particles are sufficient to describe the phenomenology of low-scale seesaw heavy neutrinos, almost all prior searches are performed using these two models. Therefore it is necessary to correctly interpret these searches in order to extract the proper bounds on the pseudo-Dirac heavy neutrinos of low-scale seesaw models. Customarily, the searches relying on displaced vertex signatures are reported for both pure Dirac and single Majorana HNLs. Since these searches usually do not rely on LNV, the major difference affecting these searches is the factor of two that appears in the decay width and is described in detail in section 3.A. Since the Dirac particle has the same decay width as the pseudo-Dirac particle, it is prudent to interpret the exclusion extracted for displaced Dirac HNLs as the correct exclusions for displaced pseudo-Dirac heavy neutrinos. The situation is more complicated in the case of prompt searches. The majority of prompt searches rely on the very clean same-sign dilepton signature of LNV decays. Since these are not generated for Dirac particles, the searches are only reported for single Majorana particles. Therefore, these searches assume an R_{ll} of one, which depending on the mass splitting, might not be a good approximation of reality. Hence the exclusion bound depends on the details of the model under consideration. In practice, one has to check the intersection between the R_{ll} band of one specific model and the reported exclusion bounds for the same-sign dilepton search in a representation such as the one presented in figure 3.18. For R_{ll} close to one (to the bottom left of the bands) the reported

exclusion bounds are valid up to the factor of two between the simulated single Majorana particle and the realistic pseudo-Dirac particle discussed in section 3.A. For R_{ll} close to zero (to the top right of the bands) there will be no LNV, rendering the searches inconsequential. Therefore, prompt searches can only be interpreted model-dependently, e.g. as a function of Δm. The model file presented in section 3.5.1 together with the example implementation of $N\overline{N}$Os in section 3.5.2 provides a unified framework for the correct simulation of prompt and displaced processes of pseudo-Dirac heavy neutrinos in low-scale seesaw models.

3.7   Conclusion

In this paper, we have reviewed the arguments that collider testable seesaw models that do not rely on tuning must be protected by an approximate LNLS. The breaking of the symmetry by small parameters simultaneously ensures small LNV, tiny SM neutrino masses, and generically generates a small mass splitting between the heavy neutrinos. The latter leads to $N\overline{N}$Os that can have macroscopic oscillation lengths such that they are potentially resolvable at high-energy colliders.

In order to simulate the effects of these oscillations, we have reviewed the SPSS that builds on a systematic expansion in the small parameter governing the breaking of the LNLS. We have then reduced it to the pSPSS that relies on the minimal number of parameters necessary to describe pseudo-Dirac heavy neutrinos and $N\overline{N}$Os in phenomenological studies. In addition to the SM parameters, the pSPSS introduces only the Majorana mass parameter m_M, the active-sterile mixing parameters $\boldsymbol{\theta} = (\theta_e,\, \theta_\mu,\, \theta_\tau)^\mathsf{T}$, the mass splitting Δm governing the oscillation period, and a damping parameter λ that captures possible decoherence effects. The last of these can be neglected in the parts of the parameter space where prospects are good to resolve the oscillations, as discussed in [1] and further elaborated in [4].

In order to facilitate MC studies using this model, we have published a FeynRules implementation of the pSPSS together with a patch extending MadGraph in such a way that it is capable of simulating $N\overline{N}$Os. Using these tools, we have calculated some example results: We have demonstrated that our implementation recovers typical prior results, such as the heavy neutrino decay width. Additionally, we have provided the maximal mass splitting Δm for which it may be feasible to resolve the oscillation pattern when only a fraction of events containing the largest Lorentz factors is considered. Furthermore, we have shown that the integrated effect of the oscillations is reproduced by our model file. We have emphasized in this context that care has to be taken when measuring R_{ll}, as the finite detector geometry can have a major impact on the derived values. Finally, we have demonstrated the dependence of the impact parameter on the angular-dependent spin correlation and have shown that this observable can be used, in principle, to distinguish between LNC and LNV decays.

Appendix 3.A   Decay widths of Majorana, Dirac, and pseudo-Dirac particles

In the main part of this article, we have discussed that in order to explain light neutrino masses, the corresponding heavy neutrino cannot be a Dirac particle. Additionally, in order to generate the observed light neutrino oscillation pattern, at least two neutrinos have to be added to the SM. Nevertheless, it is standard practice to study the phenomenology of a single heavy neutrino that is either of Majorana or Dirac type. In the following, we compare their phenomenology with the one of pseudo-Dirac heavy neutrinos with different mass splittings and comment on the

decay widths of each of these particles.

Single Majorana The relevant part of the Lagrangian describing a single Majorana particle N_1 reads

$$\mathcal{L}_{\text{Majorana}} = -y_\alpha \overline{N_1^c} \widetilde{H}^\dagger L_\alpha - \frac{1}{2} m_M \overline{N_1^c} N_1 + \text{H.c.} \ . \tag{3.A.1}$$

After EWSB, the coupling to the W bosons is obtained from the kinetic terms of the active neutrinos via the mixing of light ν_α and heavy n_4 neutrino mass eigenstates and reads

$$\mathcal{L}_{\text{Majorana}}^W = \theta_\alpha'^* \bar{l}_\alpha n_4 W + \text{H.c.}\,, \tag{3.A.2}$$

where the mixing parameter is given by $\boldsymbol{\theta}' = \boldsymbol{y} v m_M^{-1}$. The expected number of LNC and LNV events at a collider experiment can then be schematically computed using

$$|\mathcal{A}|^2 = \left| \theta_\alpha' \frac{\text{LNC}}{m} \theta_\alpha'^* \right|^2 + \left| \theta_\alpha' \frac{\text{LNV}}{m} \theta_\alpha' \right|^2 \propto 2|\theta_\alpha'|^2\,, \tag{3.A.3}$$

where the diagram encodes the production and decay of a heavy neutrino from and to charged leptons and W bosons. In this case, one expects an equal number of LNC and LNV events and therefore $R_{ll} = 1$. As long as $\Gamma \ll m$, the magnitude of the (greyed out) coupling in the decay vertex is not relevant since it is cancelled by the decay width dependence of the propagator of the heavy neutrino, which can be verified using the narrow width approximation.

In general, the value of the active-sterile mixing parameter can be obtained by measuring the production cross section and the decay width of the heavy neutrino. In the case of a single Majorana particle, the production cross section is proportional to $|\boldsymbol{\theta}'|^2$. Generically, the decay width can be obtained by scanning the p^2 distribution of any process with the heavy neutrino mass eigenstate on the s-channel and comparing it to the Breit-Wigner shape. Furthermore, regarding long-lived particles, it can be extracted from the decay exponential reconstructed by counting the number of displaced vertices per distance interval. In the case of a single Majorana particle, the decay width is proportional to $|\boldsymbol{\theta}'|^2$.

Dirac A heavy Dirac neutrino can be described as two mass-degenerate Majorana neutrinos $N_{1/2}$ with an exact phase difference of $-i$ in their couplings. The relevant part of the Lagrangian is given by

$$\mathcal{L}_{\text{Dirac}} = -y_\alpha \overline{N_1^c} L_\alpha \widetilde{H}^\dagger - m_M \overline{N_1^c} N_2 + \text{H.c.} \ . \tag{3.A.4}$$

After EWSB, the mass matrix of the neutrinos can be diagonalised, and the active SM neutrino interaction eigenstates can be expressed as a linear combination of the heavy neutrino mass eigenstates. These linear combinations are the heavy neutrino N and heavy antineutrino $\overline{N}$ introduced in section 3.4.1

$$N = \frac{\theta^*}{\sqrt{2}}(-in_4 + n_5)\,, \qquad\qquad \overline{N} = \frac{\theta^*}{\sqrt{2}}(in_4 + n_5)\,, \tag{3.A.5}$$

which leads to the coupling to the gauge bosons via

$$\mathcal{L}_{\text{Dirac}}^W = \theta_\alpha^* \bar{l}_\alpha \frac{1}{\sqrt{2}}(-in_4 + n_5)W + \text{H.c.}\,, \tag{3.A.6}$$

where $\boldsymbol{\theta} = \boldsymbol{y} v m_M^{-1}$. Compared to the case of a single Majorana particle, the coupling of the gauge bosons to each heavy neutrino mass eigenstate obtains an additional factor of $1/\sqrt{2}$, which originates from the diagonalisation of the heavy neutrino 2×2 block in the mass matrix. The number of LNC and LNV events can be derived using the Feynman diagrams

$$
|\mathcal{A}|^2 = \left| \frac{\pm i\theta_\alpha}{\sqrt{2}} \underset{m_4}{\text{LNC}} \frac{(\pm i\theta_\alpha)^*}{\sqrt{2}} + \frac{\theta_\alpha}{\sqrt{2}} \underset{m_5}{\text{LNC}} \frac{\theta_\alpha^*}{\sqrt{2}} + \frac{\pm i\theta_\alpha}{\sqrt{2}} \underset{m_4}{\text{LNV}} \frac{\pm i\theta_\alpha}{\sqrt{2}} + \frac{\theta_\alpha}{\sqrt{2}} \underset{m_5}{\text{LNV}} \frac{\theta_\alpha}{\sqrt{2}} \right|^2
$$

$$
= \left| \pm i \frac{\theta_\alpha}{\sqrt{2}} \underset{m_4}{\text{LNC}} \frac{(\pm i\theta_\alpha)^*}{\sqrt{2}} + \frac{\theta_\alpha}{\sqrt{2}} \underset{m_5}{\text{LNC}} \frac{\theta_\alpha^*}{\sqrt{2}} \right|^2 = 4 \left| \frac{\theta_\alpha}{\sqrt{2}} \underset{m_{4/5}}{\text{LNC}} \frac{\theta_\alpha^*}{\sqrt{2}} \right|^2 \propto 4 \left| \frac{\theta_\alpha}{\sqrt{2}} \right|^2 = 2|\theta_\alpha|^2 .
$$

$$(3.\text{A}.7)$$

where the Dirac condition ensures mass degeneracy $m_4 = m_5$. In contrast to the Majorana heavy neutrino, the Dirac heavy neutrino generates only LNC decays and, therefore, $R_{ll} = 0$. In the picture where the heavy Dirac neutrino is represented by two Majorana DOFs, this is due to the phase difference of $-i$ between the couplings of the mass eigenstates, ensuring that the LNV diagrams cancel exactly. Both the Dirac and the Majorana heavy neutrino yield the same total number of events, such that it is not possible to distinguish them just by the observation of the overall number of events.

The production cross section of a single mass eigenstate $n_{4/5}$ in (3.A.6) is proportional to $|\boldsymbol{\theta}|^2/2$. However, since it is intrinsically impossible to distinguish the two identical mass eigenstates in a single Dirac particle, the measured production cross section is proportional to $|\boldsymbol{\theta}|^2$. Nonetheless, the decay width is only proportional to $|\boldsymbol{\theta}|^2/2$ as one does not sum over the two DOFs in order to calculate the total decay width. Therefore, in comparison to the single Majorana heavy neutrino, the decay width is reduced by a factor of two.

Naively one might expect to distinguish Dirac from Majorana heavy neutrinos in this way. However, this is impossible as we will demonstrate using different limits of a model consisting of a pair of two heavy Majorana neutrinos with finite mass splitting.

Majorana pair   The Majorana and Dirac heavy neutrinos can both be described as limiting cases of a model with two Majorana particles also encompassing the pseudo-Dirac heavy neutrino. Starting from the Dirac heavy neutrino, a small perturbation of the LNLS, such that the two masses of the Majorana DOFs, as well as the modulus of their couplings, are no longer exactly degenerate, generates a pseudo-Dirac heavy neutrino, as explicitly shown in section 3.4.2. Conversely, the Dirac heavy neutrino can be seen as the limit of the pseudo-Dirac heavy neutrino in which the perturbation of the LNLS goes to zero, such that the symmetry is restored. In the limit of large mass splitting, the phenomenology of two well-separated Majorana heavy neutrinos is recovered. In the following, when we refer to the size of the mass splitting, we imply that the Yukawa couplings are also perturbed compared to the degeneracy given in the Dirac case.

Pseudo-Dirac   For small mass splittings as described in section 3.4.2, the mass eigenstates $n_{4/5}$ in (3.A.7) are still produced coherently describing the phenomenology of a pseudo-Dirac pair. However, the LNV diagrams do not cancel exactly anymore, leading to LNV processes. While the total number of produced events stays the same, $N\overline{N}$Os are possible such that a part of generated events are now LNV leading to $0 < R_{ll} < 1$. However, the arguments for the production and decay of a pure Dirac particle apply also to this case.

Intermediate mass splitting   While intermediate mass splitting can still be too small to experimentally distinguish different mass eigenstates, it is still possible that decoherence already

| | Pure Dirac | Majorana Pair | | | Single Majorana |
| | | Pseudo-Dirac | | | |
Mass splitting		Small	Intermediate	Large	
Production	$|\boldsymbol{\theta}|^2$	$|\boldsymbol{\theta}|^2$	$|\boldsymbol{\theta}|^2$	$|\boldsymbol{\theta}'|^2$	$|\boldsymbol{\theta}'|^2$
Decay	$|\boldsymbol{\theta}|^2/2$	$|\boldsymbol{\theta}|^2/2$	$|\boldsymbol{\theta}|^2/2$	$|\boldsymbol{\theta}'|^2$	$|\boldsymbol{\theta}'|^2$
R_{ll}	0	$0 < R_{ll} < 1$	1	1	1

Table 3.3: Production ratios and decay widths for different types of heavy neutrinos. The primed mixing parameters occur in models without mass mixing between two heavy states, while the unprimed mixing parameters occur in models with mass mixing between the two heavy neutrinos.

sets in. This effect is governed by the observability conditions [1, 4] and by the damping factor included in the patch. In this case, the interference between diagrams with different mass eigenstates in (3.A.6) is destroyed. Therefore the LNC and LNV processes become both equally likely while the total number of events is proportional to

$$
|\mathcal{A}|^2 = \left| \begin{array}{c} \pm i\theta_\alpha \\ \sqrt{2} \end{array} \text{LNC} \begin{array}{c} (\pm i\theta_\alpha)^* \\ \sqrt{2} \end{array} \right|^2 + \left| \begin{array}{c} \theta_\alpha \\ \sqrt{2} \end{array} \text{LNC} \begin{array}{c} \theta_\alpha \\ \sqrt{2} \end{array} \right|^2 + \left| \begin{array}{c} \pm i\theta_\alpha \\ \sqrt{2} \end{array} \text{LNV} \begin{array}{c} \pm i\theta_\alpha \\ \sqrt{2} \end{array} \right|^2 + \left| \begin{array}{c} \theta_\alpha \\ \sqrt{2} \end{array} \text{LNV} \begin{array}{c} \theta_\alpha \\ \sqrt{2} \end{array} \right|^2
$$

$$
\propto 4 \left| \frac{\theta_\alpha}{\sqrt{2}} \right|^2 = 2|\theta_\alpha|^2 \quad \text{(3.A.8)}
$$

and thus remains the same. The production cross section corresponds to the sum of the production cross sections of both mass eigenstates, i.e. it is proportional to $|\boldsymbol{\theta}|^2$, while the decay width is the one of each individual mass eigenstate and therefore proportional to $|\boldsymbol{\theta}|^2/2$. Although the ratio between LNC and LNV processes is identical to the case of a single heavy Majorana neutrino, one still obtains a decay width that is a factor of two smaller compared to the case of a single Majorana particle. Therefore, from the comparison of the decay width and the production cross section of a newly discovered heavy neutrino, one can gain information about the number of Majorana DOFs taking part in the production cross section. However, it is not possible to distinguish a Dirac particle from two Majorana particles with a small or intermediate mass splitting just by the comparison of the production cross sections, decay widths or total event numbers.

Large mass splitting For large mass splitting, the individual mass eigenstates can be experimentally distinguished. As before, one finds for each mass eigenstate the production cross section as well as the decay width to be approximately proportional to $|\boldsymbol{\theta}|^2/2$. Considering that it is likely that the lighter of the two mass eigenstates is discovered first, it is insightful to express the coupling in the language of a single Majorana, which would lead to $|\boldsymbol{\theta}'|^2 =: |\boldsymbol{\theta}|^2/2$. Therefore, one obtains exactly the same phenomenology as if the two mass eigenstates are two distinct Majorana particles, avoiding the unnecessary interpretation as a quasi pseudo-Dirac particle with large mass splitting.

Summary We summarise the discussion above in table 3.3 and conclude by noting that the comparison of the decay widths yields insight into whether there are two Majorana DOFs, as in the case of Dirac particles, or only one, as in the case of a single Majorana particle, but it cannot prove the Dirac property of the heavy neutrino. This is already clear from the fact that the factor of two in the decay widths approximately remains when a small LNV term is added, which turns the pure Dirac heavy neutrino into a pseudo-Dirac heavy neutrino. In order to test the Dirac

```
1  for event in lhe:
2      for particle in event:
3          id = particle.pid
4          width = param_card['decay'].get((abs(id),)).value
5          if width:
6              vtim = c * random.expovariate(width/cst)
7              if vtim > threshold:
8                  particle.vtim = vtim
9      #write this modify event
10     output.write(str(event))
11 output.write('</LesHouchesEvents>\n')
12 output.close()
```

Listing 3.1: Original MADGRAPH code calculating particle TOF.

property of the heavy neutrino, it is unavoidable to test for LNV. From a measurement of the mass(es) and lifetime(s), one can, at best, conclude that there are two Majorana particles with almost identical properties. But whether these two DOFs can be combined to form a LNC Dirac heavy neutrino depends on the phase between the Yukawa couplings of the two mass-degenerate Majorana particles. Only when the phase is $-i$, then, on the one hand, LNV cancels out and on the other hand, the two Majorana particle DOFs can be combined into a Dirac heavy neutrino. As long as this phase (related to LNV) is not tested, one can only speak of two Majorana DOFs.

Appendix 3.B   MADGRAPH Patch

The patch presented here is used to include $N\overline{N}$Os in MADGRAPH. It is applied to the [pSPSS] /bin/internal/madevent_interface.py[8] generated by MADGRAPH5_AMC@NLO 2.9.10 (LTS). To apply the patch, the main event loop, responsible for adding TOF information to the .lhe file given in listing 3.1, has to be replaced by the code presented in listing 3.2.[9] The loop over the particles in the event, starting in line 6, is used to determine the leptonnumber of the event. Electrons, muons and τ-leptons are counted as leptons, whereas their antiparticles are counted as antileptons. The masssplitting is extracted from the PSPSS block in the param.card in line 1 and the damping factor damping similar in line 1. In line 16 the program executes the new code of the patch if the particle is a heavy neutrino with particle ID 8000011 or 8000012 as defined in the model file presented in section 3.5.1. First, the proper time at which the heavy neutrino decays is obtained in line 17. Next, the formula for the oscillation probability in the proper time frame is used together with a random number to decide if the event should be LNC or LNV. Subsequently, if the leptonnumber agrees with the result from line 18, the switch write_event is set to True. Otherwise, it is set to False. In line 22, the proper time is converted to mm as in the unpatched code from MADGRAPH. Finally, using the write_event switch from above, it is decided if the event should be kept or discarded in line 28.

Note that when using the automated width computation of MADGRAPH, for some parameter points, there are issues with the computation of the phase space volume in the decay $n_5 \to n_4\nu\nu$, where n_5 is the heaviest neutrino, and the ν are massless neutrinos, due to the unusually small mass splitting. Since we found this decay channel to be negligible, we fixed the issue by replacing the argument of the square root of the return value of the function calculate_apx_psarea in

---

[8] In other versions, the relevant section might be found in the [pSPSS]/bin/internal/common_run_ interface.py file.

[9] The relevant lines can be found by searching for the keyword vtim.

```
1  mass_splitting = param_card.get_value('PSPSS', 2)
2  damping = param_card.get_value('PSPSS', 6)
3  for event in lhe:
4      leptonnumber = 0
5      write_event = True
6      for particle in event:
7          if particle.status == 1:
8              if particle.pid in [11, 13, 15]:
9                  leptonnumber += 1
10             elif particle.pid in [−11, −13, −15]:
11                 leptonnumber −= 1
12     for particle in event:
13         id = particle.pid
14         width = param_card['decay'].get((abs(id),)).value
15         if width:
16             if id in [8000011, 8000012]:
17                 tau0 = random.expovariate(width / cst)
18                 if 0.5 * (1 + math.exp(−damping)*math.cos(mass_splitting * tau0 / cst))
                        >= random.random():
19                     write_event = (leptonnumber == 0)
20                 else:
21                     write_event = (leptonnumber != 0)
22                 vtim = tau0 * c
23             else:
24                 vtim = c * random.expovariate(width / cst)
25             if vtim > threshold:
26                 particle.vtim = vtim
27     # write this modify event
28     if write_event:
29         output.write(str(event))
30 output.write('</LesHouchesEvents>\n')
31 output.close()
```

Listing 3.2: Patched MADGRAPH code calculating particle TOF and $N\overline{N}$Os. Note that the sterile neutrino particle IDs and the position of the **mass splitting** parameter in the **param.card** are model file dependent and might need to be adjusted.

the file [MadGraph]/mg5decay/decay_objects.py by its absolute value. However, this can be a drastic change in the MADGRAPH behaviour. Therefore we have checked that the results are physically meaningful [99]. In our case, that was found to be true since the problematic decay channel is discarded by MADGRAPH at a later step independently of the change, so there is no impact on any physical results. Additionally, we also compared the automated computed width for a parameter point with a small mass splitting of the heavy neutrinos to a parameter point with a large mass splitting, changing the other parameters in such a way that the mass of n_4, as well as its couplings constant, stays constant. The two computations yield the same results, showing that there is no impact from the extremely small mass splitting in the computation performed by MADGRAPH.

Chapter 4

Beyond lepton number violation at the HL-LHC: Resolving heavy neutrino-antineutrino oscillations

Abstract:

Collider testable low-scale seesaw models predict pseudo-Dirac heavy neutrinos, that can produce an oscillating pattern of lepton number conserving and lepton number violation events. We explore if such heavy neutrino-antineutrino oscillations can be resolved at the HL-LHC. To that end, we employ the first ever full Monte Carlo simulation of the oscillations, for several example benchmark points, and show under which conditions the CMS experiment is able to discover them. The workflow builds on a FEYNRULES model file for the *phenomenological symmetry protected seesaw scenario* (pSPSS) and a patched version of MADGRAPH, able to simulate heavy neutrino-antineutrino oscillations. We use the fast detector simulation DELPHES and present a statistical analysis capable of inferring the significance of oscillations in the simulated data. Our results demonstrate that, for heavy neutrino mass splittings smaller than about $100\,\mu\text{eV}$, the discovery prospects for heavy neutrino-antineutrino oscillations at the HL-LHC are promising.

4.1　Introduction

The observed light neutrino flavour oscillations [69] can be explained by introducing at least two mass splittings between the light neutrinos. It follows that at least two of the neutrinos have to be massive. However, the SM of particle physics lacks the corresponding mass terms. Therefore, it needs to be extended with a model able to generate these light neutrino masses, such as the type I seesaw mechanism [18, 19, 21–24]. In order to generate the two light neutrino masses in this model at least two sterile neutrinos have to be added to the particle content of the SM. In general, the type I seesaw mechanism is governed by two sets of parameters, that can be adjusted to obtain light neutrino masses at the right order of magnitude. Besides their Yukawa couplings, the second set is given by their Majorana masses m_M, which are only possible since the additional neutrinos are SM singlets. After EWSB the Yukawa couplings result in Dirac mass terms $\boldsymbol{m}_D^{(i)}$ between each of the sterile neutrinos N_i and the active neutrinos ν_α.[1] For the case of two heavy neutrinos, the generated light neutrino mass matrix then follows from the seesaw equation

$$M_\nu = \frac{\boldsymbol{m}_D^{(1)} \otimes \boldsymbol{m}_D^{(1)}}{m_M^{(1)}} + \frac{\boldsymbol{m}_D^{(2)} \otimes \boldsymbol{m}_D^{(2)}}{m_M^{(2)}} \,. \tag{4.1.1}$$

In order to obtain light neutrino masses, one could take the Yukawa couplings to be very small or choose the Majorana masses of the heavy neutrinos to be very large. Those two limits of the seesaw mechanism are referred to as the small coupling and the high scale limit, respectively. In both cases the parameters have to be taken to such extreme values that a direct detection of the sterile neutrinos at current collider experiments is not feasible. A third possibility, which leads to collider testable low-scale seesaw models, consists in heavy neutrino pairs forming a pseudo-Dirac structure. This leads to a cancellation between the two terms in (4.1.1) and can be justified by an approximate symmetry. The symmetry can be realised as an extension of the SM lepton number and we refer to it as a LNLS [2, 31, 32]. It allows for the heavy neutrinos to be light enough, and at the same time have sufficiently large Yukawa couplings, to be directly observable at e.g. the LHC [26–29, 95].

When the LNLS is exact, the light neutrinos are massless and the two heavy neutrinos are precisely mass-degenerate, forming a single Dirac neutrino. However, if the LNLS is broken by small parameters, light neutrino masses are generated and typically a mass splitting between the heavy neutrinos is introduced. The corresponding seesaw scenario is referred to as *SPSS* [2, 31, 32]. The phenomenological effects of the slightly broken LNLS are captured by the pSPSS introduced in [2]. Similar to the case of other neutral particles, this leads to particle-antiparticle oscillations [75–78], which are in this context called $N\overline{N}$Os [44]. The QFT framework of external wave packets, which has been developed in [35–38] and applied to the case of $N\overline{N}$Os in [1], allows to describe this phenomenon including decoherence effects.

Although the small breaking of the LNLS generates LNV processes, one can argue on principle grounds that for prompt heavy neutrino decays it is not possible to observe LNV at the LHC [72]. In contrast, $N\overline{N}$Os generate observable amounts of LNV when the heavy neutrinos are sufficiently long-lived compared to their oscillation period. When the heavy neutrinos have large enough lifetimes, such that their time of decay can be reconstructed, it can be possible to resolve the oscillation pattern of the $N\overline{N}$Os. This allows to deduce the mass splitting of the heavy neutrinos, which might not be possible from measuring the amount of LNC and LNV processes alone. The possibility of resolving the $N\overline{N}$Os at colliders has been estimated to be feasible during the HL-LHC in [44].

---

[1] We indicate quantities with a suppressed vector index by bold font.

The goal of the present paper is to explore under which conditions it is possible to resolve $N\overline{N}$Os at the HL-LHC at the reconstructed level, employing the process shown in figure 4.2. To this end, the FEYNRULES implementation of the pSPSS [91] is used to simulate $N\overline{N}$Os in MADGRAPH. Subsequently, PYTHIA is employed to simulate QCD effects such as hadronisation, and the fast detector simulation DELPHES is used to simulate the CMS phase II detector. A cut based analysis of the generated events is performed using custom C++ code. Finally, the prospects to resolve oscillation patterns for several BM scenarios of long-lived nearly mass degenerate heavy neutrinos at the HL-LHC are derived, using a detailed statistical analysis implemented in MATHEMATICA.

This paper is structured as follows: First, the pSPSS and $N\overline{N}$Os are briefly reviewed in section 4.2. Subsequently, in section 4.3 the simulation of signal events containing these oscillations and relevant background processes are discussed. Afterwards, the statistical analysis is introduced in detail in section 4.4. Finally, the results are presented in section 4.5 and the paper is concluded in section 4.6. In section 4.A we comment on the induction of residual oscillations through cuts on the transverse impact parameter.

4.2 Symmetry protected seesaw scenario

When considering two heavy neutrinos under the assumption of an intact LNLS, the only allowed additions to the SM Lagrangian are

$$\mathcal{L}_{\mathrm{SPSS}}^{L} = \overline{N_i^c}\,i\slashed{\partial}N_i - y_{1\alpha}\overline{N_1^c}\widetilde{H}^\dagger\ell_\alpha - \overline{N_1^c}m_M N_2 + \cdots + \mathrm{H.c.}\,, \tag{4.2.1}$$

where N_1 and N_2 are sterile neutrinos written here as left-chiral four-component spinor fields. The Higgs and lepton doublets of the SM are denoted by H and ℓ, respectively, and $\boldsymbol{y}_1$ is the Yukawa coupling vector with components $y_{1\alpha}$. The ellipses capture further contributions that can be generated by additional sterile neutrinos, but are assumed to be subdominant here. In this case the two terms in the seesaw formula (4.1.1) cancel precisely. In addition, the following symmetry breaking terms can be introduced

$$\mathcal{L}_{\mathrm{SPSS}}^{\slashed{L}} = -y_{2\alpha}\overline{N_2^c}\widetilde{H}^\dagger\ell_\alpha - \mu_M'\overline{N_1^c}N_1 - \mu_M\overline{N_2^c}N_2 + \cdots + \mathrm{H.c.}\,. \tag{4.2.2}$$

When the Yukawa coupling vector $\boldsymbol{y}_2$ times the VEV as well as the Majorana mass parameters μ_M and μ_M' are *small* compared to m_M, the light neutrino masses are guaranteed to be small as well. Due to the approximate LNLS, it is possible for the heavy neutrinos to have a mass well below the W boson mass, while at the same time their coupling can be large enough to obtain a sizable number of events at e.g. the HL-LHC, without violating constraints from light neutrino experiments such as searches for $0\nu\beta\beta$ decay.

4.2.1 Phenomenological symmetry protected seesaw scenario

In the SPSS with exact LNLS (4.2.1), the neutrino mass matrix for the interaction eigenstates $n = (\nu_e,\,\nu_\mu,\,\nu_\tau,\,N_1,\,N_2)^\mathsf{T}$ is given by

$$M_n^L = \begin{pmatrix} 0 & \boldsymbol{m}_D & 0 \\ \boldsymbol{m}_D^\mathsf{T} & 0 & m_M \\ 0 & m_M & 0 \end{pmatrix} \tag{4.2.3}$$

where $\boldsymbol{m}_D = \boldsymbol{y}_1 v$ with the SM Higgs VEV $v \approx 174\,\mathrm{GeV}$. The mass term of the Lagrangian after EWSB is given by

$$\mathcal{L}_{\mathrm{mass}} = -\frac{1}{2}\overline{n^c}M_n n + \mathrm{H.c.}\,. \tag{4.2.4}$$

BM	$\Delta m/\mathrm{\mu eV}$	$c\tau_{\mathrm{osc}}/\mathrm{mm}$	R_{ll}
1	82.7	15	0.9729
2	207	6	0.9956
3	743	1.67	0.9997

Table 4.1: All BM points have a mass of $14\,\mathrm{GeV}$ and an active-sterile mixing parameter satisfying $|\theta_\mu|^2 = 10^{-7}$, which results for all points in a decay width of $\Gamma = 13.8\,\mathrm{\mu eV}$. However, they vary in their mass splitting and consequently have different oscillation periods τ_{osc}, which leads to different LNV to LNC ratios R_{ll}, defined in (4.2.11).

This mass matrix does not generate neutrino masses. Furthermore, the two heavy neutrinos are mass degenerate with a relative phase of $-i$ in their Yukawa couplings and can therefore be described as a single Dirac fermion.

However, in the presence of the small symmetry breaking terms (4.2.2) the complete mass matrix reads

$$M_n^{\not{L}} = \begin{pmatrix} 0 & \boldsymbol{m}_D & \boldsymbol{\mu}_D \\ \boldsymbol{m}_D^\intercal & \mu'_M & m_M \\ \boldsymbol{\mu}_D^\intercal & m_M & \mu_M \end{pmatrix}, \tag{4.2.5}$$

where $\boldsymbol{\mu}_D = \boldsymbol{y}_2 v$. This mass matrix not only generates small masses for the light neutrinos, but additionally introduces a mass splitting between the two heavy neutrinos, that is also suppressed by the same small LNLS breaking parameters. Thus, the pair of two Majorana fermions can no longer be described as a pure Dirac particle, but as a pseudo-Dirac particle.

The symmetry breaking terms can arise from specific low scale seesaw models, such as the linear or the inverse seesaw, which yield only the terms proportional to $\boldsymbol{\mu}_D$ and μ_M, respectively. However, the complete mass matrix (4.2.5) can be generated from more complicated seesaw models. Since the symmetry breaking terms are very small, their phenomenological effects can often be neglected in collider studies with the notable exception of $N\overline{N}$Os, which can be phenomenologically significant as they are an interference effect.

At LO, the $N\overline{N}$Os are fully described by the mass splitting Δm between the heavy neutrinos together with an additional damping parameter λ, capturing the potential decoherence effects discussed in section 4.2.3. Therefore, instead of adding the terms (4.2.2) to the Lagrangian (4.2.1), in the pSPSS, the mass splitting is directly introduced as a model parameter. Consequently, the masses of the heavy neutrinos are given by

$$m_{4/5} = m_M \left(1 + \frac{1}{2}|\boldsymbol{\theta}|^2\right) \mp \frac{1}{2}\Delta m, \tag{4.2.6}$$

where $\boldsymbol{\theta} = \boldsymbol{m}_D/m_M$ is the active-sterile mixing parameter. A detailed description of the pSPSS can be found in [2].

4.2.2 Benchmark models

In order to obtain the significance with which $N\overline{N}$Os could be observed at colliders, three BMs that differ only in their mass splitting are used and given in table 4.1. The Majorana mass parameter and the active-sterile mixing parameters for all BM points are chosen to be $m_M = 14\,\mathrm{GeV}$ and $|\theta_\mu|^2 = 10^{-7}$, leading to a decay width of $\Gamma = 13.8\,\mathrm{\mu eV}$. The active-sterile mixing parameter corresponds to a Yukawa coupling of $y_\mu = 2.55 \times 10^{-5}$, while the Yukawa couplings to the electron and τ-lepton have been set to zero. The number of expected events with
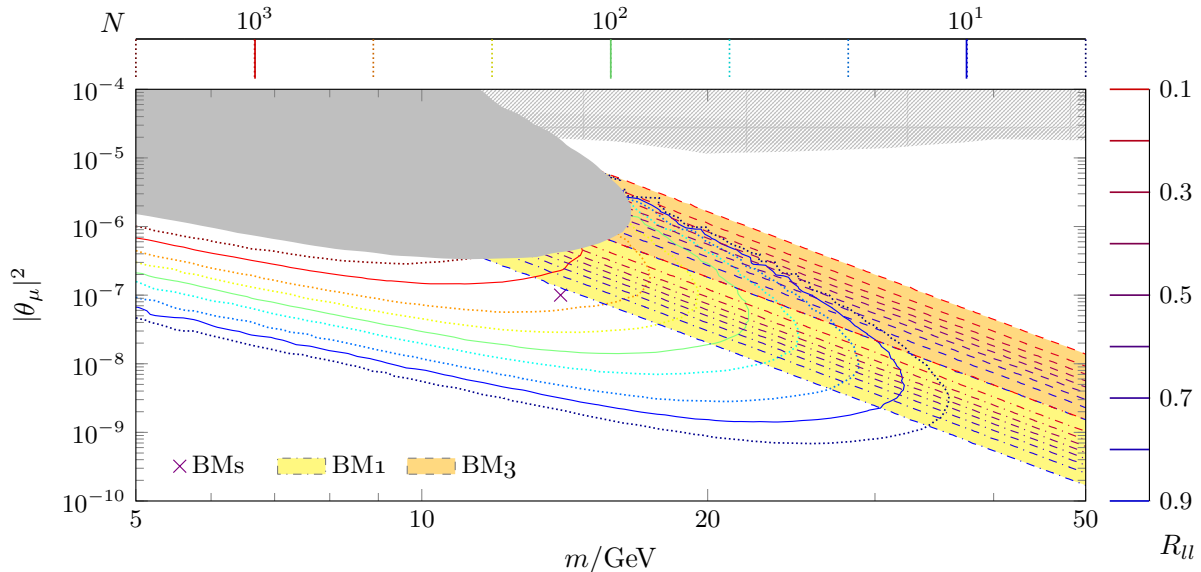
Figure 4.1: Contour lines for the number of expected displaced vertex events N as well as bands for the LNV over LNC event ratio R_{ll}, cf. definition (4.2.11), for the three BMs defined in table 4.1. The contour lines for N apply to the CMS detector at the HL-LHC with $\mathscr{L} = 3\,\text{ab}^{-1}$ and cuts as defined in sections 4.3.1 and 4.3.2. They have a nose-like shape and depend only on the heavy neutrino mass m and the active-sterile mixing parameter θ_μ, with $\theta_e = \theta_\tau = 0$. N is therefore identical for all three BMs, which differ only in their mass splittings Δm. The position of the BMs in the parameter plane is indicated by a purple cross. The different Δm of the BMs result in different R_{ll} bands. The contour lines where $R_{ll} \in [0.1, 0.9]$ are shown in yellow and orange for BM1 and BM3, respectively. The relative position of the cross to the bands shows that the BMs have an R_{ll} close to one. The grey area corresponds to the exclusion bounds from displaced vertex searches [28, 29] and the shaded grey area to the bounds from searches for prompt LNV processes [26, 27]. Since the prompt searches rely on LNV signals, they apply only to models with an R_{ll} close to one.

muons as final state leptons in conjunction with the cuts presented in sections 4.3.1 and 4.3.2, are shown in figure 4.1. It becomes clear that the chosen BMs lie comfortably beyond the current bounds [28, 29].

In the minimal linear seesaw model, only one pseudo-Dirac pair of heavy neutrinos is added to the SM. This results in the lightest neutrino being massless and the mass splitting of the heavy neutrinos Δm being identical to the mass splitting of the light neutrinos, cf. [44]. The mass splitting of BM3 is chosen to represent this possibility, where the light neutrino mass splitting is taken from a recent global fit assuming inverse light neutrino mass hierarchy [89]. However, in top-down realisations of low scale seesaw models, e.g. the low scale linear seesaw models in [63, 64], it is common to have multiple pseudo-Dirac pairs of heavy neutrinos. Since the light neutrino masses get contributions from all these heavy neutrinos, it is possible for the pseudo-Dirac pairs to have smaller mass splittings than in BM3 without the need of cancellations in the mass matrix. For simplicity it might be assumed that the collider phenomenology is dominated by only one of the pseudo-Dirac pairs. We introduce two additional BM points reflecting this possibility.

4.2.3 Oscillations

Oscillations of neutral particles, and thus $N\overline{N}$Os, can be described in the QFT framework of external wave packets. Compared to simple methods relying on plane waves, wave packets

allow for a self-consistent description of oscillations. This is due to the finite uncertainty in energy-momentum and spacetime, that allows to produce a coherent superposition of non-degenerate mass eigenstates, while simultaneously makes it possible to introduce the notion of a travelled time and distance. The QFT framework also allows to calculate the possible suppression of oscillations due to the loss of coherence between the propagating mass eigenstates. For phenomenological studies these effects can be captured by a damping parameter λ, which is thus included in the pSPSS.

At LO, the probability to obtain a LNC or LNV event is given by

$$P_{\text{osc}}^{\text{LNC/LNV}}(\tau) = \frac{1 \pm \cos(\Delta m \tau) \exp(-\lambda)}{2} \, . \tag{4.2.7}$$

Therefore, the oscillation period, defined in the proper time frame, is[2]

$$\tau_{\text{osc}} = \frac{2\pi}{\Delta m} \, . \tag{4.2.8}$$

Since the probability density of the heavy neutrino to decay is

$$P_{\text{decay}}(\tau) = -\frac{\mathrm{d}}{\mathrm{d}\tau} \exp(-\Gamma \tau) = \Gamma \exp(-\Gamma \tau) \, , \tag{4.2.9}$$

the probability for a heavy neutrino to decay between the proper times τ_{min} and τ_{max} and forming an LNC or LNV event is given by

$$P_{ll}^{\text{LNC/LNV}}(\tau_{\text{min}}, \tau_{\text{max}}) = \int_{\tau_{\text{min}}}^{\tau_{\text{max}}} P_{\text{osc}}^{\text{LNC/LNV}}(\tau) P_{\text{decay}}(\tau) \, \mathrm{d}\tau \, . \tag{4.2.10}$$

By integrating the oscillations from the origin to infinity, one derives the total ratio between LNV and LNC events [2, 41, 50]

$$R_{ll} = \frac{P_{ll}^{\text{LNV}}}{P_{ll}^{\text{LNC}}} = \frac{\Delta m^2}{\Delta m^2 + 2\Gamma^2} \, , \tag{4.2.11}$$

that can be directly deduced from cut and count based analyses. The expected number of events in a collider experiment is given by

$$N^{\text{LNC/LNV}} = \mathscr{L}\sigma \, \text{BR} \int D(\vartheta, \gamma) P_{ll}^{\text{LNC/LNV}}(\tau_{\text{min}}(\vartheta, \gamma), \tau_{\text{max}}(\vartheta, \gamma)) \, \mathrm{d}\vartheta \, \mathrm{d}\gamma \, , \tag{4.2.12}$$

where the collider luminosity $\mathscr{L}$, the heavy neutrino production cross section σ, and the branching ratio (BR) are used and $D(\vartheta, \gamma)$ is the probability density of the heavy neutrino to have a Lorentz factor γ and an angle ϑ with respect to the beam axis. The detector geometry is incorporated in the parameters τ_{min} and τ_{max} when boosting to the laboratory frame via $\tau(\vartheta, \gamma) = (\gamma^2 - 1)^{-1/2} L(\vartheta)$. The $N\overline{N}$Os in the pSPSS have been discussed in detail in [2]. We have checked that for the parameter points under consideration decoherence effects can be neglected and we thus take $\lambda = 0$ in the following.

4.3 Simulation

In order to simulate events exhibiting $N\overline{N}$Os, we employ the FEYNRULES [92] implementation of the pSPSS [91]. FEYNRULES is used to generate an UFO output, passed to MAD-GRAPH5_AMC@NLO 2.9.10 (LTS) [93] in order to generate events at parton level. We use the

---

[2] We use *time* for quantities in the proper time frame and *length* for quantities in the lab frame, independent from the units of those quantities.

p μ^+ $\mu^{\pm}$ j

oscillations

W^+ N $\sum n_i$ $\overline{N}/N$ $W^{\mp}$

p
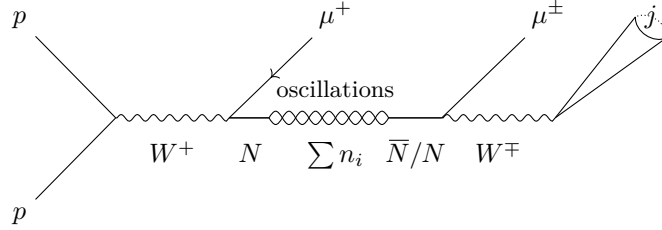
Figure 4.2: Diagram depicting the production, oscillation, and decay of a heavy neutrino. The heavy neutrino interaction eigenstate N is produced in association with a prompt antimuon. Subsequently, the mass eigenstates oscillate such that finally a neutrino or antineutrino interaction eigenstate decays into a displaced muon or antimuon, respectively. We indicate that the process is initiated by proton collisions and that, for our parameter points, the two final quarks, originating from the hadronic W decay, immediately hadronise into a single jet.

patch introduced in [2], that modifies the function calculating the particle's TOF, to implement the oscillations. When evaluating the matrix element, MADGRAPH treats the process as prompt, adding the TOF information afterwards. Therefore, almost no LNV is obtained when interference between diagrams with different mass eigenstates are taken into account. In order to circumvent this, the process is initially specified in such a way as to prevent interference between the heavy neutrino mass eigenstates. This is achieved by writing the heavy neutrinos explicitly as intermediate states. As a consequence the total cross sections for the LNC and LNV process are identical and the amount of generated LNC and LNV events is, except for statistical variations, the same. The correct interference effects, including $N\overline{N}$Os, are then included via the patch described in [2]. The syntax to generate a process, as the one given in figure 4.2, is

```
generate p p > ww, (ww > mu nn, (nn > mu j j))
```

where, in addition to the jet `j` and proton `p` multi particles, containing quarks and gluons, the multi particles

```
define mu = mu+ mu-
define ww = w+ w-
define nn = N4 N5
```

are used. Here, the initial W boson is additionally taken to be on-shell, since we focus on heavy neutrinos with masses far below the W boson mass. An additional hard initial jet is included by using

```
add process p p > ww j, (ww > nn mu, (nn > mu j j))
```

where MLM matching was enabled with the standard parameter choices of MADGRAPH to prevent double counting.

MADGRAPH utilises PYTHIA 8.306 in order to hadronise and shower the parton level events [100]. Finally DELPHES 3.5.0 is used with the standard CMS phase II card `CMS_PhaseII_oPU` to simulate the detector effects [101].

Secondary vertex reconstruction and smearing   Since DELPHES neither simulates displaced tracks properly, nor reconstructs secondary vertices, we implemented a smearing function affecting the displaced vertices, with the idea to capture experimental uncertainties. To our knowledge, no results for the overall precision of the vertex reconstruction have been published by CMS so far. Therefore, we vary it in our simulations between zero and 4 mm, which we assume to be a

conservative parametrisation of our ignorance, relying on private communication with members on the experimental collaborations. We like to emphasise that it would be highly welcome if the experimental collaborations could provide such information and, ideally, if such uncertainties could be implemented in DELPHES directly. In detail, it is assumed that each reconstructed vertex is distributed with a Gaussian, with a standard deviation of n mm, around its actual value. The true value of the displaced vertex is obtained from the displaced muon. The results are presented for different values of n, demonstrating the effects of the uncertainty in the vertex reconstruction.

4.3.1 Signal

In order to observe LNV via $N\overline{N}$Os using the process given by the diagram presented in figure 4.2, the two leptons have to be measured. For the BMs given in table 4.1 and indicated in figure 4.1, the final state quarks are soft and immediately hadronise into a multi pion state, which then forms a single jet that can be captured with a cone radius of $\Delta R = 0.4$. Furthermore, the BM points are chosen such that the heavy neutrinos are long-lived. Hence, the signal contains one prompt muon, one displaced muon, and one displaced jet.

A cut is used, which requires the muon to have an impact parameter of $|d_0| \leq 100\,\mu$m, to ensure **exactly one prompt μ**. Furthermore, this muon is required to have a transverse momentum p_T greater than $20\,$GeV, ensuring that the event can be triggered. Events that do not contain **at least one displaced μ** are excluded by a cut that requires at least one muon with an impact parameter of $|d_0| \geq 2\,$mm. Furthermore, the displaced muon candidate is only valid if it emerges from the same vertex as the displaced jet. A jet is considered displaced if it contains at least two displaced tracks that originate from the same vertex within a radius of $100\,\mu$m. A track is considered displaced if it has an impact parameter of $|d_0| \geq 2\,$mm. Signal events are required to have **exactly one displaced j**.

In addition to those basic cuts that define the signal, we demand **μ isolation** by requiring that the displaced muon and displaced jet have a ΔR larger than 0.4 in order to reject muons radiated from the jet. Furthermore, restricting the reconstructed heavy neutrino mass to the **N mass window** of $\pm 2\,$GeV around its theoretical value results in a cleaner signal. Generally, displaced particles are only considered if their origin falls inside a cylinder with dimensions given by half the tracker size in each direction. For the CMS phase II detector, this means that displaced tracks must have an origin with a transverse distance smaller than $60\,$cm, and a longitudinal distance smaller than $150\,$cm, from the primary vertex. This requirement ensures that the produced particles propagate through a volume of the tracker that should be large enough to facilitate detection. At the moment this is an optimistic assumption about the performance of the displaced track reconstruction in the CMS tracker, however, we think that pushing this capability is a worthwhile goal for the collaboration (see also [95] and references therein). Although the reconstruction of $N\overline{N}$Os discussed here mostly relies on displaced vertices appearing in the inner tracker, it is also possible to reconstruct muon tracks and vertices using the muon chambers [102–104].

4.3.2 Background

The cuts introduced above define the basic search strategy for the signal, which is based on reconstructing a displaced vertex. The main sources of background for such a process are given by heavy flavour SM processes generating long-lived heavy hadrons, interaction of particles with dense detector material, and cosmic ray muons [28, 29].

		Signal	Background Heavy hadrons
Produced events	Physical	2854	8.882×10^7
	Simulated	5×10^4	1.1×10^7
Cuts	Exactly one prompt μ	-23196	-6.50×10^6
	Exactly one displaced j	-21652	-4.48×10^6
	At least one displaced μ	-1396	-17411
	μ isolation	-838	-45
	Vertex direction	0	0
	Prompt e veto	0	0
	W mass window	-111	-3
	N mass window	-1211	0
Remaining events	Simulated	1596	0
	Physical	91	0

Table 4.2: Cut flow for the signal and the heavy hadron background events. The physical events are given at an integrated luminosity of $\mathscr{L} = 3\,\mathrm{ab}^{-1}$ with a signal cross section of $\sigma = 951\,\mathrm{ab}$.

The heavy SM hadrons can travel macroscopic distances before they decay, potentially forming displaced vertices. However, this is only possible if those heavy flavour particles, and consequently their decay products, are highly boosted. Since the selection rules that define the signal already require the displaced muon and the displaced jet to have a $|d_0| > 2\,\mathrm{mm}$, this background is strongly reduced [28, 105]. A **W mass window** cut around the reconstructed W boson mass of $\pm 20\,\mathrm{GeV}$ is employed to reduce the background even further. We simulated this background using the same programs as for the signal events. The MADGRAPH syntax we used is

```
generate p p > mu all bb
```

where the additional multi particle

```
define bb = b b~
```

is defined. An additional hard initial jet was included by using

```
add process p p > mu all bb j
```

where MLM matching was enabled with the standard parameter choices of MADGRAPH. The whole process was simulated using the model `sm-no_b_mass`, which employs the five flavour scheme in the definitions of the protons and jets. After the parton level events are passed to PYTHIA and DELPHES, the above mentioned cuts and event selection rules were used, and it has been found that the background is eliminated entirely. The cut flow for the simulated signal and background is given in table 4.2.

Interactions of SM particles with detector material can also result in a displaced vertex signature and thus have to be considered as part of the background. A map of regions containing dense detector material is required in order to accept only displaced vertices that are outside that region. Simulating this background requires detailed knowledge about the detector structure and is beyond the scope of this work. However, requiring a displaced vertex to be reconstructed from enough *good* tracks reduces this background. In an experimental analysis, a sophisticated track reconstruction algorithm judges which tracks are good, in the sense that the track is likely to be produced from a charged particle rather than detector noise. With no specific insight about this algorithm, we define the tracks as being good that pass our cut and selection rules, which

ensure that the charged particles traverse at least half the tracker. With the cuts introduced to define the signal, it is ensured that each event contains at least three displaced tracks from which the displaced vertex can be reconstructed.

In order to veto against cosmic ray muons, the **vertex direction** cut is implemented that requires the reconstructed heavy neutrino momentum to be in the same direction as the displaced vertex. For this the distance in (η, ϕ)-space between the reconstructed momentum $\boldsymbol{p}_N$ and the displaced vertex direction $\boldsymbol{d}$ is limited to $\Delta R \leq 1.5$. We assume that this background is eliminated when using this cut in combination with additional timing information, therefore we have not attempted to simulate it.

With the cuts described above, the signal region can be assumed to be background free. Additionally we found that a **prompt e veto**, where prompt is again defined as $|d_0| < 100\,\mu\text{m}$, with a $p_T \geq 20\,\text{GeV}$ does not affect the signal, such that it could be used to eliminate further background if that becomes necessary.

4.4   Statistical Analysis

The number of events entering the cut based analysis is given by the luminosity times the cross section for the considered process. The number of expected events after the cut based analysis N_{exp} is then given by

$$N_{\text{exp}} = \mathscr{L}\sigma f_{\text{eff}}\,, \qquad\qquad f_{\text{eff}} = \frac{N_{\text{after cuts}}}{N_{\text{all events}}}\,, \qquad\qquad (4.4.1)$$

where the efficiency factor captures how the cuts summarised in table 4.2 impact the number of signal events. The set of events surviving all cuts is labeled $\mathcal{D}_{\text{all}}$, and can be divided into LNC events $\mathcal{D}_{\text{LNC}}$ and LNV events $\mathcal{D}_{\text{LNV}}$. These datasets are then binned in the proper time τ space and the number of events in the i-th bin are given by

$$N_i = |\{E \in \mathcal{D} \mid \tau_E \text{ in } i\text{-th bin}\}|\,, \qquad\qquad (4.4.2)$$

where $|\cdot|$ is the cardinality such that e.g. $N_{\text{exp}} = |\mathcal{D}_{\text{all}}|$. The heavy neutrino TOF τ_E is defined as the proper time at which it decays in the event E.

4.4.1   Hypotheses

The shape of the histograms describing the heavy neutrino TOF may be predicted by two hypotheses. In contrast to the null hypothesis, the alternative hypothesis features oscillations.

Null hypothesis   The hypothesis without oscillations $\mathcal{M}_0$ is based on the assumption that, for each bin, the probability of the heavy neutrino superposition to decay in a LNC process is equal to the probability to decay in a LNV process. Therefore, the mean number of predicted events in the i-th bin is given by

$$\mu_i^{\text{LNC/LNV}}(\mathcal{M}_0) = \frac{1}{2}\mu_i^{\text{all}}(\mathcal{M}_0)\,. \qquad\qquad (4.4.3)$$

The probability of a given bin count can then be computed assuming a Poisson distribution of bin counts around this mean. In principle, one would expect the predicted mean values of this hypothesis to follow an exponential due to the finite lifetime of the heavy neutrinos. However,
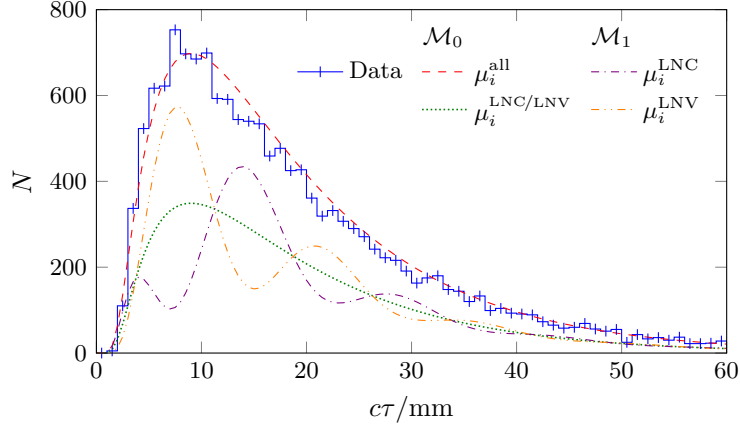
Figure 4.3: Example histogram (——) with 15 k events, demonstrating the proper time distribution after applying the cuts summarised in table 4.2. The inverse Gaussian distribution $\mu_i^{\mathrm{all}}(\mathcal{M}_0)$ described in (4.4.4) is depicted (- - -) together with the prediction of the null hypothesis $\mu_i^{\mathrm{LNC/LNV}}(\mathcal{M}_0)$ (·········). The inverse Gaussian is shown with the parameters given in point 1 on page 74, where the normalisation is approximated as $N_0 = 15500$. The distribution of the alternative hypothesis (4.4.5) is shown for LNC (-·-·-) and LNV (-··-) events of BM1, with example value $\alpha = 0.05$ for the washout parameter.

the employed cuts change this distribution into a non trivial one, which can be approximated by the PDF of a generalized inverse Gaussian, described by four free parameters, yielding

$$\mu_i^{\mathrm{all}}(\mathcal{M}_0) = \frac{N_0}{2} \frac{\tau_i^{\theta-1}}{\mu^\theta K_\theta(\lambda/\mu)} \exp\left(-\frac{\lambda}{\mu^2} \frac{\tau_i^2 + \mu^2}{2\tau_i}\right), \tag{4.4.4}$$

where N_0 denotes the overall normalisation, θ is the index parameter, μ is the mean of the distribution, and λ is a scale parameter. Additionally, τ_i denotes the position of the middle point of the i-th bin, and $K_\alpha(z)$ is the modified Bessel function of the second kind. The distribution is shown in figure 4.3, where the parameters correspond to the best fit point estimated in point 1 on page 74.

Alternative hypothesis The second hypothesis $\mathcal{M}_1$ includes oscillations, with an oscillation period given by (4.2.8), on top of the distribution described by the first hypothesis. Due to the imperfect reconstruction of the Lorentz factor, an additional washout effect obscures the oscillation pattern for larger τ. This effect is included by an exponential factor α, suppressing the oscillation. The prediction for the mean number of expected events in a bin is then given by

$$\mu_i^{\mathrm{LNC/LNV}}(\mathcal{M}_1) = \left[1 \pm \cos(\Delta m \tau_i)e^{-\alpha\tau_i}\right]\mu_i^{\mathrm{LNC/LNV}}(\mathcal{M}_0), \tag{4.4.5}$$

where the two additional parameters Δm and α are incorporated, resulting in a total of six free parameters. Again, a Poisson distribution of bin counts, around this mean, is assumed. One example of such oscillations is given in figure 4.3.

4.4.2 Likelihood ratio test

To test whether the hypothesis including oscillations is statistically preferred by the simulated data, we use a likelihood ratio test. The main idea is to decide if the null hypothesis, given by $\mathcal{M}_0$, can be discarded in favour of the alternative hypothesis, given by $\mathcal{M}_1$. The likelihood is denoted by $P(\{N_i\}, \mathcal{M})$ and describes the probability of finding the measured bin counts $\{N_i\}$ given the hypothesis $\mathcal{M}$. It is given by the product of likelihoods for all bins in both, the LNC

and LNV, cases. With the assumed Poisson distributed number of events around the mean value μ_i in the i-th bin, the likelihood of a single bin is given by

$$P(N_i, \mu_i) = \frac{\mu_i^{N_i} e^{-\mu_i}}{N_i!} \,, \tag{4.4.6}$$

where, as introduced above, N_i is the number of events in the i-th bin, which depends on the dataset and the binning.

The best fit point for each hypothesis, given the bin counts $\{N_i\}$, is evaluated by maximising the corresponding likelihood. A hypothesis at its best fit point is denoted with a hat, e.g. $\widehat{\mathcal{M}}_0$. Therefore, the likelihood ratio can be computed, given the bin counts, and yields

$$L(\{N_i\}) = \frac{P(\{N_i\}, \widehat{\mathcal{M}}_0)}{P(\{N_i\}, \widehat{\mathcal{M}}_1)} = \prod_i \frac{P(N_i^{\mathrm{LNC}}, \widehat{\mathcal{M}}_0) P(N_i^{\mathrm{LNV}}, \widehat{\mathcal{M}}_0)}{P(N_i^{\mathrm{LNC}}, \widehat{\mathcal{M}}_1) P(N_i^{\mathrm{LNV}}, \widehat{\mathcal{M}}_1)} \,. \tag{4.4.7}$$

Taking the washout parameter to infinity in the alternative hypothesis reproduces the null hypothesis. The two hypotheses are therefore nested and as a consequence the inequality[3]

$$P(\{N_i\}, \widehat{\mathcal{M}}_0) \leq P(\{N_i\}, \widehat{\mathcal{M}}_1) \,, \tag{4.4.8}$$

holds and hence the likelihood ratio is restricted by

$$0 \leq L(\{N_i\}) \leq 1 \,. \tag{4.4.9}$$

A likelihood ratio close to zero means that the given binned data are much better fitted by the alternative hypothesis than by the null hypothesis. In contrast, a ratio close to one shows that there is no clear distinction between the two hypotheses for the given binned data. Since in practice the logarithm of the likelihood is better suited for numerical computations, we continue the discussion using the logarithm of the likelihood ratio (LLR) which is defined as

$$\Lambda(\{N_i\}) = -2 \log(L(\{N_i\})) \,. \tag{4.4.10}$$

The LLR ranges from zero to infinity, where now a value near zero states that both, the null hypothesis and the alternative hypothesis, produce an equally good fit of the binned data. Contrary, a high value states that the alternative hypothesis produces a better fit.

Probability Caused by statistical fluctuations of the bin counts around their predicted mean, the null hypothesis $\widehat{\mathcal{M}}_0$ can also feature an oscillation pattern, as demonstrated in figure 4.4. Therefore, the value of a LLR alone does not contain enough information to decide whether oscillations in a given dataset are significant or not. To translate the LLR into a significance, it is crucial to know the probability that the null hypothesis produces the same LLR due to fluctuations. Per construction, the most likely LLRs produced by $\widehat{\mathcal{M}}_0$ are small, and the larger the LLR the less likely it is to be produced. The distribution of LLRs, generated by statistical fluctuations, is the PDF of the LLR under the assumption that the null hypothesis is true. We label it $\mathcal{P}$.

The challenge is then to find a value k_p, for which the probability of obtaining a $\Lambda(\{N_i\}) \geq k_p$ through statistical fluctuations, is smaller than p. This means that p is the probability of

---

[3] This inequality can by violated if not a global but a local maximum of the likelihood is found, while searching for $\widehat{\mathcal{M}}_1$. Such a local maximum might result in a smaller likelihood for the alternative hypothesis than the likelihood obtained by a fit of the null hypothesis.

$\Lambda = 5.70,\ p = 21.5\,\%,\ Z = 0.79\,\sigma$ $\Lambda = 13.59,\ p = 0.82\,\%,\ Z = 2.4\,\sigma$ $\Lambda = 17.71,\ p = 0.13\,\%,\ Z = 3.01\,\sigma$

(a) Low significance (b) Intermediate significance (c) High significance
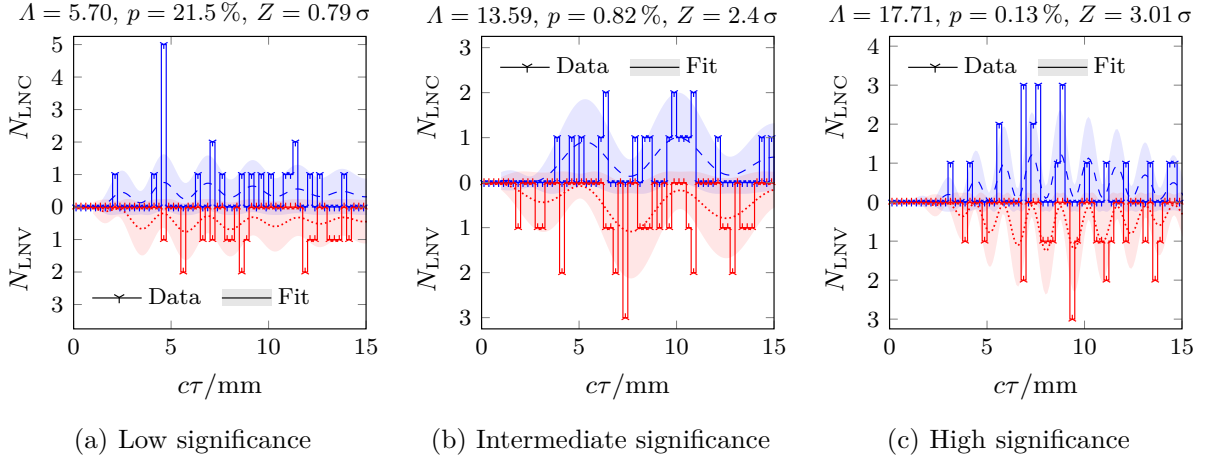
Figure 4.4: Three examples of statistical fluctuations in the null hypothesis, producing patterns that mimic $N\bar{N}$O. From panel (a) to panel (c) the oscillatory pattern becomes more distinct while the probability that the depicted histogram is generated decreases.

rejecting the null hypothesis with respect to the alternative hypothesis, even though the null hypothesis is true. Given $\mathcal{P}$, the value of k_p can be obtained via

$$\int_{k_p}^{\infty} \mathcal{P}(k)\,\mathrm{d}k = p\,. \tag{4.4.11}$$

While in the limit of large sample sizes the PDF is typically assumed to approach a χ^2 distribution, the form of the PDF for finite sample sizes is generally unknown. Therefore a simulation is performed, with the goal to sample the PDF, as follows

1. All simulated events that survive the cut based analysis are used to estimate the true distribution of the null hypothesis $\widehat{\mathcal{M}}_0$, which is depicted in figure 4.3. For those events, the best fit parameters of $\widehat{\mathcal{M}}_0$ are given by $\mu = 10.81$, $\lambda = 17.28$, and $\theta = 0.71$. The overall normalisation parameter N_0 is not relevant for the following steps as they only depend on the PDF, which is normalised to unity.

2. To obtain a set of events that follows the null hypothesis, taking statistical fluctuations into account, TOFs are taken according to the PDF from point 1. This is done until the set contains N_{exp} signal events.

3. Using these TOF values, bin counts are computed using the binning parameters based on equation (4.4.2).

4. The LLR is computed based on the bin counts from point 3.

By repeating points 2 to 4 the desired distribution can be obtained.

The obtained distributions are well approximated by χ^2 distributions, where the DOFs are treated as a free parameter. The values of the DOFs for the three BMs are given in table 4.3.

Significance With the so obtained PDF it is possible to compute the probability that a given LLR produced from statistical fluctuations of the null hypothesis $\widehat{\mathcal{M}}_0$. This probability p can be translated to a significance Z by comparing it to a standard normal distribution. A smaller probability translates to a larger significance and a higher threshold k_p. A significance of $5\,\sigma$ corresponds to a probability of $p \approx 2.87 \times 10^{-7}$, which for BM1 corresponds to a LLR threshold of

BM	χ^2 DOFs	$k(5\,\sigma)$
1	2.25	30.94
2	3.28	34.05
3	3.92	35.82

Table 4.3: Statistical fluctuations in the bin counts, following the null hypothesis, lead to a χ^2 distribution with given DOFs. The distributions are computed following the points 1 to 4 on page 74. The LLR corresponding to a p value of $5\,\sigma$ are found to be increasing from BM1 to BM3.

$k_p \approx 30.94$. See table 4.3 for the values of the other BMs. Therefore, in the case of BM1, a LLR greater than 30.94 can be interpreted as a discovery, where oscillations have been found with a significance larger than $5\,\sigma$. For very small LLRs, it is possible that the obtained probability is greater than $50\,\%$. Since for the translation into a significance a standard Gaussian is used, cf. [106], the corresponding significance would be smaller than zero . However, in cases where the LLRs are so small, the result should just be interpreted in the way that no oscillations could be proven in the given data. The simulated events and the resulting statistical fit for two example oscillations are shown in figure 4.5.

4.4.3   Data pre-processing

Some pre-processing of the events is performed to stabilise the numerics. In principle, it is expected that for sufficiently large proper times alternative hypotheses with a washout parameter greater zero produce the same bin counts as the corresponding null hypotheses. Therefore, the LLRs are dominated by small proper times, for which the washout effect is also small. We have found that the fitting algorithm used by us gives more reliable results when we consider only these dominant oscillations. Therefore we do not use all events for the statistical analysis but consider only a window containing the first oscillations. The details of this restriction for each BM point are given in table 4.4. To help reduce noise in the data a Gaussian filter of radius $r = 1$, which corresponds to a standard deviation of $\sigma = r/2$ in bin space, is applied to the bin counts before the maximisation takes place.

4.5   Results

In this paper, the first ever analysis of $N\overline{N}$Os at reconstructed level is performed. A detailed statistical analysis is employed to obtain a significance describing the feasibility to resolve the oscillations at the HL-LHC. To that end, three BM points with different oscillation periods, given in table 4.1, have been simulated. All BM points feature a mean mass of the heavy neutrinos of $14\,\mathrm{GeV}$ as well as an active-sterile mixing parameter of $|\theta_\mu|^2 = 10^{-7}$. This leads to a decay width of $\Gamma = 13.8\,\mu\mathrm{eV}$. The parameters are chosen such that the bounds of current collider searches are well evaded. While BM3 captures the mass splitting of the minimal linear seesaw model, producing the measured light neutrino data with an inverted hierarchy, BM1 and BM2 feature a smaller mass splitting as discussed in section 4.2.2.

Secondary vertex smearing   Since Delphes does not provide the experimental uncertainty to reconstruct secondary vertices, we have introduced a free parameter governing Gaussian smearing of the otherwise perfectly reconstructed secondary vertices. Figure 4.6a shows the expected confidence with which oscillations could be observed in the data for a given smearing of the secondary vertex. With our BM points, the number of signal events that survive the cuts, shown in table 4.2, is roughly 90. This assumes a luminosity of $3\,\mathrm{ab}^{-1}$ which is the expected
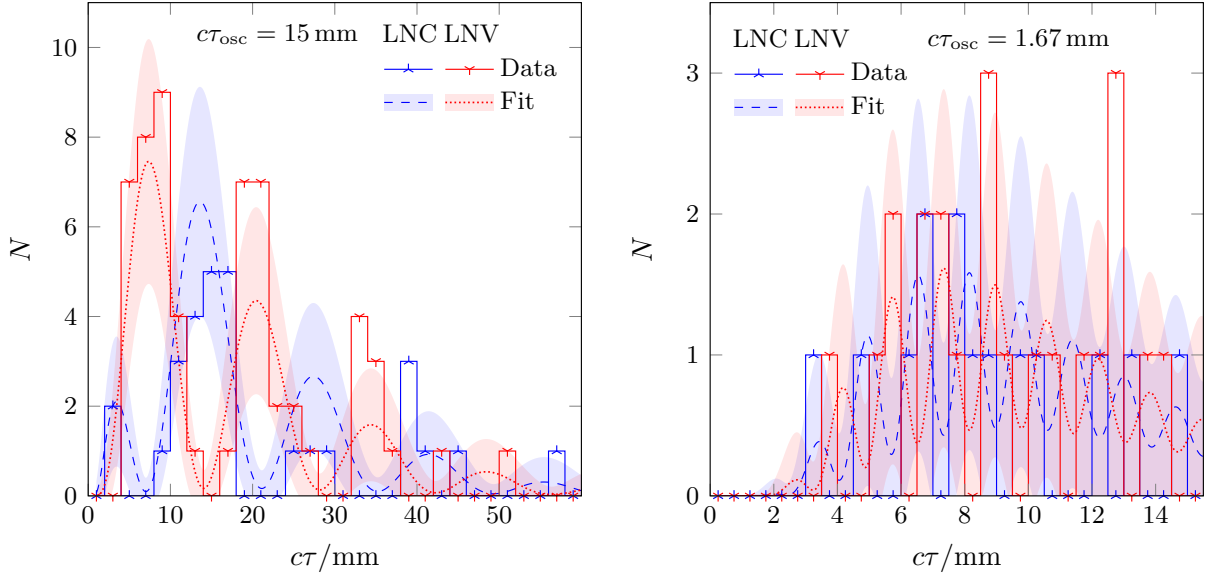
(a) The simulated events are based on BM1 with an oscillation period of 15 mm. The best fit parameters are given by an oscillation period of $14.08^{+0.85}_{-0.71}$ mm and a washout parameter of $\alpha = 3.66^{+31.73}_{-3.66} \times 10^{-3}$. The LLR was found to be 51.0, which in this case yields a significance of $6.66\,\sigma$.

(b) The simulated events are based on BM3 with an oscillation period of 1.67 mm. The best fit parameters are given by an oscillation period of $1.63^{+0.03}_{-0.04}$ mm and a washout parameter of $\alpha = 7.44^{+17.76}_{-5.45} \times 10^{-2}$. The LLR was found to be 5.29, which in this case yields a significance of $0.67\,\sigma$.

Figure 4.5: Examples for the best fit of the alternative hypothesis to the data. For each parameter point a luminosity of $3\,\mathrm{ab}^{-1}$ is used, resulting in a total of about 90 events after cuts. However, the number of events contributing to the fit is based on the range of τ values used as given in table 4.4 and therefore differs between the BMs. The fit has been performed based on the binning options in table 4.4. In these examples the secondary vertex smearing has been neglected. The bands around the oscillations depict the errors of one standard deviation, assuming a Poisson distribution for the event count in each bin.

total integrated luminosity of the HL-LHC [30]. A factor of two in the number of events can easily be achieved by choosing BM points closer to the excluded region. Therefore we regard this analysis as conservative. For each data point in the plot, 100 LLRs have been computed to obtain a mean value and a standard deviation for the significance. The figure shows that for an oscillation period of 15 mm in proper time space, corresponding to BM1, a significance of $5.19\,\sigma$ can be expected if no smearing is taken into account. Moreover, the significance is above $5\,\sigma$ up to a smearing of 2 mm, dropping to $4.46\,\sigma$ for a smearing of 4 mm. Parameter points with smaller oscillation periods are affected stronger by the smearing. This is expected since a smaller oscillation period in proper time space is related to a smaller oscillation length in lab space. A larger smearing therefore results in a stronger washout for smaller oscillation periods.

Lorentz factor reconstruction Since it is crucial to reconstruct the Lorentz factor on an event by event basis, we show in figure 4.6b how a better reconstruction of the Lorentz factor as well as a higher luminosity makes it possible to observe oscillations even for BM3. The reconstruction error directly effects the quality of the reconstructed oscillations in the proper time frame. Therefore, if the error is too large for the mass splitting one wants to resolve oscillations for, a higher event numbers only yields a limited improvement. This is shown by the lowest line in figure 4.6b. In contrast the higher lines, that represent a smaller reconstruction error of the Lorentz factor, benefit much more from a larger event number.

BM	$c\tau_{\max}/\mathrm{mm}$	Bins	Used events
1	60	30	87
2	60	30	85
3	15	60	42

Table 4.4: Binning parameters for the different BM points, as well as the number of events used in the computation of the LLR. Note that for small samples of event surviving the cut based analysis, as it is the case here, the number of events participating in the computation of the LLR undergoes fluctuations, which contribute to the fluctuations in the obtained significances.

The quality of the reconstruction of the Lorentz factor is measured using the relative error of the Lorentz factor, which is defined as

$$\Delta\gamma = \frac{|\gamma_{\mathrm{gen}}^2 - \gamma_{\mathrm{reco}}^2|}{\gamma_{\mathrm{gen}}^2 - 1}, \tag{4.5.1}$$

where γ_{gen} is the true Lorentz factor of the heavy neutrino and γ_{reco} is the reconstructed one. The set of events used for the analysis yields an exponential distribution of the relative errors of the Lorentz factor. Most events have a small $\Delta\gamma$, while only a small fraction of events have a large $\Delta\gamma$. The overall quality in the reconstruction can be measured by the standard deviation of that exponential distribution. While a large standard deviation corresponds to many events with a large relative error, and therefore to a poor reconstruction, the opposite is true for a small standard deviation. Without any improvement, with respect to the Lorentz factor achieved in this analysis, the events of BM3 yield $\Delta\gamma$'s that result in an exponential distribution with a standard deviation of 0.16. By improving the reconstruction such that the standard deviation is reduced to 0.0096, the significance is improved from around zero to $(3.37 \pm 1.10)\,\sigma$ for 90 events. Additionally doubling the number of events yields a significance of $(5.13 \pm 2.28)\,\sigma$. This scaling is justified since we assume that it is possible to improve the LHC analysis presented here, such that more signal events survive while the background is still eliminated. Additionally, it is possible to choose a BM point closer to the experimentally excluded region as mentioned earlier. Furthermore, future collider experiments, such as the ones at the FCC [107, 108], might yield much higher luminosities as well as better reconstruction possibilities of the Lorentz factor of the heavy neutrino.

Mass splitting dependency Oscillations can be used to resolve very small mass splittings. However, from the discussion above it is clear that if the mass splitting becomes too large, i.e. the oscillation period becomes too small, the reconstruction of oscillation patterns will be challenging. This is shown in figure 4.7 where the oscillation period has been varied, using a fast simulation described below. One can see that larger oscillation periods produce higher significances. It is expected that the significance drops again if the oscillation period reaches the mean lifetime of the heavy neutrinos, since then oscillations can not develop before the mass eigenstates decay.

The fast simulation is based on the assumption that the kinematics of the events is independent of the oscillation period. With this assumption, the oscillation period has no impact on the cut based analysis. As a consequence, the sum of LNC and LNV events follows for all BM points the same distribution, given by the null hypothesis. Thus it is possible to obtain a large sample of valid signal events by combining the events passing all cuts of the three simulated BM points. It is then possible to give each event a new *tag*, describing if that events should be counted as LNC or as LNV. For this the TOF of the heavy neutrino is computed on a per event basis,
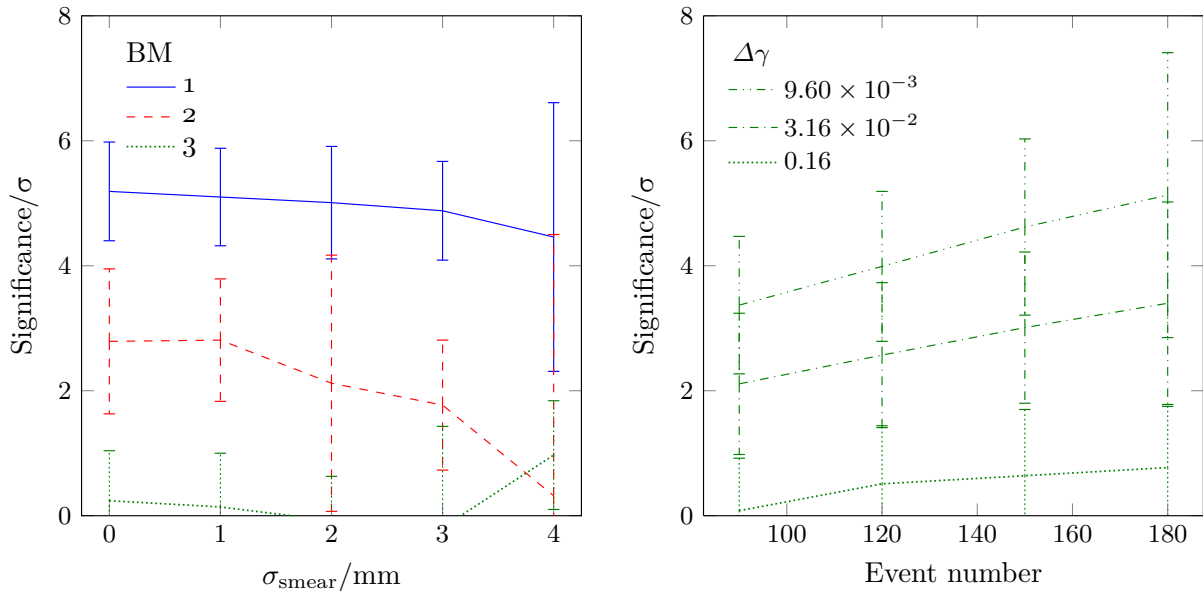
(a) Secondary vertex smearing for 90 signal events.

(b) Lorentz factor reconstruction error in BM3.

Figure 4.6: Panel (a): Significance of the three BM points at a luminosity of $\mathscr{L} = 3\,\mathrm{ab}^{-1}$ as a function of the secondary vertex smearing. Panel (b): Significance of BM3, as function of the number of events surviving the analysis, for three different relative errors of the reconstruction of the Lorentz factor (4.5.1). For this comparison no smearing has been taken into account.

using the relation

$$\tau = \frac{|\boldsymbol{d}|}{\sqrt{\gamma^2 - 1}}\,, \tag{4.5.2}$$

where $\boldsymbol{d}$ is the position of the displaced vertex with respect to the primary vertex. The formula for the oscillation probability can then be used to tag the event based on the new oscillation period. At this point one has generated a sample of valid signal events with the new oscillation period. After that, one can pick a random subset of this sample containing the physical number of events, that can be computed using (4.4.1). Subsequently, the analysis to obtain the significance can be applied to this subset of events. This strategy is orders of magnitude faster than performing the full MC simulation and cut based analysis for each oscillation period separately.

4.6 Conclusion

In this paper, we have performed a first full analysis of $N\overline{N}$Os at the reconstructed level. The simulations are based on the FEYNRULES implementation of the pSPSS introduced in [2]. After the generation of events at parton level with a patched version of MADGRAPH, hadronisation and showers are simulated using PYTHIA. Subsequently, a fast detector simulation of the CMS detector has been preformed using DELPHES. The uncertainty in the reconstruction of the displaced vertex has been implemented with a smearing function, that randomly selects a value of the displaced vertex around its true value, based on a Gaussian. The analysis of the events is performed using custom C++ and MATHEMATICA code.

In our analysis we have focused on three BMs within the pSPSS, defined in table 4.1, with heavy neutrino parameters conservatively chosen inside the region allowed by current experimental constraints. The BMs differ by the heavy neutrino mass splitting, which is largest for BM1 and
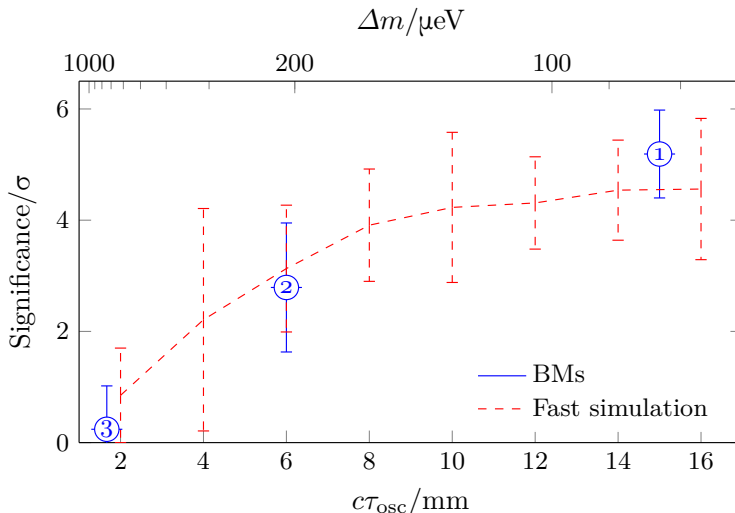
Figure 4.7: Significance as function of the oscillation period for 90 events. Three independently simulated BM points as well as eight points simulated using a fast simulation are depicted. Smearing of the secondary vertices is neglected.

smallest for BM3. Simulating events containing heavy SM hadrons, we have shown that with the event selection rules and cuts as defined in sections 4.3.1 and 4.3.2 the corresponding background is completely evaded. It has also been argued that with the given cuts other backgrounds that could not be simulated should also be evaded. Thus, the surviving signal events can be treated as background-free. The statistical method to obtain the significance with which oscillations can be found in the simulated data is described in section 4.4.

Our analysis shows that for small enough heavy neutrino mass splittings, corresponding to large enough oscillation periods, it is possible to discover $N\overline{N}$Os with the CMS detector at the HL-LHC assuming $3\,\mathrm{ab}^{-1}$ integrated luminosity. The impact of the oscillation period, the displaced vertex smearing, the number of events, and the error in the reconstruction of the heavy neutrino Lorentz factor on the significance are shown in figures 4.6 and 4.7. For resolving the $N\overline{N}$Os, it is important that the smearing is smaller than the oscillation length in lab space. Similarly, the variance of the TOF, due to the error in reconstructing the Lorentz factor, should be smaller than the oscillation period. This is the case for BM1, for which a significance of $(5.01 \pm 0.9)\,\sigma$ is obtained, assuming a smearing of $2\,\mathrm{mm}$ and around 90 total events relevant for the analysis, cf. table 4.4. For smaller oscillation periods, as in BM2 and BM3, the significance is below $3\,\sigma$ even if smearing is not taken into account.

However, we like to stress that smaller mass splittings might also be resolved with higher significance if the reconstruction of the Lorentz factor is improved. This would not only increase the significance itself but also improve the effect for larger event numbers as shown in figure 4.6b. The event number could, e.g., be increased by choosing a parameter point closer to the experimentally excluded region, cf. figure 4.1. Additionally, it might be possible to increase the significance for smaller mass splittings by increasing the decay width of the heavy neutrinos, i.e. parameter points with increased Yukawa couplings or mass. Then the heavy neutrinos would decay faster and there would be more events in the first oscillation cycles such that resolving the pattern becomes more feasible. However, more events would be lost by the d_0 cut in this case. In order to study the interdependence between such considerations, a scan over a larger sample of benchmark parameters is necessary. In addition, the presented study might be improved by more sophisticated background reduction and by optimising the window of considered TOFs

(a) Impact of a d_T cut

(b) LNV oscillation pattern after a d_0 cut
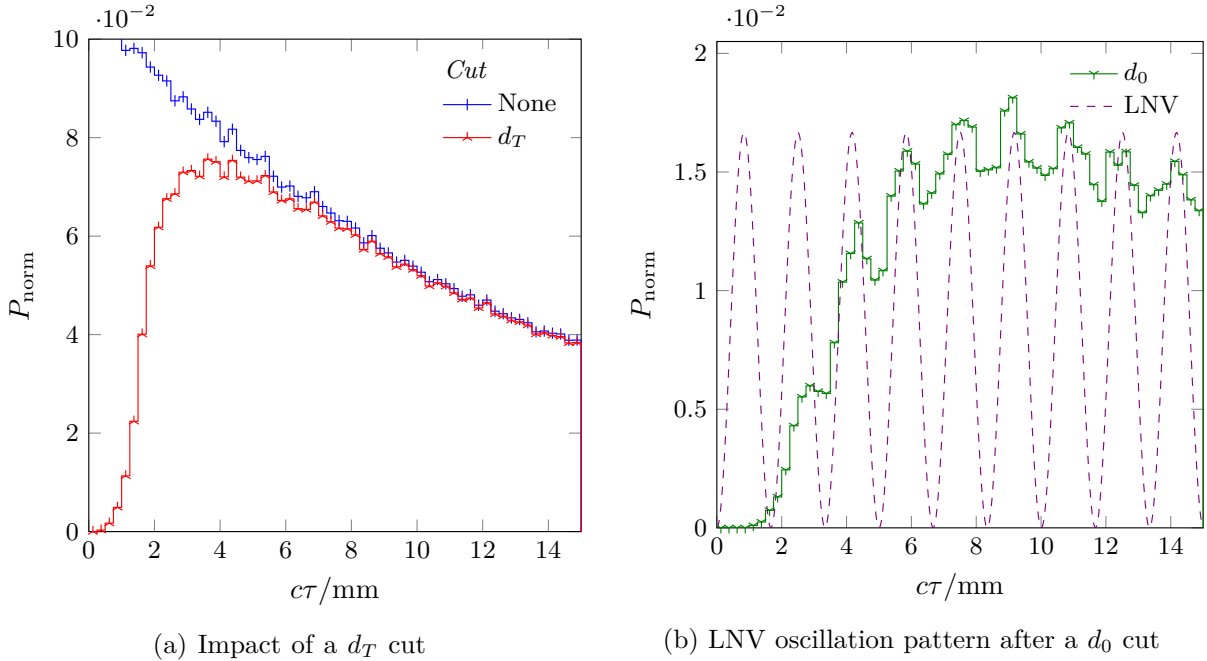
Figure 4.8: Effects of the spin correlation sensitive cut d_0, in comparison to the non-sensitive cut d_T, on a set of $N_{\mathrm{LNC}} + N_{\mathrm{LNV}}$ events. For each of the three datasets, represented by histograms, 5×10^5 generator level events, based on the values of BM3, have been simulated. All histograms are normalised with the same factor, that ensures that the area under the uncut histogram in (a) sums to unity. Panel (a): Comparison of the MC data before and after a d_T cut of $4\,\mathrm{mm}$. Panel (b): Impact of a d_0 cut of $4\,\mathrm{mm}$ overlayed by the pattern of LNV oscillations. Due to the angular dependence appearing in (4.A.1) the d_0 cut does not only generate a delayed onset but additionally imprints an oscillatory pattern originating in the LNV oscillations.

defined in table 4.4.

In summary, we have shown that the HL-LHC offers the exciting possibility to not only discover the LNV induced by $N\overline{N}$Os of long-lived heavy neutrinos, but also to resolve the $N\overline{N}$O pattern. Reconstructing the oscillation period would allow to measure this mass splitting and therefore discover the pseudo-Dirac nature of the heavy neutrino pair. This would provide deep insight into the mechanism of neutrino mass generation and could help to shed light on whether leptogenesis is able to generate the baryon asymmetry of the universe (as discussed e.g. in [51]).

Appendix 4.A   Residual oscillations

The transverse impact parameter d_0, calculated for displaced tracks, is not only proportional to the transverse lifetime of the decaying particle, but additionally contains a component depending on the angle between the displaced vertex direction and the observed particle momentum. If the magnetic field can be neglected, which we explicitly checked to be the case for the BM points discussed in this paper, the transverse impact parameter is given by [2]

$$d_0 = d_T \sin(\varphi(\boldsymbol{p}_T^N, \boldsymbol{p}_T^\mu)) \,, \tag{4.A.1}$$

where d_T is the transverse distance of the displaced vertex and the sine measures the angle in the transverse plane between the momenta of the heavy neutrino and the muon it decays into. This sine introduces an angular dependency, sensitive to spin correlations in the process under consideration. Since the LNC and LNV processes expose dissimilar spin correlations, the d_0

cut effects them differently. This leads to the observation of $N\overline{N}$Os patterns in event samples that are a priory insensitive to the difference between LNC and LNV processes. As an example, figure 4.8 shows the residual oscillations appearing in a large sample of $N_{\mathrm{LNC}} + N_{\mathrm{LNV}}$ events after introducing a d_0 cut. While the event sample with no cuts does not feature any oscillation pattern, it is shown that the d_0 cut results in residual oscillations, with peaks aligning with the ones of the LNV oscillation pattern. It can be concluded that the d_0 cut affect the LNC events more severely than the LNV ones. By contrast, a cut on d_T is independent of spin correlations and thus no residual oscillations appear. We found that this effect is subdominant for smaller event samples, such as in this analysis, and therefore neglected it in the main part of the paper.

Chapter 5

Decoherence effects on lepton number violation from heavy neutrino-antineutrino oscillations

Abstract:

We study decoherence effects and phase corrections in $N\overline{N}$Os, based on quantum field theoretical with external wave packets. Decoherence damps the oscillation pattern, making it harder to resolve experimentally. Additionally, it enhances LNV for processes in symmetry-protected low-scale seesaw models by reducing the destructive interference between mass eigenstates. We discuss a novel time-independent shift in the phase and derive formulae for calculating decoherence effects and the phase shift in the relevant regimes, which are the no dispersion regime and transverse dispersion regime. We find that the phase shift can be neglected in the parameter region under consideration since it is small apart from parameter regions with large damping. In the oscillation formulae, decoherence can be included by an effective damping parameter. We discuss this parameter and present averaged results, which apply to simulations of $N\overline{N}$Os in the dilepton-dijet channel at the HL-LHC. We show that including decoherence effects can dramatically change the theoretical prediction for the ratio of LNV over LNC events.

5.1 Introduction

The origin of the observed neutrino masses is one of the great open questions in current particle physics. When the new particles involved in the neutrino mass generation have masses close to the EW scale, it is possible to investigate this question at the LHC and future accelerators. One possible extension of the SM of elementary particles that explains the observed light neutrino masses is based on the introduction of sterile neutrinos, i.e. fermions which are uncharged under the gauge symmetry of the SM [18], see also [19–24].

When they form Yukawa interaction terms with the lepton and Higgs doublets and, in addition, have Majorana mass terms [25], light neutrino masses can be generated, which are then of Majorana-type. However, when the sterile neutrino masses are around the EW scale, care has to be taken not to exceed the bounds on the light neutrino masses [72]. When the Yukawa couplings are not tiny, the smallness of the light neutrino masses is realised by an approximate LNLS. The sterile neutrinos then form pseudo-Dirac pairs of nearly mass-degenerate heavy neutrinos. Although LNV is significantly suppressed for prompt heavy neutrino decays, cf. [72], it can lead to observable effects via the phenomenon of $N\overline{N}$Os [1, 2], see also [40, 41, 44]. Since the light neutrino masses become zero in the limit of exact LNC, observing LNV processes is crucial for probing the origin of neutrino masses.

Due to the $N\overline{N}$Os, the number of LNC and LNV events in a given process depends on the time difference between the production and decay of the heavy neutrinos. Recently it has been shown for a selected BMpoint consistent with present constraints, featuring a long-lived pseudo-Dirac heavy neutrino pair, that $N\overline{N}$Os could be resolved during the HL-LHC [3], see also [44]. However, even when the oscillations are not resolvable, they can induce LNV. The total ratio of LNV over LNC events, R_{ll}, can be used to quantify the effect.

Decoherence and phase correction effects on $N\overline{N}$Os are so far unexplored at the quantitative level. Previous studies have used estimates to verify that decoherence effects can be neglected for the considered BMparameters, e.g. [1, 3], or have assumed this to be the case. While decoherence can, in principle, depend on various parameters, it has to be a function of the mass splitting of the heavy neutrinos. This can be argued from the fact that for experimentally resolvable mass splittings, the pseudo-Dirac pair must reproduce the phenomenology of two separate Majorana neutrinos. In such cases, $N\overline{N}$Os are expected to vanish. Thus, in regions where decoherence effects are relevant, the simple $N\overline{N}$O formulae have to be modified. Phase corrections for $N\overline{N}$Os have not yet been discussed.

One can calculate the possible decoherence and phase correction effects in $N\overline{N}$Os using QFT with external wave packets. The formalism is discussed in [38] and has been adapted to the case of $N\overline{N}$Os in [1]. In [2], the effective damping parameter λ is introduced, which contains the collective effects of decoherence onto the LO oscillation formulae. In the present work, we explore how decoherence and a time-independent phase shift affect $N\overline{N}$Os as well as the quantitative prospects for observing LNV.

The remainder of this publication is organised as follows: In section 5.2, we introduce the external wave packet formalism. Afterwards, in section 5.3, we describe the derivation of the damped oscillation probability for the general case and subsequently apply the results to the case of $N\overline{N}$Os in the SPSS. We show that the effects of decoherence can be summarised by a damping parameter λ, leading to a simple extension of the oscillation formulae. Results for λ, including its impact on R_{ll} and searches for LNV, are discussed in section 5.4. Finally, we conclude in section 5.5. Details of the analytical derivations of the oscillation probabilities are presented in the appendices. The detailed steps necessary to integrate the transition amplitude

over the intermediate particles' momentum and travelled distance are presented in sections 5.A and 5.B, respectively. The constant phase shift is discussed in section 5.C. The algorithm to compute the damping parameter λ numerically is discussed in section 5.D, where the kinematics of the considered process is simulated using the pSPSS introduced in [2, 91].

5.2 External wave packet formalism

In this section, we derive the transition amplitude between two external states that are prepared as wave packets. This essential quantity is the main ingredient to derive an oscillation probability following the arguments made in [1, 38]. It is defined as a function of a distance $(t, \boldsymbol{x})$ in spacetime[1]

$$\mathcal{A}(t, \boldsymbol{x}) = \left\langle \Phi(t'', \boldsymbol{x}'') \left| \mathcal{T} \exp\left[-\mathrm{i} \int [\mathrm{d}t^\backprime] \int [\mathrm{d}^3\boldsymbol{x}^\backprime] \mathcal{H}(t^\backprime, \boldsymbol{x}^\backprime)\right] - \mathbb{1} \right| \Phi(t', \boldsymbol{x}') \right\rangle, \tag{5.2.1}$$

where $\mathcal{H}(t^\backprime, \boldsymbol{x}^\backprime)$ is the interaction Hamiltonian and $\mathcal{T}$ is the time ordering operator. In comparison to the usual QFT approach, in which plane wave states $|\Phi(\boldsymbol{p})\rangle$ with momentum $\boldsymbol{p}$ are used, the initial $|\Phi(t', \boldsymbol{x}')\rangle$ and final $\langle\Phi(t'', \boldsymbol{x}'')|$ states are wave packets centred at the indicated points in spacetime and can be written as a function of a plane wave state using

$$|\Phi(t, \boldsymbol{x})\rangle = \int \left[\frac{\mathrm{d}^3\boldsymbol{p}}{(2\pi)^3\sqrt{2E(\boldsymbol{p})}}\right] \psi(t, \boldsymbol{x}, \boldsymbol{p}, \boldsymbol{p}_0) |\Phi(\boldsymbol{p})\rangle, \tag{5.2.2}$$

where $E(\boldsymbol{p})$ is the energy of the particle, and $\psi(t, \boldsymbol{x}, \boldsymbol{p}, \boldsymbol{p}_0)$ is the wave packet envelope which describes the shape of the wave packet and is centred around the momentum $\boldsymbol{p}_0$. Assuming that the external wave packets are Gaussian and approximating the matrix element at the peak of those Gaussian functions, it is possible to evaluate the momentum integration over the external wave packets, yielding the transition amplitude for a mass eigenstate i [38]

$$\mathcal{A}_i(t, \boldsymbol{x}) = \mathcal{N} \int [\mathrm{d}E] \int [\mathrm{d}^3\boldsymbol{p}] M_i(E, \boldsymbol{p}) G_i(s) \exp[-f(E, \boldsymbol{p}) - \mathrm{i}\,\phi(t, \boldsymbol{x}, E, \boldsymbol{p})]. \tag{5.2.3}$$

Here $G_i(s)$ is the denominator of the renormalised propagator with $s = E^2 - |\boldsymbol{p}|^2$, $M_i(E, \boldsymbol{p})$ denotes the interaction amplitude, defined as the matrix element without the denominator of the propagator, and $\mathcal{N}$ is a normalisation constant.[2] The imaginary part of the exponent contains the phase

$$\phi(t, \boldsymbol{x}, E, \boldsymbol{p}) = Et - \boldsymbol{p} \cdot \boldsymbol{x}. \tag{5.2.4}$$

Here $\boldsymbol{x}$ is the distance, and t is the time difference between the production and detection point. The real part of the exponent contains the energy-momentum envelope (EME). This name is derived from the fact that it describes the shape of the intermediate particle's wave packet as a function of its energy and momentum. Its shape is defined by the shapes of the external particles' wave packets at the production P and detection D vertices V and is given by [38]

$$f(E, \boldsymbol{p}) = \left|\frac{\boldsymbol{p} - \boldsymbol{p}_0}{2\sigma_{\boldsymbol{p}P}}\right|^2 + \left[\frac{e_P(E, \boldsymbol{p})}{2\sigma_{EP}}\right]^2 + (P \to D), \tag{5.2.5}$$

---

[1] Quantities with a suppressed vectorial index are indicated by boldface.

[2] The precise form of the normalisation constant $\mathcal{N}$ changes throughout the paper. However, the normalisation constant can always be evaluated using an appropriate normalisation condition, as discussed in section 5.3.5.

where

$$e_V(E, \boldsymbol{p}) = E - E_0 - (\boldsymbol{p} - \boldsymbol{p}_0) \cdot \boldsymbol{v}_V \,, \qquad\qquad V \in \{P, D\} \,, \qquad (5.2.6)$$

Here E_0 and $\boldsymbol{p}_0$ are the energy and momentum of the intermediate particle obtained from the peaks of the external particles' wave packets using energy-momentum conservation either at the detection or production vertex. They are thus called reconstructed energy and momentum. The $(P \to D)$ is a shorthand notation where quantities at production are replaced by similar quantities at detection. If the EME is approximated as a Gaussian, its width can be interpreted as the *effective width* σ_{eff} of the intermediate particles' wave packet.

The total energy and momentum widths are given by the reciprocal sum of the respective widths at the production and detection vertices

$$\frac{1}{\sigma_E^2} = \frac{1}{\sigma_{EP}^2} + \frac{1}{\sigma_{ED}^2} \,, \qquad\qquad \frac{1}{\sigma_{\boldsymbol{p}}^2} = \frac{1}{\sigma_{\boldsymbol{p}P}^2} + \frac{1}{\sigma_{\boldsymbol{p}D}^2} \,. \qquad (5.2.7)$$

Each of these widths can be expressed in terms of the widths of the external particles in position space. The widths of the external particles in position space are parameters of the theory and are determined by the experimental situation under consideration. In the following, we only explicitly write definitions for quantities at production, while analogous definitions hold for quantities at detection. The energy and momentum widths at this vertex are given by

$$\frac{\sigma_{EP}^2}{\sigma_{\boldsymbol{p}P}^2} = \Sigma_P - |\boldsymbol{v}_P|^2 \,, \qquad\qquad \sigma_{\boldsymbol{p}P}\sigma_{\boldsymbol{x}P} = \frac{1}{2} \,, \qquad\qquad \frac{1}{\sigma_{\boldsymbol{x}P}^2} = \sum_n \frac{1}{\sigma_{\boldsymbol{x}P_n}^2} \,, \qquad (5.2.8)$$

where $\sigma_{\boldsymbol{x}P_n}$ is the width of the external particle n in position space and

$$\Sigma_P = \sigma_{\boldsymbol{x}P}^2 \sum_n \frac{|\boldsymbol{v}_{P_n}|^2}{\sigma_{\boldsymbol{x}P_n}^2} \,. \qquad (5.2.9)$$

The velocity of the production region is defined by

$$\boldsymbol{v}_P = \sigma_{\boldsymbol{x}P}^2 \sum_n \frac{\boldsymbol{v}_{P_n}}{\sigma_{\boldsymbol{x}P_n}^2} \,, \qquad\qquad \boldsymbol{v}_{P_n} = \frac{\boldsymbol{p}_{P_n}}{E_{P_n}} \,. \qquad (5.2.10)$$

The particle with the smallest width dominates these terms unless its velocity is much smaller than the velocities of the other particles. Since it holds that [38]

$$0 \le |\boldsymbol{v}_P|^2 \le \Sigma_P \le 1 \,, \qquad\qquad 0 \le \Sigma_P - |\boldsymbol{v}_P|^2 \le 1 \,, \qquad (5.2.11)$$

one can calculate that the energy and momentum widths obey the inequality

$$\sigma_E \le \sigma_{\boldsymbol{p}} \,. \qquad (5.2.12)$$

From the EME equation (5.2.5), it follows that energies E and momenta $\boldsymbol{p}$ *far* from the reconstructed energy E_0 and momentum $\boldsymbol{p}_0$ are exponentially suppressed, where *far* is defined according to the energy or momentum width, respectively. Additionally, damping from the propagator is expected when the reconstructed energy and momentum are such that the reconstructed mass

$$m_0^2 = E_0^2 - |\boldsymbol{p}_0|^2 \qquad (5.2.13)$$

is *far* from the intermediate particles' masses m_i. This damping defines the shape of the resonance, which in plane wave QFT would be given by the Breit–Wigner distribution.
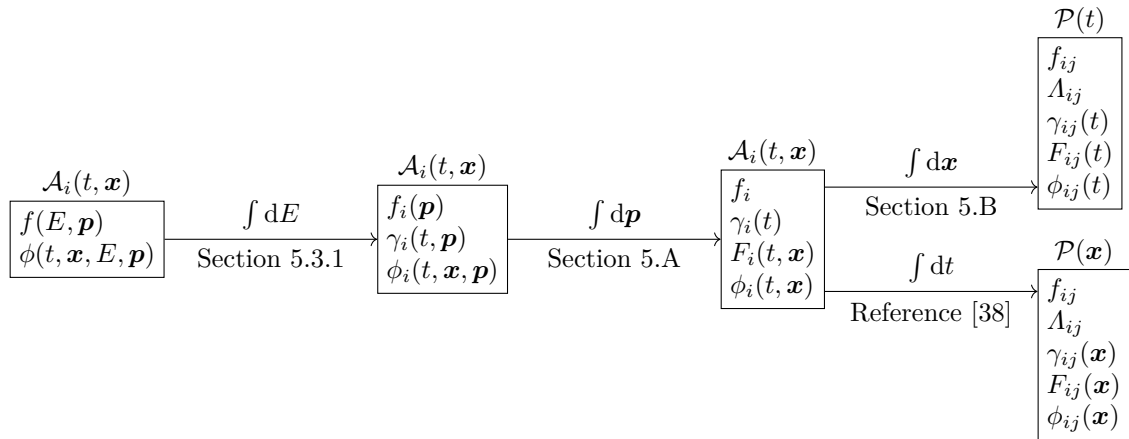
Figure 5.1: Flowchart depicting the integration steps from the spacetime-dependent transition amplitude $\mathcal{A}_i(t, \boldsymbol{x})$ of the mass eigenstate i to the time and distance-dependent oscillation probabilities $\mathcal{P}(t)$ and $\mathcal{P}(\boldsymbol{x})$, respectively. The terms appearing in the exponential part of the transition amplitude and the oscillation probability are the energy-momentum envelope (EME) f, the phase ϕ, the decay term γ, the dispersion term F, and the localisation term Λ. The last two terms give the main contribution to decoherence. Thus they dominate the damping parameter λ.

5.3 Derivation of the damped oscillation probability

The transition amplitude equation (5.2.3) needs to be integrated over the energy and momentum of the intermediate particle. The strategy to perform these integration steps is depicted in figure 5.1. While the energy integral is performed using the Jacob-Sachs theorem in the following section, the subsequent momentum integral is evaluated in section 5.A. The final step is a distance average performed in section 5.B, contrasting the time average used in [38]. In this publication, we express the oscillation probability as a function of elapsed time instead of distance since the relevant observables naturally depend on the proper time of the oscillating particles rather than their travelled distance.

For example, since the heavy neutrinos, once they are detected at a collider experiment, will exhibit a range of Lorentz boosts, the oscillation pattern has to be translated into the proper time frame of the heavy neutrino in order to be reconstructable, see [1, 3, 44]. Therefore, an oscillation probability as a function of time, averaged over the distance, is more suited for this purpose. The same applies to measurements of the R_{ll} ratio, which is sensitive to the interplay between $N\overline{N}$Os and the decay of heavy neutrinos and, hence, naturally defined in the proper time frame of the neutrinos. Furthermore, a distance average is more straightforward from a technical point of view since there are fewer distance-dependent terms than time-dependent terms in the relevant exponential, as can be seen in figure 5.1.

5.3.1 Energy integration via Jacob-Sachs theorem

To further evaluate the transition amplitude equation (5.2.3), the energy integral is evaluated using the Jacob-Sachs (JS) theorem [54]. This theorem states that for times larger than a threshold time t_{JS}, which is estimated in section 5.3.2, and for functions $\Psi(E, \boldsymbol{p})$ that are non-zero only for a finite range of $s = E^2 - |\boldsymbol{p}|^2$, the energy integral can be approximately evaluated using

$$\int [\mathrm{d}E] \Psi(E, \boldsymbol{p}) G_i(s) \exp[-\mathrm{i}\, Et] \approx \mathcal{N} \Psi(E_i'(\boldsymbol{p}), \boldsymbol{p}) \exp\left[-\mathrm{i}\, E_i'(\boldsymbol{p})t\right], \tag{5.3.1}$$

where the complex pole energy is defined in terms of the complex pole of the propagator as

$$E_i'^2(\boldsymbol{p}) = |\boldsymbol{p}|^2 + z_i \,, \qquad\qquad z_i = m_i^2 - \mathrm{i}\, m_i \Gamma_i \,. \qquad (5.3.2)$$

while m_i and Γ_i are the mass and decay width of the mass eigenstate i, respectively. After this approximate integration, the transition amplitude reads

$$\mathcal{A}_i(t, \boldsymbol{x}) = \mathcal{N} \int [\mathrm{d}^3\boldsymbol{p}] M_i(E'(\boldsymbol{p}), \boldsymbol{p}) \exp\!\left[-f(E_i'(\boldsymbol{p}), \boldsymbol{p}) - \mathrm{i}\, \phi(t, \boldsymbol{x}, E_i'(\boldsymbol{p}), \boldsymbol{p})\right] . \qquad (5.3.3)$$

The pole energy can be rewritten as

$$E_i'^2(\boldsymbol{p}) = [1 - 2\,\mathrm{i}\, \epsilon_i(\boldsymbol{p})] E_i^2(\boldsymbol{p}) \,, \qquad (5.3.4)$$

where the decay width expansion parameter, $\epsilon_i(\boldsymbol{p})$, and the mass eigenstate energy, $E_i(\boldsymbol{p})$, are defined as

$$\epsilon_i(\boldsymbol{p}) := \frac{\gamma_i(\boldsymbol{p})}{E_i(\boldsymbol{p})} \,, \qquad \gamma_i(\boldsymbol{p}) := \frac{m_i \Gamma_i}{2 E_i(\boldsymbol{p})} \,, \qquad E_i^2(\boldsymbol{p}) = |\boldsymbol{p}|^2 + m_i^2 \,. \qquad (5.3.5)$$

Under the assumption that the decay width is small compared to the mass eigenstate energy, the phase, equation (5.2.4), can be expanded in the decay width expansion parameter, which yields

$$\phi(t, \boldsymbol{x}, E_i'(\boldsymbol{p}), \boldsymbol{p}) = \left[1 - \mathrm{i}\, \epsilon_i(\boldsymbol{p}) + \mathcal{O}\!\left(\epsilon_i^2(\boldsymbol{p})\right)\right] E_i(\boldsymbol{p}) t - \boldsymbol{p} \cdot \boldsymbol{x} \,, \qquad \epsilon_i(\boldsymbol{p}) \ll 1 \,. \qquad (5.3.6)$$

The real part results in the phase of the mass eigenstate i, while the imaginary part generates an exponential decay term

$$\phi_i(t, \boldsymbol{x}, \boldsymbol{p}) := E_i(\boldsymbol{p}) t - \boldsymbol{p} \cdot \boldsymbol{x} \,, \qquad\qquad \gamma_i(t, \boldsymbol{p}) := \gamma_i(\boldsymbol{p}) t \,. \qquad (5.3.7)$$

After the energy integration, the EME equation (5.2.5) of the mass eigenstate i can be approximated to be

$$f(E_i'(\boldsymbol{p}), \boldsymbol{p}) = f(E_i(\boldsymbol{p}), \boldsymbol{p}) + \mathcal{O}(\epsilon_i(\boldsymbol{p})) \,, \qquad (5.3.8)$$

such that the LO term reads

$$f_i(\boldsymbol{p}) := f(E_i(\boldsymbol{p}), \boldsymbol{p}) = \left|\frac{\boldsymbol{p} - \boldsymbol{p}_0}{2\sigma_{\boldsymbol{p}P}}\right|^2 + \left[\frac{e_{iP}(\boldsymbol{p})}{2\sigma_{EP}}\right]^2 + (P \to D) \,, \qquad (5.3.9)$$

where

$$e_{iV}(\boldsymbol{p}) := e_V(E_i(\boldsymbol{p}), \boldsymbol{p}) = E_i(\boldsymbol{p}) - E_0 - (\boldsymbol{p} - \boldsymbol{p}_0) \cdot \boldsymbol{v}_V \,. \qquad (5.3.10)$$

The derivation from which follows that higher orders in the decay width expansion parameter can generically be neglected is presented in section 5.A.1. However, for very short times, the $\mathcal{O}(\epsilon_i(\boldsymbol{p}))$ terms can lead to a time-independent phase shift, discussed in section 5.C. In the numerical calculation presented in section 5.D, these corrections are explicitly taken into account by identifying the imaginary part as a correction to the phase.

Finally, the transition amplitude equation (5.2.3) after the energy integration equation (5.3.3) takes the form

$$\mathcal{A}_i(t, \boldsymbol{x}) = \mathcal{N} \int [\mathrm{d}^3\boldsymbol{p}] M_i(\boldsymbol{p}) \exp[-f_i(\boldsymbol{p}) - \gamma_i(t, \boldsymbol{p}) - \mathrm{i}\, \phi_i(t, \boldsymbol{x}, \boldsymbol{p})] \,, \qquad (5.3.11)$$

where NLO terms in the decay width expansion of the interaction amplitude $M_i(\boldsymbol{p}) = M_i(E_i, \boldsymbol{p})$ are neglected. The remaining integrals are the three-momentum integral and an integral that averages over distance or time.

5.3.2 Applicability of the formalism

The Jacob-Sachs (JS) theorem used in the previous section is only valid for times larger than the Jacob-Sachs threshold time t_{JS}. It is defined via the diameter of the support of the intermediate particle's wave packet

$$t \geq t_{\mathrm{JS}} := \frac{1}{|\mathrm{supp}\,\exp[-f(E, \boldsymbol{p})]|}\,. \tag{5.3.12}$$

Since the interaction amplitude, and therefore the wave packet envelope, must vanish for values of $\sqrt{s} - m_i$ larger than the uncertainties, this support is estimated by the experimental uncertainty in reconstructing the mass m_i in [38, 54]. In the case of $N\overline{N}$Os, where the mass of the heavy neutrino has to be reconstructed from semi-leptonic decay products, assuming this uncertainty to be of the order of one per cent of the heavy neutrino mass yields a time threshold of

$$t_{\mathrm{JS}} \approx \frac{100}{m} = \frac{1\,\mathrm{GeV}}{m} 6.58 \times 10^{-23}\,\mathrm{s}\,. \tag{5.3.13}$$

In order to have a fraction f of particles decaying beyond that time requires decay widths of

$$\Gamma \leq \Gamma_{\mathrm{JS}} := \frac{\gamma}{t_{\mathrm{JS}}} \ln\frac{1}{f}\,, \tag{5.3.14}$$

where γ denotes the Lorentz boost factor. Demanding $99\,\%$ of all particles decaying later than that time results in a JS width of

$$\Gamma_{\mathrm{JS}} \approx \frac{m}{1\,\mathrm{GeV}} 100\,\mathrm{MeV}\,, \tag{5.3.15}$$

when assuming a Lorentz boost factor of $\gamma \approx 10$, which is a reasonable estimate for the parameter region considered in this work.

In contrast, the width of the wave packets of the external particles is estimated in section 5.4 using the size of the silicon atom radius and the proton-proton distance in a beam bunch for final and initial states, respectively. This line of argument suggests that the neutrino wave packet should be zero outside a range defined by the width of the wave packet in the squared four-momentum $s = p^2$

$$\frac{1}{2\sigma_s^2} = \frac{s}{2E_0^2 \sigma_E^2} + \mathcal{O}(\boldsymbol{p} - \boldsymbol{p}_0) \tag{5.3.16}$$

Using the approximations derived in section 5.4.3, the numerical values given in table 5.1 and further approximating $\sqrt{s} = m$, this estimate leads to a time threshold of

$$t_{\mathrm{JS}} \approx \frac{\gamma}{n\sigma_E} \approx \frac{2\gamma\sigma_p}{n} \approx \frac{\gamma}{n} 200\,\mathrm{nm} \approx \frac{\gamma}{n} 6.66 \times 10^{-16}\,\mathrm{s} \tag{5.3.17}$$

where n is the number of standard deviations which is taken to define the support of the Gaussian distribution. Requiring a fraction $f = 99\,\%$ of particles decaying later than that time leads to a decay width of

$$\Gamma_{\mathrm{JS}} \approx n0.0199\,\mathrm{eV}\,. \tag{5.3.18}$$

Taking the $5\,\sigma$ range leads to a JS decay width of about $0.1\,\mathrm{eV}$. In order to be conservative, we use this more restrictive value in the following.

5.3.3 Dispersion regimes of the momentum integration

The integration over the three-momentum is carried out differently in three separate regimes depending on how fast the phase varies over the effective width. For slowly varying phases, the integral is evaluated using Laplace's method. This regime is called the no dispersion regime (NDR) since time-dependent dispersion effects can be neglected. In this regime, the argument of the exponential in the transition amplitude equation (5.3.11) is expanded up to second order in the momentum $\boldsymbol{p}$ around the position of the minimum of the EME at $\boldsymbol{p}_i$. Therefore, the momentum $\boldsymbol{p}_i$ maximises the exponential of the EME

$$\boldsymbol{p}_i = \underset{\boldsymbol{p}}{\operatorname{argmax}}\, \exp[-f_i(\boldsymbol{p})]\,, \tag{5.3.19}$$

The Hessian of the EME equation (5.3.9) with respect to the momentum is given at LO, i.e. neglecting the mass splitting, by equation (5.A.10)[3]

$$\boldsymbol{\Sigma}_0 = \frac{\mathbb{1}}{2\sigma_{\boldsymbol{p}P}^2} + \frac{\boldsymbol{u}_P \otimes \boldsymbol{u}_P}{2\sigma_{EP}^2} + (P \to D)\,, \qquad\qquad \boldsymbol{u}_V := \boldsymbol{v}_V - \boldsymbol{v}_0\,, \tag{5.3.20}$$

and defines the inverse of the *effective width* of the intermediate particle.

$$2\sigma_{\text{eff}}^2 = \boldsymbol{\Sigma}_0^{-1}\,. \tag{5.3.21}$$

The matrix structure of $\boldsymbol{\Sigma}_0$ is defined by the two vectors $\boldsymbol{u}_P$ and $\boldsymbol{u}_D$. Therefore, there exists a vector which is orthogonal to both, and the corresponding eigenvalue is

$$|\boldsymbol{\Sigma}_0|_{\text{smallest}} = \frac{1}{2\sigma_{\boldsymbol{p}}^2}\,. \tag{5.3.22}$$

Due to the inequality equation (5.2.12), this is the smallest eigenvalue leading to the largest effective width. The other two eigenvalues, which are dominated by the energy width, are therefore larger and approximately given by

$$|\boldsymbol{\Sigma}_0|_{\text{larger}} = \frac{|\boldsymbol{u}|^2}{2\sigma_E^2} + \mathcal{O}\left(\frac{\sigma_E}{\sigma_{\boldsymbol{p}}}, |\boldsymbol{v}_P - \boldsymbol{v}_D|\right)\,. \tag{5.3.23}$$

This approximation is justified when the velocity vectors are almost aligned $\boldsymbol{u} :\approx \boldsymbol{u}_P \approx \boldsymbol{u}_D$ and the inequality equation (5.2.12) is large $\sigma_E \ll \sigma_{\boldsymbol{p}}$. The NDR applies to times shorter than the short-time threshold equation (5.A.20)

$$t \lesssim t^{\text{short}}\,, \qquad\qquad t^{\text{short}} = |\boldsymbol{\Sigma}_0|_{\text{smallest}} E_0 = \frac{E_0}{2\sigma_{\boldsymbol{p}}^2}\,. \tag{5.3.24}$$

Since, in its derivation, the phase is required to vary slowly over the effective width of the EME in all directions, the short-time threshold depends on the largest effective width and, therefore, the smallest eigenvalue of the Hessian. The detailed computation is described in section 5.A.1.

When wave packets travel longer, the phase oscillates more rapidly as a function of $\boldsymbol{p}$, such that Laplace's method, used in the short time regime, becomes unsuitable. Since the wave packets are broader in directions transversal to the reconstructed momentum $\boldsymbol{p}_0$, an intermediate regime exists in which Laplace's method can only be used for the longitudinal direction. In contrast, transversal directions are integrated using the method of stationary phase. This intermediate regime is called the transverse dispersion regime (TDR). The method of stationary phase

---

[3] Quantities with suppressed matrix indices are indicated by sans-serif font.

(a) Lab frame.

(b) Proper time frame.
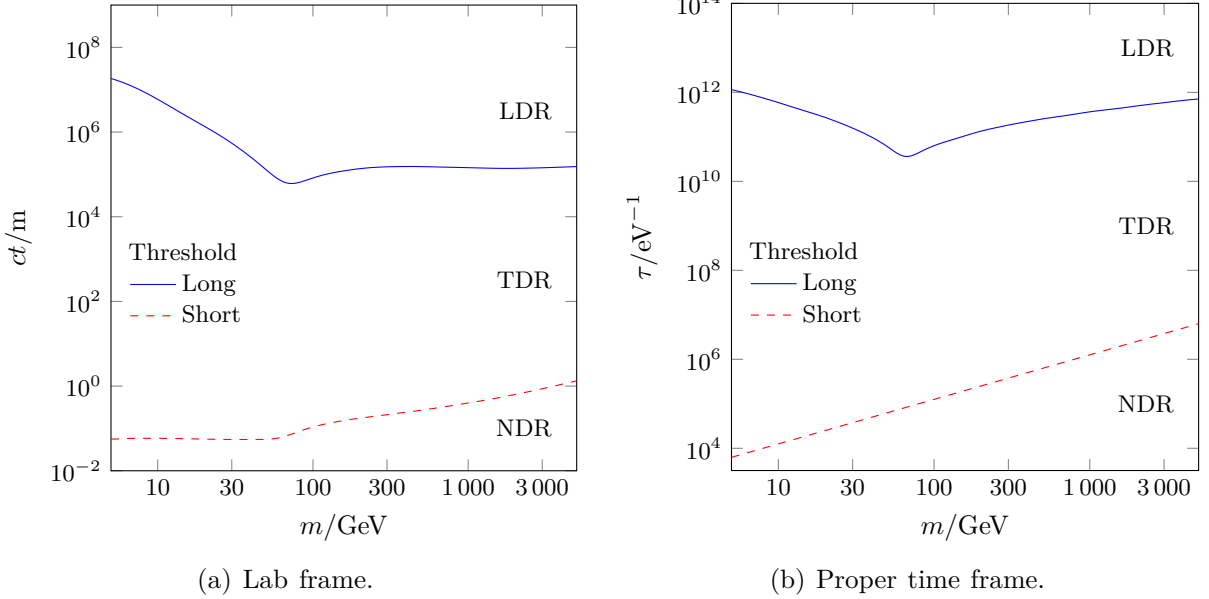
Figure 5.2: Partition of the parameter space into longitudinal dispersion regime (LDR), transverse dispersion regime (TDR), and no dispersion regime (NDR) through the long- and short-time thresholds as a function of the heavy neutrino mass m. Panel (a) shows the partition in the lab frame distance ct as defined in equations (5.3.24) and (5.3.28) and panel (b) shows the partition in the proper time τ frame as defined in equation (5.3.29).

yields $p_x = p_y = 0$, assuming that the longitudinal component, indicated by hatted variables, is $\boldsymbol{p}_0 = \widehat{p}_0 \boldsymbol{e}_z$. Laplace's method in the longitudinal direction results in

$$\boldsymbol{p}_i|_z = \widehat{p}_i = \underset{\widehat{p}}{\operatorname{argmax}} \exp[-f_i(\widehat{p})] \,, \qquad\qquad \boldsymbol{p}|_x = \boldsymbol{p}|_y = 0 \,. \qquad (5.3.25)$$

The Hessian at LO is given by equation (5.A.38)

$$\widehat{\Sigma}_0 = \frac{1}{2\sigma_{\boldsymbol{p}P}^2} + \frac{\widehat{u}_P^2}{2\sigma_{EP}^2} + (P \to D) = \frac{\widehat{u}^2}{2\sigma_E^2} + \mathcal{O}\left(\frac{\sigma_E}{\sigma_{\boldsymbol{p}}}, |\widehat{v}_P - \widehat{v}_D|\right) \,, \quad \widehat{u}_V := \widehat{v}_V - \widehat{v}_0 \,, \quad (5.3.26)$$

where the last approximation holds for $\widehat{u} :\approx \widehat{u}_D \approx \widehat{u}_P$ and when the inequality equation (5.2.12) is large, i.e. $\sigma_E \ll \sigma_{\boldsymbol{p}}$. Similar to the definition in the NDR equation (5.3.21), the effective width in the TDR is defined as

$$2\widehat{\sigma}_{\text{eff}}^2 = \widehat{\Sigma}_0^{-1} \,. \qquad (5.3.27)$$

and the long-time threshold, which forms the upper bound for this regime equation (5.A.42), is defined by

$$t^{\text{short}} \lessapprox t \lessapprox t^{\text{long}} \,, \qquad t^{\text{long}} = \widehat{\Sigma}_0 \frac{E_0^3}{m_0^2} = \frac{\widehat{u}^2}{2\sigma_E^2} \frac{E_0^3}{m_0^2} + \mathcal{O}\left(\frac{\sigma_E}{\sigma_{\boldsymbol{p}}}, |\widehat{v}_P - \widehat{v}_D|\right) \,. \qquad (5.3.28)$$

The computation leading to this result is presented in detail in section 5.A.2.

Longer times $t \gtrapprox t^{\text{long}}$ are not relevant for the discussion of heavy neutrinos in the parameter space of interest for this paper. However, for the respective regime, called the longitudinal dispersion regime (LDR), the distance-dependent formulae derived in [1, 38] can be used.

The short- and long-time thresholds equations (5.3.24) and (5.3.28) are given in the lab frame. Using $\tau = t\, m_0/E_0$ they can be reexpressed in the proper time frame as

$$\tau_{\text{short}} = |\mathbf{\Sigma}_0|_{\text{smallest}}\, m_0 = \frac{m_0}{2\sigma_{\boldsymbol{p}}^2}\,, \qquad \tau_{\text{long}} = \widehat{\Sigma}_0 \frac{E_0^2}{m_0} = \frac{\widehat{u}^2}{2\sigma_E^2}\frac{E_0^2}{m_0} + \mathcal{O}\!\left(\frac{\sigma_E}{\sigma_{\boldsymbol{p}}}, |\widehat{v}_P - \widehat{v}_D|\right). \qquad (5.3.29)$$

For heavy neutrinos appearing in the process presented in figure 5.3, these regimes are depicted in figure 5.2 after averaging over 100 events. The partition based on distances is presented in figure 5.2a. It shows that for experimental length scales smaller than about 100 km, only the NDR and TDR are relevant, and the short-time threshold is of $\mathcal{O}(\text{dm})$. The regimes in the proper time frame are shown in figure 5.2b. For decay widths leading to lifetimes comparable to the short-time threshold, it becomes relevant to quantify the fraction of events that fall into the NDR and the TDR, respectively. Decay widths $\Gamma \approx \tau_{\text{short}}^{-1}$ result in a fraction of $1 - e^{-1}$ events decaying before the threshold, and therefore inside the NDR. For decay widths $\Gamma \gtrsim 10\tau_{\text{short}}^{-1}$ practically all events decay before the threshold. Contrary, for decay widths $\Gamma \lesssim 10^{-1}\tau_{\text{short}}^{-1}$, practically all events decay beyond the threshold, and therefore in the TDR. For decay widths $\Gamma \lesssim 10\,\text{peV}$, the LDR, becomes relevant.

5.3.4 Time dependent oscillation probability

The probability for a superposition of mass eigenstates i and j to yield the transition between the given initial and final states, defined in the amplitude equation (5.2.1), is given by

$$\mathcal{P}(t) = \mathcal{N} \int [\mathrm{d}\boldsymbol{x}]_{\boldsymbol{x}_0-\Delta\boldsymbol{x}}^{\boldsymbol{x}_0+\Delta\boldsymbol{x}} \sum_{ij} \mathcal{A}_i(t,\boldsymbol{x})\mathcal{A}_j^*(t,\boldsymbol{x})\,. \qquad (5.3.30)$$

The normalisation constant $\mathcal{N}$ can be evaluated using the condition

$$\sum_{\text{outgoing}} \mathcal{P}(t) = 1\,, \qquad (5.3.31)$$

where the sum is understood to include all possible processes, i.e. decay channels of the intermediate particle. Since mass eigenstates acquire a complex phase while propagating, the superposition of distinct eigenstates depends on a phase difference that varies with time and distance, leading to a periodic fluctuation of the probability. Therefore, we refer to the probability equation (5.3.30) as an oscillation probability. The position space integral in this probability is performed in section 5.B.1 for the NDR and in section 5.B.2 for the TDR. After this integration, the oscillation probability reads, according to results equations (5.B.16) and (5.B.31),

$$\mathcal{P}(t) = \mathcal{N} \sum_{ij} M_{ij} \exp\!\left[-\lambda'_{ij}(t) - \mathrm{i}\,\phi_{ij}(t)\right], \qquad \lambda'_{ij}(t) = f_{ij} + \Lambda_{ij} + \gamma_{ij}(t) + F_{ij}(t)\,, \qquad (5.3.32)$$

where the product of the interaction amplitudes with their momenta evaluated at the peak of the intermediate particle's wave packet is

$$M_{ij} = M_i M_j^*\,, \qquad\qquad M_i = M_i(\boldsymbol{p}_i)\,. \qquad (5.3.33)$$

From the definition of the oscillation probability equation (5.3.30), it can be seen that it depends on the sum over the two mass eigenstates of the absolute value squared transition amplitudes. Since the EME equation (5.3.9) and the decay term equation (5.3.7) are real-valued, the probability depends on their sum

$$f_{ij} = f_i + f_j\,, \qquad\qquad \gamma_{ij}(t) = \gamma_i(t) + \gamma_j(t)\,, \qquad (5.3.34)$$
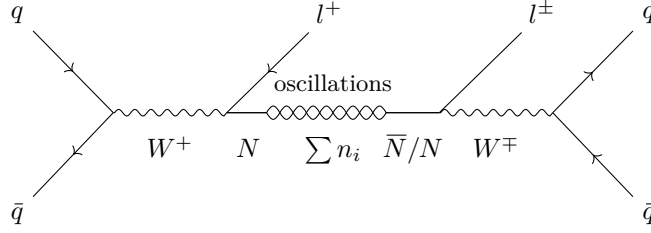
Figure 5.3: Feynman diagram depicting the heavy neutrino production at a hadron collider with subsequent oscillation and semi-leptonic decay. In the external wave packet formalism, each external particle's width is a free parameter and needs to be adjusted according to the experimental setting. We present our estimates for the external widths in table 5.1.

where their values at the minimum of the EME are given by

$$ f_i = f(E_i, \boldsymbol{p}_i)\,, \qquad \gamma_i(t) := \gamma_i t\,, \qquad \gamma_i := \gamma_i(\boldsymbol{p}_i) = \frac{m_i \Gamma_i}{2E_i}\,, \qquad E_i^2 = |\boldsymbol{p}_i|^2 + m_i^2\,. \qquad (5.3.35) $$

Contrary, the exponential term describing the phase equation (5.3.7) is imaginary, such that the probability depends on the phase difference calculated in equations (5.B.13) and (5.B.27),

$$ \phi_{ij}(t) = m_{ij}\tau(t)\,, \qquad m_{ij} = m_i - m_j\,, \qquad \tau(t) = \frac{m_0}{E_0}t\,, \qquad (5.3.36) $$

where E_0/m_0 is the Lorentz factor of the intermediate particle and $\tau(t)$ denotes the proper time the intermediate particle travels between production and decay. It vanishes when the mass splitting becomes zero, e.g. if $i = j$. This expression is modified by subdominant NLO terms [1, 38] and augmented by a time-independent shift, see section 5.C.

From the derivation of the localisation term Λ_{ij} in equations (5.B.15) and (5.B.30) as well as the dispersion term $F_{ij}(t)$ in equation (5.B.21a), it can be seen that they inherit this dependence on the mass splitting and that they are given by

$$ \Lambda_{ij} = \frac{1}{4} \begin{cases} \boldsymbol{p}_{ij}^{\mathsf{T}} \boldsymbol{\Sigma}_0 \boldsymbol{p}_{ij} & \text{NDR}\,, \\ \widehat{\Sigma}_0 \widehat{p}_{ij}^2 & \text{TDR}\,, \end{cases} \qquad F_{ij}(t) = \frac{1}{4} \begin{cases} 0 & \text{NDR}\,, \\ \widehat{\Sigma}_0^{-1} \widehat{v}_{ij}^2 t^2 & \text{TDR}\,, \end{cases} \qquad (5.3.37) $$

with

$$ \boldsymbol{p}_{ij} = \boldsymbol{p}_i - \boldsymbol{p}_j\,, \qquad \widehat{p}_{ij} = \widehat{p}_i - \widehat{p}_j\,, \qquad \widehat{v}_{ij} = \widehat{v}_i - \widehat{v}_j\,, \qquad (5.3.38) $$

where the inverse of the effective width Σ_0 is defined in equations (5.3.20) and (5.3.26). Both the localisation and the dispersion term are decoherence terms and thus lead to a damping of the oscillations. While the time-dependent dispersion term is absent in the NDR, it becomes relevant in the TDR.

5.3.5 Heavy neutrino-antineutrino oscillation probability

From here on, we restrict to the LO phenomenology of symmetry-protected low-scale seesaw models and heavy neutrino-antineutrino oscillations ($N\overline{N}$Os) appearing in processes such as the one presented in figure 5.3. The discussion is based on the symmetry protected seesaw scenario (SPSS), recently introduced with its minimal phenomenological version, the pSPSS, in [2]. The generation of light neutrino masses in seesaw models is directly related to the presence of LNV. The process in figure 5.3 is LNC if the two charged leptons have opposite charges and LNV if

they have equal charge. In this scenario the oscillation probability equation (5.3.32) for these two possible processes takes the form

$$\mathcal{P}_{\alpha\beta}^{\mathrm{LNV/LNC}}(t) = \mathcal{N}_\alpha(t) \sum_{i,j} V_{\alpha\beta ij}^{\mathrm{LNV/LNC}} \exp\left[-\lambda'_{ij}(t) - \mathrm{i}\,\phi_{ij}(t)\right]. \tag{5.3.39}$$

In comparison to reference [1, equation 2.28], the exponential has been replaced by the one of the oscillation probability equation (5.3.32) containing, apart from the phase, additional terms due to the wave packet nature of the involved particles. An additional term in [1], which summarises the effects of the mass splitting in the interaction amplitudes, is neglected here since we treat the oscillations at LO. The factors of the leptonic mixing matrix at production α and decay β are collected in the terms

$$V_{\alpha\beta ij}^{\mathrm{LNC}} := V_{\beta i} V_{\alpha i}^* V_{\beta j}^* V_{\alpha j}, \qquad\qquad V_{\alpha\beta ij}^{\mathrm{LNV}} := V_{\beta i}^* V_{\alpha i}^* V_{\beta j} V_{\alpha j}. \tag{5.3.40}$$

For the SPSS this results at LO in [2]

$$V_{\alpha\beta ij}^{\mathrm{LNC/LNV}} = \pm \frac{|\theta_\alpha|^2 |\theta_\beta|^2}{4} \begin{cases} \text{for LNC and for LNV with } i = j, \\ \text{for LNV with } i \neq j. \end{cases} \tag{5.3.41}$$

where the active-sterile mixing angle is defined by

$$\boldsymbol{\theta} = \boldsymbol{y}\,\frac{v}{m_M}, \tag{5.3.42}$$

with the SM Higgs VEV $v \approx 174\,\mathrm{GeV}$ and the Yukawa coupling of one sterile neutrino labelled $\boldsymbol{y}$, see [2]. The normalisation condition equation (5.3.31) for this scenario is evaluated for each flavour at production and yields

$$\begin{aligned} 1 = \sum_\beta \sum_{\substack{\mathrm{LNC} \\ \mathrm{LNV}}} \mathcal{P}_{\alpha\beta}^{\mathrm{LNC/LNV}}(t) &= \sum_\beta \sum_{\substack{\mathrm{LNC} \\ \mathrm{LNV}}} \mathcal{N}_\alpha(t) \sum_{ij} V_{\alpha\beta ij}^{\mathrm{LNC/LNV}} \exp\left[-\lambda'_{ij}(t) - \mathrm{i}\,\phi_{ij}(t)\right] \\ &= \sum_\beta \mathcal{N}_\alpha(t) \frac{|\theta_\alpha|^2 |\theta_\beta|^2}{2} \sum_{i=j} \exp[-f_{ij} - \gamma_{ij}(t)]. \end{aligned} \tag{5.3.43}$$

In the last step, it has been used that the sum of leptonic mixing matrix factors over LNC and LNV processes vanishes for $i \neq j$. Since the dispersion term, the localisation term, and the phase difference vanish for $i = j$, they are absent in the last line.

The oscillation probability equation (5.3.39) between the two mass eigenstates N_4 and N_5 is then given by

$$\mathcal{P}_{\alpha\beta}^{\mathrm{LNC/LNV}}(t) = \frac{|\theta_\beta|^2}{2 \sum_\gamma |\theta_\gamma|^2} (1 \pm \exp[-\lambda_{45}(t)] \cos[\phi_{45}(t)]) \qquad \forall\alpha, \tag{5.3.44}$$

where the damping parameter takes the form

$$\exp[-\lambda_{45}(t)] = \frac{2\exp[-\lambda'_{45}(t)]}{\exp[-f_{44} - \gamma_{44}(t)] + \exp[-f_{55} - \gamma_{55}(t)]}, \tag{5.3.45}$$

and can be expressed as

$$\lambda_{45}(t) := \Lambda_{45} + F_{45}(t) - \ln \operatorname{sech}[f_4 - f_5 + \gamma_4(t) - \gamma_5(t)]. \tag{5.3.46}$$

Here $\text{sech}(x)$ denotes the hyperbolic secant function, which is equal to one at the origin, and decays exponentially for values $|x| \gg 1$. For the parameter region and time scales considered in this work, it is justified to assume that the two decay parameters are approximately equal such that

$$\lambda_{45}(t) = \Lambda_{45} + F_{45}(t) - \ln\text{sech}[f_4 - f_5] + \mathcal{O}(\varepsilon), \qquad \varepsilon = |\gamma_4(t) - \gamma_5(t)|, \qquad (5.3.47)$$

From the EME equation (5.3.9), it can be seen that its minimum goes to zero if $m_i = m_0$. However, heavy neutrinos with distinct masses cannot have $m_4 = m_0$ and $m_5 = m_0$ simultaneously. Therefore, we consider two more limiting cases:

On the one hand, in cases where the reconstructed mass is *near* the mean of the heavy neutrino masses, with respect to the energy and momentum widths, the values of the EMEs are approximately equal $f_4 \approx f_5$. The normalisation then cancels these contributions, such that the damping factor becomes

$$\lambda_{45}(t) = \Lambda_{45} + F_{45}(t) + \mathcal{O}(\varepsilon^2), \qquad \mathcal{O}(\varepsilon) = \mathcal{O}(|\gamma_4(t) - \gamma_5(t)|) = \mathcal{O}(|f_4 - f_5|). \qquad (5.3.48)$$

On the other hand, configurations in which either the EMEs or the decay terms are significantly different between the two mass eigenstates can lead to a damping of the oscillations. For example, for mass splittings much larger than the energy and momentum widths, the minima f_4 and f_5 are very different. The result is that one of the mass eigenstates is favoured by the available energy and momentum of the process, such that each event is dominated by one of the two Majorana particles, and the phenomenology is that of a pair of Majorana neutrinos without $N\overline{N}$Os. If, e.g., $\varepsilon = |\gamma_4(t) - \gamma_5(t)| \ll 1$ but $f_4 \ll f_5$ the damping parameter is given by

$$\lambda_{45}(t) = \Lambda_{45} + F_{45}(t) - \ln\text{sech}\, f_5 + \mathcal{O}(\varepsilon) = \Lambda_{45} + F_{45}(t) + f_5 + \ln\frac{1 + e^{-2f_5}}{2} + \mathcal{O}(\varepsilon). \quad (5.3.49)$$

This leads to significant damping if $f_5 \gg 1$. A similar argument holds for $\gamma_4(t) \ll \gamma_5(t)$. The interpretation, in this case, is that if one of the mass eigenstates decays much faster than the other, oscillations are significantly suppressed, and damping is large.

The reconstructed mass m_0 has to be *near* to one of the pole masses m_4 or m_5 since otherwise, the whole process is suppressed. This effect is similar to the resonant scattering, described by an *s*-channel process with an intermediate particle of mass m. For cases in which $|s - m| \gg \Gamma$, the process is suppressed compared to $|s - m| \ll \Gamma$. In the present case, s is labelled m_0, and the width of the resonance is dominated by the energy and momentum widths.

While the definition of the damping parameter is derived in the context of $N\overline{N}$Os in the SPSS, the presented strategies for its evaluation also apply to more general processes.

5.4   Damped heavy neutrino-antineutrino oscillations

For the simulation of the damped oscillations discussed in the previous section, the parameters that can impact the damping are

- The masses of the heavy neutrinos.

- The decay widths of the heavy neutrinos, correlated with the time the heavy neutrinos propagate between production and decay.

- The momentum configuration of the external particles.

94

	Production			Detection		
	$\bar{q}$	q	l	l	q	$\bar{q}$
Particle	W				W	
Width	σ_p		σ_l	σ_l	σ_j	

(a) Classes.

σ_p	σ_l	σ_j
100	0.111	1.11

(b) Values in nm.

Table 5.1: Position space widths assumed for the external wave packets of the incoming and outgoing particles appearing in the process presented in figure 5.3. For simplicity, we assume that the widths fall into three distinct classes. The widths of the incoming particles σ_p are estimated by the LHC beam bunch proton-proton distance. The widths of the outgoing leptons σ_l are estimated by the atom radius of the silicon in the detector, and the width of the outgoing quarks and W bosons σ_j are estimated to be ten times as large. Panel (a) shows the different classes the widths fall into, and panel (b) shows our baseline estimates assumed for the simulations performed in this work.

- The wave packet widths of the external particles.

The masses of the heavy neutrinos can be described in terms of their mean mass and their mass splitting

$$m = \frac{m_4 + m_5}{2}\,, \qquad\qquad \Delta m = m_{45} = m_5 - m_4\,. \qquad\qquad (5.4.1)$$

The considered process and the heavy neutrinos' mean mass restrict the external particles' momentum configuration. Since the exact momentum configuration changes on an event-per-event basis, a general result is obtained by averaging the computed damping parameter over several events. Realistic momentum configurations are generated using the general purpose MC generator MADGRAPH5_AMC@NLO [109] together with the FEYNRULES [92] implementation of the pSPSS defined in [2, 91]. The numerical computation, obtained using the algorithm presented in section 5.D, takes the decay time of the heavy neutrino into account and is accordingly performed either in the NDR or in the TDR.

In order to simulate the process shown in figure 5.3, the widths of the external particles' wave packets in position space need to be estimated. When the heavy neutrino is lighter than the W boson, the first W boson can be on-shell such that its width can be directly estimated. In contrast, the second W boson is off-shell, and the external widths of its decay products must be estimated. The situation is reversed if the heavy neutrino is heavier than the W boson. The wave packet widths in configuration space of the incoming particles σ_p are assumed to be defined by the average distance between two protons in a beam bunch [110]. The wave packet width of the outgoing leptons σ_l is assumed to be defined by the atom radius of silicon present in the detector material. Final quarks and the final W boson are expected to have a larger uncertainty than final leptons, such that their width σ_j is given by $10\sigma_l$. See table 5.1 for more details.

5.4.1 Decay width dependence of the damping parameter

The mean decay width of the heavy neutrinos determines the time range the neutrino can propagate before it decays. It is thus possible to examine the time dependence of the damping parameter $\lambda = \lambda_{45}(t)$ by studying its dependence on the decay width. A numerical computation of the damping parameters for fixed mean masses of heavy neutrinos is presented in figure 5.4a. The shape of the contours depicting constant damping consists of three regions:

- To the right is a plateau stretching over several orders of magnitude. The plateau demonstrates that the effects due to varying decay widths, and with it, the time de-

95

(a) Onset of damping.

(b) Validity of approximations.
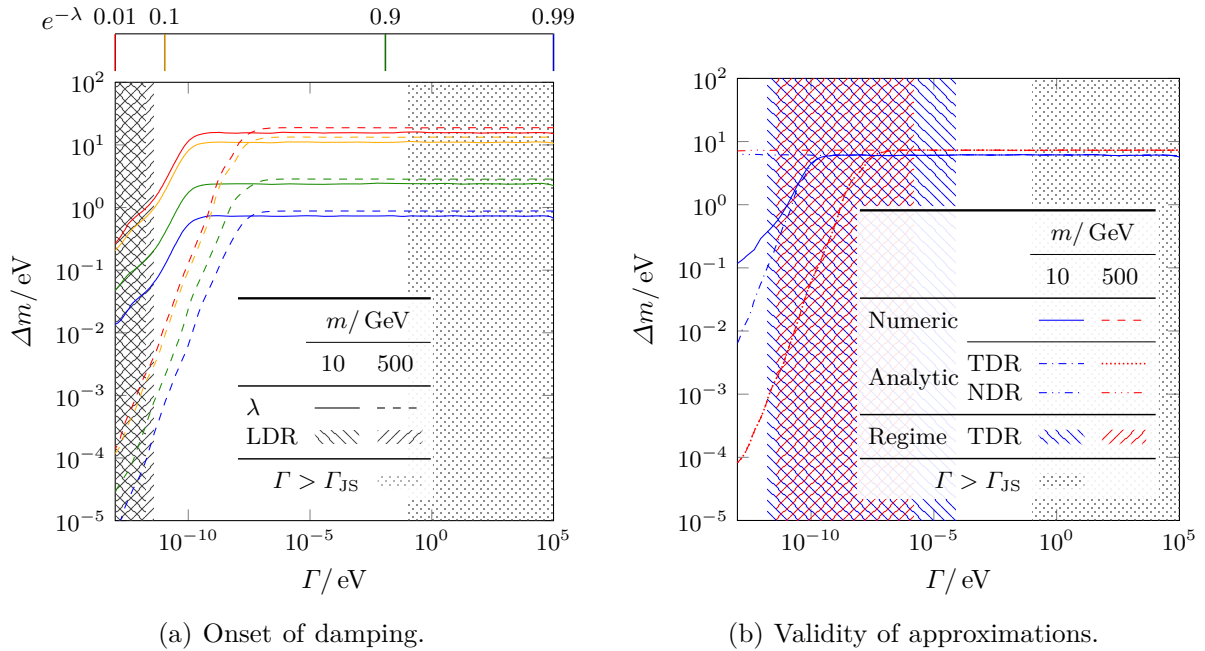
Figure 5.4: Damping parameter λ as a function of Γ and Δm. The contour lines for the damping parameter are shown for two different masses m as a function of the decay width Γ and the mass splitting Δm. The numerical results for the damping parameter λ averaged over 500 events per parameter point are given four fixed values of $\exp(-\lambda)$ and in panel (a). The comparison between the numerical results and the analytical approximations for the no dispersion regime (NDR) and the transverse dispersion regime (TDR) are given for $\lambda = \ln 2$ in panel (b). The mass dependence is given in more detail in figure 5.5. Very small decay widths of $\Gamma \lesssim 10\,\mathrm{peV}$ are governed by the longitudinal dispersion regime (LDR), which is not calculated in this work. Therefore, the predictions for these events are simulated using the same techniques as for the events falling into the TDR and hence are not reliable. Note that in the $m = 500\,\mathrm{GeV}$ case, the analytical TDR line and the numerical line coincide.

pendence of λ, are not significant in this region. The plateau can be understood from the result equation (5.3.37), noting that neither the momentum differences $\boldsymbol{p}_{ij}$ nor the matrix Λ_{ij} contains any terms in Γ or t at LO.

- For smaller decay widths $\Gamma \lesssim 0.1\,\mathrm{\mu eV}$ the damping increases with decreasing decay width. This effect is due to non-identical group velocities of wave packets of different mass eigenstates, which causes the wave packets to separate over time and, in turn, causes decoherence. The effect becomes larger for heavy neutrinos that live longer. However, if only the first 100 oscillation cycles are considered, the effect vanishes, and the plateau in the central section continues for small decay widths. Alternatively, the effect also vanishes if decays inside a sphere of radius 50 cm are considered.[4] Since these two restrictions cover most phenomenologically interesting cases, the effects of decoherence due to the separation of wave packets can be neglected in the parameter region under consideration. In the following discussions, we assume these restrictions. They imply that the damping parameter depends, in addition to the width of the external wave packet in position space, only on the mean mass and the mass splitting of the heavy neutrinos, i.e. $\lambda = \lambda(m, \Delta m)$.

In figure 5.4 the plateau extends beyond $\Gamma = 0.1\,\mathrm{eV}$, until where our numerical calculations are applicable, as we discussed in section 5.3.2. Since the physics leading to the damping as a

---

[4] Note that the 50 cm represents a somewhat randomly chosen value for which we have checked that the effects can be neglected. It does not represent a boundary at which those effects become relevant.

function of Δm is independent of Γ at LO according to our analytical derivations in section 5.C, we conjecture that we can extrapolate the plateau also to larger Γ. We make use of this conjecture when we analyse the consequence of damping on R_{ll} in sections 5.4.4 and 5.4.5.

The analytical damping formula equation (5.3.47), together with the approximated expressions for decoherence equation (5.3.37), reproduces the plateau found in the numerical evaluation for both regimes, as shown in figure 5.4b. Since the time-dependent dispersion is disregarded in the NDR, the respective formulae do not feature the increased damping for small decay widths. In the region where they are applicable, the analytical formulae are in good agreement with the numerical results for $m = 10\,\mathrm{GeV}$ and in almost perfect agreement for $m = 500\,\mathrm{GeV}$.

5.4.2 Mass dependence of the damping parameter

With the restrictions established in the last section, the damping parameter is time-independent and can be studied as a function of the mean mass m and the mass splitting Δm of the heavy neutrino. This dependency is presented in figure 5.5. The numerical results are shown in figure 5.5a, the results for the time-dependent analytic formulae equation (5.3.47) are presented in figure 5.5b, and the results for a distance-dependent oscillation probability, as obtained in [1, 38], are shown in figure 5.5c. While the numerical results in the NDR and the TDR are approximately equal, the results for the approximated analytic formulae derived in sections 5.A and 5.B differ between those regimes. Therefore, the results obtained from the analytical computation are presented for each regime individually, while the presented numerical results are valid in both regimes.

Since the time-dependent formulae for the damping factor are similar in the NDR and TDR, the LO effects of the momentum dependence can be explained by studying the time-independent part of the damping factor equation (5.3.48)

$$\lambda_{45} = \Lambda_{45} + \mathcal{O}\left(\varepsilon, \frac{t}{t^{\mathrm{short}}}\right) = 2\left(\boldsymbol{p}_{45} \cdot \frac{\boldsymbol{u}_P}{2\sigma_{EP}}\right)^2 + \mathcal{O}\left(\varepsilon, \frac{t}{t^{\mathrm{short}}}, \frac{\sigma_{\boldsymbol{p}}}{\sigma_E}\right), \qquad (5.4.2)$$

where equations (5.3.23) and (5.3.37) are used, and the last approximation is obtained by observing that, in both regimes, the energy width at production dominates the reciprocal sum in the localisation term for the baseline estimate of external widths, defined in table 5.1b. Although the exact dependence of the damping factor on the mass is complicated since the process-dependent orientation of momenta and velocities change with varying mass, the sudden decrease of damping around the W boson mass can be explained by a change in the energy width. The energy width at production is given by a sum of all external particles at the production vertex. For heavy neutrinos lighter than the W mass, this includes the initial W boson and the initial charged lepton. For heavy neutrinos above the W mass, the initial W boson is off-shell, and thus, the relevant particles are given by the two incoming quarks and the initial charged lepton. An increase in the number of external particles participating in the production process results in a sudden increase in the energy width, which results in a sudden decrease in damping.

The shape of the contours describing constant damping is very similar for all computation methods in all regimes, except for the distance-dependent formulae in the NDR. This difference can be traced back to the localisation term in the NDR, which takes the form

$$\Lambda_{ij} = \frac{1}{2}\begin{Bmatrix}\boldsymbol{p}_{ij}^{\mathsf{T}}(\partial_{\boldsymbol{x},\boldsymbol{x}}F_{ij}(t,\boldsymbol{x}))^{-1}\boldsymbol{p}_{ij} \\ E_{ij}(\partial_{t,t}F_{ij}(t,\boldsymbol{x}))^{-1}E_{ij}\end{Bmatrix} = \frac{1}{4}\begin{Bmatrix}\boldsymbol{p}_{ij}^{\mathsf{T}}\Sigma_0\boldsymbol{p}_{ij} & \text{time dependent}, \\ E_{ij}^2\left(\boldsymbol{v}_0^{\mathsf{T}}\Sigma_0^{-1}\boldsymbol{v}_0\right)^{-1} & \text{distance dependent}.\end{Bmatrix} \qquad (5.4.3)$$

where $E_{ij} := E_i - E_j$ and $F_{ij}(t,\boldsymbol{x})$ is the spacetime envelope (STE) in the NDR equation (5.B.5). The time-dependent formula is given in equation (5.3.37), and the distance-dependent one
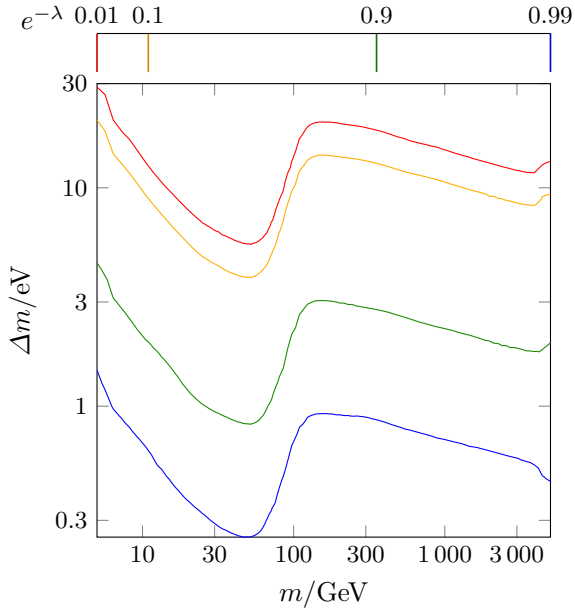
(a) Numerical derivation.
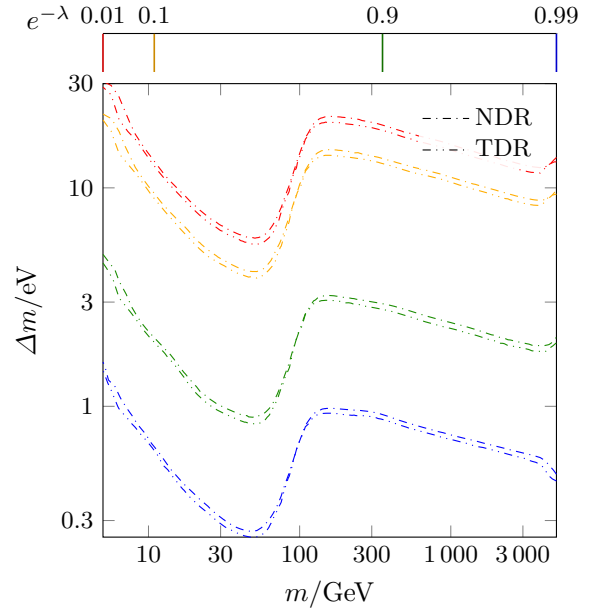
(b) Time dependent formulae.
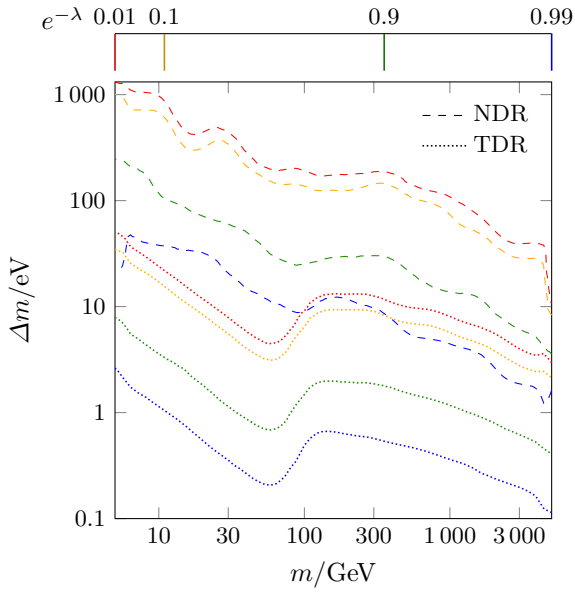
(c) Distance dependent formulae.
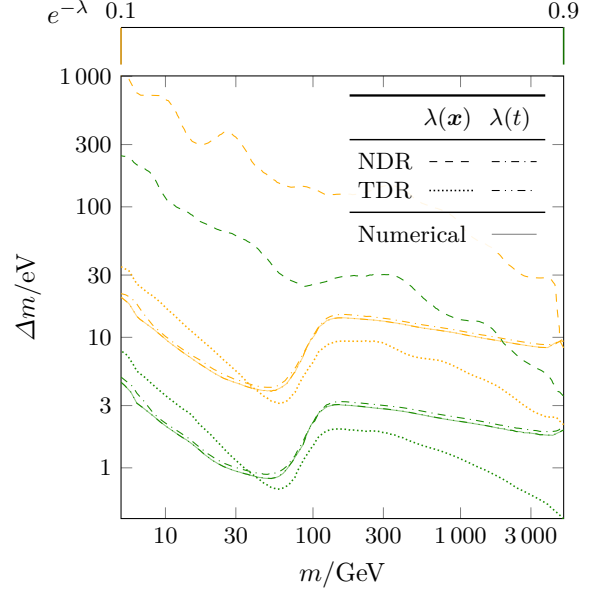
(d) Overall comparison.

Figure 5.5: Simulation results for the damping parameter λ for four values of $\exp(-\lambda)$ as a function of the mass m and the mass splitting Δm using the numerical analysis from section 5.D in panel (a), the time-dependent results from section 5.B in panel (b), and the distance-dependent results from [38] in panel (c). Panel (d) compares these techniques. For the analytic results in panels (b) to (d), the results for the no dispersion regime (NDR) and transverse dispersion regime (TDR) are shown separately.

(a) Time thresholds.

(b) Damping parameter.
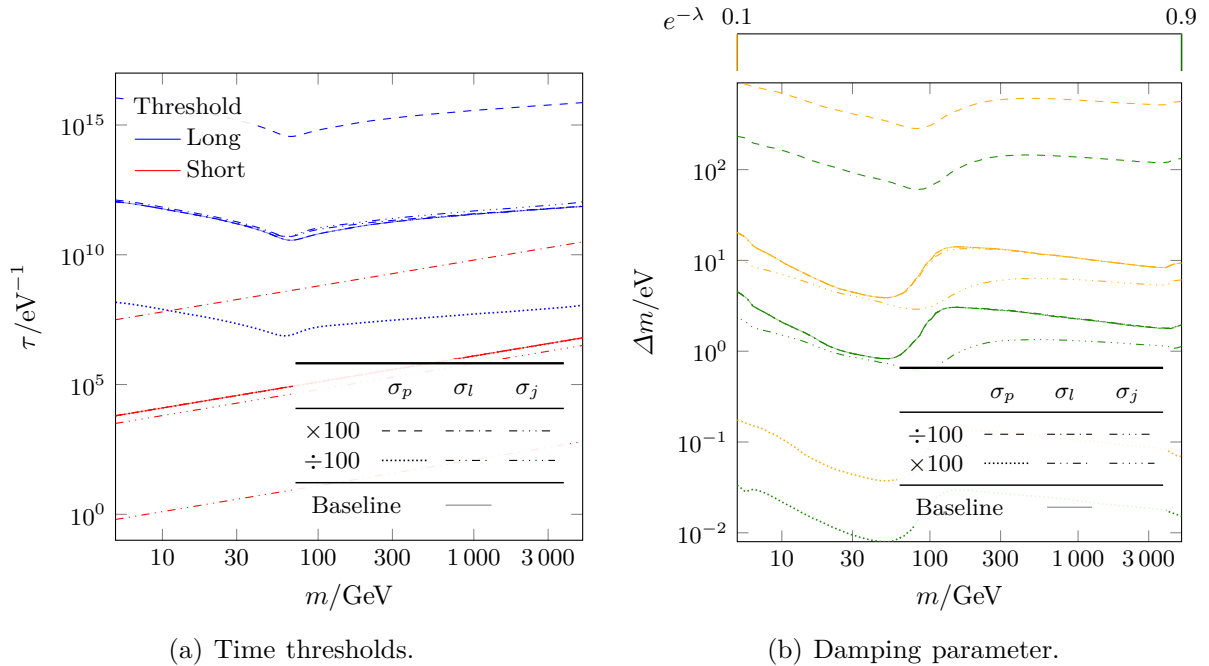
Figure 5.6: Dependence of the time thresholds and the damping parameter on the scaling of each external wave packet width. The values for the widths of the baseline scenarios are given in table 5.1. The baseline scenario for the time thresholds shown in panel (a) is given in figure 5.2, and the baseline scenario for the damping parameter in panel (b) is given in figure 5.5a. The short- and long-time thresholds in panel (a) are most sensitive to the scaling of the lepton σ_l and the proton σ_p widths, respectively. The damping parameter in panel (b) is most sensitive to the scaling of the proton width.

can be found in [38, section 6.1.2, equation 99]. While the upper formula is proportional to the eigenvalues of Σ_0, the lower formula is proportional to the inverse of the eigenvalues of Σ_0^{-1}. Therefore, as long as the reconstructed neutrino velocity $\boldsymbol{v}_0$ is not parallel to one of the eigenvectors of the effective width, this lead to significantly different damping behaviour.

The absence of the dispersion term in the NDR can yield different damping for each regime. However, for the restrictions discussed in section 5.4.1, the effects of this term are expected to be negligible. Together with the fact that all other additional effects considered in the numerical derivation compared to the analytic one are small, the numerical and time-dependent analytical results in both regimes are expected to be approximately identical. This is confirmed by the results shown in figure 5.5. Therefore, the time-dependent results feature a smooth transition of the damping between the NDR and the TDR. In contrast, for the distance-dependent results, the damping in the NDR differs significantly from the results in the TDR. This smooth transition can be seen as a further advantage of the time-dependent formulae, as derived in this work, over the distance-dependent ones.

5.4.3 Wave packet widths dependencies

In order to understand the impact of the estimates for the widths of the external wave packets, we rederive the previous results after rescaling individual widths by a factor of one hundred and present their dependence on this scaling in figure 5.6.[5]

---

[5] This scaling factor is chosen to generate large deviations from the baseline estimates to illustrate the parameter dependence and does not represent uncertainty in the baseline estimates.

The effects on the relevant time thresholds are presented in figure 5.6a. They can be understood by considering their dependence on the external width given in equations (5.3.24) and (5.3.28). While the momentum width $\sigma_{\boldsymbol{p}}$ depends on the smallest width in configuration space at production and detection, which is given by the widths of the charged leptons σ_l, the energy width σ_E depends, according to the following argument, mainly on the proton width σ_p.

The energy width depends on the two smallest widths at production and detection. While the smallest width is cancelled by the global factor of $\sigma_{\boldsymbol{p}P}$ or $\sigma_{\boldsymbol{p}D}$, respectively, the second smallest width dominates the energy width equation (5.2.8). For the baseline of external widths, see table 5.1, the energy width at production is much smaller than the corresponding energy width at detection. The reciprocal sum of those energy widths, precisely σ_E, is thus dominated by the proton width.

In figure 5.6b, we show that the main impact on the damping parameter is due to the proton width by individually varying the external widths. This relation can be traced back to the fact that the damping is dominated by the energy width, see approximation equation (5.4.2).

The effect of the non-monotonous behaviour of the contour around the W boson mass in figure 5.6b is reduced when varying the jet width. The non-monotonous behaviour can be explained by a change in the number of particles participating in production and detection, as described in section 5.4.2. The change in the number of particles is the opposite for production and detection, such that it weakens if the energy widths at production and detection are similar. Multiplying the jet width by a factor of 100 has precisely the effect of equalising those energy widths.

From the above results, it becomes clear that the value of the external widths plays an essential role in the prediction of decoherence and merits further dedicated studies.

5.4.4 Decoherence effects on R_{ll}

The ratio between the number of LNV and LNC decays is called R_{ll}. Since it is calculated by integrating over the $N\overline{N}$Os, it is affected by decoherence. Therefore, it is necessary to know the amount of damping to predict its value as a function of, e.g., the mean mass and the active-sterile mixing parameter.

The probability of obtaining an LNC or LNV event, between proper times $\tau_{\min}$ and $\tau_{\max}$, is given by the integral [2]

$$P_{ll}^{\text{LNC/LNV}}(\tau_{\min}, \tau_{\max}) = \int_{\tau_{\min}}^{\tau_{\max}} P_{\text{decay}}(\tau) P_{\text{osc}}^{\text{LNC/LNV}}(\tau)\,\mathrm{d}\tau\,, \tag{5.4.4}$$

where $\tau = {}^{m_0}/{}_{E_0}t$ is the proper time. Here, the decay probability density is given by

$$P_{\text{decay}}(\tau) = -\frac{\mathrm{d}}{\mathrm{d}\tau}\exp(-\Gamma\tau) = \Gamma\exp(-\Gamma\tau)\,, \tag{5.4.5}$$

and the oscillation probability is given by equation (5.3.44)

$$P_{\text{osc}}^{\text{LNC/LNV}}(\tau) = \mathcal{N}\left(1 \pm \exp\left[-\lambda - \frac{\mu^2\tau^2}{4}\right]\cos[\Delta m\tau]\right)\,, \tag{5.4.6}$$

where the time dependence of the damping parameter equation (5.3.47) has been made explicit by defining the parameter μ using the dispersion term in the TDR equation (5.3.37). In the

limit $\tau_{\min} \to 0$ and $\tau_{\max} \to \infty$ the integral and the ratio of LNV over LNC events is given by

$$P_{ll}^{\text{LNC/LNV}}(\lambda, \mu) \propto \frac{1 \pm f(\lambda, \mu)}{2}, \qquad R_{ll}(\lambda, \mu) = \frac{2}{1 + f(\lambda, \mu)} - 1. \qquad (5.4.7)$$

where the function that appears in both quantities is

$$f(\lambda, \mu) = \frac{\text{erfcx}[\Gamma'_-(\mu)] + \text{erfcx}[\Gamma'_+(\mu)]}{2} \Gamma'_\lambda(\mu), \qquad (5.4.8)$$

which is defined in terms of

$$\text{erfcx}(x) = \exp(x^2)[1 - \text{erf}(x)], \qquad \Gamma'_\pm(\mu) = \frac{\Gamma \pm i\,\Delta m}{\mu}, \qquad \Gamma'_\lambda(\mu) = \frac{\Gamma}{\mu} \frac{\sqrt{\pi}}{\exp \lambda}. \qquad (5.4.9)$$

Here $\text{erfcx}(x)$ is the scaled complementary error function, which decays exponentially for negative x approaches one for small x and is inversely proportional to x for large x. For a subleading time dependence in the damping parameter, the function can be approximated using

$$f(\lambda, \mu) = f(\lambda, 0) \left(1 - \frac{\Gamma^2 - 3\Delta m^2}{\Gamma^2 + \Delta m^2} \frac{\varepsilon}{2} + \mathcal{O}(\varepsilon^2) \right), \quad \varepsilon = \frac{1}{\Gamma'_-(\mu)\Gamma'_+(\mu)} = \frac{\mu^2}{\Gamma^2 + \Delta m^2}. \quad (5.4.10)$$

The LO term corresponds to the limit $\mu \to 0$, which captures the NDR. In this limit the equations simplify to

$$f(\lambda, 0) = \frac{f(0,0)}{\exp \lambda}, \qquad R_{ll}(\lambda) := R_{ll}(\lambda, 0) = 1 - \frac{2}{1 + (1 + {}^{\Delta m^2}/\Gamma^2) \exp \lambda}, \qquad (5.4.11)$$

where the damping independent term $f(0,0)$ corresponds to the term that appears when taking furthermore the limit that also the constant localisation term can be neglected, $\lambda \to 0$, which recovers for the ratio of LNV over LNC events the known result [2, 41]

$$f(0,0) = \frac{\Gamma^2}{\Gamma^2 + \Delta m^2}, \qquad R_{ll}(0,0) = \frac{\Delta m^2}{\Delta m^2 + 2\Gamma^2}. \qquad (5.4.12)$$

In cases where the damping is large $\lambda(\tau) \gg 1$, the coherence between the propagating mass eigenstates is lost, and the phenomenology is that of two independent Majorana neutrinos. Increasing λ, therefore, increases the observed R_{ll} compared to the naive case that does not take damping into account. This behaviour is depicted for time-independent damping in figure 5.7a. Therefore, when considering $R_{ll}(\lambda)$ as a function of Δm and Γ, parameter regions with large damping must have a large R_{ll} and lines representing a smaller R_{ll} cannot penetrate those regions. As depicted in figure 5.7b, the contours representing the naive R_{ll} are given by constant ratios between Γ and Δm. However, damped R_{ll} contours are bound from above by regions of large damping. Therefore, once damping becomes relevant, the R_{ll} bands follow the contour lines of the damping parameter shown in figure 5.4.

5.4.5 Decoherence effects on prompt searches for lepton number violation

For the part of the parameter space where heavy neutrinos decay promptly, direct discovery of oscillations by resolving them as proposed in [3] is not possible. However, the integrated R_{ll} ratio introduced in the last section can still be measured. Hence, it is relevant to predict this ratio for the realistic benchmark models (BMs) of the linear and inverse seesaw, introduced and motivated

(a) $R_{ll}(\lambda)$ (b) $R_{ll}(\Gamma, \Delta m)$
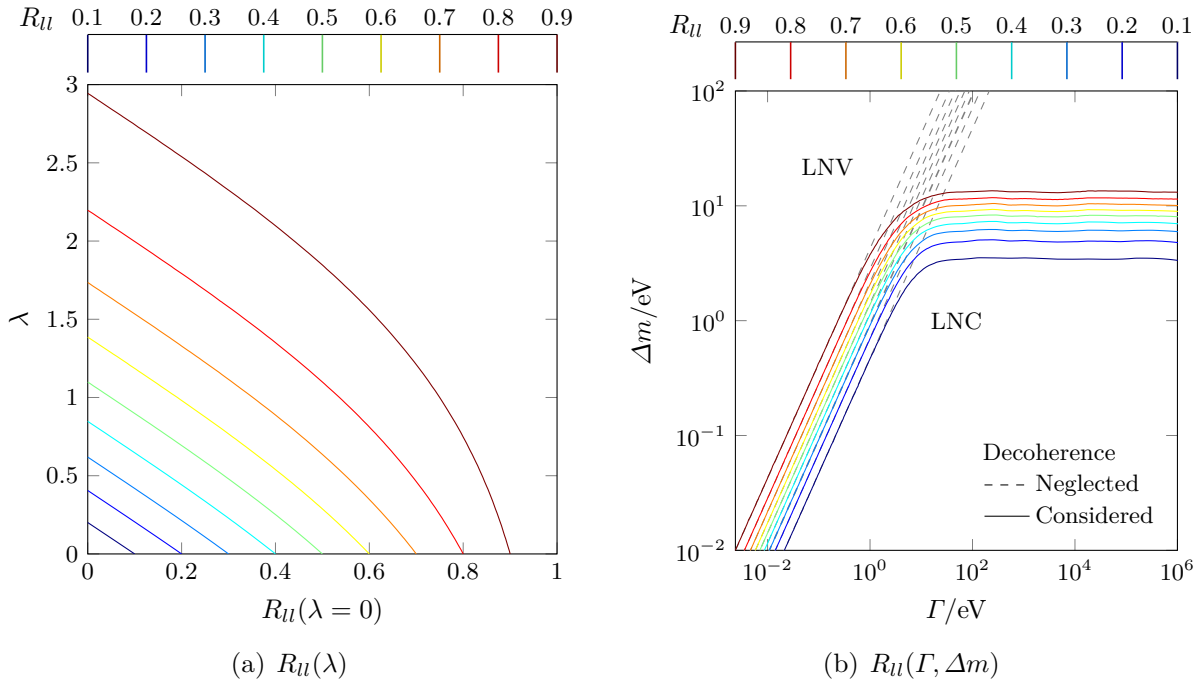
Figure 5.7: Decoherence effects on the R_{ll} ratio for values in $R_{ll} \in [0.1, 0.9]$. Panel (a) depicts the functional dependence given in equation (5.4.11) as a function of the naive value equation (5.4.12), i.e. assuming $\lambda = 0$ and the damping parameter. The simulation results for the impact of decoherence effects in the $(\Gamma, \Delta m)$ parameter space are presented in panel (b). Results for the damping parameter λ are used, as discussed in section 5.4.1.

in [2] and summarised in table 5.2. While the heavy neutrino mass splitting in the inverse seesaw scenarios depends on the active-sterile mixing parameter, defined in equation (5.3.42),

$$\Delta m = m_\nu |\boldsymbol{\theta}|^{-2} \, , \tag{5.4.13}$$

the mass splitting in the linear seesaw scenarios is fixed for each BMpoint. Therefore, in the inverse seesaw, it is always possible to restore coherence and the naive value of R_{ll} by considering larger values of the active-sterile mixing parameter and, accordingly, smaller mass splittings. However, in the linear seesaw, the damping solely depends on the mass of the heavy neutrinos. When it becomes relevant, coherence is lost independently of the value of the active-sterile mixing parameter.

The effects of decoherence onto the R_{ll} bands of the linear and inverse seesaw BMscenarios are depicted in figure 5.8. For our baseline estimates of external particle widths, the damping becomes relevant for mass splittings $\Delta m \gtrsim 1\,\mathrm{eV}$ as shown in figure 5.5a. The presented BMpoints for the inverse seesaw feature such mass splittings for values of the active-sterile coupling in the range of $10^{-4} < |\boldsymbol{\theta}|^2 < 10^{-1}$. Therefore, the R_{ll} bands deviate from the naive ones in that region. As discussed above, the bands then follow the contour lines of the damping parameter, such that large damping results in an R_{ll} of one. The mass splittings for the BMpoints for the linear seesaw are such that decoherence effects can be neglected for our baseline estimate of external particle widths, defined in table 5.1. Consequently, the R_{ll} bands do not deviate from the naive ones in this case.

However, the situation changes if different widths of the external wave packets are assumed. As shown in figure 5.6b, the most significant effect on the damping is given by varying the

Seesaw	Δm	Hierarchy	BM
Linear	Δm_ν	Normal	$\Delta m_\nu = (41.46 \pm 0.29)\,\text{meV}$
		Inverted	$\Delta m_\nu = (749 \pm 21)\,\text{\textmu eV}$
Inverse	$m_\nu |\boldsymbol{\theta}|^{-2}$		$m_\nu = 0.5\,\text{meV}$
			$m_\nu = 5\,\text{meV}$
			$m_\nu = 50\,\text{meV}$

Table 5.2: Summary of the five benchmark models (BMs)considered in this publication, resulting in various mass splittings of the heavy neutrinos Δm. Since the SPSS with one pseudo-Dirac pair captures the minimal linear seesaw, it suffices to define one BMfor each light neutrino mass hierarchy that reproduces the observed mass splitting between two massive light neutrinos Δm_ν [89]. In the case of the inverse seesaw, the single pseudo-Dirac SPSS represents an incomplete theory since the model generates only one of the two light neutrino masses. Therefore, we define the mass splitting as a function of the generated neutrino mass m_ν, for which three BMvalues are defined.
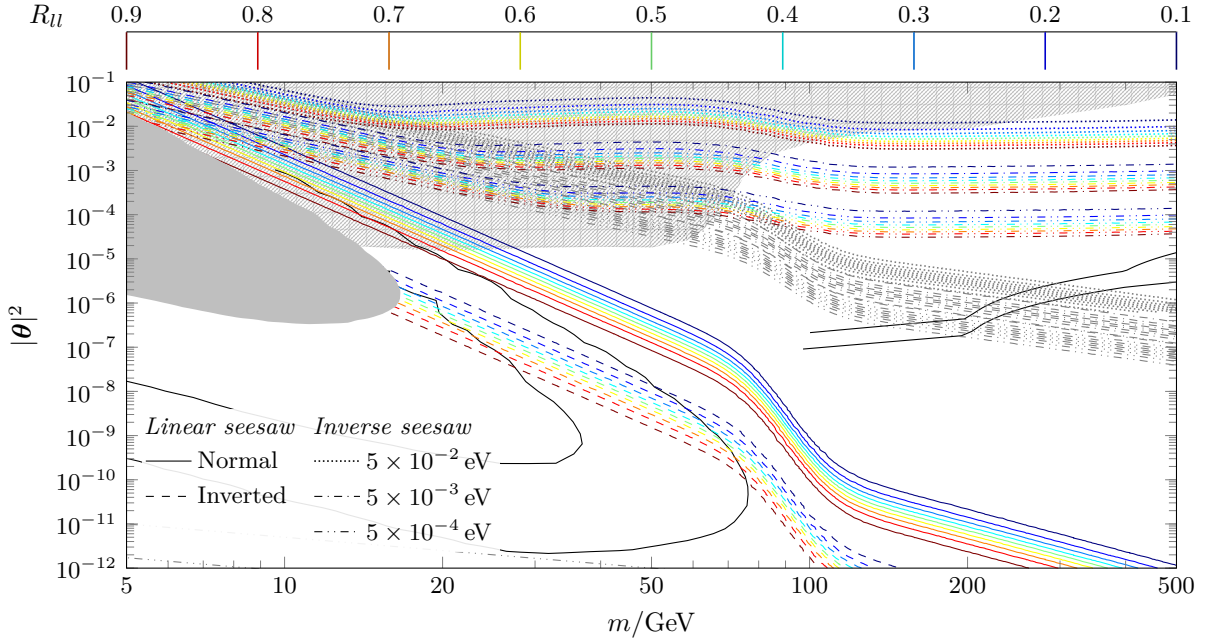
Figure 5.8: Bands of the LNV over LNC event ratio $R_{ll} \in [0.1, 0.9]$ for the five BMs defined in table 5.2. The genuine results, taking damping into account as discussed in section 5.4.1, are depicted as coloured bands, while the naive results that neglect damping are shown as grey bands. The mass splittings of the two BMs of the linear seesaw are too small to be affected by decoherence, as seen at the lowest two bands. However, the three BMs for the inverse seesaw, forming the uppermost three bands, deviate from the grey bands beneath them. Hence, for a fixed prediction of R_{ll}, the value of the squared active-sterile mixing parameters between the genuine and the naive results can vary by up to four orders of magnitude. The grey area indicates displaced searches by CMS, and ATLAS [28, 29]. The shaded grey areas indicate searches for LNV signals by CMS and ATLAS [26, 27]. The two black lines at low masses indicate the reach of the HL-LHC and the FCC-*ee* [95, 96, 111]. The two black lines at high masses indicate the reach of the LH*e*C and FCC-*eh* [98].

(a) Scaling of σ_p by $\div 100$.   (b) Scaling of σ_p by $\times 100$.
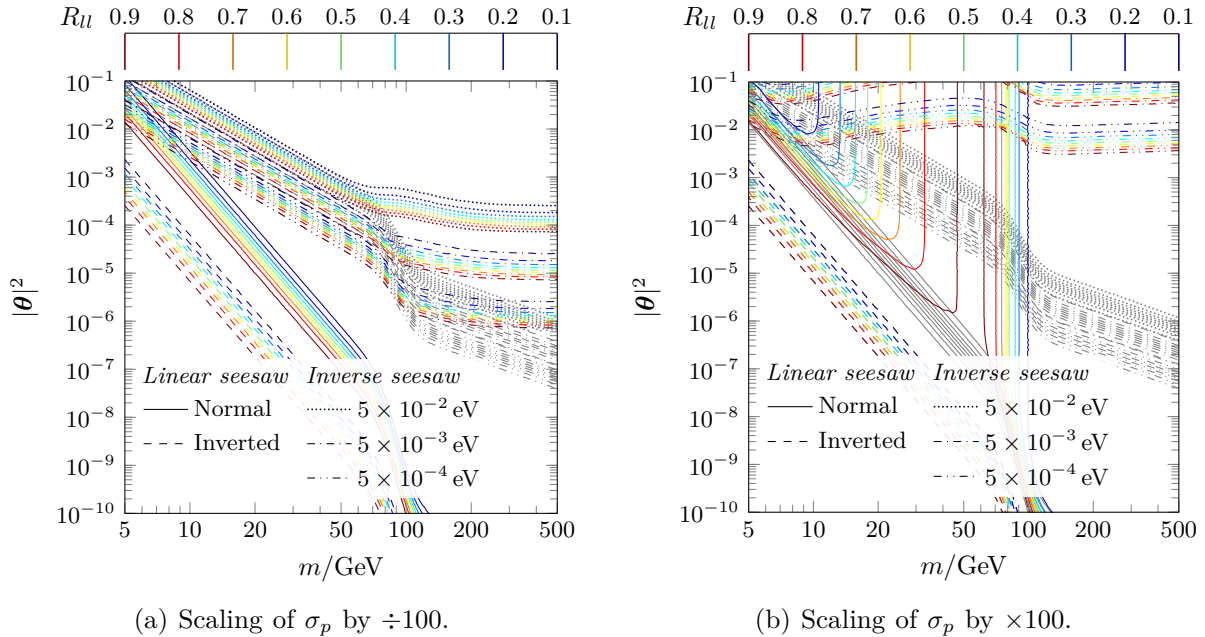
Figure 5.9: Impact of scaling the proton width σ_p on the R_{ll} ratio. The naive R_{ll} bands are depicted as grey lines, and the coloured lines represent the R_{ll} taking decoherence into account. Dividing the proton width by a factor of 100 reduces damping, as shown in panel (a). Therefore, the effects in the inverse seesaw are only significant for smaller values of the active-sterile mixing parameter. Contrary, multiplying the proton width by a factor of 100 results in enhanced damping, see panel (b). The effects in the inverse seesaw are then already significant for larger values of the active-sterile mixing parameter. With enhanced damping, decoherence becomes relevant also for the linear seesaw with normal ordered light neutrino masses. Since the mass splitting of the heavy neutrinos in the linear seesaw is fixed, the damping parameter only varies as a function of the mass. Therefore, damping is relevant for masses in the range $10\,\mathrm{GeV} \lessgtr m \lessgtr 120\,\mathrm{GeV}$, where the contours in figure 5.5a show a local minimum.

proton width σ_p. Hence the effect of this variation on the R_{ll} bands are depicted in figure 5.9. If the proton width is divided by 100, the damping becomes relevant only above mass splittings $\Delta m \gtrsim 120\,\mathrm{eV}$. This results in the deviation from the naive R_{ll} only at smaller values of the active-sterile mixing parameter in the inverse seesaw, while the linear seesaw is still not affected as depicted in figure 5.9a. On the contrary, if the proton width is multiplied by 100, the damping already becomes relevant for mass splittings $\Delta m \gtrsim 10\,\mathrm{meV}$. The R_{ll} bands of the inverse seesaw BMpoints now deviate from the naive results already for larger values of the active-sterile mixing parameter, and the effects on the linear seesaw BMpoints are also relevant, as shown in figure 5.9b. The mass splitting of the linear seesaw with inverted ordering of the light neutrino masses is still too small for decoherence to become relevant. However, for the normal ordered linear seesaw, damping must be considered. From figure 5.6b, it can be seen that the mass splitting of the normal ordered linear seesaw results in a small damping for masses $m \lesssim 10\,\mathrm{GeV}$ and $120\,\mathrm{GeV} \lesssim m$. However, for masses in the range $10\,\mathrm{GeV} \lesssim m \lesssim 120\,\mathrm{GeV}$, corresponding to the local minimum observable in figure 5.5a, decoherence becomes relevant. The largest damping is around $m \approx 50\,\mathrm{GeV}$, and thus the observed R_{ll} deviates from the naive one in this region. Since, as discussed above, coherence cannot be restored by varying the active-sterile mixing parameter as in the case of the inverse seesaw, the observed R_{ll} is close to one in this mass range for all values of the active-sterile mixing angle. Therefore, the R_{ll} bands form a pole around $m \approx 50\,\mathrm{GeV}$ as shown in figure 5.9b.

The effects of the damping parameter are crucial when reinterpreting prompt searches for LNV

signals. Regions that result in an R_{ll} close to zero for a considered model do not yield any LNV events and, thus, are not restricted by these searches. However, if damping is significant, the true value of R_{ll} might significantly deviate from the naive one, as discussed above. Therefore, decoherence effects can result in prompt searches for LNV becoming applicable in regions of the parameter space that seem unconstrained when neglecting decoherence.

5.5 Conclusion

Low-scale symmetry-protected seesaw models generically predict the appearance of pseudo-Dirac pairs of heavy neutrinos. It is usually expected that for such models, LNV is severely suppressed [72]. However, these considerations omit the crucial possibility of heavy neutrino-antineutrino oscillations ($N\overline{N}$Os) which can lead to a sizable number of LNV events if the oscillation period is shorter or of the same order as the lifetime of the heavy neutrinos [2]. In particular, for long-lived heavy neutrinos, the oscillation pattern between LNC and LNV events may be reconstructible in collider experiments [3]. Apart from $N\overline{N}$Os, decoherence can yield observable amounts of LNV by reducing the destructive interference between propagating mass eigenstates and, with it, the suppression of LNV. While this obstructs the reconstruction of the oscillation pattern, it also enhances the chances of observing LNV when the heavy neutrino's lifetime is smaller than its oscillation period. In this work, we have quantitatively studied this effect for the first time.

To this end, we have derived oscillation probabilities for $N\overline{N}$Os in the framework of QFT with external wave packets, extending previous results, see [38], with a reformulation that depends on the time difference between production and decay of the heavy neutrinos. The derivations presented here are not only technically simpler than results that depend on the distance between production and decay of the heavy neutrinos but also more readily applicable to cases where an interplay between the oscillation period and lifetime is relevant, such as the LNV over LNC event ratio R_{ll} and the reconstruction of the $N\overline{N}$O pattern, which requires a translation of the oscillations into the proper time frame of the heavy neutrinos [1, 3, 44]. The analytical calculation relies on expansions in small parameters and differentiates between the NDR and the TDR that apply for short and longer-lived particles. The numerical comparison shows that the time-dependent results for the NDR and TDR are almost identical, such that a smooth transition connects the two regimes. On the contrary, in the distance-dependent results, the differences between the two regimes are significant such that no smooth transition is possible. We have compared the time-dependent analytical results with a numeric calculation using MC data and confirmed a broad range of applicability.

In [2], we proposed using a single damping parameter λ that encodes all decoherence effects in $N\overline{N}$Os. Here, we provide the formulae necessary to calculate this damping parameter from first principles as a function of the heavy neutrinos' mean mass and mass splitting. To that end, we provide the conditions under which the dependence on the decay width Γ and, therefore, the dependence on the propagation time between the production and detection of the heavy neutrinos can be neglected. Based on our analytical results, we conjecture that the dependence of λ on m and Δm also extends to Γ larger than the ones we calculated numerically.

Furthermore, we discussed a novel time-independent contribution to the phase and derived analytical formulae for this phase shift in the no dispersion regime and transverse dispersion regime. However, in the parameter region under consideration, the phase shift can be neglected since it is either small or damping is large, which results in a suppression of the phase shift effects.

The employed framework depends on the widths of the external particles' wave packets in position space. These input parameters need to be adjusted to the described experimental situation. We have picked well-motivated values in order to present our results. Additionally, we have discussed the dependence of relevant quantities on changes in these parameters. We have also discussed possible limitations of applicability of the formalism from the JS time threshold. In our computations, we followed a conservative approach restricted to $\Gamma < \Gamma_{\mathrm{JS}} = 0.1\,\mathrm{eV}$.

We illustrate the impact of decoherence by presenting bands of R_{ll} in the $(m, |\boldsymbol{\theta}|^2)$-parameter plane and show significant deviations from the predictions when decoherence is neglected. Hence, we quantify for the first time how the transition of a coherently oscillating pseudo-Dirac pair to two independently acting Majorana particles affects the phenomenology and, therefore, the discovery prospects of symmetry-protected low-scale seesaw models.

From the results of this work, it is clear that the possibility of decoherence has to be considered when studying LNV signatures. Large decoherence not only suppresses the oscillation pattern but also disables the mechanism that suppresses LNV for a pseudo-Dirac pair. Therefore, the phenomenology of a pseudo-Dirac pair changes significantly in regions of parameter space that exhibit sizable decoherence.

Acknowledgment

Appendix 5.A   Momentum integration

The integration of the transition amplitude equation (5.3.11) over the three-momentum of the intermediate particle is performed using different techniques depending on how fast the complex phase varies over the width of the intermediate particles' wave packet. In the no dispersion regime (NDR), the phase varies slowly such that the integral is approximated around the maximum of the intermediate wave packet up to the second order in the momentum. This method is referred to as Laplace's method. If the phase varies rapidly over the intermediate wave packet, the method of stationary phase is used, where the largest contribution to the integral is obtained near the point for which the phase has an extremum. In the transverse dispersion regime (TDR), the phase varies slowly in directions transversal to the reconstructed momentum $\boldsymbol{p}_0$, while in the longitudinal direction, Laplace's method can still be used. The third regime, called the longitudinal dispersion regime (LDR), in which the method of stationary phase has to be used for all directions of the momentum $\boldsymbol{p}$, is not relevant to the phenomenology considered in this work. In the following, we treat the NDR and the TDR separately and derive an oscillation probability in each of them.

5.A.1   No dispersion regime

For short times the phase equation (5.3.7) varies slowly, as a function of the momentum, over the size of the intermediate particles' wave packet given by the EME equation (5.3.9). Thus the momentum integration can be performed using Laplace's method, where the integral is approximated around the momentum $\boldsymbol{p}_i$ for which the EME together with the decay term equation (5.3.7) is minimal. Hence a necessary condition that needs to be fulfilled in order to

apply Laplace's method is

$$\frac{\mathrm{d}}{\mathrm{d}\boldsymbol{p}}(f_i(\boldsymbol{p}) + \gamma_i(t, \boldsymbol{p}))\bigg|_{\boldsymbol{p}=\boldsymbol{p}_i} = 0\,. \tag{5.A.1}$$

While the EME yields a Gauss-like shape for the amplitude with a maximum near the reconstructed momentum, the decay term favours large momenta. Therefore we are interested in the minima of the EME. For the analytic computation, it is assumed that the impact of the decay term on the position of the maximum is negligible, which can be justified if the decay term varies slowly over the width of the intermediate particles' wave packet. The condition for this assumption to be valid is derived in equation (5.A.24). However, in the numerical computation in section 5.D, the effects of the decay term are taken into account. With the decay term neglected, the position of the maximum is expanded around the maximum of the reconstructed momentum

$$\boldsymbol{p}_i = \boldsymbol{p}_0 + \boldsymbol{p}_1\delta_i + \mathcal{O}(\delta_i^2)\,. \tag{5.A.2}$$

where the mass splitting expansion parameter and the NLO term are

$$\delta_i = \frac{m_i^2 - m_0^2}{2E_0^2}\,, \quad \boldsymbol{p}_1 = E_0\boldsymbol{\Sigma}_0^{-1}\left(\frac{\boldsymbol{u}_P}{2\sigma_{EP}^2} + \frac{\boldsymbol{u}_D}{2\sigma_{ED}^2}\right)\,, \quad \boldsymbol{u}_V = \boldsymbol{v}_V - \boldsymbol{v}_0\,, \quad V \in \{P, D\}\,, \tag{5.A.3}$$

The matrix $\boldsymbol{\Sigma}_0^{-1}$ appearing in the NLO term of the expansion is the inverse of the Hessian of the EME at LO in the momentum expansion, which is given in equation (5.A.10). Its eigenvalues can be interpreted as effective widths of the wave packet of the intermediate particle mass eigenstates in different directions, see section 5.3.3. The corresponding expansion of the energy of the mass eigenstate at the minimum of the EME around the reconstructed energy yields

$$E_i = E_0 + E_1\delta_i + \mathcal{O}(\delta_i^2)\,, \qquad E_1 = \boldsymbol{p}_1 \cdot \boldsymbol{v}_0 + E_0\,, \qquad E_i = E_i(\boldsymbol{p}_i)\,. \tag{5.A.4}$$

Finally, the expansion of the velocity of the mass eigenstate at the minimum reads

$$\boldsymbol{v}_i = \boldsymbol{v}_0 + \boldsymbol{v}_1\delta_i + \mathcal{O}(\delta_i^2)\,, \qquad \boldsymbol{v}_1 = \frac{\boldsymbol{p}_1 - \boldsymbol{v}_0E_1}{E_0}\,, \qquad \boldsymbol{v}_i = \boldsymbol{v}_i(\boldsymbol{p}_i)\,. \tag{5.A.5}$$

Expansion

In order to evaluate the momentum integral in the amplitude equation (5.3.11), each exponential term is expanded up to second order in the momentum $\boldsymbol{p}$ around the minimum of the EME at $\boldsymbol{p}_i$ resulting in a function that can be evaluated using Gaussian integration as demonstrated in section 5.A.1.

Energy-momentum envelope   The expansion of the EME equation (5.3.9) around its minimum at $\boldsymbol{p}_i$ results in

$$f_i(\boldsymbol{p}) = f_i + \frac{1}{2}(\boldsymbol{p} - \boldsymbol{p}_i)^\mathsf{T}\boldsymbol{\Sigma}_i(\boldsymbol{p} - \boldsymbol{p}_i) + \mathcal{O}(|\boldsymbol{p} - \boldsymbol{p}_i|^3)\,, \tag{5.A.6}$$

where the linear term vanishes since the evaluation is performed at the minimum. The constant term and the Hessian of the EME at the minimum read

$$f_i = f_i(\boldsymbol{p}_i)\,, \qquad\qquad \boldsymbol{\Sigma}_i = \boldsymbol{\Sigma}_0 + \mathcal{O}(\delta_i)\,, \tag{5.A.7}$$

where the constant term to LO in the mass splitting expansion defines the mass width

$$f_i = f_1\delta_i^2 + \mathcal{O}(\delta_i^4)\,, \qquad f_1 = \left|\frac{\boldsymbol{p}_1}{2\sigma_{\boldsymbol{p}P}}\right|^2 + \left[\frac{e_{1P}}{2\sigma_{EP}}\right]^2 + (P \to D)\,, \qquad \sigma_m := \frac{E_0}{2\sqrt{f_1}} \tag{5.A.8}$$

where

$$e_{iV} := e_{iV}(\boldsymbol{p}_i) = e_{1V}\delta_i \,, \qquad\qquad e_{1V} := E_1 - \boldsymbol{p}_1 \cdot \boldsymbol{v}_V \,. \qquad (5.\text{A}.9)$$

and the LO term in the mass splitting expansion of the Hessian is

$$\boldsymbol{\Sigma}_0 = \frac{\mathbb{1}}{2\sigma_{\boldsymbol{p}P}^2} + \frac{\boldsymbol{u}_P \otimes \boldsymbol{u}_P}{2\sigma_{EP}^2} + (P \to D)\,. \qquad (5.\text{A}.10)$$

From the inequality equation (5.2.12) follows that the Hessian can be estimated to take values within

$$\frac{1}{2\sigma_{\boldsymbol{p}}^2} \lessapprox |\boldsymbol{\Sigma}_i| \lessapprox \frac{1}{2\sigma_E^2} \,, \qquad (5.\text{A}.11)$$

where $|\boldsymbol{\Sigma}_i|$ denotes that the considered inequality has to hold for all eigenvalues of $\boldsymbol{\Sigma}_i$.

Jacob-Sachs integration Solving the energy integral via the JS theorem as demonstrated in section 5.3.1 introduces the complex pole energy equation (5.3.2). The dependence on the mass eigenstate energy equation (5.3.4) can then be used to estimate the effects of the decay width expansion parameter equation (5.3.5) on the EME

$$f_i(E_i'(\boldsymbol{p}), \boldsymbol{p}) = \left[\frac{e_P(E_i'(\boldsymbol{p}), \boldsymbol{p})}{2\sigma_{EP}}\right]^2 + \dots \,, \qquad (5.\text{A}.12)$$

where

$$e_P(E_i'(\boldsymbol{p}), \boldsymbol{p}) = \sqrt{1 - 2\,\mathrm{i}\,\epsilon_i(\boldsymbol{p})}\sqrt{|\boldsymbol{p}|^2 + m_i^2} - E_0 - (\boldsymbol{p} - \boldsymbol{p}_0) \cdot \boldsymbol{v}_P \,. \qquad (5.\text{A}.13)$$

and the ellipses denote terms that do not depend on the decay width expansion parameter, and for simplicity, we only consider the term at production, keeping in mind that the same arguments hold for the equivalent term at detection. Furthermore, assuming that the energy and mass splitting expansion parameters are of the same order, the constant term and the Hessian of the momentum expanded EME equation (5.A.7) are to LO

$$f_i = \left(\frac{\delta_i - \mathrm{i}\,\epsilon_i(\boldsymbol{p})}{2\sigma_{EP}} E_0\right)^2 + \dots \,, \qquad \boldsymbol{\Sigma}_i = \left(\frac{\boldsymbol{u}_P}{2\sigma_{EP}}\right)^2 + \mathcal{O}(\delta_i) + \mathcal{O}\big(\epsilon_i^2(\boldsymbol{p})\big) + \dots \,. \qquad (5.\text{A}.14)$$

The effects of the decay width expansion parameter on the Hessian are subleading and can therefore be neglected. While the effects on the EME are relevant, the term itself does only contribute to the damping of the amplitude equation (5.3.11) if it differs greatly between different mass eigenstates. This is due to the normalisation discussed in section 5.3.5. The effects of the decay width expansion parameter are therefore neglected in the analytical derivation by using equation (5.3.9) while they are taken into account in the numerical calculations in section 5.D.

Phase The expansion of the phase equation (5.3.7) around the minimum of the EME results in

$$\phi_i(t, \boldsymbol{x}, \boldsymbol{p}) = \phi_i(t, \boldsymbol{x}) + \boldsymbol{\Delta}_i(t, \boldsymbol{x}) \cdot (\boldsymbol{p} - \boldsymbol{p}_i) + \frac{1}{2}(\boldsymbol{p} - \boldsymbol{p}_i)^\mathsf{T} R_i(t)\,(\boldsymbol{p} - \boldsymbol{p}_i) + \mathcal{O}\big(|\boldsymbol{p} - \boldsymbol{p}_i|^3\big)\,, \quad (5.\text{A}.15)$$

where the constant term, the linear coefficient, the Hessian, and the velocity of the i-th mass eigenstate are

$$\phi_i(t, \boldsymbol{x}) = \phi_i(t, \boldsymbol{x}, \boldsymbol{p}_i)\,, \quad \boldsymbol{\Delta}_i(t, \boldsymbol{x}) = \boldsymbol{v}_i t - \boldsymbol{x}\,, \quad R_i(t) = \frac{\mathbb{1} - \boldsymbol{v}_i \otimes \boldsymbol{v}_i}{E_i} t\,, \quad \boldsymbol{v}_i = \frac{\boldsymbol{p}_i}{E_i}\,. \quad (5.\text{A}.16)$$

Since the inverse of Σ_i can be interpreted as an effective width of the intermediate wave packet equations (5.3.20) and (5.3.26), it can be used to quantify the condition that the phase varies slowly over the width of the intermediate wave packet. Replacing $|\boldsymbol{p} - \boldsymbol{p}_i|^2$ in the expansion series of the phase equation (5.A.15) with $2|\Sigma_i|^{-1}$ and requiring that the linear and quadratic terms are small results in

$$2|\boldsymbol{\Delta}_i(t,\boldsymbol{x})|^2 \ll |\Sigma_i| \,, \qquad\qquad |R_i(t)| \ll |\Sigma_i| \,, \qquad\qquad (5.A.17)$$

These conditions can be approximated to read

$$2|\boldsymbol{v}_i t - \boldsymbol{x}|^2 \ll |\Sigma_0| \,, \qquad\qquad \frac{|\mathbb{1} - \boldsymbol{v}_i \otimes \boldsymbol{v}_i|}{E_i} t \ll |\Sigma_0| \,. \qquad\qquad (5.A.18)$$

Since the averaging over the distance (or time) in a later step ensures that $\boldsymbol{v}_i t \approx \boldsymbol{x}$, the linear condition is automatically satisfied. The quadratic condition can be approximated as

$$\frac{t}{E_i} \ll \frac{1}{2\sigma_{\boldsymbol{p}}^2} \,, \qquad\qquad (5.A.19)$$

where the eigenvalue of Σ_0 containing $\sigma_{\boldsymbol{p}}^2$ is used since it imposes the most restrictive condition, see equation (5.3.22). For the same reason, the velocity-dependent parts in the contribution from the phase can be neglected. This condition defines the short-time threshold up to which this integration method is valid. It is given by

$$t_i^{\text{short}} = t^{\text{short}} + \mathcal{O}(\delta_i) = E_i |\Sigma_i|_{\text{smallest}} \,, \qquad t^{\text{short}} = \frac{E_0}{2\sigma_{\boldsymbol{p}}^2} \,, \qquad t \lesssim t^{\text{short}} \,, \qquad (5.A.20)$$

and it is usually sufficient to work with the LO approximation.

Decay term The decay term equation (5.3.7) is also expanded up to second order in its momenta around the minimum of the EME yielding

$$\gamma_i(t,\boldsymbol{p}) = \gamma_i(t) - \boldsymbol{F}_i \cdot (\boldsymbol{p} - \boldsymbol{p}_i) + \frac{1}{2}(\boldsymbol{p} - \boldsymbol{p}_i)^{\mathsf{T}} W_i(t) \, (\boldsymbol{p} - \boldsymbol{p}_i) + \mathcal{O}\big(|\boldsymbol{p} - \boldsymbol{p}_i|^3\big) \,, \qquad (5.A.21)$$

where the constant term, the linear coefficient, the Hessian and the parameter appearing in equation (5.3.5) evaluated at the minimum of the EME are given by

$$\gamma_i(t) = \gamma_i t \,, \quad \boldsymbol{F}_i(t) = \boldsymbol{v}_i \epsilon_i t \,, \quad W_i(t) = \frac{3\boldsymbol{v}_i \otimes \boldsymbol{v}_i - \mathbb{1}}{E_i} \epsilon_i t \,, \quad \gamma_i = \frac{m_i \Gamma_i}{2 E_i} \,, \quad \epsilon_i = \frac{\gamma_i}{E_i} \,. \quad (5.A.22)$$

Similar to the conditions appearing in the evaluation of the phase equation (5.A.17), two conditions can be derived, ensuring that the decay term varies slowly over the width of the wave packet

$$2|\boldsymbol{F}_i(t)|^2 \ll |\Sigma_i| \,, \qquad\qquad |W_i(t)| \ll |\Sigma_i| \,. \qquad\qquad (5.A.23)$$

For times earlier than the short-time threshold equation (5.A.20), these conditions become

$$|\boldsymbol{p}_i| \epsilon_i \ll \sigma_{\boldsymbol{p}} \,, \qquad\qquad \epsilon_i \ll \frac{1}{|3\boldsymbol{v}_i \otimes \boldsymbol{v}_i - \mathbb{1}|} \,. \qquad\qquad (5.A.24)$$

The linear condition holds as long as the decay width is of the same order or smaller as the momentum width, while the quadratic condition is satisfied for the assumptions used in the decay width expansion during the JS integration in section 5.3.1.

Integration

The momentum integral can then be evaluated using a standard technique for multidimensional Gaussian integrals over the coordinates $\boldsymbol{x}$ with a symmetric positive definite matrix A and a linear term $\boldsymbol{b}$

$$\int [\mathrm{d}^3 \boldsymbol{x}] \exp\left[\boldsymbol{b} \cdot \boldsymbol{x} - \frac{1}{2} \boldsymbol{x}^{\mathsf{T}} A \boldsymbol{x} \right] = \exp\left[\frac{1}{2} \boldsymbol{b}^{\mathsf{T}} A^{-1} \boldsymbol{b} \right] . \tag{5.A.25}$$

The vector $\boldsymbol{b}$ contains the linear order coefficients appearing in the momentum expansion of the phase equation (5.A.15) and the decay term equation (5.A.22) and reads

$$\boldsymbol{b} = \mathrm{i}\, \boldsymbol{\Delta}_i(t, \boldsymbol{x}) + \boldsymbol{F}_i(t) = \mathrm{i}\, \boldsymbol{\Delta}_i(t, \boldsymbol{x}) + \mathcal{O}(\epsilon_i) \,, \tag{5.A.26}$$

For the analytical derivation, we neglect the correction from the decay term and proceed solely with the linear coefficient from the expansion of the phase around the minimum of the energy-momentum integral. In the numerical calculation presented in section 5.D the minimum $\boldsymbol{p}_i$ is computed for the sum of the EME and the decay term, such that the linear contribution $\boldsymbol{F}_i(t)$ is absent all together. The matrix A collects the Hessian matrices resulting from the momentum expansion of the EME equation (5.A.7), the phase equation (5.A.16), and the decay term equation (5.A.22) around the minimum of the EME and reads

$$A = -\Sigma_i - W_i(t) - \mathrm{i}\, R_i(t) = -\Sigma_i + \mathcal{O}\left(\frac{t}{t^{\mathrm{short}}} \right) . \tag{5.A.27}$$

For times earlier than the short-time threshold equation (5.A.20), it is justified to approximate this sum with just the contribution from the EME, see the conditions equations (5.A.18) and (5.A.23).

Hence the Hessian from the EME expansion equation (5.A.7) together with the linear term of the phase expansion equation (5.A.15) integrated over the momentum using the Gaussian integral equation (5.A.25) yield the spacetime envelope (STE)

$$F_i(t, \boldsymbol{x}) := \frac{1}{2} \boldsymbol{\Delta}_i^{\mathsf{T}}(t, \boldsymbol{x}) \Sigma_i^{-1} \boldsymbol{\Delta}_i(t, \boldsymbol{x}) \,. \tag{5.A.28}$$

For a given time and velocity, this term leads to an exponential damping of the transition amplitude for values of $\boldsymbol{x}$ *far* from $\boldsymbol{v}_i t$. Here, *far* is defined by the eigenvalues of Σ_i. We have explicitly discussed the effects of the decay width expansion parameter after equation (5.A.12) and found the STE to agree with [38].

The oscillation amplitude in the NDR after momentum integration is therefore given by

$$\mathcal{A}_i(t, \boldsymbol{x}) \propto \exp[-f_i - \gamma_i(t) - F_i(t, \boldsymbol{x}) - \mathrm{i}\, \phi_i(t, \boldsymbol{x})] \,. \tag{5.A.29}$$

where the terms in the exponential are the constant EME equation (5.A.7), the time dependent decay term equation (5.A.22), the spacetime dependent STE equation (5.A.28), and the spacetime dependent phase equation (5.A.16).

5.A.2 Transverse dispersion regime

For times later than the short-time threshold equation (5.A.20), derived in the previous section, the oscillations are fast compared to the width of the wave packet such that Laplace's method is no longer the preferred method for evaluating the momentum integral. However, this argument depends on the direction of the heavy neutrino momentum. The second order term of the phase

equation (5.A.15) yields a contribution $|\boldsymbol{p}|^2 t/E$ for momenta orthogonal to $\boldsymbol{v}_i$, while momenta in the direction of $\boldsymbol{v}_i$ obtain an additional Lorentz contraction factor that leads to $(1 - \boldsymbol{v}_i^2)|\boldsymbol{p}|^2 t/E$. Since at LO $\boldsymbol{v}_i = \boldsymbol{v}_0$, this factor slows down the oscillations in the direction of the reconstructed momentum. Laplace's method is therefore still preferred in the direction along $\boldsymbol{p}_0$, while in directions orthogonal to it, the method of stationary phase is used.

Stationary phase

The linear term of the expanded phase equation (5.A.15) averages oscillations to zero for momenta transversal to $\boldsymbol{x}$. Therefore it can be assumed that $\boldsymbol{p}$ is parallel to $\boldsymbol{x}$. Additionally, the EME requires that $\boldsymbol{p}$ is parallel to $\boldsymbol{p}_0$, which yields that $\boldsymbol{x}$ has to be parallel to $\boldsymbol{p}_0$. Assuming that $\boldsymbol{p}_0$ is in the z direction the method of stationary phase can be used for $\boldsymbol{x}|_x$ and $\boldsymbol{x}|_y$ which yields

$$\frac{\partial}{\partial p_x}\phi(t, \boldsymbol{x}, \boldsymbol{p}) = \frac{\partial}{\partial p_y}\phi(t, \boldsymbol{x}, \boldsymbol{p}) = 0\,, \tag{5.A.30}$$

resulting in $p_x = p_y = 0$. Using those, the argument of the exponential of the amplitude equation (5.2.1) does not depend on p_x and p_y anymore such that only the integration over $\widehat{p} = \boldsymbol{p}|_z$ is left. This integration is done using Laplace's method, as in section 5.A.1.

The argument of the EME equation (5.2.5) can then be expressed as

$$f_i(E_i(\widehat{p}), \widehat{p}) = \left(\frac{\widehat{p} - \widehat{p}_0}{2\sigma_{\boldsymbol{p}P}}\right)^2 + \left(\frac{e_{iP}(\widehat{p})}{2\sigma_{EP}}\right)^2 + (P \to D)\,, \tag{5.A.31}$$

where

$$e_{iV}(\widehat{p}) = E_i(\widehat{p}) - E_0 - (\widehat{p} - \widehat{p}_0)\widehat{v}_V\,. \tag{5.A.32}$$

Similar to the NDR, the phase, the EME, and the decay term are all expanded around the momentum $\widehat{p}_i$ for which the EME is minimal. The effects of the decay term onto the position of the maximum are neglected in the analytical derivation, and the exact conditions for this approximation to hold are given in equation (5.A.46). The position of the maximum up to linear order in the mass splitting expansion parameter equation (5.A.3) is

$$\widehat{p}_i = \widehat{p}_0 + \widehat{p}_1\delta_i + \mathcal{O}(\delta_i^2)\,, \qquad \widehat{p}_1 = \frac{E_0}{\widehat{\Sigma}_0}\left(\frac{\widehat{u}_P}{2\sigma_{EP}^2} + \frac{\widehat{u}_D}{2\sigma_{ED}^2}\right)\,, \qquad \widehat{u}_V := \widehat{v}_V - \widehat{v}_0\,, \tag{5.A.33}$$

the mass splitting expansion of the mass eigenstate energy reads

$$E_i = E_0 + E_1\delta_i + \mathcal{O}(\delta_i^2)\,, \qquad E_1 = E_0 + \widehat{p}_1\widehat{v}_0\,, \qquad E_i = E_i(\widehat{p}_i)\,, \tag{5.A.34}$$

and the mass splitting expansion of the mass eigenstate velocity is

$$\widehat{v}_i = \widehat{v}_0 + \widehat{v}_1\delta_i + \mathcal{O}(\delta_i^2)\,, \qquad \widehat{v}_1 = \frac{\widehat{p}_1 - E_1\widehat{v}_0}{E_0}\,, \qquad \widehat{v}_i = \widehat{v}_i(\widehat{p}_i)\,. \tag{5.A.35}$$

The effects of the decay width expansion parameter are neglected here for the same reasons as in section 5.A.1.

Expansion

Just as in the NDR, the terms in the exponent of the amplitude equation (5.3.11) need to be expanded up to second order in the momentum in order to perform a Gaussian integration in section 5.A.2.

Energy-momentum envelope   The expansion of the EME equation (5.A.31) around the momentum of the minimum is given by

$$f_i(E_i(\widehat{p}), \widehat{p}) = f_i + \frac{1}{2}\widehat{\Sigma}_i(\widehat{p} - \widehat{p}_i)^2 + \mathcal{O}\left(|\widehat{p} - \widehat{p}_i|^3\right), \tag{5.A.36}$$

where the linear term vanishes since the expansion is evaluated at the minimum, while the constant term and the Hessian are given by

$$f_i = f_1\delta_i^2 + \mathcal{O}\left(\delta_i^4\right) = f_i(E_i, \widehat{p}_i), \qquad\qquad \widehat{\Sigma}_i = \widehat{\Sigma}_0 + \mathcal{O}(\delta_i), \tag{5.A.37}$$

and their LO contributions in the mass splitting expansion are given by

$$f_1 = \left(\frac{\widehat{p}_1}{2\sigma_{\widehat{p}P}}\right)^2 + \left(\frac{E_1 - \widehat{p}_1\widehat{v}_P}{2\sigma_{EP}}\right)^2 + (P \to D), \quad \widehat{\Sigma}_0 = \frac{1}{2\sigma_{\boldsymbol{p}P}^2} + \frac{\widehat{u}_P^2}{2\sigma_{EP}^2} + (P \to D). \tag{5.A.38}$$

Phase   The expansion of the phase equation (5.3.7) around the momentum of the minimum of the EME yields

$$\phi_i(t, \widehat{x}, \widehat{p}) = \phi_i(t, \widehat{x}) + \widehat{\Delta}_i(t, \widehat{x})(\widehat{p} - \widehat{p}_i) + \frac{1}{2}\widehat{R}_i(t)(\widehat{p} - \widehat{p}_i)^2 + \mathcal{O}\left(|\widehat{p} - \widehat{p}_i|^3\right), \tag{5.A.39}$$

where the constant term, the linear coefficient, the Hessian, and the velocity of the mass eigenstate are given by

$$\phi_i(t, \widehat{x}) = \phi_i(t, \widehat{x}, \widehat{p}_i), \qquad \widehat{\Delta}_i(t, \widehat{x}) = \widehat{v}_i t - \widehat{x}, \qquad \widehat{R}_i(t) = \frac{m_i^2}{E_i^3}t, \qquad \widehat{v}_i = \frac{\widehat{p}_i}{E_i}. \tag{5.A.40}$$

Similar to the case of the NDR, a time threshold can be obtained by requiring that the phase varies slowly over the width of the wave packet. The wave packet width is approximated by $\widehat{\Sigma}_i^{-1/2}$ and used to reexpress the momentum deviations. The conditions resulting from the requirement that the linear and quadratic terms are small are

$$2\widehat{\Delta}_i^2(t, \widehat{x}) \ll \widehat{\Sigma}_i, \qquad\qquad \widehat{R}_i(t) \ll \widehat{\Sigma}_i. \tag{5.A.41}$$

The linear condition is ensured by the distance average performed in the next section, while the quadratic condition defines the long-time threshold. A time threshold independent of the mass eigenstates can be defined by approximating it at LO in the mass splitting expansion equation (5.A.2), leading to the validity range of the TDR

$$t_i^{\text{long}} = t^{\text{long}} + \mathcal{O}(\delta_i) = \widehat{\Sigma}_i\frac{E_i^3}{m_i^2}, \qquad t^{\text{long}} := \widehat{\Sigma}_0\frac{E_0^3}{m_0^2}, \qquad t^{\text{short}} \lessapprox t \lessapprox t^{\text{long}}. \tag{5.A.42}$$

Decay term   The expansion of the decay term equation (5.3.7) is the same as in the NDR equation (5.A.21) where all vector quantities are replaced by their corresponding longitudinal component.

$$\gamma_i(t, \widehat{p}) = \gamma_i(t) - \widehat{F}_i \cdot (\widehat{p} - \widehat{p}_i) + \frac{1}{2}(\widehat{p} - \widehat{p}_i)^{\mathsf{T}}\widehat{W}_i(t)\,(\widehat{p} - \widehat{p}_i) + \mathcal{O}\left(|\widehat{p} - \widehat{p}_i|^3\right). \tag{5.A.43}$$

The constant term, the linear coefficient, the Hessian and the terms appearing in equation (5.3.5) are given by

$$\gamma_i(t) = \gamma_i t, \qquad \gamma_i = \frac{m_i \Gamma_i}{2E_i}, \qquad \widehat{F}_i(t) = \widehat{v}_i\epsilon_i t, \qquad \widehat{W}_i(t) = \frac{3\widehat{v}_i^2 - 1}{E_i}\epsilon_i t, \qquad \epsilon_i = \frac{\gamma_i}{E_i}. \tag{5.A.44}$$

The conditions for the decay term to vary slowly over the width of the neutrino wave packet read

$$2\widehat{F}_i^2(t) \ll \widehat{\Sigma}_i \,, \qquad\qquad \widehat{W}_i(t) \ll \widehat{\Sigma}_i \,. \qquad\qquad (5.\text{A}.45)$$

assuming $t \lesssim t_i^{\text{long}}$, these conditions reduce to

$$\epsilon_i \widehat{p}_i \frac{E_i^2}{m_i^2} \ll \sigma_E \,, \qquad\qquad \left(3\widehat{v}_i^2 - 1\right)\epsilon_i \ll \frac{m_i^2}{E_i^2} \,. \qquad\qquad (5.\text{A}.46)$$

Similar to the situation in the NDR equation (5.A.24), the quadratic condition is automatically satisfied. The linear condition requires the decay width to be of the same order or smaller than the effective momentum width of the wave packet, which is typically of the order of the energy width σ_E and thus much smaller compared to the width in the NDR. Additionally, the factor E_i/m_i can result in a violation of the condition for ultra-relativistic particles. This reflects the fact that for such particles, the TDR is valid up to arbitrarily large times, such that eventually, the decay term becomes important. In the numerical estimation of the damping, the effect of the decay term is taken into account.

Integration

The integral in the transition amplitude equation (5.3.11) can be solved using the general result equation (5.A.25) where the vector $\boldsymbol{b}$, now scalar, contains the first order terms from the expansion of the phase equation (5.A.39) and the decay term equation (5.A.43) and reads

$$b = \mathrm{i}\,\widehat{\Delta}_i(t,\widehat{x}) + \widehat{F}_i(t) = \mathrm{i}\,\widehat{\Delta}_i(t,\widehat{x}) + \mathcal{O}(\epsilon_i) \,. \qquad\qquad (5.\text{A}.47)$$

In the following, the decay width expansion parameter correction is neglected for the analytical derivation but taken into account for the numerical calculation. The Hessians resulting from the momentum expansion of the EME equation (5.A.36), the phase equation (5.A.39), and the decay term equation (5.A.43) are collected in A which is now a scalar and reads

$$A = -\widehat{\Sigma}_i - \widehat{W}_i(t) - \mathrm{i}\,\widehat{R}_i(t) = -\widehat{\Sigma}_i + \mathcal{O}\!\left(\frac{t}{t^{\text{long}}}\right) \,. \qquad\qquad (5.\text{A}.48)$$

For times earlier than the long-time threshold equation (5.A.42), the LO contribution is given by the Hessian of the EME, see conditions equations (5.A.41) and (5.A.45). For the numerical results, the contribution from the Hessian of the phase and the decay term are taken into account.

The integration equation (5.A.25) over the momentum yields the STE

$$F_i(t,\widehat{x}) := \frac{\widehat{\Delta}_i^2(t,\widehat{x})}{2\widehat{\Sigma}_i(t)} \,, \qquad\qquad (5.\text{A}.49)$$

and the amplitude equation (5.2.1) after integration is given by

$$\mathcal{A}_i(t,\widehat{x}) \propto \exp[-f_i - \gamma_i(t) - F_i(t,\widehat{x}) - \mathrm{i}\,\phi_i(t,\widehat{x})] \,, \qquad\qquad (5.\text{A}.50)$$

where the terms in the exponent are the EME equation (5.A.37), the decay term equation (5.A.44), the STE equation (5.A.49), and the phase equation (5.A.40).

Appendix 5.B Distance integration

In order to obtain an oscillation probability, the amplitudes for different mass eigenstates are coherently summed over

$$\mathcal{P}(t, \boldsymbol{x}) \propto \sum_{ij} \mathcal{A}_i(t, \boldsymbol{x}) \mathcal{A}_j^*(t, \boldsymbol{x}) \,. \tag{5.B.1}$$

An average over the oscillation distance is performed to obtain a formula dependent on the time. For the NDR as well as for the TDR the only distance-dependent components in the amplitudes equations (5.A.29) and (5.A.50) are the phases equations (5.A.16) and (5.A.40) and the STEs equations (5.A.28) and (5.A.49). Since the STE restricts the values of t and $\boldsymbol{x}$ to a range, similar to how the EME equation (5.2.5) restricts the values of p and E, the probability is expanded up to second order around $\boldsymbol{x}_{ij}$, the position of the minimum of the STE, before the resulting Gauss-like integral is evaluated.

Typically, neither the oscillation distance $\boldsymbol{x}$ nor the oscillation time t are measured with perfect precision. Therefore, the oscillation probability equation (5.B.1) is either integrated over a span of time, as in [38], or over a region of space in order to address the experimental uncertainty. In the following, the second possibility is employed, which yields an oscillation probability as a function of time. The distance-integrated oscillation probability reads

$$\mathcal{P}(t) \propto \int [\mathrm{d}\boldsymbol{x}]_{\boldsymbol{x}_0 - \Delta\boldsymbol{x}}^{\boldsymbol{x}_0 + \Delta\boldsymbol{x}} \mathcal{P}(t, \boldsymbol{x}) \,, \tag{5.B.2}$$

where $\Delta\boldsymbol{x}$ labels the experimental uncertainty in determining the distance travelled by the intermediate particle between its production and decay. This distance has to be larger than the width of the intermediate particle in spacetime, which describes the minimal uncertainty due to the wave packet nature of the intermediate particle. Due to the exponential damping stemming from the STEs equations (5.A.28) and (5.A.49) for values $|\boldsymbol{x} - \boldsymbol{x}_0| \gtrsim |\boldsymbol{\Sigma}_0|$, the distance integration can be taken to infinity $\Delta\boldsymbol{x} \to \infty$.

5.B.1 No dispersion regime

Since the oscillation probability equation (5.B.1) depends on the absolute value square of the transition amplitude, the EME equation (5.A.7) and equation (5.A.22) need to be summed

$$f_{ij} = f_i + f_j = f_1(\delta_i^2 + \delta_j^2) + \mathcal{O}(\delta_i^4) \,, \qquad \gamma_{ij}(t) = \gamma_i(t) + \gamma_j(t) = (\gamma_i + \gamma_j)t \,. \tag{5.B.3}$$

The same holds true for the STE equation (5.A.28)

$$F_{ij}(t, \boldsymbol{x}) := F_i(t, \boldsymbol{x}) + F_j(t, \boldsymbol{x}) \,, \tag{5.B.4}$$

Since dispersion effects are neglected in the NDR, the STE can be approximated by its LO term in the mass splitting expansion

$$F_{ij}(t, \boldsymbol{x}) = F_0(t, \boldsymbol{x}) + \mathcal{O}(\delta_i) \,, \quad F_0(t, \boldsymbol{x}) = \boldsymbol{\Delta}_0^{\mathsf{T}}(t, \boldsymbol{x}) \boldsymbol{\Sigma}_0^{-1} \boldsymbol{\Delta}_0(t, \boldsymbol{x}) \,, \quad \boldsymbol{\Delta}_0(t, \boldsymbol{x}) = \boldsymbol{v}_0 t - \boldsymbol{x} \,. \tag{5.B.5}$$

Since it is quadratic in the spacial coordinates, there are no constant or linear terms. The position of the minimum of the STE is thus at LO given by

$$\boldsymbol{x}_{ij}(t) = \boldsymbol{x}_0(t) + \mathcal{O}(\delta_i) \,, \qquad\qquad \boldsymbol{x}_0(t) = \boldsymbol{v}_0 t \,. \tag{5.B.6}$$

Expansion   The expansion of the STE in $\boldsymbol{x}$ around $\boldsymbol{x}_{ij}(t)$ reads at LO in the mass splitting expansion

$$F_0(t, \boldsymbol{x}) = (\boldsymbol{x} - \boldsymbol{x}_0(t))^{\mathsf{T}} \Sigma_0^{-1} (\boldsymbol{x} - \boldsymbol{x}_0(t)) + \mathcal{O}(\delta_i). \tag{5.B.7}$$

Since dispersion is neglected, there is no constant term. The phase equation (5.A.15) is rewritten in terms of the deviation from the maximum in position space $\boldsymbol{x} - \boldsymbol{x}_{ij}(t)$ yielding

$$\phi_i(t, \boldsymbol{x}) = \phi_i(t) - \boldsymbol{p}_i \cdot (\boldsymbol{x} - \boldsymbol{x}_{ij}(t)), \qquad \phi_i(t) = E_i t - \boldsymbol{p}_i \cdot \boldsymbol{x}_{ij}(t). \tag{5.B.8}$$

Since the oscillation probability equation (5.B.1) is proportional to the absolute value square of the transition amplitude, the phase difference

$$\phi_{ij}(t, \boldsymbol{x}) = \phi_i(t, \boldsymbol{x}) - \phi_j(t, \boldsymbol{x}) = \phi_{ij}(t) - \boldsymbol{p}_{ij} \cdot (\boldsymbol{x} - \boldsymbol{x}_{ij}(t)), \tag{5.B.9}$$

needs to be considered. The constant term encodes the phase difference in time, while the linear coefficient consists of a momentum difference

$$\phi_{ij}(t) := \phi_i(t) - \phi_j(t) = E_{ij} t - \boldsymbol{p}_{ij} \cdot \boldsymbol{x}_{ij}(t), \qquad E_{ij} = E_i - E_j, \qquad \boldsymbol{p}_{ij} = \boldsymbol{p}_i - \boldsymbol{p}_j. \tag{5.B.10}$$

Using the mass splitting expansion of the energy equation (5.A.4) and momentum equation (5.A.2) yields

$$E_{ij} = (E_0 - \boldsymbol{v}_0 \cdot \boldsymbol{p}_1)\delta_{ij} + \mathcal{O}(\delta_i^2), \qquad \boldsymbol{p}_{ij} = \boldsymbol{p}_1 \delta_{ij} + \mathcal{O}(\delta_i^2), \qquad \delta_{ij} := \delta_i - \delta_j, \tag{5.B.11}$$

and the appearing difference in the mass splitting expansion parameter equation (5.A.3) can be approximated to be

$$\delta_{ij} = \frac{m_i^2 - m_j^2}{2E_0^2} = \frac{m_{ij} m_0}{E_0^2} + \mathcal{O}\left(\frac{m_{ij}^2}{E_0^2}\right), \qquad m_{ij} = m_i - m_j. \tag{5.B.12}$$

It is used that the reconstructed mass m_0 cannot be far from the mean of the mass eigenstate masses m, since otherwise, it is not possible to have $\boldsymbol{p}_i \approx \boldsymbol{p}_0$ and $E_i \approx E_0$ for both mass eigenstates at the same time, and thus one of the two f_i terms in the amplitude equation (5.A.29) would lead to large damping of oscillations. Therefore, the phase difference is at LO in terms of the proper time

$$\phi_{ij}(t) = m_{ij} \tau(t) + \mathcal{O}\left(\delta_i^2, \frac{m_{ij}^2}{E_0^2}\right), \qquad \tau(t) = \frac{m_0}{E_0} t. \tag{5.B.13}$$

Integration   The integral equation (5.B.2) can be evaluated as a Gaussian integral, using relation equation (5.A.25) with the linear term from the phase expansion equation (5.B.10) and the Hessian from the STE expansion equation (5.B.7)

$$\boldsymbol{b} = \boldsymbol{p}_{ij}, \qquad A = 2\Sigma_0^{-1}, \tag{5.B.14}$$

resulting in the time-independent localisation term

$$\Lambda_{ij} = \frac{1}{4} \boldsymbol{p}_{ij}^{\mathsf{T}} \Sigma_0 \boldsymbol{p}_{ij} + \mathcal{O}(\delta_i^3). \tag{5.B.15}$$

The transition amplitude after this distance integration is, therefore,

$$\mathcal{P}(t) \propto \sum_{ij} \exp\left[-\lambda'_{ij}(t) - \mathrm{i}\, \phi_{ij}(t)\right], \qquad \lambda'_{ij}(t) = f_{ij} + \Lambda_{ij} + \gamma_{ij}(t), \tag{5.B.16}$$

where the STE and the decay term are given by equation (5.B.3), the phase is given by equation (5.B.13), and the localisation term is given by equation (5.B.15).

5.B.2 Transverse dispersion regime

The calculations for the TDR are very similar to the ones described in section 5.B.1. However, compared to the NDR dispersion is not neglected, and therefore, the approximation $v_i \approx v_j$ does not apply, which leads to a separation of wave packets of different mass eigenstates over time. The sum of the EME equation (5.A.37) and the decay terms equation (5.A.44) are

$$f_{ij} = f_i + f_j = f_1(\delta_i^2 + \delta_j^2) + \mathcal{O}(\delta_i^4) , \qquad \gamma_{ij}(t) = \gamma_i(t) + \gamma_j(t) = (\gamma_i + \gamma_j)t , \qquad (5.B.17)$$

The distance average is performed by extending the terms in the exponent of the transition amplitude equation (5.A.50) around the minimum of the sum of the STEs equation (5.A.49) of the two mass eigenstates appearing in the oscillation probability

$$F_{ij}(t, \widehat{x}) = F_i(t, \widehat{x}) + F_j(t, \widehat{x}) . \qquad (5.B.18)$$

The minimum is given at the position

$$\widehat{x}_{ij}(t) = \frac{\widehat{\Sigma}_i(t)\widehat{v}_j + \widehat{\Sigma}_j(t)\widehat{v}_i}{\widehat{\Sigma}_i(t) + \widehat{\Sigma}_j(t)}t = \frac{\widehat{v}_i + \widehat{v}_j}{2}t + \mathcal{O}(\delta_i) , \qquad (5.B.19)$$

Expansion   The expansion of the STE yields

$$F_{ij}(t, \widehat{x}) = F_{ij}(t) + \frac{1}{2}Z_{ij}(\widehat{x} - \widehat{x}_{ij}(t))^2 + \mathcal{O}(|\widehat{x} - \widehat{x}_{ij}(t)|^3) . \qquad (5.B.20)$$

where the constant term and the Hessian are

$$F_{ij}(t) = \frac{v_{ij}^2}{2}\frac{t^2}{\widehat{\Sigma}_i(t) + \widehat{\Sigma}_j(t)} = \frac{1}{4}\widehat{\Sigma}_0^{-1}\widehat{v}_{ij}^2 t^2 + \mathcal{O}(\delta_i^3) , \qquad v_{ij} = \widehat{v}_i - \widehat{v}_j , \qquad (5.B.21a)$$

$$Z_{ij}(t) = \frac{1}{\widehat{\Sigma}_i(t)} + \frac{1}{\widehat{\Sigma}_j(t)} = \frac{2}{\widehat{\Sigma}_0(t)} + \mathcal{O}(\delta_i) , \qquad (5.B.21b)$$

using the expansion equation (5.A.35) the velocity difference can be written as

$$v_{ij} = \widehat{v}_1\delta_{ij} + \mathcal{O}(\delta_i^2) = \frac{\widehat{p}_1 - E_1\widehat{v}_0}{E_0}\delta_{ij} + \mathcal{O}(\delta_i^2) , \qquad \delta_{ij} := \delta_i - \delta_j . \qquad (5.B.22)$$

Since the expansion is performed around the minimum, the linear term is still absent. However, since dispersion is not neglected, the constant term does not vanish. The phase can be rewritten similarly to the NDR in terms of a constant and a linear term

$$\phi_i(t, \widehat{x}) = \phi_i(t) - \widehat{p}_i(\widehat{x} - \widehat{x}_{ij}) , \qquad \phi_i(t) = E_i t - \widehat{p}_i\widehat{x}_{ij} . \qquad (5.B.23)$$

Since the phase contains the imaginary contributions to the amplitude, the difference between the two mass eigenstates appears in the oscillation probability

$$\phi_{ij}(t, \widehat{x}) = \phi_i(t, \widehat{x}) - \phi_j(t, \widehat{x}) = \phi_{ij}(t) + \widehat{p}_{ij}(x - \widehat{x}_{ij}) , \qquad (5.B.24)$$

the constant term and the linear coefficient are

$$\phi_{ij}(t) = E_{ij}t - \widehat{p}_{ij}\widehat{x}_{ij} , \qquad E_{ij} = E_i - E_j , \qquad \widehat{p}_{ij} = \widehat{p}_i - \widehat{p}_j . \qquad (5.B.25)$$

Using the expansions equations (5.A.33) and (5.A.34) yielding

$$E_{ij} = E_1\delta_{ij} + \mathcal{O}(\delta_i^2) = (E_0 - \widehat{v}_0\widehat{p}_1)\delta_{ij} + \mathcal{O}(\delta_i^2) , \qquad \widehat{p}_{ij}(t) = \widehat{p}_1\delta_{ij} + \mathcal{O}(\delta_i^2) , \qquad (5.B.26)$$

together with the approximation equation (5.B.12), leads for the phase difference to

$$\phi_{ij}(t) = m_{ij}\tau(t) + \mathcal{O}\left(\delta_i^2, \frac{m_{ij}^2}{E_0^2}\right) , \qquad \tau(t) = \frac{m_0}{E_0}t . \qquad (5.B.27)$$

which is identical to the phase difference in the NDR equation (5.B.13).

Integration of the oscillation probability   The integration

$$\mathcal{P}(t) \propto \int [\mathrm{d}\widehat{x}]_{\widehat{x}_{ij}-\Delta\widehat{x}}^{\widehat{x}_{ij}+\Delta\widehat{x}} \mathcal{P}(t,\widehat{x}) \,, \tag{5.B.28}$$

can be performed using equation (5.A.25) with

$$b = \widehat{p}_{ij} \,, \qquad\qquad\qquad A = \widehat{Z}_{ij} \,, \tag{5.B.29}$$

resulting in the constant localisation term

$$\Lambda_{ij} = \frac{1}{2}\widehat{Z}_{ij}^{-1} p_{ij}^2 = \frac{1}{2}\frac{\widehat{\Sigma}_i(t)\widehat{\Sigma}_j(t)}{\widehat{\Sigma}_i(t)+\widehat{\Sigma}_j(t)}\widehat{p}_{ij}^2 = \frac{1}{4}\widehat{\Sigma}_0 \widehat{p}_{ij}^2 + \mathcal{O}(\delta_i^3) \,. \tag{5.B.30}$$

Finally, the oscillation probability reads

$$\mathcal{P}(t) \propto \sum_{ij} \exp\left[\lambda'_{ij}(t) - \mathrm{i}\,\phi_{ij}(t)\right] \,, \qquad \lambda'_{ij}(t) = f_{ij} + \Lambda_{ij} + F_{ij}(t) + \gamma_{ij}(t) \,, \tag{5.B.31}$$

where the EME and the decay term are given by equation (5.B.17), the phase difference is given by equation (5.B.27), the dispersion term is given by equation (5.B.21a), and the localisation term is given by equation (5.B.30).

Appendix 5.C   Phase shift

For short times, corrections to the LO expression of the phase equation (5.3.36), which scale linearly with the decay width expansion parameter ϵ_i become relevant. The expansion in the mass splitting expansion parameter δ_i is given in equations (5.B.13) and (5.B.27) in detail. Therefore, we derive an analytical correction to the phase for parameter points in which ϵ_i is non-negligible and test how the numerical phase as obtained via the algorithm described in section 5.D deviates from the LO expression for the phase equation (5.3.36).

As presented in section 5.3.1, the NLO contribution in ϵ_i to the phase results in the usual decay term $\gamma_i(t,\boldsymbol{p})$ equation (5.3.7). However, there is also a contribution from the EME, which yields

$$\phi_i(t,\boldsymbol{x},\boldsymbol{p}) = E_i(\boldsymbol{p})t - \boldsymbol{p}\cdot\boldsymbol{x} - \gamma_i(\boldsymbol{p})\left[\frac{e_{iP}(\boldsymbol{p})}{2\sigma_{EP}^2} - \frac{e_{iD}(\boldsymbol{p})}{2\sigma_{ED}^2}\right] + \mathcal{O}(\epsilon_i^2) \,. \tag{5.C.1}$$

While the direct contribution of the correction term to the phase $\phi_i(t,\boldsymbol{x},\boldsymbol{p})$ is negligible, it has a significant effect on the STE equation (5.B.5) since the corrections appear in the linear term

$$\boldsymbol{\Delta}_0(t,\boldsymbol{x}) = \boldsymbol{v}_0 t - \boldsymbol{x} + \gamma_0\left(\frac{\boldsymbol{u}_P}{2\sigma_{EP}^2} - \frac{\boldsymbol{u}_D}{2\sigma_{ED}^2}\right) + \mathcal{O}(\epsilon_i^2) \,. \qquad \gamma_0 = \frac{m_0\Gamma}{2E_0} \,, \tag{5.C.2}$$

This correction to the STE results in a shift of the position of its minimum equation (5.B.6), which is now at

$$\boldsymbol{x}_{ij}(t) = \boldsymbol{v}_0 t + \gamma_0\left(\frac{\boldsymbol{u}_P}{2\sigma_{EP}^2} - \frac{\boldsymbol{u}_D}{2\sigma_{ED}^2}\right) + \mathcal{O}(\delta_i,\epsilon_i^2) \,. \tag{5.C.3}$$

The correction becomes relevant for *large* decay widths since then the particle's lifetime becomes small, while simultaneously, the correction term becomes larger. The resulting phase is then given by

$$\phi_{ij}(t) = \phi_{ij} + m_{ij}\tau(t) \,, \tag{5.C.4}$$
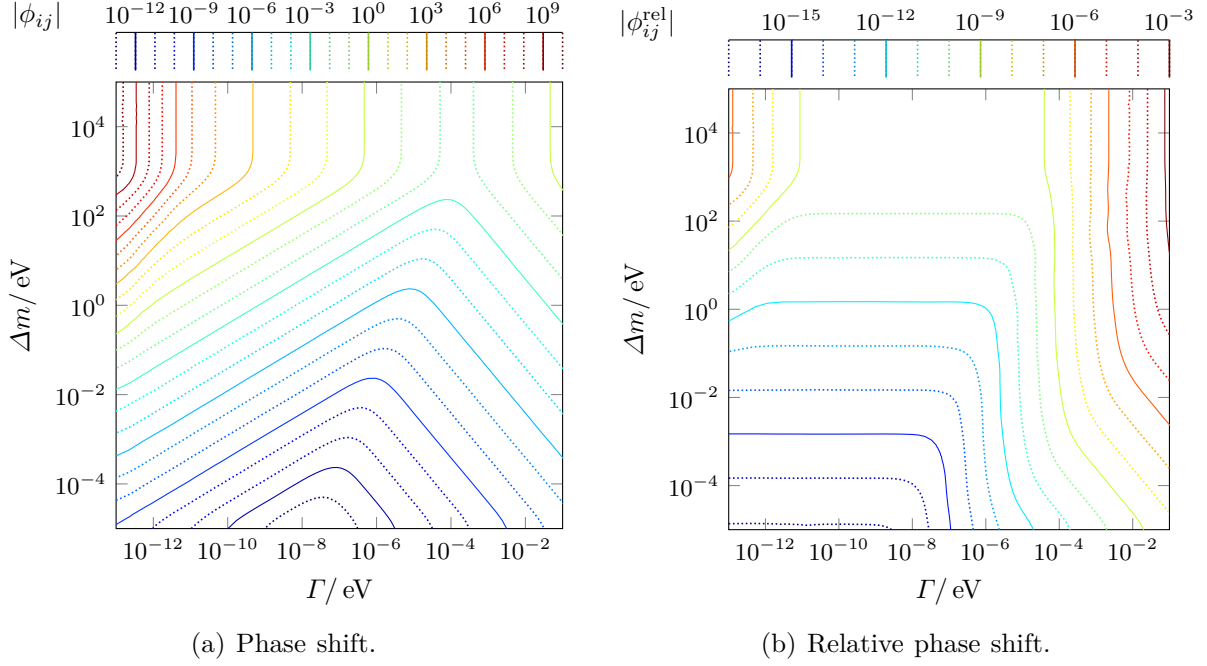
(a) Phase shift.

(b) Relative phase shift.

Figure 5.10: The absolute value of the phase shift ϕ_{ij} in panel (a) and the absolute value of the relative phase shift ϕ_{ij}^{rel}, defined in equation (5.C.7), in panel (b) as functions of the decay width and mass splitting.

where the constant phase shift is

$$\phi_{ij} = -\boldsymbol{p}_{ij}\left(\frac{\boldsymbol{u}_P}{2\sigma_{EP}^2} - \frac{\boldsymbol{u}_D}{2\sigma_{ED}^2}\right)\gamma_0 \, . \tag{5.C.5}$$

Since $\boldsymbol{\Sigma}_0$ is symmetric, this can be simplified to read

$$\phi_{ij} = \frac{\boldsymbol{u}_D^{\mathsf{T}}}{2\sigma_{ED}^2}\boldsymbol{\Sigma}_0^{-1}\frac{\boldsymbol{u}_D}{2\sigma_{ED}^2}mm_{ij}\epsilon_0 - (D \to P) + \mathcal{O}\left(\epsilon_i^2, \delta_i^2, \frac{m_{ij}^2}{E_0^2}\right), \qquad \epsilon_0 = \frac{\gamma_0}{E_0} \, . \tag{5.C.6}$$

Numerical results for the phase shift are shown in figure 5.10. As can be seen from figure 5.10a, in the considered parameter region, the total value of the modulus of the phase shift is small for most of the parameter space except for part of the region with large Δm, where it can get large. However, we remark that in this parameter region, many oscillations take place before the heavy neutrino decays, and thus the phase shift per oscillation is still small. This is illustrated in figure 5.10b, which shows the modulus of the relative phase shift

$$\phi_{ij}^{\mathrm{rel}} := \frac{\phi_{ij}}{\max(2\pi, |m_{ij}\tau|)} \, . \tag{5.C.7}$$

Furthermore, comparing with figure 5.4, one can see that in the region with a large total phase shift, the damping λ is very large, such that the oscillation term is strongly suppressed, making the phase shift practically unobservable. In summary, the numerical results show that, for current collider simulations, one can safely neglect the phase shift in the considered parameter region.

However, outside the applicability region the phase shift can become significant, which can be seen from equation (5.C.5). The numerical results match this behaviour. Since these results are

```
1   define $E_0$, $\boldsymbol{p}_0$, $m_0$
2   for $V$ in $\{P,\ D\}$ do define $\sigma_{\boldsymbol{x}V}$, $\sigma_{\boldsymbol{p}V}$, $\sigma_{EV}$, $\Sigma_V$, $\boldsymbol{v}_V$
3   for $i$ in $\{4,\ 5\}$ do define $m_i$, $\Gamma_i$
4
5   $t$ = rand.variate[expdistri[mean[$\Gamma_4$, $\Gamma_5$]]] $E_0/m_0$
6
7   for $V$ in $\{P,\ D\}$ do
8       $e_V[E,\boldsymbol{p}]$ = $E - E_0 - (\boldsymbol{p} - \boldsymbol{p}_0) \cdot \boldsymbol{v}_V$
9       $f_V[E,\boldsymbol{p},\gamma]$ = $|\boldsymbol{p} - \boldsymbol{p}_0|^2/(2\sigma_{\boldsymbol{p}V})^2 + (e_V^2[E,\boldsymbol{p}] - e_V[0,\boldsymbol{p}]\gamma^2/E)/(2\sigma_{EV})^2$
10
11  for $i$ in $\{4,\ 5\}$ do
12      $E_i[\boldsymbol{p}]$ = sqrt[$|\boldsymbol{p}|^2 + m_i^2$]
13      $\gamma_i[\boldsymbol{p}]$ = $m_i \Gamma_i/2E_i[\boldsymbol{p}]$
14      $f_i[\boldsymbol{p}]$ = $f_P[E_i[\boldsymbol{p}],\boldsymbol{p},\gamma_i[\boldsymbol{p}]] + f_D[E_i[\boldsymbol{p}],\boldsymbol{p},\gamma_i[\boldsymbol{p}]]$
15      $\lambda_i[\boldsymbol{p}]$ = $f_i[\boldsymbol{p}] + \gamma_i[\boldsymbol{p}]t$
16      $e_i[\boldsymbol{p}]$ = $e_P[E_i[\boldsymbol{p}],\boldsymbol{p}]/(2\sigma_{EP}^2) - e_D[E_i[\boldsymbol{p}],\boldsymbol{p}]/(2\sigma_{ED}^2)$
17      $\phi_i[\boldsymbol{p},\boldsymbol{x}]$ = $E_i[\boldsymbol{p}]t - \boldsymbol{p}\cdot\boldsymbol{x} - \gamma_i[\boldsymbol{p}]e_i[\boldsymbol{p}]$
18      $\alpha_i[\boldsymbol{p},\boldsymbol{x}]$ = $\lambda_i[\boldsymbol{p}] + i\phi_i[\boldsymbol{p},\boldsymbol{x}]$
19
20  for $i$ in $\{4,\ 5\}$ do // momentum integral
21      $\boldsymbol{p}_i$ = argmin[$\lambda_i[\boldsymbol{p}]$]
22      $\Sigma_i[\boldsymbol{x}]$ = hessian[$\alpha_i[\boldsymbol{p},\boldsymbol{x}],\boldsymbol{p}$] at $\boldsymbol{p} = \boldsymbol{p}_i$
23      $\boldsymbol{\Delta}_i[\boldsymbol{x}]$ = $\partial_{\boldsymbol{p}}\phi_i[\boldsymbol{p},\boldsymbol{x}]$ at $\boldsymbol{p} = \boldsymbol{p}_i$
24      $F_i[\boldsymbol{x}]$ = $\boldsymbol{\Delta}_i[\boldsymbol{x}] \cdot \Sigma_i^{-1}[\boldsymbol{x}] \cdot \boldsymbol{\Delta}_i[\boldsymbol{x}]/2$
25
26  $\alpha_{45}[\boldsymbol{x}]$ = $\alpha_4[\boldsymbol{p}_4,\boldsymbol{x}] + F_4[\boldsymbol{x}] + $ conj[$\alpha_5[\boldsymbol{p}_5,\boldsymbol{x}] + F_5[\boldsymbol{x}]$]
27
28  // distance integral
29  $\boldsymbol{x}_{45}$ = argmin[Re[$\alpha_{45}[\boldsymbol{x}]$]]
30  $Z_{45}$ = hessian[$\alpha_{45}[\boldsymbol{x}],\boldsymbol{x}$] at $\boldsymbol{x} = \boldsymbol{x}_{45}$
31  $\boldsymbol{\Pi}_{45}$ = $\partial_{\boldsymbol{x}}$Im[$\alpha_{45}[\boldsymbol{x}]$] at $\boldsymbol{x} = \boldsymbol{x}_{45}$
32  $\Lambda_{45}$ = $\boldsymbol{\Pi}_{45} \cdot Z_{45}^{-1} \cdot \boldsymbol{\Pi}_{45}/2$
33
34  $\beta_{45}$ = $\Lambda_{45} + \alpha_{45}[\boldsymbol{x}_{45}]$
35  $\mathcal{N}_{45}$ = log[exp[$-2\lambda_4[\boldsymbol{p}_4]$]/2 + exp[$-2\lambda_5[\boldsymbol{p}_5]$]/2]
36
37  $\lambda_{45}$ = Re[$\beta_{45} + \mathcal{N}_{45}$]
38  $\phi_{45}$ = Im[$\beta_{45} + \mathcal{N}_{45}$]
```

Listing 5.1: Algorithm describing the strategy to calculate decoherence effects.

based on values of the decay width larger than Γ_{JS}, and since we do not see a physical reasons for the phase shift to become arbitrarily large, we neglect the phase shift for the main part of this work.

Appendix 5.D   Numerical decoherence derivation

In this section, the algorithm for the numerical computation of the damping parameter λ is presented. The algorithm expects the momenta of the external particles and the widths of the wave packets of the external particles as input. Our estimates for the external widths in the process in figure 5.3 are given in table 5.1. Realistic momentum configurations can be generated using a MC generator such as MadGraph together with the implementation of the pSPSS

introduced in [2, 91].

We present an algorithm for the derivation of the numerical results in listing 5.1. In the first lines, the kinematics of the event and the wave packet widths of the external particles are used to define the given quantities as input to the algorithm. In particular, in line 1, the kinematics of the external particles are used to define the reconstructed quantities equation (5.2.13), in line 2 the definitions equations (5.2.7), (5.2.8), and (5.2.10) are used to define relevant widths, and in line 3 the masses and decay widths of the heavy neutrino mass eigenstates are defined. In line 5, the propagation time between production and decay of the heavy neutrino superposition is drawn from an exponential distribution, defined by the mean decay width of the neutrinos. In line 9, the EMEs equation (5.3.9) at production and detection are defined, where the LO corrections in the decay width expansion equation (5.3.4), are taken into account. In the following lines, quantities for the mass eigenstates are defined. In line 13, the decay term is calculated, line 14 defines the EME for the heavy neutrino, and in line 17 the phase, taking into account the imaginary part stemming from the decay width expansion of the EME, is calculated. All exponential terms relevant for the transition amplitude equation (5.3.11) are collected in line 18. The integration over the three-momentum of the heavy neutrino wave packet is performed by approximating all terms up to second order around the maximum of the wave packet. The maximum of the wave packet is defined in line 21 by the minimum of the EME, where the effects of the decay term are taken into account. Subsequently, the terms of the exponential quadratic in $\boldsymbol{p} - \boldsymbol{p}_i$ are computed in line 22. Since the expansion is around the minimum of $f_i(\boldsymbol{p}) + \gamma_i(\boldsymbol{p})$, only the complex phase has to be considered for the linear terms in line 23. The integration results in the STE in line 26, which is defined in equations (5.A.28) and (5.A.49). The following steps are valid for the $\mathcal{A}_i \mathcal{A}_j^*$ terms in the probability since the damping term is relevant for terms $i \neq j$, which are responsible for oscillations. The distance integral is evaluated in the same fashion as the three-momentum integral. The only terms in the exponential that depend on the distance are the STE $F_{ij}(\boldsymbol{x})$ and the complex phase $\phi_{ij}(\boldsymbol{x}, t)$. The expansion is around the minimum of the STE computed in line 29. Since the phase is linear in $\boldsymbol{x}$, the only contribution to the quadratic terms in $\boldsymbol{x} - \boldsymbol{x}_{ij}$ are given by the Hessian of the STE computed in line 30. After the integration, the final exponent term is defined by

$$\mathcal{A}_i(t)\mathcal{A}_j^*(t) = \mathcal{N}_{ij}(t) \exp(-\beta_{ij}(t)) \tag{5.D.1}$$

in line 34. The normalisation is computed in line 35 based on the condition equation (5.3.43). For the computation of the damping in the case of $N\overline{N}$Os in this paper, the decay terms $\gamma_i[\boldsymbol{p}_i]$ in β and in $\mathcal{N}$ have been neglected, as we found them to be not significant. Finally, the damping parameter and the complex phase are computed in lines 37 and 38.

While the algorithm is presented with the NDR in mind, it can easily be applied to the TDR by replacing vector quantities denoted with bold font by their projection onto the direction of $\boldsymbol{p}_0$.

Chapter 6

Afterword

The aim of this chapter is to give a Summary of the work that is contained in this thesis, followed by a conclusion that synthesizes the main points that can be drawn from the presented research. Finally, an outlook is given with suggestions for further research opportunities.

6.1 Summary

The work presented in this thesis focuses on the phenomenology of an extension of the SM by sterile neutrinos. While several scenarios lead to the desired mass splittings of the light neutrinos, measured experimentally, the SPSS allows the sterile neutrinos to be within range of current collider experiments. A key feature of heavy neutrinos protected by an approximate LNLS is their small mass splitting, which renders particle oscillations relevant for phenomenology.

The effects of HNANOs are explored, which are derived in a QFT model of external wave packets in [1] . General formulae for an oscillation probability between neutrinos and antineutrinos are derived and subsequently applied to a dilepton dijet process within a low scale SPSS. The so-called observability conditions that can lead to decoherence of the mass eigenstate superposition of heavy neutrinos, and thus to damping of oscillations, are discussed and found to be negligible for a considered benchmark point. The LO results of the probability are found to agree with the results of [40, 41, 44]. Further, it is found that the NLO contributions feature flavour oscillations which are too small to be of phenomenological interest around the considered example parameter point. It is shown that for the example parameter point, the LO effects of HNANOs can be described by two sets of parameters; the active-sterile mixing angles θ_α and the mass squared difference δm_{45}^2 between the two heavy neutrinos.

To further explore the low-scale phenomenology of HNANOs, we introduce the pSPSS in [2], a model that describes the LO effects of a pseudo-Dirac pair of HNLs with the minimal set of relevant parameters. The pSPSS is based on the assumption that a single pair of neutrinos, forming a pseudo-Dirac particle, dominates the phenomenology at collider-accessible scales. However, it includes the possibility of additional heavy neutrinos at a higher energy scale, which allows for its parameters to be freely chosen compared to a minimal model. To facilitate MC studies using the pSPSS, particularly for simulating HNANOs, a FeynRules implementation and a patch are published, extending the general purpose MC generator MadGraph to be capable of simulating HNANOs. Those tools are used to derive the maximal possible mass splitting of heavy neutrinos for which HNANOs may be reconstructable if only a fraction of events with the largest Lorentz boost is considered. The effects of finite detector geometry on the LNV over

LNC event ration, labelled R_{ll}, are examined by applying various cuts to the simulated events. In particular, the effects of a minimum distance and impact parameter cut are relevant to the observed R_{ll}, which, in this cases, may exceed the value of one, representing an upper bound in the naive case. Further, the impact parameter d_0 is found to be sensitive to momentum correlations in the considered process, affecting the LNC events differently than the LNV events. Consequently, the application of a d_0 cut is expected to introduce an oscillation of the total number of events as a function of the heavy neutrino proper time of flight. The existence of such an effect opens up the possibility to observe HNANOs in cases where it is not possible to reconstruct the lepton number of the process. Such processes are relevant, e.g., for future electron-positron colliders, when external leptons are light neutrinos that escape the detector.

In [3], the first-ever full collider simulation of $N\overline{N}$Os and cut-based analysis at the reconstructed level are presented. Events are generated at the parton level using the pSPSS and the patched version of MADGRAPH. QCD effects are incorporated by PYTHIA, and a fast detector analysis of a CMS-like detector is performed using DELPHES. The cut-based analysis is implemented via custom C++ code. Since DELPHES is missing a feature that simulates reconstructed displaced vertices, Gaussian smearing around the true displaced vertex is implemented to simulate the effects of experimental uncertainty. The analysis is performed for three different example parameter points that result in heavy neutrino parameters not excluded by experimental constraints. It is found that the simulated background of heavy hadrons, resulting in a displaced vertex and thus being capable of mimicking the signal process, can be evaded with the defined cuts. It is also argued that other backgrounds, e.g. from cosmic muons, should be eliminated by the given cuts, such that the signal events can be treated as background free. A detailed statistical analysis is performed which results in a significance of $5.19\,\sigma$ for the benchmark parameter point featuring a mass splitting of $\Delta m = 82.7\,\mu\text{eV}$. The benchmark point of $\Delta m = 743\,\mu\text{eV}$, which coincides with the mass splitting of the minimal linear seesaw model, results in a significance near zero. However, if the reconstruction of the Lorentz factor is improved and twice the signal events are considered, which is easily achieved by moving the benchmark point closer to the experimentally excluded region, the significance is improved to $5.13\,\sigma$. The effects of the smearing are found to be relevant for parameter points with a small oscillation length in lab space. The benchmark point featuring $\Delta m = 207\,\mu\text{eV}$ and hence an oscillation length of $6\,\text{mm}$ in proper space results in a significance slightly below $3\,\sigma$. If the displaced vertex is smeared with a Gaussian of $4\,\text{mm}$ standard deviation, the significance is reduced close to zero.

In [4], formulae for the oscillation probability as a function of time are derived in the no dispersion and transverse dispersion regimes. Additionally, the general algorithm for a numerical calculation of the damping factor λ is presented. The damping factor contains all decoherence effects relevant to the considered process that stem from the wave packet nature of the involved particles or distinct decay widths of propagating mass eigenstates. Numerical results are presented for a dilepton dijet process, averaged over several events to obtain a suppression independent of the angular distributions of momenta. For fixed heavy neutrino masses, the conditions for which the damping is independent of the mean decay width Γ are discussed. Under these conditions, the damping factor is presented and discussed as a function of the heavy neutrinos' mean mass and mass splitting. As an overall summary, it is found that for mass splittings of heavy neutrinos around $1\,\text{eV}$, the effects of decoherence become significant, considering a baseline of widths of external wave packets. The effects of varying the widths of the external wave packets are discussed. For very fast decaying heavy neutrinos, care has to be taken that the time of decay is still above the threshold defined by the theorem of Jacob-Sachs [54] since otherwise, the obtained formulae are no longer valid. As an example application of the derived results, the effects of the damping factor on the observed values of R_{ll} are presented.

Overall it has been found that symmetry-protected sterile neutrinos exhibit the interesting phenomenology of HNANOs. In cases where the mass splitting is smaller than around $100\,\mu\text{eV}$, the prospects of resolving the oscillation pattern at the HL-LHC are promising. For bigger mass splittings, the assumed experimental capabilities of reconstructing the Lorentz boost have to be improved. Care has to be taken if a measured LNV over LNC event ratio is used to derive results for the heavy neutrinos' mass splitting. This is because the observed R_{ll} might significantly deviate from a naive computation if effects of cuts or decoherence effects are taken into account. In particular, regions in parameter space that feature large damping result in an R_{ll} of one. This allows prompt searches of HNLs that require a LNV signature to be applicable in those regions, even if, from the underlying symmetry protection, one would expect very few LNV events compared to LNC events.

6.2   Conclusion

Introducing sterile neutrinos is a possible extension to the SM that can explain the observed light neutrino masses. A mechanism that suppresses LNV and protects the smallness of the light neutrino masses is needed to avoid the constraints from experimental searches if, at the same time, the additional heavy neutrinos should be within reach of current colliders. Such a mechanism is realised in the SPSS, which results in the heavy neutrinos forming pseudo-Dirac pairs. When studying the phenomenology of such pseudo-Dirac HNLs, particularly their LNV signature, it is crucial to consider HNANOs.

Typically the LNV caused by pseudo-Dirac HNLs is assumed to be non-observable, which is valid as long as the HNLs decay prompt and if coherence between the propagating mass eigenstates is present. This work shows, for the first time quantitatively, that detectable amounts of LNV are introduced if

- HNLs propagate long enough for HNANOs to develop, or

- Coherence between propagating mass eigenstates is lost.

To study the essential effects of decoherence and obtain theoretically sound formulae for HNANOs, a QFT formalism with external wave packets is used. While the derivation is somewhat technical, the final formulae are elegant and simple. They describe decoherence effects by a single damping parameter and oscillations by the well-known formulae that can also be obtained in a – conceptually problematic – QM derivation.

HNANOs produce an oscillating pattern in the amount of LNV as a function of the propagation time of the HNLs. If this pattern can be resolved experimentally, conclusions can be drawn for the mass splitting of the HNLs and, consequently, for the mechanism of neutrino mass generation. It is shown, under conservative assumptions, that the HL-LHC and a CMS-like detector are capable of resolving HNANOs for non-excluded parameter points of HNLs. If the Lorentz boost of the HNLs can be reconstructed more accurately, compared to what has been considered in this work, resolving the oscillation pattern even in the minimal linear seesaw case with inverted light neutrino mass hierarchy is feasible. With even better reconstruction efficiency or a higher number of signal events, as a future collider might provide, additional minimal and non-minimal scenarios for neutrino mass generation can be probed. However, it is crucial to consider the effects of damping, which can suppress the oscillations, especially for large values of the HNL's mass splitting, and thus reduce the chances of resolving the oscillation pattern.

Also, in cases where the oscillation pattern cannot be resolved, HNANOs provide interesting phenomenology by impacting the LNV over LNC event ratio, often called R_{ll}. For HNL lifetimes

much smaller than the oscillation period of HNANOs, the amount of LNV is typically negligible and the R_{ll} close to one. However, already for lifetimes equal to the oscillation period, the resulting R_{ll} is close to one. Additionally, significant decoherence effects, described by a large damping factor λ, also increase the amount of LNV and thus the value of R_{ll}. Both effects are studied in detail in this work, and it is shown that they are critical when reinterpreting prompt searches that rely on a LNV signature for pseudo-Dirac HNLs. From a measurement of R_{ll}, it is possible to draw conclusions about the HNLs mass splitting if their decay widths are also measured. However, if such an argument is made, it is paramount to consider the effects of damping and the detector geometry, including cuts, e.g., on the impact parameter. It is shown that both effects can result in a significant deviation of the observed R_{ll} compared to a naive R_{ll}, i.e. one that only takes HNANOs into account. Therefore, comparing the measured R_{ll} to a naive calculation of the R_{ll} would result in the wrong HNL's mass splitting.

Generally, this work shows that the effects of HNANOs, including the possibility of decoherence, are crucial for the phenomenological study of LNV at current and future colliders.

6.3 Outlook

The work in this thesis derives oscillation probabilities for HNANOs based on a QFT framework featuring external wave packets and applies the results to study the feasibility of reconstructing the oscillation pattern at the HL-LHC for a CMS-like detector.

It would be interesting to see how far the capabilities of the HL-LHC and related detectors can be pushed to resolve the oscillation pattern of HNANOs. Using more sophisticated analysis techniques that allow for a better reconstruction of the Lorentz boost of the heavy neutrino is crucial to successfully resolve the oscillation pattern for mass splittings larger than several hundred μeV.

The ignorance of the external particles' wave packet widths is a major source of uncertainty for the damping factor λ. A further investigation aimed to obtain a better description of the wave packet nature of external particles could solve those issues. To this end, processes have to be considered that are close to the boundary at which decoherence effects due to the wave packet nature of the involved particles become relevant. Given the typically microscopic dimensions of the wave packet widths, the kinematics of a considered process must be measured with extreme precision. A future electron-position collider might be best suited for those investigations.

If the experimental uncertainty in the reconstruction of the heavy neutrino mass is improved, the Jacob Sachs threshold [54] is pushed to larger values. Consequently, heavy neutrinos must have smaller decay widths for the formulae derived in this work to be applicable. For neutrinos that have lifetimes close to Jacob Sachs threshold, additional corrections to the energy contour integral, and thus to the oscillation formulae, become relevant [38, 54]. For even larger decay widths, the application of the theorem of Jacob Sachs is no longer justified. However, resolving the oscillation pattern, if it even exists in those circumstances, seems not feasible for such prompt decays. A better description of such processes could be provided by standard QFT methods, which, even though they do not yield HNANOs, might still be used to obtain LNV over LNC event ratios. A detailed analysis of these methods and their connection to the oscillation formulae, which require the theorem of Jacob Sachs, might provide useful insights for future collider experiments regarding the observation of LNV.

The possibilities of HNANOs have to be considered when planning future colliders and their detectors since their impact on LNV signatures is significant. To obtain the feasibility of resolving

the oscillation pattern, a dedicated study on electron-positron colliders would be useful. Since in cases where one of the external charged leptons is replaced by a light neutrino, the lepton number of the process can no longer be derived from the measured charges of the particles, a new strategy is needed. A possible solution might be to take advantage of spin correlations. Events could be divided into LNC and LNV based on the momentum configuration of the external particles. Such an effect has already been found and discussed in terms of the impact parameter cut in [2]. However, better observables sensitive to spin correlations might be found using more sophisticated techniques, e.g. machine learning.

Finally, it would be interesting to see to what degree HNANOs play a role in other fields of physics, such as cosmology.

Bibliography

[1] S. Antusch and J. Rosskopp. 'Heavy Neutrino-Antineutrino Oscillations in Quantum Field Theory'. In: *JHEP* 03 (2021), p. 170. DOI: 10.1007/JHEP03(2021)170. arXiv: 2012.05763 [hep-ph].

[2] S. Antusch, J. Hajer, and J. Rosskopp. 'Simulating Lepton Number Violation Induced by Heavy Neutrino-Antineutrino Oscillations at Colliders' (Oct. 2022). arXiv: 2210.10738 [hep-ph].

[3] S. Antusch, J. Hajer, and J. Rosskopp. 'Beyond Lepton Number Violation at the HL-LHC: Resolving Heavy Neutrino-Antineutrino Oscillations' (Dec. 2022). arXiv: 2212.00562 [hep-ph].

[4] S. Antusch, J. Hajer, and J. Rosskopp. 'Decoherence effects on lepton number violation from heavy neutrino-antineutrino oscillations' (July 2023). arXiv: 2307.06208 [hep-ph].

[5] R. Davis, D. S. Harmer, and K. C. Hoffman. 'Search for Neutrinos from the Sun'. In: *Phys. Rev. Lett.* 20.21 (May 1968), pp. 1205–1209. DOI: 10.1103/PhysRevLett.20.1205.

[6] V. Gribov and B. Pontecorvo. 'Neutrino Astronomy and Lepton Charge'. In: *Physics Letters B* 28.7 (1969), pp. 493–496. ISSN: 0370-2693. DOI: 10.1016/0370-2693(69)90525-5.

[7] J. C. Pati and A. Salam. 'Is Baryon Number Conserved?' In: *Phys. Rev. Lett.* 31.10 (Sept. 1973), pp. 661–664. DOI: 10.1103/PhysRevLett.31.661.

[8] H. Georgi and S. L. Glashow. 'Unity of All Elementary-Particle Forces'. In: *Phys. Rev. Lett.* 32.8 (Feb. 1974), pp. 438–441. DOI: 10.1103/PhysRevLett.32.438.

[9] J. C. Pati and A. Salam. 'Lepton Number as the Fourth "Color"'. In: *Phys. Rev. D* 10.1 (July 1974), pp. 275–289. DOI: 10.1103/PhysRevD.10.275.

[10] H. Georgi, H. R. Quinn, and S. Weinberg. 'Hierarchy of Interactions in Unified Gauge Theories'. In: *Phys. Rev. Lett.* 33.7 (Aug. 1974), pp. 451–454. DOI: 10.1103/PhysRevLett.33.451.

[11] H. Fritzsch and P. Minkowski. 'Unified Interactions of Leptons and Hadrons'. In: *Annals of Physics* 93.1 (1975), pp. 193–266. ISSN: 0003-4916. DOI: 10.1016/0003-4916(75)90211-0.

[12] H. Georgi. 'The State of the Art—Gauge Theories'. In: *AIP Conference Proceedings* 23.1 (1975), pp. 575–582. DOI: 10.1063/1.2947450. eprint: https://aip.scitation.org/doi/pdf/10.1063/1.2947450.

[13] M. S. Chanowitz, J. Ellis, and M. K. Gaillard. 'The Price of Natural Flavour Conservation in Neutral Weak Interactions'. In: *Nuclear Physics B* 128.3 (1977), pp. 506–536. ISSN: 0550-3213. DOI: 10.1016/0550-3213(77)90057-8.

[14] A. Buras, J. Ellis, M. Gaillard, and D. Nanopoulos. 'Aspects of the Grand Unification of Strong, Weak and Electromagnetic Interactions'. In: *Nuclear Physics B* 135.1 (1978), pp. 66–92. ISSN: 0550-3213. DOI: 10.1016/0550-3213(78)90214-6.

[15] J. R. Bond, G. Efstathiou, and J. Silk. 'Massive Neutrinos and the Large-Scale Structure of the Universe'. In: *Phys. Rev. Lett.* 45.24 (Dec. 1980), pp. 1980–1984. DOI: 10.1103/PhysRevLett.45.1980.

[16] W. Hu, D. J. Eisenstein, and M. Tegmark. 'Weighing Neutrinos with Galaxy Surveys'. In: *Phys. Rev. Lett.* 80.IASSNS-AST-97-73 (1998), pp. 5255–5258. DOI: 10.1103/PhysRevLett.80.5255. arXiv: astro-ph/9712057.

[17] *Planck.* 'Planck 2018 Results. VI. Cosmological Parameters'. In: *Astron. Astrophys. A* 6 (2020), p. 641. DOI: 10.1051/0004-6361/201833910. arXiv: 1807.06209 [astro-ph.CO]. Erratum in: *Astron. Astrophys. C* 4 (2021), p. 652. DOI: 10.1051/0004-6361/201833910e].

[18] P. Minkowski. '$\mu \to e\gamma$ at a Rate of One out of 10^9 Muon Decays?' In: *Phys. Lett. B* 67.Print-77-0182 (BERN) (1977), pp. 421–428. DOI: 10.1016/0370-2693(77)90435-X.

[19] M. Gell-Mann, P. Ramond, and R. Slansky. 'Complex Spinors and Unified Theories'. In: *Conf. Proc. C* 790927.PRINT-80-0576 (1979), pp. 315–321. arXiv: 1306.4669 [hep-th].

[20] S. L. Glashow. 'The Future of Elementary Particle Physics'. *Quarks and Leptons.* Summer Institute (Cargèse). Ed. by M. Levy, J. L. Basdevant, D. Speiser, J. Weyers, R. Gastmans, and M. Jacob. Vol. 61. NATO Sci. Ser. B. France, 1980, p. 687. DOI: 10.1007/978-1-4684-7197-7_15.

[21] J. Schechter and J. W. F. Valle. 'Neutrino Masses in SU(2)×U(1) Theories'. In: *Phys. Rev. D* 22.SU-4217-167, COO-3533-167 (1980), p. 2227. DOI: 10.1103/PhysRevD.22.2227.

[22] R. N. Mohapatra and G. Senjanovic. 'Neutrino Mass and Spontaneous Parity Nonconservation'. In: *Phys. Rev. Lett.* 44.MDDP-TR-80-060, MDDP-PP-80-105, CCNY-HEP-79-10 (1980), p. 912. DOI: 10.1103/PhysRevLett.44.912.

[23] T. Yanagida. 'Horizontal Symmetry and Masses of Neutrinos'. In: *Prog. Theor. Phys.* 64.TU-80-208 (1980), p. 1103. DOI: 10.1143/PTP.64.1103.

[24] J. Schechter and J. W. F. Valle. 'Neutrino Decay and Spontaneous Violation of Lepton Number'. In: *Phys. Rev. D* 25.SU-4217-203, COO-3533-203 (1982), p. 774. DOI: 10.1103/PhysRevD.25.774.

[25] E. Majorana. 'Teoria Simmetrica Dell'elettrone e Del Positrone'. In: *Nuovo Cim.* 14.RX-888 (1937), pp. 171–184. DOI: 10.1007/BF02961314.

[26] *ATLAS.* 'Search for Heavy Majorana Neutrinos with the ATLAS Detector in pp Collisions at s = 8 TeV'. In: *JHEP* 07.CERN-PH-EP-2015-070 (2015), p. 162. DOI: 10.1007/JHEP07(2015)162. arXiv: 1506.06020 [hep-ex].

[27] *CMS.* 'Search for Heavy Neutral Leptons in Events with Three Charged Leptons in Proton-Proton Collisions at s = 13 TeV'. In: *Phys. Rev. Lett.* 120.CMS-EXO-17-012, CERN-EP-2018-006 (2018), p. 221801. DOI: 10.1103/PhysRevLett.120.221801. arXiv: 1802.02965 [hep-ex].

[28] *ATLAS.* 'Search for Long-Lived, Massive Particles in Events with a Displaced Vertex and a Muon with Large Impact Parameter in pp Collisions at s = 13 TeV with the ATLAS Detector'. In: *Phys. Rev. D* 102.CERN-EP-2019-219 (2020), p. 32006. DOI: 10.1103/PhysRevD.102.032006. arXiv: 2003.11956 [hep-ex].

[29] *CMS*. 'Search for Long-Lived Heavy Neutral Leptons with Displaced Vertices in Proton-Proton Collisions at s = 13 TeV'. In: *JHEP* 07.CMS-EXO-20-009, CERN-EP-2021-264 (2022), p. 81. DOI: 10.1007/JHEP07(2022)081. arXiv: 2201.05578 [hep-ex].

[30] I. Zurbano Fernandez et al. 'High-Luminosity Large Hadron Collider (HL-LHC): Technical Design Report'. 10/2020.CERN-2020-010 (Dec. 2020). Ed. by I. Béjar Alonso, O. Brüning, P. Fessia, L. Rossi, L. Tavian, and M. Zerlauth. DOI: 10.23731/CYRM-2020-0010.

[31] S. Antusch and O. Fischer. 'Testing Sterile Neutrino Extensions of the Standard Model at Future Lepton Colliders'. In: *JHEP* 05.MPP-2015-24 (2015), p. 53. DOI: 10.1007/JHEP05(2015)053. arXiv: 1502.05915 [hep-ph].

[32] S. Antusch, E. Cazzato, and O. Fischer. 'Sterile Neutrino Searches at Future e⁻e⁺, pp, and e⁻p Colliders'. In: *Int. J. Mod. Phys. A* 32.14 (2017), p. 1750078. DOI: 10.1142/S0217751X17500786. arXiv: 1612.02728 [hep-ph].

[33] B. Pontecorvo. 'Mesonium and Anti-Mesonium'. In: *Sov. Phys. JETP* 6 (1957), p. 429. Original in: *Zh. Eksp. Teor. Fiz.* 33 (1957), pp. 549–551.

[34] Z. Maki, M. Nakagawa, and S. Sakata. 'Remarks on the Unified Model of Elementary Particles'. In: *Prog. Theor. Phys.* 28 (1962), pp. 870–880. DOI: 10.1143/PTP.28.870.

[35] R. G. Sachs. 'Interference Phenomena of Neutral K Mesons'. In: *Annals of Physics* 22.2 (1963), pp. 239–262. DOI: 10.1016/0003-4916(63)90055-1.

[36] B. Kayser. 'On the Quantum Mechanics of Neutrino Oscillation'. In: *Phys. Rev. D* 24.SLAC-PUB-2685 (1981), p. 110. DOI: 10.1103/PhysRevD.24.110.

[37] C. Giunti, C. W. Kim, J. A. Lee, and U. W. Lee. 'On the Treatment of Neutrino Oscillations without Resort to Weak Eigenstates'. In: *Phys. Rev. D* 48.JHU-TIPAC-930011, DFTT-22-93 (1993), pp. 4310–4317. DOI: 10.1103/PhysRevD.48.4310. arXiv: hep-ph/9305276.

[38] M. Beuthe. 'Oscillations of Neutrinos and Mesons in Quantum Field Theory'. In: *Phys. Rept.* 375 (2003), pp. 105–218. DOI: 10.1016/S0370-1573(02)00538-0. arXiv: hep-ph/0109119.

[39] A. G. Cohen, S. L. Glashow, and Z. Ligeti. 'Disentangling Neutrino Oscillations'. In: *Phys. Lett. B* 678 (2009), pp. 191–196. DOI: 10.1016/j.physletb.2009.06.020. arXiv: 0810.4602 [hep-ph].

[40] G. Cvetic, C. S. Kim, R. Kogerler, and J. Zamora-Saa. 'Oscillation of Heavy Sterile Neutrino in Decay of B →μeπ'. In: *Phys. Rev. D* 92.USM-TH-335 (2015), p. 13015. DOI: 10.1103/PhysRevD.92.013015. arXiv: 1505.04749 [hep-ph].

[41] G. Anamiati, M. Hirsch, and E. Nardi. 'Quasi-Dirac Neutrinos at the LHC'. In: *JHEP* 10.IFIC-16-48 (2016), p. 10. DOI: 10.1007/JHEP10(2016)010. arXiv: 1607.05641 [hep-ph].

[42] J. Gluza and T. Jeliński. 'Heavy Neutrinos and the Pp→lljj CMS Data'. In: *Phys. Lett. B* 748 (2015), pp. 125–131. DOI: 10.1016/j.physletb.2015.06.077. arXiv: 1504.05568 [hep-ph].

[43] P. S. Bhupal Dev and R. N. Mohapatra. 'Unified Explanation of the eejj, Diboson and Dijet Resonances at the LHC'. In: *Phys. Rev. Lett.* 115.MAN-HEP-2015-14, TUM-HEP-1008-15, UMD-PP-015-012 (2015), p. 181803. DOI: 10.1103/PhysRevLett.115.181803. arXiv: 1508.02277 [hep-ph].

[44] S. Antusch, E. Cazzato, and O. Fischer. 'Resolvable Heavy Neutrino–Antineutrino Oscillations at Colliders'. In: *Mod. Phys. Lett. A* 34.07n08 (2019), p. 1950061. DOI: 10.1142/S0217732319500615. arXiv: 1709.03797 [hep-ph].

[45] M. Drewes, J. Klarić, and P. Klose. 'On Lepton Number Violation in Heavy Neut-rino Decays at Colliders'. In: *JHEP* 11 (2019), p. 32. DOI: 10.1007/JHEP11(2019)032. arXiv: 1907.13034 [hep-ph].

[46] G. Cvetič, A. Das, and J. Zamora-Saá. 'Probing Heavy Neutrino Oscillations in Rare W Boson Decays'. In: *J. Phys. G* 46.0954-3899; 1361-6471 (2019), p. 75002. DOI: 10.1088/1361-6471/ab1212. arXiv: 1805.00070 [hep-ph].

[47] G. Cvetič, A. Das, S. Tapia, and J. Zamora-Saá. 'Measuring the Heavy Neutrino Oscilla-tions in Rare W Boson Decays at the Large Hadron Collider'. In: *J. Phys. G* 47.1 (2020), p. 15001. DOI: 10.1088/1361-6471/ab4ee8. arXiv: 1905.03097 [hep-ph].

[48] J. Zamora-Saa. 'Resonant CP Violation in Rare $\tau^\pm$ Decays'. In: *JHEP* 05 (2017), p. 110. DOI: 10.1007/JHEP05(2017)110. arXiv: 1612.07656 [hep-ph].

[49] S. Tapia and J. Zamora-Saá. 'Exploring CP-Violating Heavy Neutrino Oscillations in Rare Tau Decays at Belle II'. In: *Nucl. Phys. B* 952 (2020), p. 114936. DOI: 10.1016/j.nuclphysb.2020.114936. arXiv: 1906.09470 [hep-ph].

[50] A. Das, P. S. B. Dev, and R. N. Mohapatra. 'Same Sign versus Opposite Sign Dileptons as a Probe of Low Scale Seesaw Mechanisms'. In: *Phys. Rev. D* 97.UMD-PP-017-30 (2018), p. 15018. DOI: 10.1103/PhysRevD.97.015018. arXiv: 1709.06553 [hep-ph].

[51] S. Antusch, E. Cazzato, M. Drewes, O. Fischer, B. Garbrecht, D. Gueter, and J. Klaric. 'Probing Leptogenesis at Future Colliders'. In: *JHEP* 09.TUM-1160/18, CP3-17-48 (2018), p. 124. DOI: 10.1007/JHEP09(2018)124. arXiv: 1710.03744 [hep-ph].

[52] P. S. Bhupal Dev, R. N. Mohapatra, and Y. Zhang. 'CP Violating Effects in Heavy Neutrino Oscillations: Implications for Colliders and Leptogenesis'. In: *JHEP* 11 (2019), p. 137. DOI: 10.1007/JHEP11(2019)137. arXiv: 1904.04787 [hep-ph].

[53] A. Denner, H. Eck, O. Hahn, and J. Kublbeck. 'Feynman Rules for Fermion Number Violating Interactions'. In: *Nucl. Phys. B* 387.CERN-TH-6549-92 (1992), pp. 467–481. DOI: 10.1016/0550-3213(92)90169-C.

[54] R. Jacob and R. G. Sachs. 'Mass and Lifetime of Unstable Particles'. In: *Phys. Rev.* 121.1 (Jan. 1961), pp. 350–356. DOI: 10.1103/PhysRev.121.350.

[55] J.-L. Tastet and I. Timiryasov. 'Dirac vs. Majorana HNLs (and Their Oscillations) at SHiP'. In: *JHEP* 04 (2020), p. 5. DOI: 10.1007/JHEP04(2020)005. arXiv: 1912.05520 [hep-ph].

[56] S. Antusch, E. Cazzato, and O. Fischer. 'Sterile Neutrino Searches via Displaced Ver-tices at LHCb'. In: *Phys. Lett. B* 774 (2017), pp. 114–118. DOI: 10.1016/j.physletb.2017.09.057. arXiv: 1706.05990 [hep-ph].

[57] *LHCb*. 'LHCb Detector Performance'. In: *Int. J. Mod. Phys. A* 30.LHCB-DP-2014-002, CERN-PH-EP-2014-290 (2015), p. 1530022. DOI: 10.1142/S0217751X15300227. arXiv: 1412.6352 [hep-ex].

[58] J. Rich. 'Quantum Mechanics of Neutrino Oscillations'. In: *Phys. Rev. D* 48.9 (Nov. 1993), pp. 4318–4325. DOI: 10.1103/PhysRevD.48.4318.

[59] W. Grimus, P. Stockinger, and S. Mohanty. 'The Field Theoretical Approach to Coherence in Neutrino Oscillations'. In: *Phys. Rev. D* 59.UWTHPH-1998-40, PRL-TH-1998 (1999), p. 13011. DOI: 10.1103/PhysRevD.59.013011. arXiv: hep-ph/9807442.

[60] W. Grimus, S. Mohanty, and P. Stockinger. 'Neutrino Oscillations and the Effect of the Finite Lifetime of the Neutrino Source'. In: *Phys. Rev. D* 61.UWTHPH-1999-14, PRL-TH-1999 (2000), p. 33001. DOI: 10.1103/PhysRevD.61.033001. arXiv: hep-ph/9904285.

[61] J. Campagne. 'Neutrino Oscillations from Pion Decay in Flight'. In: *Physics Letters B* 400.1 (1997), pp. 135–144. ISSN: 0370-2693. DOI: 10.1016/S0370-2693(97)00328-6.

[62] A. D. Dolgov. 'Neutrino Oscillations and Cosmology'. *International School of Astrophysics, Daniel Chalonge: 7th Course: Current Topics in Astrofundamental Physics (A NATO Advanced Study Institute Euroconference)*. Dec. 1999, pp. 565–584. arXiv: hep-ph/0004032.

[63] M. Malinsky, J. C. Romao, and J. W. F. Valle. 'Novel Supersymmetric SO(10) Seesaw Mechanism'. In: *Phys. Rev. Lett.* 95.IFIC-05-28 (2005), p. 161801. DOI: 10.1103/PhysRevLett.95.161801. arXiv: hep-ph/0506296.

[64] S. Antusch, C. Hohl, S. F. King, and V. Susic. 'Non-Universal Z' from SO(10) GUTs with Vector-like Family and the Origin of Neutrino Masses Tmptmp'. In: *Nucl. Phys. B* 934 (2018), pp. 578–605. DOI: 10.1016/j.nuclphysb.2018.07.022. arXiv: 1712.05366 [hep-ph].

[65] S. Antusch, S. Blanchet, M. Blennow, and E. Fernandez-Martinez. 'Non-Unitary Leptonic Mixing and Leptogenesis'. In: *JHEP* 01.MPP-2009-175, UMD-PP-09-056 (2010), p. 17. DOI: 10.1007/JHEP01(2010)017. arXiv: 0910.5957 [hep-ph].

[66] M. B. Gavela, T. Hambye, D. Hernandez, and P. Hernandez. 'Minimal Flavour Seesaw Models'. In: *JHEP* 09.FTUAM-09-09, IFT-UAM-CSIC-09-27, ULB-TH-09-15, IFIC-09-22, FTUV-09-0607 (2009), p. 38. DOI: 10.1088/1126-6708/2009/09/038. arXiv: 0906.1461 [hep-ph].

[67] I. Esteban, M. C. Gonzalez-Garcia, M. Maltoni, T. Schwetz, and A. Zhou. *NuFIT 4.1. Three-neutrino Fit Based on Data Available in 2019.* http://www.nu-fit.org. 2019.

[68] I. Esteban, M. C. Gonzalez-Garcia, A. Hernandez-Cabezudo, M. Maltoni, and T. Schwetz. 'Global Analysis of Three-Flavour Neutrino Oscillations: Synergies and Tensions in the Determination of ϑ_{23}, δ_{CP}, and the Mass Ordering'. In: *JHEP* 01.IFT-UAM/CSIC-18-112, YITP-SB-18-34 (2019), p. 106. DOI: 10.1007/JHEP01(2019)106. arXiv: 1811.05487 [hep-ph].

[69] *SNO.* 'Direct Evidence for Neutrino Flavor Transformation from Neutral Current Interactions in the Sudbury Neutrino Observatory'. In: *Phys. Rev. Lett.* 89 (2002), p. 11301. DOI: 10.1103/PhysRevLett.89.011301. arXiv: nucl-ex/0204008.

[70] J. Schechter and J. W. F. Valle. 'Neutrinoless Double Beta Decay in SU(2)×U(1) Theories'. In: *Phys. Rev. D* 25.SU-4217-213, COO-3533-213 (1982), p. 2951. DOI: 10.1103/PhysRevD.25.2951.

[71] W. H. Furry. 'On Transition Probabilities in Double Beta-Disintegration'. In: *Phys. Rev.* 56 (1939), pp. 1184–1193. DOI: 10.1103/PhysRev.56.1184.

[72] J. Kersten and A. Y. Smirnov. 'Right-Handed Neutrinos at CERN LHC and the Mechanism of Neutrino Mass Generation'. In: *Phys. Rev. D* 76 (2007), p. 73005. DOI: 10.1103/PhysRevD.76.073005. arXiv: 0705.3221 [hep-ph].

[73] M. Gell-Mann and A. Pais. 'Behavior of Neutral Particles under Charge Conjugation'. In: *Phys. Rev.* 97 (1955), pp. 1387–1389. DOI: 10.1103/PhysRev.97.1387.

[74] B. Pontecorvo. 'Neutrino Experiments and the Problem of Conservation of Leptonic Charge'. In: *Sov. Phys. JETP* 26 (1968), pp. 984–988. Original in: *Zh. Eksp. Teor. Fiz.* 53 (1967), pp. 1717–1725.

[75] K. Lande, E. T. Booth, J. Impeduglia, L. M. Lederman, and W. Chinowsky. 'Observation of Long-Lived Neutral V Particles'. In: *Phys. Rev.* 103 (1956), pp. 1901–1904. DOI: 10.1103/PhysRev.103.1901.

[76] *ARGUS*. 'Observation of B⁰-B̄⁰ Mixing'. In: *Phys. Lett. B* 192.DESY-87-029 (1987). Ed. by J. Tran Thanh Van, pp. 245–252. DOI: 10.1016/0370-2693(87)91177-4.

[77] *CDF*. 'Observation of B_s^0 - $\bar{B}_s^0$ Oscillations'. In: *Phys. Rev. Lett.* 97.FERMILAB-PUB-06-344-E, CDF-8522 (2006), p. 242003. DOI: 10.1103/PhysRevLett.97.242003. arXiv: hep-ex/0609040.

[78] *LHCb*. 'Observation of D^0 - $\bar{D}^0$ Oscillations'. In: *Phys. Rev. Lett.* 110.CERN-PH-EP-2012-333, LHCB-PAPER-2012-038 (2013), p. 101802. DOI: 10.1103/PhysRevLett.110.101802. arXiv: 1211.1230 [hep-ex].

[79] C. Giunti. 'Neutrino Wave Packets in Quantum Field Theory'. In: *JHEP* 11 (2002), p. 17. DOI: 10.1088/1126-6708/2002/11/017. arXiv: hep-ph/0205014.

[80] D. Wyler and L. Wolfenstein. 'Massless Neutrinos in Left-Right Symmetric Models'. In: *Nucl. Phys. B* 218.CERN-TH-3435 (1983), pp. 205–214. DOI: 10.1016/0550-3213(83)90482-0.

[81] E. K. Akhmedov, M. Lindner, E. Schnapka, and J. W. F. Valle. 'Left-Right Symmetry Breaking in NJL Approach'. In: *Phys. Lett. B* 368.IC-95-125, TUM-HEP-221-95, MPI-PHT-95-35, FTUV-95-34, IFIC-95-36 (1996), pp. 270–280. DOI: 10.1016/0370-2693(95)01504-3. arXiv: hep-ph/9507275.

[82] E. K. Akhmedov, M. Lindner, E. Schnapka, and J. W. F. Valle. 'Dynamical Left-Right Symmetry Breaking'. In: *Phys. Rev. D* 53.IC-95-126, TUM-HEP-222-95, MPI-PHT-95-70, FTUV-95-36, IFIC-95-38 (1996), pp. 2752–2780. DOI: 10.1103/PhysRevD.53.2752. arXiv: hep-ph/9509255.

[83] R. N. Mohapatra and J. W. F. Valle. 'Neutrino Mass and Baryon Number Nonconservation in Superstring Models'. In: *Phys. Rev. D* 34.MdDP-PP-86-127 (1986), p. 1642. DOI: 10.1103/PhysRevD.34.1642.

[84] R. N. Mohapatra. 'Mechanism for Understanding Small Neutrino Mass in Superstring Theories'. In: *Phys. Rev. Lett.* 56 (1986), pp. 561–563. DOI: 10.1103/PhysRevLett.56.561.

[85] S. Nandi and U. Sarkar. 'A Solution to the Neutrino Mass Problem in Superstring E6 Theory'. In: *Phys. Rev. Lett.* 56.DOE-ER40200-036 (1986), p. 564. DOI: 10.1103/PhysRevLett.56.564.

[86] A. Pilaftsis. 'Radiatively Induced Neutrino Masses and Large Higgs Neutrino Couplings in the Standard Model with Majorana Fields'. In: *Z. Phys. C* 55.MZ-TH-91-32 (1992), pp. 275–282. DOI: 10.1007/BF01482590. arXiv: hep-ph/9901206.

[87] A. Pilaftsis and T. E. J. Underwood. 'Electroweak-Scale Resonant Leptogenesis'. In: *Phys. Rev. D* 72 (2005), p. 113001. DOI: 10.1103/PhysRevD.72.113001. arXiv: hep-ph/0506107.

[88] J. Lopez-Pavon, E. Molinaro, and S. T. Petcov. 'Radiative Corrections to Light Neutrino Masses in Low Scale Type I Seesaw Scenarios and Neutrinoless Double Beta Decay'. In: *JHEP* 11 (2015), p. 30. DOI: 10.1007/JHEP11(2015)030. arXiv: 1506.05296 [hep-ph].

[89] I. Esteban, M. C. Gonzalez-Garcia, M. Maltoni, T. Schwetz, and A. Zhou. 'The Fate of Hints: Updated Global Analysis of Three-Flavor Neutrino Oscillations'. In: *JHEP* 09.IFT-UAM/CSIC-112, YITP-SB-2020-21 (2020), p. 178. DOI: 10.1007/JHEP09(2020)178. arXiv: 2007.14792 [hep-ph].

[90] I. Esteban, M. C. Gonzalez-Garcia, M. Maltoni, T. Schwetz, and A. Zhou. *NuFIT 5.2. Three-neutrino Fit Based on Data Available in November 2022*. http://www.nu-fit.org. 2022.

[91] S. Antusch, J. Hajer, and J. Rosskopp. *pSPSS. FeynRules Model File. Phenomenological Symmetry Protected Seesaw Scenario.* https://feynrules.irmp.ucl.ac.be/wiki/pSPSS. Oct. 2022. DOI: 10.5281/zenodo.7268362. GitHub: heavy-neutral-leptons/pSPSS.

[92] A. Alloul, N. D. Christensen, C. Degrande, C. Duhr, and B. Fuks. 'FeynRules 2.0. A Complete Toolbox for Tree-Level Phenomenology'. In: *Comput. Phys. Commun.* 185.CERN-PH-TH-2013-239, MCNET-13-14, IPPP-13-71, DCPT-13-142, PITT-PACC-1308 (2014), pp. 2250–2300. DOI: 10.1016/j.cpc.2014.04.012. arXiv: 1310.1921 [hep-ph]. Code: *FeynRules. A Mathematica Package to Calculate Feynman Rules.* https://feynrules.irmp.ucl.ac.be. June 2008.

[93] J. Alwall et al. 'The Automated Computation of Tree-Level and next-to-Leading Order Differential Cross Sections, and Their Matching to Parton Shower Simulations'. In: *JHEP* 07.CERN-PH-TH-2014-064, CP3-14-18, LPN14-066, MCNET-14-09, ZU-TH-14-14 (2014), p. 79. DOI: 10.1007/JHEP07(2014)079. arXiv: 1405.0301 [hep-ph]. Code: *MadGraph5_aMC@NLO. A Monte Carlo at next-to-Leading Order.* http://madgraph.phys.ucl.ac.be. Jan. 1994. GitHub: mg5amcnlo/mg5amcnlo.

[94] E. Fernández-Martínez, X. Marcano, and D. Naredo-Tuero. 'HNL Mass Degeneracy: Implications for Low-Scale Seesaws, LNV at Colliders and Leptogenesis'. IFT-UAM/CSIC-22-104 (Sept. 2022). arXiv: 2209.04461 [hep-ph].

[95] M. Drewes and J. Hajer. 'Heavy Neutrinos in Displaced Vertex Searches at the LHC and HL-LHC'. In: *JHEP* 02.CP3-19-11 (2020), p. 70. DOI: 10.1007/JHEP02(2020)070. arXiv: 1903.06100 [hep-ph].

[96] M. Chrząszcz, M. Drewes, and J. Hajer. 'HECATE: A Long-Lived Particle Detector Concept for the FCC-ee or CEPC'. In: *Eur. Phys. J. C* 81.CP3-20-48 (2021), p. 546. DOI: 10.1140/epjc/s10052-021-09253-y. arXiv: 2011.01005 [hep-ph].

[97] J. Alimena et al. 'Searches for Long-Lived Particles at the Future FCC-ee' (Mar. 2022). DOI: 10.3389/fphy.2022.967881. arXiv: 2203.05502 [hep-ex].

[98] S. Antusch, O. Fischer, and A. Hammad. 'Lepton-Trijet and Displaced Vertex Searches for Heavy Neutrinos at Future Electron-Proton Colliders'. In: *JHEP* 03 (2020), p. 110. DOI: 10.1007/JHEP03(2020)110. arXiv: 1908.02852 [hep-ph].

[99] J. Rosskopp and O. Mattelaer. *Automatic Width Computation with Small Mass Gap.* https://answers.launchpad.net/mg5amcnlo/+question/702099. June 2022.

[100] C. Bierlich et al. 'A Comprehensive Guide to the Physics and Usage of PYTHIA 8.3'. LU-TP 22-16, MCNET-22-04, FERMILAB-PUB-22-227-SCD (Mar. 2022). arXiv: 2203.11601 [hep-ph].

[101] J. de Favereau, C. Delaere, P. Demin, A. Giammanco, V. Lemaître, A. Mertens, and M. Selvaggi. 'DELPHES 3. A Modular Framework for Fast Simulation of a Generic Collider Experiment'. In: *JHEP* 02 (2014), p. 57. DOI: 10.1007/JHEP02(2014)057. arXiv: 1307.6346 [hep-ex].

[102] S. Bobrovskyi, W. Buchmüller, J. Hajer, and J. Schmidt. 'Quasi-Stable Neutralinos at the LHC'. In: *JHEP* 09.DESY-11-077 (2011), p. 119. DOI: 10.1007/JHEP09(2011)119. arXiv: 1107.0926 [hep-ph].

[103] S. Bobrovskyi, J. Hajer, and S. Rydbeck. 'Long-Lived Higgsinos as Probes of Gravitino Dark Matter at the LHC'. In: *JHEP* 02.DESY-12-175 (2013), p. 133. DOI: 10.1007/JHEP02(2013)133. arXiv: 1211.5584 [hep-ph].

[104] *CMS*. 'Search for Long-Lived Particles That Decay into Final States Containing Two Muons, Reconstructed Using Only the CMS Muon Chambers'. CMS-PAS-EXO-14-012 (2015). CDS: 2005761.

[105] *CMS*. 'Search for Displaced Supersymmetry in Events with an Electron and a Muon with Large Impact Parameters'. In: *Phys. Rev. Lett.* 114.CMS-B2G-12-024, CERN-PH-EP-2014-219 (2015), p. 61801. DOI: 10.1103/PhysRevLett.114.061801. arXiv: 1409.4789 [hep-ex].

[106] *Particle Data Group*. 'Review of Particle Physics'. In: *PTEP* 2022 (2022), p. 83C01. DOI: 10.1093/ptep/ptac097.

[107] *FCC*. 'FCC-ee: The Lepton Collider: Future Circular Collider Conceptual Design Report Volume 2'. In: *Eur. Phys. J. ST* 228.CERN-ACC-2018-0057 (2019), pp. 261–623. DOI: 10.1140/epjst/e2019-900045-4.

[108] *FCC*. 'FCC-hh: The Hadron Collider: Future Circular Collider Conceptual Design Report Volume 3'. In: *Eur. Phys. J. ST* 228.CERN-ACC-2018-0058 (2019), pp. 755–1107. DOI: 10.1140/epjst/e2019-900087-0.

[109] J. Alwall, M. Herquet, F. Maltoni, O. Mattelaer, and T. Stelzer. 'MadGraph 5. Going Beyond'. In: *JHEP* 06.FERMILAB-PUB-11-448-T (2011), p. 128. DOI: 10.1007/JHEP06(2011)128. arXiv: 1106.0522 [hep-ph].

[110] O. Aberle et al. 'High-Luminosity Large Hadron Collider (HL-LHC): Technical Design Report'. Version 0.1. In: *CERN Yellow Reports: Monographs* 4 (2017). Ed. by G. Apollinari, I. Béjar Alonso, O. Brüning, P. Fessia, M. Lamont, L. Rossi, and L. Tavian. DOI: 10.23731/CYRM-2017-004. №: CERN-2017-007-M.

[111] A. Blondel et al. 'Searches for long-lived particles at the future FCC-*ee*'. In: *Front. in Phys.* 10 (2022), p. 967881. DOI: 10.3389/fphy.2022.967881. arXiv: 2203.05502 [hep-ex].